PhD Thesis

Optimising MRI Magnetic Susceptibility Mapping for Applications in Challenging Regions of the Body

Anita Karsa

Supervisors: **Karin Shmueli**
Department of Medical Physics
and Biomedical Engineering

Shonit Punwani
Centre for Medical Imaging

University College London

2018

Acknowledgements

I would like to acknowledge all the people who helped my work over the past few years.

Firstly, I would like to express my sincere gratitude to my supervisors, Assoc Prof Dr Karin Shmueli and Prof Shonit Punwani, for their excellent supervision and guidance.

I would like to thank my colleagues in the MRI group, Dr Emma Biondetti, Dr Emma Dixon, Russell Murdoch, and Dr Barbara Dymerska for their friendly support and help with my work.

I highly appreciate the help of Dr Magdalena Sokolska, Dr Vincent Evans, and Dr Lebina Kakkar for their assistance with my late-night scanning sessions and Kyrie Phimister for her help organising these sessions. I am grateful to all the people who kindly volunteered to undergo an MRI scan for my research.

I would like to thank Dr Torben Schneider for his help with the Philips Pulse Programming Environment and issues related to image acquisition.

I am grateful to Dr Timothy J.P. Bray for his work in our collaborative project in bone marrow Quantitative Susceptibility Mapping, and for kindly allowing me to use the pelvic images he acquired as test cases for SEGUE, the phase unwrapping algorithm I developed.

I greatly appreciate that Assoc Prof Dr Simon Robinson kindly sent me the code for his simulated complex phase topography as a test case for SEGUE.

I am grateful to Dr Weng Sie Wong and Marina Santilli for their help with the dissemination of SEGUE through UCLB's online licensing portal.

I would like to thank Dr Alexey Dimov for his support with using SPURS, a recently developed fat-correction technique.

I appreciate the assistance of Maathini Balachandran, Fiona Gong, and Teresita Beeston in dealing with the administrative work and organising meetings.

I am grateful to Prof Daniel Alexander and Assoc Prof Dr Simon Robinson for kindly agreeing to examine this thesis.

Finally, I am infinitely thankful for my family and friends, especially my husband Máté Balogh, for their emotional support throughout my PhD.

Declaration

I, Anita Karsa confirm that the work presented in this thesis is my own. Where information has been derived from other sources, I confirm that this has been indicated in the thesis.

Abstract

Quantitative Susceptibility Mapping (QSM) is a recently developed Magnetic Resonance Imaging (MRI) technique that calculates the tissue magnetic susceptibility from MR phase images. While QSM is mostly used in brain images, it has great potential in other areas such as the head and neck where it has not yet been applied. Poorly oxygenated regions in head-and-neck tumours are expected to have a higher susceptibility due to the high concentration of paramagnetic deoxyhaemoglobin in the microvessels. Therefore, QSM could provide a non-invasive method for identifying hypoxic sites which are more resistant to radiation therapy.

Therefore, the main goal of this work was to develop and optimise a QSM pipeline for the head-and-neck region. Applying the complicated processing procedure of QSM to this region is particularly challenging due to:

- unavoidable subject motion (e.g. swallowing),
- air-tissue interfaces inducing large background fields to be removed,
- and fatty tissue introducing an additional, chemical shift-induced phase component to the MRI signal.

Moreover, as I have shown in the thesis, acquisition parameters such as image resolution and coverage of the region of interest have a substantial effect on measured susceptibilities. Therefore, tailoring the MRI acquisition is also crucial for accurate QSM in the head-and-neck region.

I conducted a comprehensive optimisation of both the MRI acquisition and the QSM pipeline for head-and-neck images and addressed all the aforementioned problems. I developed and optimised a 6-minute acquisition protocol and a QSM processing pipeline. I also created a highly efficient phase unwrapping algorithm for challenging regions. Then, I showed that QSM, using the optimised protocol and pipeline, has high repeatability in the head and neck.

Further, I applied this experience with a challenging region to clinical, pelvic MR images of the sacroiliac joint. I showed that bone marrow fat metaplasia has significantly higher susceptibility than normal bone marrow mainly due to its fat content.

Impact Statement

Magnetic Resonance Imaging (MRI) Quantitative Susceptibility Mapping (QSM) is moving closer to clinical application. Clinical MR images are often acquired with high in-plane resolution, but with thick slices and low through-plane coverage to decrease scan time, and increase patient comfort and throughput. I have shown that for accurate susceptibility maps, high through-plane resolution (i.e. more isotropic voxels) and sufficient coverage of the structure of interest are generally required. These results will likely influence clinical acquisition protocols to enable QSM to be utilised.

There is a pressing clinical need to identify hypoxic sites in head-and-neck cancer non-invasively to improve radiaton therapy prognosis. QSM is a promising candidate for measuring tissue oxygenation, but it has yet to be applied in head-and-neck studies. Here I have optimised the MRI acquisition and QSM pipeline for head-and-neck images. I have also shown that the optimised protocol is highly repeatable in healthy volunteers. Future proof-of-principle studies will now be possible to correlate the susceptibility and independently measured oxygenation of head-and-neck tumours. In the long term, this protocol might be used to routinely detect hypoxia in head-and-neck cancer.

Optimising the susceptibility mapping pipeline for head-and-neck images provided some general conclusions on applying QSM to challenging anatomical regions. I have found that while most current background field removal methods are suitable for brain images, Projection onto Dipole Fields is more robust than the Laplacian Boundary Value method when high susceptibility gradients are present. I have also demonstrated that using a Tikhonov regularisation term for the susceptibility calculation step outperforms many of the state-of-the-art methods in the head and neck, even though this approach is rarely used within the QSM community. These results could inform future studies focusing on challenging anatomical regions.

I have developed SEGUE, a new, fast, spatial, 3D phase unwrapping technique to deal with highly-wrapped phase images and challenging anatomical regions that were very difficult or time-consuming to unwrap using the current state-of-the-art method. SEGUE will be disseminated through UCL XIP as downloadable MATLAB scripts. Since phase unwrapping is the first step of the QSM pipeline, this technique has the potential to accelerate state-of-the-art research investigating a wide range of new QSM applications. Spatially unwrapped phase images are also routinely used for distortion correction in functional and diffusion MRI. SEGUE could substantially accelerate large-scale studies requiring distortion correction in the brain.

In collaboration with Dr Timothy J.P. Bray, I investigated QSM as a candidate technique to non-invasively measure bone mineral density (BMD) in inflamed bone marrow with the aim of monitoring disease progression in the future. We found that susceptibility has a linear relationship with both fat and bone content. This confirms that QSM can be used to measure the concentration of paramagnetic or diamagnetic substances in the tissue. However, we also demonstrated that susceptibility was more sensitive to changes in fat content and that fat contributions to susceptibility need to be accounted for to accurately estimate BMD. Our conclusions could inform future studies of QSM for musculoskeletal applications.

Contents

List of Abbreviations

3PD Three-point Dixon

AP Anterior-posterior

B0-NICE B0 off-resonance mapping by non-iterative correction of phase errors

BET Brain extraction tool

BFR Background field removal

BMD Bone mineral density

CSF Cerebrospinal fluid

CT Computed tomography

FF Fat fraction

FOV Field of view

GM Gray matter

GOOSE Globally optimal surface estimation

GRAPPA Generalized autocalibrating partially parallel acquisitions

GRE Gradient recalled echo

HF Head-foot

HNSCC Head-and-neck squamous cell carcinoma

IGCA Iterative graph cut algorithm

iLF Inverse Laplacian filtering

ISMRM International Society for Magnetic Resonance in Medicine

LBV Laplacian boundary value

LPU Laplacian phase unwrapping

LSQR Least squares

MEDI Morphology enabled dipole inversion

MR Magnetic resonance

MRI Magnetic resonance imaging

NPD N-point Dixon

NRMSE Normalised root mean square error

PDF Projection onto dipole fields

PRELUDE Phase region expanding labeller for unwrapping discrete estimates

PSF Point spread function

QSM Quantitative Susceptibility Mapping

RESHARP Regularisation-enabled SHARP

RF Radio frequency

RL Right-left

ROI Region of interest

RT Radiation therapy

SAD short-axis diameter

SAR Specific absorption rate

SC Susceptibility calculation

SD Standard deviation

SEGUE Speedy region-growing algorithm for unwrapping estimated phase

SENSE Sensitivity encoding

SHARP Sophisticated harmonic artifact reduction for phase data

SNR Signal-to-noise ratio

SPGR Spoiled gradient echo

SPURS Simultaneous phase unwrapping and removal of chemical shift

TE Echo time

TKD Truncated k-space division

TR Repetition time

TV Total variation

VOL volume

VSHARP Variable-radius SHARP

WM White matter

Thesis Overview

In chapter 1, I discuss the motivation behind my thesis, i.e. using Magnetic Resonance Imaging (MRI) Quantitative Susceptibility Mapping (QSM) could improve head-and-neck cancer prognosis. I introduce the theory of MRI and QSM as well as the challenges associated with optimising the MRI acquisition and QSM processing pipeline for the head and neck. As this is the first time QSM is applied to this anatomical region, the main goal of my thesis was to perform the aforementioned optimisation in chapter 6 informed by additional review and research I present in chapter 2–5.

One of the main challenges of adopting QSM, a method primarily applied in the brain, to the head and neck is the presence of fatty tissue in this region. There is a wide variety of fat correction strategies available to overcome this issue, but no established gold standard method exists for robust fat correction in the head and neck. Similarly, a range of different techniques have been developed in the past decade for each step of the QSM pipeline: (i) field fitting and phase unwrapping, (ii) background field removal, and (iii) susceptibility calculation, but there is no widely accepted optimal pipeline even for brain images. Therefore, in chapter 2, I describe and review state-of-the-art methods for reducing artifacts induced by fat content and a range of current techniques for each step of the QSM pipeline with a view to comparing the most promising methods using in-vivo head-and-neck images in chapter 6.

In chapter 3, I discuss the noise propagation along the QSM pipeline and the use of signal-to-noise ratio as a potential measure of image quality when comparing different methods, described in chapter 2, in in-vivo images in chapter 6.

In chapter 4, I introduce SEGUE, a new and fast phase unwrapping algorithm (step (i) of the QSM pipeline) I developed for highly wrapped images and challenging anatomical regions such as the head and neck.

In chapter 5, I demonstrate that acquiring images with high resolution and sufficient coverage of the structures of interest is necessary for accurate susceptibility mapping.

Chapter 6 focuses on the optimisation of the MRI acquisition and QSM processing pipeline for accurate susceptibility mapping in the head-and-neck region. In section 6.1, I identify the most accurate and robust method (of the ones described in chapter 2) for overcoming artifacts induced by fatty tissue using in-vivo head-and-neck images. Section 6.2 focuses on the optimisation of the MRI acquisition for head-and-neck QSM informed by the conclusions of chapter 5. Section 6.3 contains a quantitative comparison of dif-

ferent background field removal methods (step (ii) of the QSM pipeline) using ground truth evaluation and a realistic, numerical head-and-neck phantom. Finally, section 6.4 compares current techniques for each step of the QSM pipeline (described in chapter 2) using in-vivo head-and-neck images.

Finally, in chapter 7, I investigate the repeatability of the optimised MRI acquisition and QSM processing pipeline from chapter 6 in several brain regions, healthy lymph nodes, and the parotid and submandibular glands.

Additionally, I applied my experience with QSM in challenging anatomical regions to clinical, pelvic MR images of the sacroiliac joint in chapter 8. Here I introduce a work done in collaboration with Dr Timothy J.P. Bray on the non-invasive quantification of bone mineral density in the sacroiliac joint using QSM. This anatomical region has similar challenges to the head and neck, so a similar QSM pipeline to the one optimised for head-and-neck images in chapter 6 could be adopted.

I summarise my findings and discuss future work in chapter 9.

List of publications

Journal articles

Durighel, G., P. F. Tokarczuk, P. F., **Karsa, A.**, Gordon, F., Cook, S. A., and O'Regan D. P. Acute myocardial infarction: susceptibility-weighted cardiac MRI for the detection of reperfusion haemorrhage at 1.5 T. Clinical radiology 71, no. 3 (2016): e150-e156

Karsa, A., Punwani, S., and Shmueli, K. The effect of low resolution and coverage on the accuracy of susceptibility mapping. Magnetic Resonance in Medicine (2018) DOI: 10.1002/mrm.27542

Karsa, A., Bray, T.J.P., Bainbridge, A., Sakai, N., Punwani, S., Hall-Craggs, M.A., and Shmueli, K. Association of Bone Mineral Density and Fat Fraction with Magnetic Susceptibility in Inflamed Trabecular Bone. Magnetic Resonance in Medicine (2018) (accepted)

Karsa, A. and Shmueli, K. SEGUE: a Speedy rEgion-Growing algorithm for Unwrapping Estimated phase. IEEE Transactions in Medical Imaging (2018) (accepted)

Karsa, A., Punwani, S., and Shmueli, K. High Repeatability of QSM in the Head and Neck With a View to Detecting Hypoxic Cancer Sites. (in preparation for submission to Magnetic Resonance in Medicine)

Peer Reviewed Conference Abstracts (first-authored abstracts only)

Karsa, A., Biondetti, E., Punwani, S., and Shmueli, K. The effect of large slice thickness and spacing and low coverage on the accuracy of susceptibility mapping. In Proceedings of the 24th Annual Meeting of the ISMRM, Singapore (2016): p. 1555

Karsa, A., Punwani S., and Shmueli K. Investigating the Effect of Large Slice Thickness on the Accuracy of Susceptibility Mapping Using a Realistic Head and Neck Numerical Phantom. 4th International Workshop on MRI Phase Contrast and Quantitative Susceptibility Mapping (2016)

Karsa, A., Punwani, S., and Shmueli, K. Resolution and Coverage for Accurate Susceptibility Maps: Comparing Brain Images with Simulations. In Proceedings of the 25th Annual Meeting of the ISMRM, Honolulu (2017): p. 3677

Karsa, A. and Shmueli, K. SEGUE: a Speedy rEgion-Growing algorithm for Unwrapping Estimated phase. In Proceedings of the 26th Annual Meeting of the ISMRM, Paris (2018): p. 666

Karsa, A., Punwani, S., and Shmueli, K. Fat Correction of MRI Phase Images for Accurate Susceptibility Mapping in the Head and Neck. In Proceedings of the 25th Annual Meeting of the ISMRM, Paris (2018): p. 4988

Karsa, A., Bray T.J.P., Bainbridge A., Punwani, S., Hall-Craggs M.A., and Shmueli, K. Bone Marrow Susceptibility as a Marker of Bone Mineral Density in Spondyloarthritis. In Proceedings of the 25th Annual Meeting of the ISMRM, Paris (2018): p. 4989

Chapter 1

Introduction

1.1 Clinical context: Head-and-neck cancer and Quantitative Susceptibility Mapping

Head-and-neck (HN) cancers include cancers of the upper aerodigestive tract, the paranasal sinuses, and the salivary glands. Squamous cell carninoma (SCC) constitutes more than 90% of the cases and is one of the most common cancers worldwide [25, 26]. SCC arises from squamous cells, a type of skin cell found in moist tissues that line body cavities such as the airways [27].

The signs and symptoms of HNSCC include a sore throat, earache, difficulty swallowing, a hoarse voice, or enlarged lymph nodes [28]. HNSCC can occur in the mouth, throat, and nose, but often metastasises to lymph nodes close to the primary site [29] resulting in worse prognosis. Suspicious lesions are investigated using various imaging modalities such as computed tomography [30], positron emission tomography [31], and magnetic resonance imaging [32] but the diagnosis needs to be confirmed by a biopsy from the primary site [28].

Due to the location of these tumours, treatment of HNSCC can affect important functions such as speech, taste, smell, and swallowing. Therefore, post-treatment functional impairment should also be considered during treatment planning in addition to the likelihood of survival [26]. Furthermore, failure of treatment may increase the probability of distant metastasis [33]. These facts underline the importance of improving therapies targeting HNSCC.

It has been shown that for advanced tumours, a combined use of surgery and radiation therapy (RT), or chemotherapy and RT offer the highest chance of achieving a cure [34,35]. For early stage tumours, however, RT and surgical excision have similar cure rates, but RT offers better organ preservation [26]. Surgical procedure times vary up to 12 hours which means that patients are prone to complications arising from prolonged anaesthesia. A rate of 20%-40% of postoperative surgical site infection has been reported due to the oral or pharyngeal lumen being opened at some point during the treatment [26]. Removal of important neuromuscular structures to ensure tumour clearance is often inevitable during surgery. These factors can cause long term functional problems and a deterioration in quality of life [28]. In summary, HNSCC is often treated with RT combined with surgery or chemotherapy.

Head and neck tumours are often hypoxic, or have low oxygenation levels [36]. A large body of evidence associates tumour hypoxia with adverse prognosis after RT [36,37]. This can be attributed to the fact that oxygen is a potent radiosensitiser; in other words, cells in a highly oxygenated environment are more likely to be killed by RT. In the presence of oxygen, cell damage can be inflicted indirectly: ionising radiation forms free radicals of oxygen (an oxygen atom with an unpaired valence electron) which then damage the DNA of the cell due to their high reactivity. Since RT is the standard treatment for HNSCC, there is a pressing clinical need to measure oxygenation in head-and-neck tumours non-invasively and identify hypoxic sites that may be resistant to RT [38].

Quantitative Susceptibility Mapping (QSM) is a non-invasive Magnetic Resonance Imaging (MRI) technique that has been shown to be able to quantify venous oxygenation [39], but it has not been applied to HNSCC. The susceptibility of blood strongly correlates with its oxygenation due to the paramagnetic nature of deoxyhemoglobin [17] (i.e. poorly oxygenated blood is brighter in susceptibility maps). Therefore, we hypothesise that mapping of tissue magnetic susceptibility using QSM in the head and neck could provide information about the oxygenation of HNSCC tumours and metastasised lymph nodes through the higher susceptibility of deoxyhemoglobin-rich intratumoral vasculature in and around hypoxic sites.

In sections 1.2 and 1.3, I describe the basic physics behind MRI and QSM used in this thesis. In section 1.3.1, I estimate the expected magnetic susceptibility difference between hypoxic and normoxic tissue. In section 1.3.3, I describe the aim of this thesis, the technical challenges associated with head-and-neck QSM and refer to the chapters in which these are addressed. Finally, in section 1.4, I mention two more potential applications for an optimised QSM protocol.

1.2 Magnetic Resonance Imaging (MRI)

1.2.1 The MR signal

Magnetic resonance (MR) images are generated by placing the phantom, volunteer or patient into a static, homogeneous magnetic field (B_0 = 1.5 or 3 T in most clinical settings) which induces a net magnetisation vector within the tissue in the direction of B_0 (often referred to as the z axis) by aligning the magnetic moments (spins) of all nuclei with non-zero spins [1].

For measurement, a radio frequency (RF) excitation pulse is applied to displace the magnetisation vector towards the xy plane[1]. The excited magnetisation precesses about the main magnetic field (B_0) with angular frequency ω_0 (Figure 1.1 a), the Larmor frequency, given by the Larmor equation:

$$\omega_0 = \gamma B_0 \tag{1.1}$$

where γ is the gyromagnetic ratio, specific to each nuclei[2]. The aforementioned excitation process can be viewed as the application of a magnetic field, B_1, perpendicular to the main magnetic field. Similarly to the Larmor precession, this results is precession about B_1 and the displacement of the magnetisation vector (Figure 1.1 b):

$$\omega_1 = \gamma B_1 \tag{1.2}$$

$$\alpha = \omega_1 \tau \tag{1.3}$$

The duration of the excitation pulse (τ) determines the extent of the tilt (α, also referred to as the flip angle).

[1]Note that I am describing the classical interpretation of the magnetic resonance phenomenon. There exists a quantum mechanical explanation [1] leading to the same expressions used in this thesis.

[2]Often $f_0 = \frac{\omega_0}{2\pi} = \gamma B_0$ is referred to as the Larmor frequency, where $\gamma = \frac{\gamma}{2\pi}$

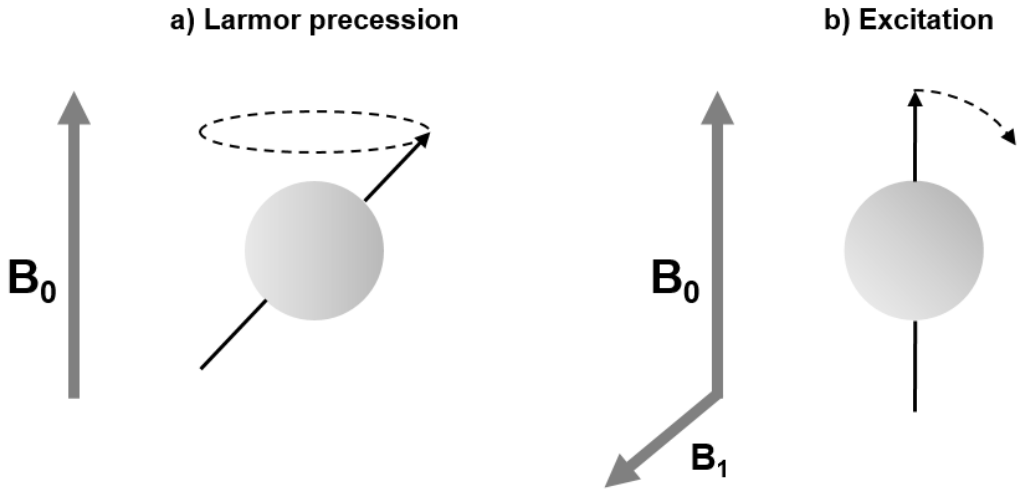

Figure 1.1: Precession of a magnetic dipole about the main magnetic field (a) and its excitation using a perpendicular RF pulse (b).

Note that $B_1 << B_0$, and all spins start precessing about B_0 the instant they are slightly tilted. Therefore, for efficient excitation, B_1 also needs to rotate about B_0 with the Larmor frequency and remain perpendicular to the spins. Since γ and, consequently, ω_0 is specific for each nuclei, this means that an RF pulse of a certain frequency can displace only the nuclei of matching Larmor frequencies. There are a number of nuclei in the human body with non-zero spins (e.g. ^{13}C, ^{23}Na, ^{35}Cl), but ^{1}H (proton) is the most commonly examined due to its very high $\gamma = 2\pi \cdot \left(42.6\frac{MHz}{T}\right)$ and its abundance in the human body, both of which translates to high measured signal.

Note that the excitation pulse deposits energy in the body which could result in burns. To avoid this, MRI scanners estimate the so-called specific absorption rate (SAR: the amount of energy accumulated in a certain mass of tissue measured in W/kg) from the sequence parameters and the total body mass of the subject. There are international guidelines for SAR limits in the human body [2].

In MRI, the projection of the excited magnetisation vector to the xy plane is measured. The xy plane can also be regarded as the complex plane where the projected magnetisation vector has real and imaginary components (Figure 1.2). These two components of the precessing magnetisation vector are measured through the alternating current it induces in the receiver coil(s) of the MR device.

Local field variations (ΔB) alter the frequency of the Larmor precession:

$$\omega = \gamma(B_0 + \Delta B) = \omega_0 + \Delta\omega \tag{1.4}$$

In practice, only the additional $\Delta\omega$ frequency affects the MR images, as the signal is measured in a rotating frame of angular frequency ω_0. In other words, frequency and field values are expressed relative to ω_0 and B_0.

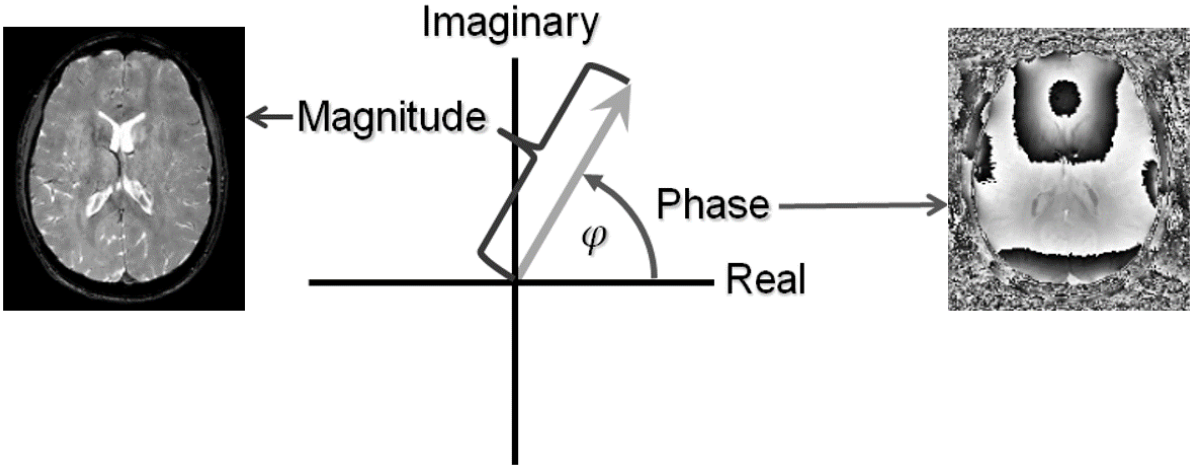

Figure 1.2: The magnetisation vector can be interpreted as a complex number with real and imaginary components as well as magnitude and phase. The magnitude (left figure) and phase (right figure) components of the MR image form separate maps. Figure courtesy of Karin Shmueli.

Instead of considering the real and imaginary components, one might also think of the MRI signal as the magnitude (M) and phase (φ) (Figure 1.2) of the magnetisation vector measured at the echo time TE. Both M and φ depend on the acquisition pulse sequence, a combination of excitation pulses and magnetic field gradients (e.g. Figure 1.4). The magnitude of the signal is affected by different relaxation processes throughout the acquisition. The spin-lattice and spin-spin relaxations are inherent and irreversible processes with relaxation times T_1 and T_2 respectively. The T_2^* relaxation is a combination of the T_2 relaxation and a dephasing process, with relaxation time T_2', caused by the microscopic local field variations (ΔB):

$$\frac{1}{T_2^*} = \frac{1}{T_2} + \frac{1}{T_2'} \tag{1.5}$$

A spin-echo sequence reverses this dephasing using a 180° refocusing pulse [3]. Gradient-echo sequences (Figure 1.4) preserve the natural phase evolution, thus the images are affected by ΔB through the T_2' relaxation process. The main sources of ΔB are the tissue susceptibility variations. Therefore, to calculate susceptibility maps, data need to be acquired with a gradient-echo pulse sequence.

Due to the Larmor precession, the temporal evolution of the phase in a gradient-echo sequence is linear and the phase value at echo time TE can be expressed as:

$$\varphi = \varphi_0 + \Delta\omega \cdot \mathrm{TE} = \varphi_0 + \gamma \Delta B \cdot \mathrm{TE} \tag{1.6}$$

where φ_0 is the initial phase that mostly reflects the complicated coil sensitivity pattern. Note that a voxel might contain different components with different corresponding Larmor frequencies, e.g. water and fat protons (sections 1.3.2 and 6.1.1). Since the measured signal is the complex sum of the signals originating from each compartment, the phase measured in a voxel can have a non-linear behaviour over time [4, 5]. In fact, frequency difference mapping is a technique used to study tissue microstructure by analysing this non-linear phase evolution [6]. Furthermore, some post-acquisition image processing algorithms can affect the linearity of the phase over time (section 2.2.2.2). In this thesis, I ignore the effects of the microstructure on the phase evolution as these are likely to be negligible in the head and neck.

Although in clinical practice, it is usually the magnitude image that is considered (Figure 1.2, left), it has been shown that in images acquired with gradient-echo, the phase map (Figure 1.2, right) carries useful and complementary information. Duyn et al. [7] have demonstrated that phase images at 7 T have better contrast between the gray matter (GM) and the white matter (WM) than magnitude images. Also, fine WM structures and variations across the cortical thickness were only visible in the phase maps.

In conclusion, MR images obtained with a gradient-echo sequence carry useful and complementary information in their magnitude and phase. The phase of the signal is related to the local magnetic field variations (ΔB) experienced by the tissue at a specific voxel (Equation 1.6).

1.2.2 The gradient-echo sequence

In MRI, signal is measured using a radio frequency (RF) pulse to excite protons within the body followed by spatial encoding to obtain a 3D volume via the use of magnetic field gradients applied in three orthogonal directions (Figure 1.3). Note that G_s, G_p and G_f can have any orientation as long as they are orthogonal.

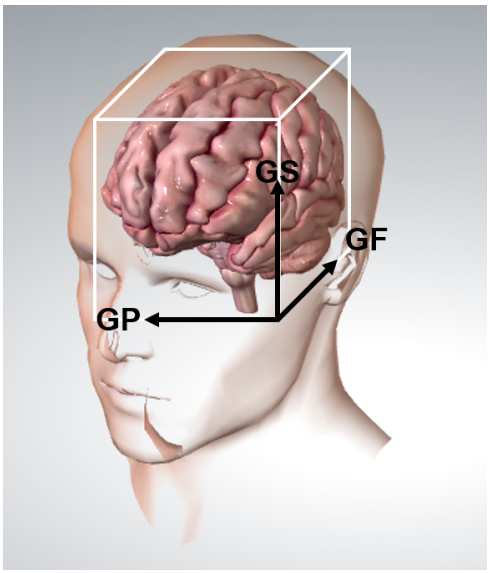

Figure 1.3: Spatial encoding gradients for: slice encoding or slice selection (G_s), phase encoding (G_p) and frequency encoding (G_f).

Figure 1.4 shows the elements of a gradient-echo sequence for both 2D and 3D acquisitions. In the next few paragraphs, I explain these components in more detail.

In standard 2D gradient-echo pulse sequences, first, protons are excited in a single slice by applying the RF pulse (Figure 1.4 a) and a slice selection gradient (G_s, Figure 1.4 b) simultaneously. This gradient slightly alters the Larmor frequencies of the protons along the slice select direction according to the following equation:

$$\omega(s) = \gamma\,(B_0 + G_s \cdot s) \tag{1.7}$$

where s is the distance along the slice selection gradient. Therefore, RF pulses of different frequencies excite different slices.

Secondly, k-space data[3] in the selected slice are acquired. Phase encoding (G_p, Figure 1.4 c) is used to select a line within the slice in k-space followed by frequency encoding or a readout gradient (G_f, Figure 1.4 d) to measure complex signal values (real and imaginary components) along said line in k-space. After repetition time TR, the same slice is excited and a different k-space line is acquired (Figure 1.4). Finally, the acquired k-space data is transformed into the image domain using the 2D inverse Fourier transform:

$$M(x,y) = \int_{-\infty}^{\infty}\int_{-\infty}^{\infty} S(k_x,k_y)e^{2\pi i(k_x x + k_y y)}dxdy \tag{1.8}$$

where (x, y) are the image domain coordinates, (k_x, k_y) are the k-space coordinates, S is the signal acquired in k-space, and M is the corresponding data in the image domain.

[3]The Fourier space in MRI.

In 3D gradient-echo pulse sequences, no slice selection gradient is used during the RF pulse, therefore the entire volume is excited[4]. A phase encoding (G_p), and a slice encoding or second phase encoding (G_s, Figure 1.4 b) gradients are used to select the k-space line to be acquired in the volume. In this case, the entire volume is acquired in k-space and is transformed into the image domain using the 3D inverse Fourier transform:

$$M(x,y,z) = \int_{-\infty}^{\infty}\int_{-\infty}^{\infty}\int_{-\infty}^{\infty} S(k_x,k_y,k_z)e^{2\pi i(k_x x+k_y y+k_z z)}dxdydz \tag{1.9}$$

$$M(\mathbf{r}) = \int_{-\infty}^{\infty} S(\mathbf{k})e^{2\pi i\mathbf{kr}}d\mathbf{r} \tag{1.10}$$

where $\mathbf{r} = (x,y,z)$ are the image domain coordinates, $\mathbf{k} = (k_x,k_y,k_z)$ are the k-space coordinates, S is the signal acquired in k-space, and M is the corresponding data in the image domain.

To obtain a ΔB map, phase maps at multiple echo times (TEs) need to be acquired during signal relaxation enabling us to perform a linear fit (Equation 1.6). This can be achieved by a series of G_f gradients in either a monopolar or a bipolar fashion (Figure 1.4 d) for both 2D and 3D imaging. Note that ΔB could also be calculated from a single echo if φ_0 (Equation 1.6) is estimated from e.g. a reference scan [8] or approximated from the acquired data [9]. However, all images presented in this thesis are multi echo.

At the end of each TR cycle, spoiler gradients may be applied in each direction (SPoiled Gradient echo - SPGR sequence, Figure 1.4 e) to cause rapid dephasing of the transverse magnetisation vector. This is used to avoid unwanted signal at later cycles appearing due to accidental coherence of these residual magnetisations.

In gradient-echo sequences, maximum signal for a given TR can be achieved by using the Ernst angle as the flip angle [3]:

$$\alpha = \arccos\left(e^{-\frac{\mathrm{TR}}{T_1}}\right) \tag{1.11}$$

[4]Alternatively, a slab-selective gradient might be used to excite only the field-of-view to be imaged followed by 3D spatial encoding.

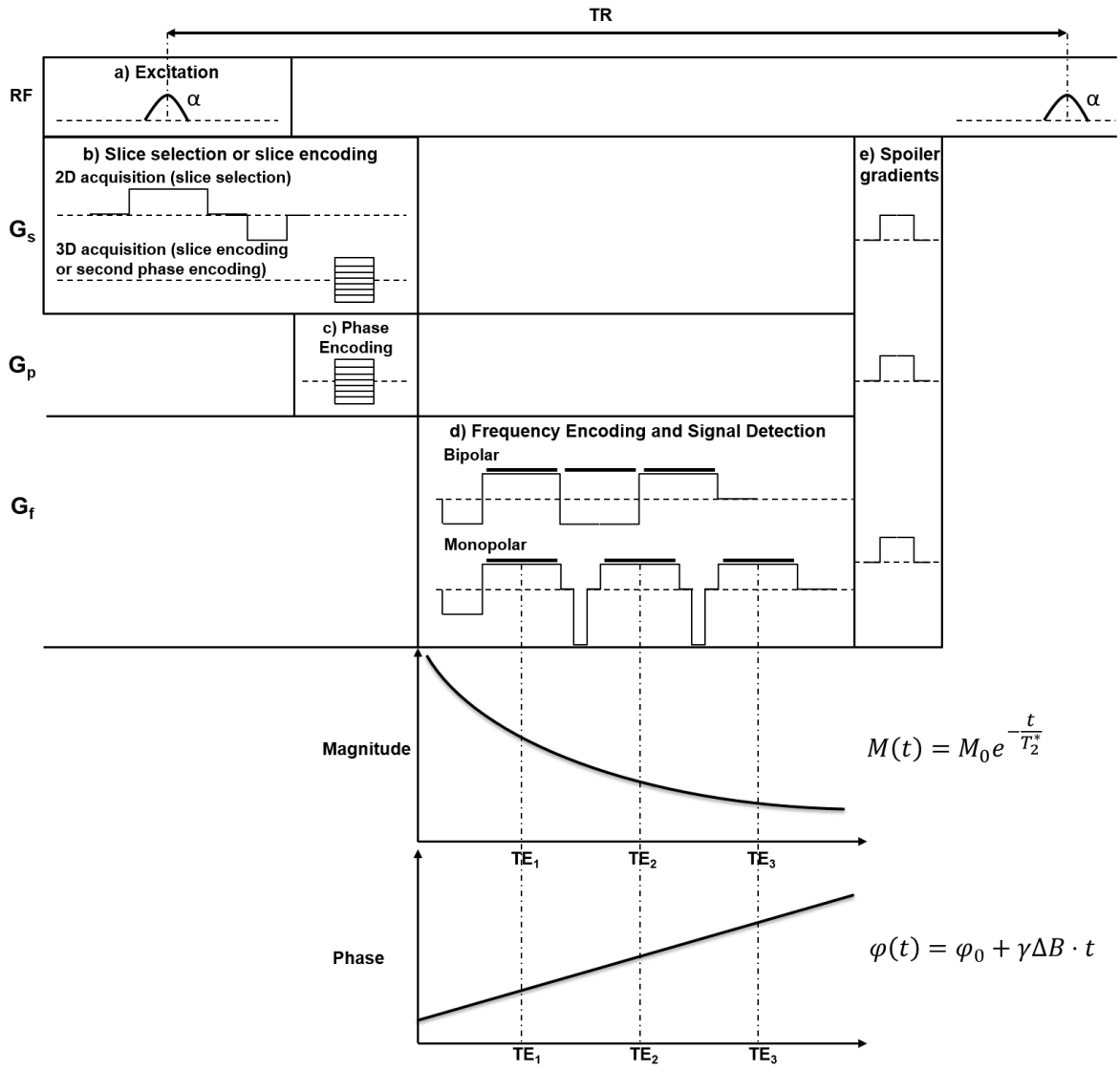

Figure 1.4: Gradient-echo pulse sequences. An excitation pulse (a) is used to tip the magnetisation vector from the z direction towards the xy plane. Slice and phase encoding gradients are applied to select a line in k-space (b and c). Frequency encoding is used and signal is measured (thick lines) along a line in k-space at multiple echoes (d, the echo times correspond to the monopolar acquisition). Spoiler gradients might be used to eliminate the xy component of the magnetisation vector before the next excitation (e).

1.2.2.1 2D and 3D gradient-echo acquisitions

In 3D acquisitions, multi-echo data along one k-space line are acquired in one TR using low flip angle and short TR for maximum signal (Equation 1.11). Therefore, TR $\sim$ TE_{last}, the last echo time, to fit all echoes in one cycle. This needs to be repeated for all phase encoding and slice encoding (or second phase encoding) steps. Therefore, the total acquisition time $T_{scan} = \mathrm{TR} \cdot N_{phase} \cdot N_{slice} \sim \mathrm{TE}_{last} \cdot N_{phase} \cdot N_{slice}$ where N_{phase} and N_{slice} are the number of phase and slice encoding steps respectively.

In multislice 2D acquisitions, k-space lines in multiple slices are excited and acquired in one cycle (Figure 1.5). This is achieved by using long TR and, consequently, a large flip angle (Equation 1.11). Data from approximately $N_{slice,\mathrm{TR}} = \lfloor \frac{\mathrm{TR}}{\mathrm{TE}_{last}} \rfloor$ slices are acquired in one cycle. Therefore, the total scan time is about $T_{scan} = \mathrm{TR} \cdot N_{phase} \cdot \frac{N_{slice}}{N_{slice,\mathrm{TR}}} \sim \mathrm{TE}_{last} \cdot N_{phase} \cdot N_{slice}$, where N_{slice} is the number of slices. In conclusion, scan time is not substantially different for a multislice 2D, and a 3D acquisition.

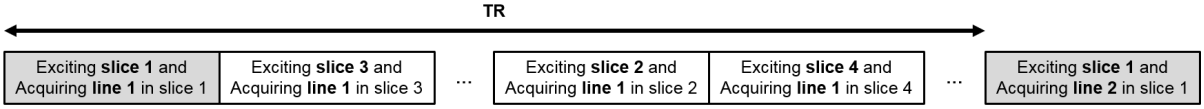

Figure 1.5: Multislice 2D acquisition. Data in multiple slices are acquired within one TR. Note that the slice ordering is 1, 3, 5 ... 2, 4, 6 to avoid spillover from neighbouring slices induced by slice profile effects.

A 2D sequence allows for the acquisition of thin, individual slices separated by gaps, while in 3D acquisition, only contiguous slices can be acquired and decreasing the resolution leads to larger voxels. However, due to practical limitations, the slice profile is not perfectly rectangular when using a 2D sequence, which can lead to slice profile artifacts and also limits how thin the excited slices can be. Moreover, 2D acquisitions might be corrupted by slice inconsistencies due to patient motion (or possibly slice profile effects) manifesting in stripes [10] (Figure 1.6).

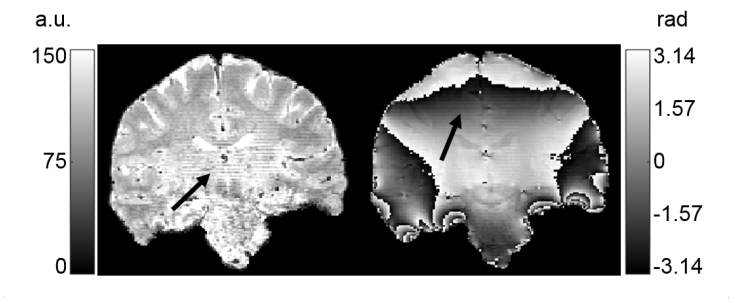

Figure 1.6: Stripes appearing in magnitude and phase images of a brain acquired with a 2D gradient echo sequence.

When the size of the imaged object exceeds the field of view (FOV) in a phase encoding (or slice encoding in 3D sequences) direction, images are often corrupted by aliasing or folding over of anatomy at the edges of the FOV [11]. Therefore, the FOV can only be substantially reduced in the frequency encoding (for 2D and 3D acquisitions) or the slice selection (for 2D acqusitions) directions to avoid aliasing. However, decreasing the coverage in the frequency encoding direction only slightly shortens the total scan time through reducing the duration of frequency encoding in the gradient-echo sequence in

Figure 1.4 d. Reducing the FOV in the slice selection direction decreases N_{slice}, meaning that T_{scan} is linearly related to the coverage which is a more efficient way of reducing scan time.

1.2.2.2 Signal-to-noise ratio (SNR) in gradient-echo images

For gradient-echo sequences, the magnitude of the MR signal at echo time TE is given by [3]:

$$M \propto \rho_0 \cdot \frac{\sin\alpha \cdot \left(1 - e^{-\frac{\mathrm{TR}}{T_1}}\right) \cdot e^{-\frac{\mathrm{TE}}{T_2^*}}}{\left(1 - \cos\alpha \cdot e^{-\frac{\mathrm{TR}}{T_1}}\right)} \tag{1.12}$$

where ρ_0 is the proton density in the observed voxel. The signal-to-noise ratio (SNR) for 2D and 3D gradient-echo pulse sequences can be approximated by [12]:

$$\mathrm{SNR} \propto M \cdot \Delta V \sqrt{\frac{N_{slice} \cdot N_{phase}}{bw}} \tag{1.13}$$

where ΔV is the volume of a single voxel, bw is the bandwidth per pixel, and $N_{slice} = 1$ for 2D sequences. Note that this expression refers to the SNR in the magnitude images. Substituting typical sequence and tissue parameters (i.e. $\alpha_{2D} = 90°$, $\alpha_{3D} = 10°$, $\mathrm{TR}_{2D} = 4$ s, $\mathrm{TR}_{3D} = 20$ ms, $N_{slice} = 200$, and $\mathrm{T}_1 = 1$ s), the ratio between the SNR of a 3D and a 2D sequence can be approximated by:

$$\frac{\mathrm{SNR_{3D}}}{\mathrm{SNR_{2D}}} \approx 1.6 \tag{1.14}$$

Though this ratio greatly depends on N_{slice} and the specific TR values [11], 3D sequences are generally more SNR efficient than 2D sequences.

SNR can be measured by selecting five smaller (few 100 voxels) regions within structures that are as homogeneous as possible [13] (e.g. white matter). SNR in all five regions is estimated as the ratio of the mean (signal estimate) and standard deviation (noise estimate). The final SNR measured in the structure of interest is obtained by averaging these five SNR estimates.

Alternatively, two identical scans can be acquired of the same object [13]. The signal is then estimated as the mean across the region of interest and the two scans, whereas the noise is approximated as the standard deviation across the same region in the difference image multiplied by $1/\sqrt{2}$. Note that this approach is more time consuming as it requires two acquisitions.

The evolution of SNR in susceptibility mapping is further discussed in chapter 3.

1.2.2.3 Sequence acceleration techniques

Two of the most common acceleration techniques are parallel imaging and partial Fourier acquisitions. Partial Fourier techniques take advantage of the phase-conjugate symmetry of k-space (Fourier-space) [11]. This means that in a noise free environment, for a full acquisition, half of the acquired data could be calculated from the other half. However, partial Fourier acquisition leads to reduced SNR and not all MRI scanners allow using partial Fourier for phase imaging (e.g. Philips scanners) as their manufacturers claim that these phase images are not usable. Also, note that the phase-conjugate symmetry of k-space is violated in the presence of local field inhomogeneities [3].

In parallel imaging, the data are undersampled and acquired simultaneously by separate receiver coils. Each receiver coil (c) has a sensitivity function ($s_c(\mathbf{r})$) describing that it efficiently detects precessing spins that are close, but fails to measure spins that are very far away. The k-space measured by coil c can be expressed as:

$$S(\mathbf{k}) = \int_{-\infty}^{\infty} M(\mathbf{r}) e^{-2\pi i \mathbf{kr}} s_c(\mathbf{r}) d\mathbf{r} \tag{1.15}$$

Note that when formulating Equation 1.10, it was assumed that the receiver coil has uniform sensitivity ($s_1(\mathbf{r}) = 1$) within the volume of interest.

These data are then either reconstructed separately and then combined based on the locations and sensitivity functions of the coils (SENSitivity Encoding or SENSE [14]) or a composite k-space matrix is built before reconstruction (GeneRalized Autocalibrating Partially Parallel Acquisitions or GRAPPA [15]). In SENSE, the measure of acceleration is called the SENSE factor and it refers to the extent of undersampling in one of the phase encoding directions (e.g. a SENSE factor of 2 means that only every other k-space line is acquired by each individual coil).

1.3 Quantitative Susceptibility Mapping (QSM)

1.3.1 Magnetic field variations and tissue susceptibility

In section 1.2.1, I discussed that there is a linear relationship between the measured phase and local field variations (Equation 1.6). Here I describe the relationship between these magnetic field variations and tissue magnetic susceptibility.

A magnetic susceptibility source is a distinct area with tissue susceptibility differing from that of its surroundings. Susceptibility (χ) is an inherent, dimensionless tissue property[5] which determines the induced magnetic field (ΔB) of a material in response to an applied magnetic field (B_0). A paramagnetic susceptibility source ($\chi > 0$) forms an internal magnetic field in the direction of the applied field, whereas a diamagnetic susceptibility source ($\chi < 0$) forms an induced magnetic field in the opposite direction.

Iron is the most abundant paramagnetic ion in the human body [16]. Most of it is stored in the blood as hemoglobin. Fe^{++} ions combined with four oxygen molecules form oxyhemoglobin which is slightly diamagnetic. However, without the bound oxygen, deoxyhemoglobin in the veins is strongly paramagnetic [17]. About a third of the iron stored in the body can be found as ferritin or hemosiderin in the liver, spleen and iron-rich brain regions such as the caudate nuclei or the globus pallidi [7]. The myelin sheath surrounding nerves is made up of proteins and lipids that are diamagnetic in general [16]. Therefore, in susceptibility maps of the brain, white matter appears to be diamagnetic [18]. Another source of diamagnetism in the human body is calcification (Ca^{++} salts) in diseased tissues [19].

Spatially varying magnetic fields ($\Delta B(\mathbf{r})$) induced by a spatially varying susceptibility distribution ($\chi(\mathbf{r})$) can be expressed as a convolution:

$$\Delta B(\mathbf{r}) = B_0 \cdot d(\mathbf{r}) * \chi(\mathbf{r}) \tag{1.16}$$

where B_0 is the main magnetic field and $d(\mathbf{r})$ is the field of a unit magnetic dipole (Figure 1.7) [20]:

$$d(\mathbf{r}) = \frac{3\cos^2\vartheta - 1}{4\pi \cdot r^3} \tag{1.17}$$

where $d(\mathbf{r})$ is expressed in spherical polar coordinates. r and ϑ are the radial distance and the polar angle respectively.

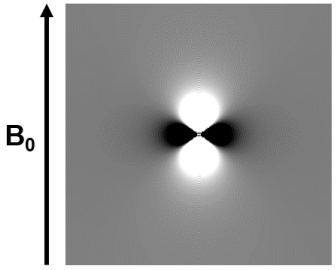

Figure 1.7: Illustration of the magnetic field induced by a unit magnetic dipole.

[5]Often measured in parts per million (ppm).

Equation 1.16 is also referred to as the forward calculation, because the resulting magnetic field map is expressed as a function of the susceptibility distribution. However, it is usually the inverse calculation, recovering the susceptibility map from the magnetic field map, that needs to be performed. The Fourier convolution theorem states that a convolution in the image domain simplifies to a multiplication in the Fourier domain. Therefore, Equation 1.16 is usually transformed into the Fourier domain (or k-space):

$$\mathcal{F}\{\Delta B(\mathbf{k})\} = B_0 \cdot D(\mathbf{k}) \cdot \mathcal{F}\{\chi(\mathbf{r})\} \tag{1.18}$$

where $\mathcal{F}$ denotes the Fourier transform operator and $D(\mathbf{k})$ is the Fourier transform of the unit dipole field described by the following equation:

$$D(\mathbf{k}) = \frac{1}{3} - \frac{k_z^2}{k^2} \tag{1.19}$$

Here, $k^2 = k_x^2 + k_y^2 + k_z^2$ and k_x, k_y, k_z are coordinates in k-space.

The above equations describe the effects of susceptibility variations on both micro- and macrostructural scales. In QSM, the smallest scale on which susceptibility is measured is a voxel. However, each voxel generally contains a number of different susceptibility sources depending on the microenvironment. Due to the linear nature of the convolution in Equation 1.16, the bulk susceptibility measured in a voxel can be approximated as the weighted sum of the different susceptibility sources contained within the voxel:

$$\chi_{voxel} = \sum_k V_k \cdot \chi_k \tag{1.20}$$

where V_k and χ_k denote the volume fraction and susceptibility of component k respectively. In iron-rich regions and calcifications, the ions of extreme magnetic susceptibility are embedded in a medium of magnetic susceptibility close to that of tissue/water (i.e. about -9 ppm [16]). Therefore, the bulk susceptibility of the voxel appears only slightly more para- or diamagnetic than the surrounding tissue. Susceptibility variations within the human body on a voxel-scale (few mms) are between ± 0.5 ppm which is a lot smaller than the difference between air and water (the aforementioned -9 ppm). Due to the fact that signal cannot be retained from the voxels containing air, the latter is not measured in QSM and its effects are eliminated at the background field removal stage (section 2.3). Therefore, what we actually calculate is the susceptibility variations relative to the susceptibility of the tissue[6]. Thus, structures appearing bright in susceptibility maps are more paramagnetic than the surrounding tissue, but can still be diamagnetic in terms of their absolute susceptibility.

[6]This baseline is also affected by the methods used in the susceptibility mapping pipeline.

Using Equation 1.20, we can estimate the expected susceptibility difference between hypoxic sites and normal tissue. The difference in susceptibility between fully oxygenated and fully deoxygenated blood has been previously investigated [17][7]:

$$\Delta\chi_{blood} = Hct \cdot 3.8 \text{ ppm} \approx 1.5 \text{ ppm} \tag{1.21}$$

where Hct, the hematocrit, can be approximated to be 0.4 for both healthy [40] and cancerous [41, 42] tissue. Based on Equation 1.20, the bulk susceptibility of a voxel with vascular density V can be expressed as:

$$\chi_{voxel} = V \cdot \chi_{blood} + (1 - V) \cdot \chi_{tissue} \tag{1.22}$$

where χ_{blood} and χ_{tissue} denote the susceptibilities of the blood and tissue respectively. V can be estimated to be around 0.2 for both healthy and cancerous environments [43]. Therefore, the difference in magnetic susceptibility between normoxic (either healthy or cancerous) and hypoxic sites can be as high as:

$$\chi_{hypoxic} - \chi_{normoxic} = V \cdot \Delta\chi_{blood} \approx \mathbf{0.3 \text{ ppm}} \tag{1.23}$$

Based on the susceptibility variations measured in recent brain studies[8] (around 0.03 ppm [44–48]), it seems feasible to detect hypoxic sites within a tumour, or identify cancerous lymph nodes with low oxygenation by comparing their susceptibilities to healthy tissue or lymph nodes.

[7] Here, the susceptibility difference was converted to SI units.

[8] Since this is the first study applying QSM to head-and-neck images, brain studies provide the most appropriate reference.

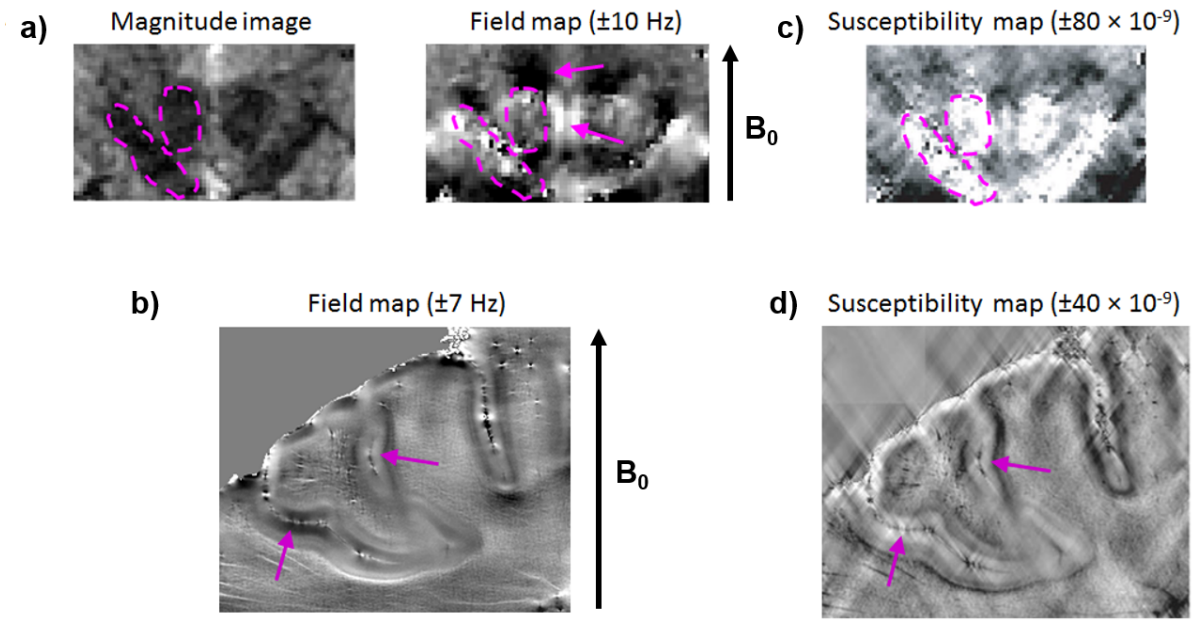

Figure 1.8: a: Non-local effect of a susceptibility source on the phase (and magnetic field) variations observed in field maps around the red nuclei and the substantia nigra. b: Orientation dependent appearance of cortical layers in magnetic field maps. c: Localised appearance of the red nuclei and the substantia nigra in the susceptibility map. d: Orientation independent appearance of the cortical layers in the susceptibility map. Images courtesy of Shmueli et al. [21].

So far, we have established the mathematical relationship between the magnetic field variations and tissue susceptibility. Now, let me illustrate the difference in appearance between the MR phase and susceptibility maps. The convolution in Equation 1.16 suggests that a susceptibility source affects the field map, and consequently the phase map, in a non-local manner. In Figure 1.8 a, there are bright and dark regions (dipolar phase variations) around the red nuclei and the substantia nigra in the magnetic field map whereas these structures are well-localised in the magnitude image. Also, the appearance of cortical layers in the field maps and phase images is orientation dependent. This is demonstrated by Figure 1.8 b, where the vertical layers appear bright while the horizontal layers are dark. As opposed to their non-local, orientation dependent effect on the phase images, susceptibility sources in the susceptibility maps appear in a local, orientation independent manner (Figure 1.8 c and d). Due to this difference, brain iron content correlates well with susceptibility as opposed to phase [21,22] and, therefore, susceptibility maps are preferred over MR phase or field images. Note that some structures, most notably the white matter, exhibit orientation dependent susceptibility contrast due to microstructural effects or inherent susceptibility anisotropy [23, 24]. This effect is likely to be negligible in the head and neck, therefore, I did not account for it in any of the subsequent chapters.

1.3.2 Other contributing factors to the MR phase

In magnetic susceptibility mapping, susceptibility-induced field inhomogeneities are inverted to obtain the susceptibility map. However, there are other origins of ΔB, namely chemical shift and flow effects, which could cause inaccuracies in the susceptibility maps if these contributions are interpreted as susceptibility-induced field variations.

Chemical shift is caused by the different chemical environment of hydrogen protons altering the static B_0 at the location of the nucleus. The circulation of electrons in the molecule induces a local magnetic field at the proton, B_e. According to Lenz's law, this field opposes the main magnetic field (B_0). Therefore the actual magnetic field at the location of the nucleus ($B_0 - B_e$) is less than the external field (B_0). The local field variation due to the chemical shift effect is $\Delta B = -B_e$. In the human body, the chemical shift effect is significant in fatty tissues. In a voxel, the measured signal is the superposition of the signal from water and fat protons. Since these protons experience different local magnetic fields and consequently precess at different Larmor frequencies[9], depending on the echo times, they can be measured in a parallel (in-phase), an antiparallel (out-of-phase) or any other state. If echo times are not chosen carefully, the linearity of the phase can be affected in voxels containing both water and fat (Type 2 chemical shift effect). Though this effect is not substantial in the brain due to the lack of fat, it could become a problem in head-and-neck images where elastin- and collagen-rich fascia between muscles, and subcutaneous fat are present. There are several ways to resolve this issue, such as choosing echo times so that the fat and water signals are always measured in-phase, using fat saturation, or applying a correction technique post-acquisition.

Another consequence of the difference in Larmor frequency between water and fat protons is mismapping (Type 1 chemical shift effect). The location of protons in the frequency encoding direction is calculated from the differences in their Larmor frequencies induced by a field gradient (Figure 1.4). Therefore, a chemical shift of $\Delta f = \gamma \cdot \Delta B$ results in a spatial shift of $\Delta f / bw$ voxels between the water and fat protons that are located in the same voxel. bw is the bandwidth per pixel that needs to be set carefully to avoid severe mismapping (by using a higher bw) while maintaining a high SNR (by using a low bw, see section 1.2.2.2). Note that in 2D acquisition, Type 1 chemical shift also results in mismapping in the slice selection direction.

Moving protons accumulate extra phase due to the spatial encoding gradients. This means that voxels in which spins flow parallel or antiparallel to a gradient appear brighter

[9]Larmor frequency in fat is less than that in water by approximately 3.4 ppm.

or darker respectively. The phase φ_G accumulated by a proton due to a spatial gradient G_x can be expressed by [1]:

$$\varphi_G(t) = \int_0^t G_x \cdot x \; dt \tag{1.24}$$

where x is the spatial coordinate of the proton along the direction of the gradient. For correct echo formation, gradients are designed so that their integral is zero at TE, therefore:

$$\varphi_G(\mathrm{TE}) = \int_0^{\mathrm{TE}} G_x \cdot x \; dt = x \int_0^{\mathrm{TE}} G_x \; dt = 0 \tag{1.25}$$

for stationary spins (i.e. $x(t) = x$). However, $\varphi_G(\mathrm{TE}) \neq 0$ for moving protons. In voxels with free diffusion or randomly oriented microvessels, this effect is not substantial as the different contributions cancel out. However, in head-and-neck imaging, flow effects could modify the appearance of large vessels (such as the carotid arteries and jugular veins) and their surroundings in the susceptibility maps. Fortunately, flow compensation is available on most clinical scanners in the form of first-order gradient moment nulling. Here the gradients are designed so that both their integrals and their first moments disappear at TE. Therefore, for spins moving at a constant velocity v:

$$\begin{aligned} \varphi_G(\mathrm{TE}) &= \int_0^{\mathrm{TE}} G_x \cdot x(t) \; dt \\ &= \int_0^{\mathrm{TE}} G_x \cdot vt \; dt \\ &= v \int_0^{\mathrm{TE}} G_x \cdot t \; dt = 0 \end{aligned} \tag{1.26}$$

This is a simple method to reduce flow artifacts. However, it only eliminates additional phase accumulated due to a constant velocity. Moreover, first-order gradient moment nulling might only apply for the first echo.

Investigating and, if necessary, correcting the effect of chemical shift and flow on the phase maps is crucial for accurate susceptibility mapping. Assuming these phase components to be susceptibility-induced might introduce unwanted errors.

1.3.3 Aims of this thesis and problems to address

It is important to note that this is the first study applying susceptibility mapping to head-and-neck images. Therefore, no gold standard acquisition protocol or QSM pipeline was available. Furthermore, imaging this region is particularly challenging due to:

- Subject motion (e.g. swallowing)
- Strong background fields originating from the susceptibility difference between air in the oropharyngeal air spaces and the surrounding tissue (section 2.3)
- Chemical shift effects in fatty tissue (section 1.3.2)
- Potential flow artifacts around the large blood vessels of the neck (section 1.3.2)

Therefore, the objective of my PhD was to optimise the MRI acquisition and the QSM pipeline to calculate clinically applicable susceptibility maps of the head and neck in healthy volunteers. A breakdown of the problems to be addressed is as follows (the chapters and sections in which these are investigated and resolved are indicated in brackets):

- Investigate the applicability of signal-to-noise ratio as a measure of image quality in QSM (chapter 3)
- Optimise the resolution, field-of-view, number of echoes and pulse sequence timing parameters for accurate susceptibility estimates, high SNR and a clinically applicable scan time in the head and neck (chapter 5 and section 6.2)
- Evaluate and include the use of parallel imaging (SENSE, section 1.2.2.3) as a potential acceleration technique to shorten scan time, increase patient comfort and throughput, and reduce motion artifacts (section 6.2)
- Investigate potential fat correction strategies (described in section 2.1) to overcome the effects of chemical shift artifacts in the head and neck (section 6.1)
- Examine the extent of the effects of flow on the resulting head-and-neck susceptibility maps and test the manufacturer-provided built-in flow compensation feature (section 6.2)
- Review, test and compare state-of-the-art susceptibility calculation techniques (described in sections 2.2, 2.3, and 2.4) in head-and-neck images (chapters 4, and sections 6.3 and 6.4)

The final step of this thesis is to perform a repeatability study using images acquired in 10 healthy volunteers (chapter 7). Intra-subject variability between scans is not expected to be significant as a previous study found T_2^* to be repeatable in patients with HNSCC [49] and T_2^* originates mainly from the underlying (microscopic) susceptibility distribution.

Therefore, we performed a repeatability study to assess the robustness of our optimised acquisition and processing technique.

One of the long-term objectives of this study is histological validation of the method developed in this thesis in cancerous tissue surgically resected from 10 patients injected with pimonidazole as a reference marker of hypoxia [50, 51]. While performing the histological validation is beyond the scope of this thesis, all necessary steps of the optimisation were carried out with this clinical end-goal in mind.

1.4 Other potential applications of an optimised QSM protocol

1.4.1 Calcifications in thyroid nodules

As mentioned earlier, QSM has not yet been applied in the head and neck possibly due to the lack of an optimised protocol. Therefore, it is important to assess other potential applications of the pipeline developed in this thesis to fully exploit its potential.

A different potential application is in thyroid nodules which manifest in 4 to 8% of the adult population [52]. The vast majority of these nodules (about 90%) are benign [53]. Identifying malignant nodules is key for the successful management of thyroid cancer. The current gold standard method for detecting thyroid malignancy is fine needle aspiration biopsy often guided by ultrasound (US) [54] which is an invasive procedure with associated risks. Thus, there is a pressing clinical need for developing non-invasive techniques differentiating benign and malignant thyroid nodules.

It has been repeatedly shown using US images that calcifications (and especially microcalcifications) are significantly more common in malignant nodules [55–57]. Moreover, in the case of malignant microcarcinomas, high calcification (as well as low vascularisation) has been reported to be an indicator of non-progressive tumours [58]. These comprise about 90% of all thyroid carcinomas and their treatment might not require surgery as opposed to progressive tumours [59]. Therefore, investigating calcification in the thyroid could potentially differentiate between benign and malignant nodules, as well as progressive and non-progressive microcarcinomas. However, US-detected calcification has low sensitivity in predicting these outcomes [57, 58] even when the calcification patterns are

also taken into consideration [60]. Furthermore, it is interesting to note that about 50% of thyroid nodules do not show calcifications on US images.

Previous studies using QSM have shown calcifications to be strongly diamagnetic [61–64]. Their susceptibility was measured to be around -0.15 ppm (relative to surrounding tissue) in brain lesions [62, 63] and as high as about -1 ppm in breast disease [61, 64]. This means that even microcalcifications (<1 mm) are likely to be detected using QSM because of the large dipole fields they generate due to their strong diamagnetic nature. Therefore, susceptibility mapping could be a more promising method for investigating the importance of calcifications in thyroid nodules than ultrasound imaging.

1.4.2 Bone marrow QSM in the sacroiliac joint

New bone formation and bone loss are both key features of spondyloarthritis [65], a group of inflammatory diseases involving the spine, lower limb joints, and entheses [66]. However, the T_1-weighted and T_2-weighted short tau inversion recovery (STIR) images which are currently used in clinical practice [67–70] provide minimal information on bone density, making this aspect of the disease difficult to monitor. Previously, Bray et al. [71] have demonstrated that $R_2^* (= 1/T_2^*)$ could be used as a quantitative biomarker of trabecular bone mineral density (BMD) in patients with spondyloarthritis due to the diamagnetic nature of bony trabeculae. We hypothesise that measuring the magnetic susceptibility of bone marrow directly could be an even more sensitive measure of BMD. Processing their data of the sacroiliac joint poses similar challenges to head-and-neck QSM, i.e. strong background fields originating from tissue/air interfaces in the bowels and chemical shift-induced phase contributions in subcutaneous fat and even within the bone marrow. In chapter 8, I applied my expertise in QSM in challenging anatomical regions to the data of Bray et al. [71] to investigate susceptibility as a biomarker of BMD.

Chapter 2

A review of current fat-correction and QSM techniques

In section 1.3.3, I described the issues associated with susceptibility mapping in the head and neck. One of the main problems is the chemical shift-induced phase component added to the susceptibility-induced phase in fatty tissue introducing errors into the susceptibility maps. Though there is a wide variety of techniques developed for overcoming this issue, there is no gold standard fat correction strategy applicable to every anatomical region. Therefore, in section 2.1, I review the existing state-of-the-art methods for fat correction and select the most promising strategies for head-and-neck QSM (section 2.1.3). In section 6.1, I compare these techniques in in-vivo head-and-neck images acquired in healthy volunteers.

QSM is the process of recovering the inherent susceptibility map from an MR phase image based on Equations 1.6 and 1.16 in four conceptual steps:

1. **Data acqusition**: Multi-echo gradient-echo phase images (Figure 2.1 a) are acquired in order to calculate the local field map (ΔB) using Equation 1.6.

2. **Field fitting and phase unwrapping**: The measured phase is an angle between 0 and 2π, as the MR scanner is unable to differentiate between φ and $\varphi + 2\pi \cdot n$, where n is an arbitrary integer. Thus, most MR images are corrupted by alternating black and white bands, called wraps (see arrow in Figure 2.1 a). Also, there is a linear relationship between ΔB and the unwrapped phase (Equation 1.6). Therefore, to calculate the total field map (ΔB, Figure 2.1 b), phase unwrapping and field fitting have to be performed.

3. **Background field removal**: The aforementioned non-local effect of susceptibility sources on the induced magnetic field variations (section 1.3.1) means that sources outside our region of interest (ROI), especially bones and the oropharyngeal air spaces, contribute to our phase images as well. These field contributions are called the background field (B_{ext}, see arrow in Figure 2.1 b). Thus the overall field perturbations can be separated into contributions from internal (B_{int}) and external (B_{ext}) susceptibility variations:

$$\Delta B(\mathbf{r}) = B_{int}(\mathbf{r}) + B_{ext}(\mathbf{r}) \tag{2.1}$$

   The local field map (Figure 2.1 c) is estimated by removing the background field contributions from the total field map.

4. **Susceptibility calculation**: A map of the internal susceptibility sources (χ_{int}, Figure 2.1 d) is calculated by solving the inverse of Equation 1.16.

There are several existing, state-of-the-art techniques with varying properties for each of these steps. However, similarly to fat correction strategies, there is no gold standard pipeline for head-and-neck images. Furthermore, there is an ongoing debate on the best techniques to be used even in brain images [93, 99, 113] which is the most commonly studied region in the QSM community. Therefore, here I described and reviewed current methods for steps 2, 3, and 4 in sections 2.2, 2.3, and 2.4 respectively and identified some clinically applicable techniques (sections 2.2.3, 2.3.5, and 2.4.3) to be compared in a numerical head-and-neck phantom (section 6.3) and in-vivo images of the head and neck acquired in a healthy volunteer (section 6.4).

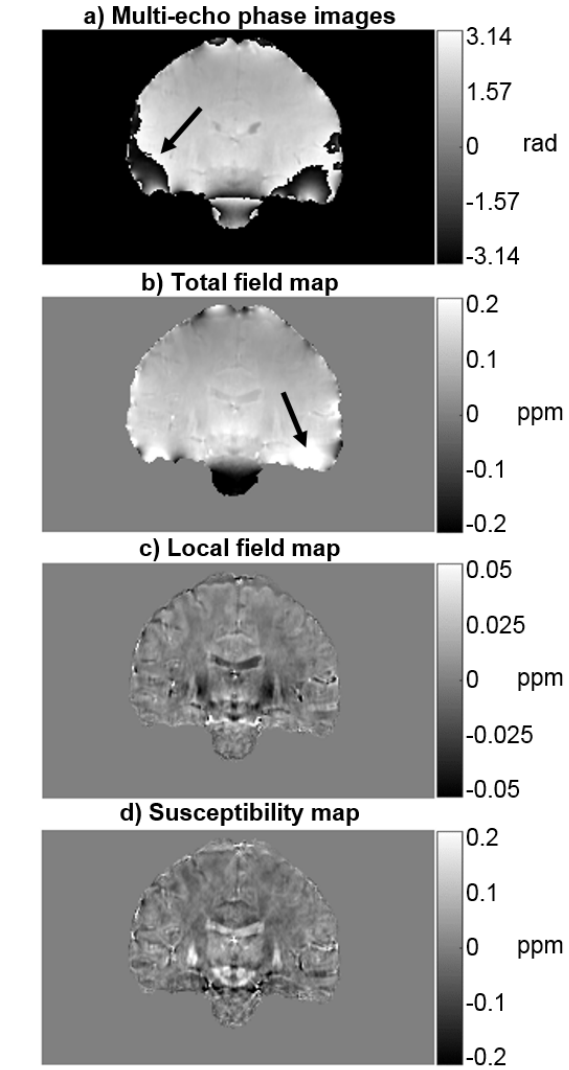

Figure 2.1: Images to illustrate steps in the susceptibility mapping pipeline: 1. Multi-echo phase images (a) are acquired with a gradient-echo sequence, 2. The total field map ΔB (b) is estimated by field fitting and phase unwrapping, 3. The local field map B_{int} (c) is obtained after background field removal, 4. The susceptibility map (d) is calculated by inversion of the dipole fields

2.1 Strategies to suppress or correct for the fat-water chemical shift effects

As I described in section 1.3.1, QSM calculates the underlying magnetic susceptibility distribution in the tissue from the phase component of the MRI signal (Equations 1.6 and 1.16). However, fat-water chemical shift also contributes to the phase images. In a voxel, the measured signal is the superposition of the signal from water and fat protons:

$$\begin{aligned} S &\propto W \cdot e^{i2\pi f_{water} \cdot \mathrm{TE}} + F \cdot e^{i2\pi f_{fat} \cdot \mathrm{TE}} \\ &\propto \left(W + F e^{i2\pi \Delta f \cdot \mathrm{TE}}\right) \cdot e^{i2\pi f_{water} \cdot \mathrm{TE}} \end{aligned} \tag{2.2}$$

where W and F are the water and fat magnitudes (proton densities) respectively. f_{water}, f_{fat} are the water and fat Larmor frequencies, while $\Delta f = f_{fat} - f_{water}$ is the chemical shift and TE is the echo time. Note that the T_2^* decay has been left out of the above expression for simplicity.

As mentioned in section 1.3.2, protons in water-based and fatty environments experience different local magnetic fields and consequently precess at different Larmor frequencies (f_{water} and f_{fat} respectively). Depending on TE, the two components can be measured in a parallel (in-phase, i.e. when $e^{i2\pi \Delta f \cdot \mathrm{TE}} = 1$), an antiparallel (opposed-phase, i.e. $e^{i2\pi \Delta f \cdot \mathrm{TE}} = -1$) or any other state.

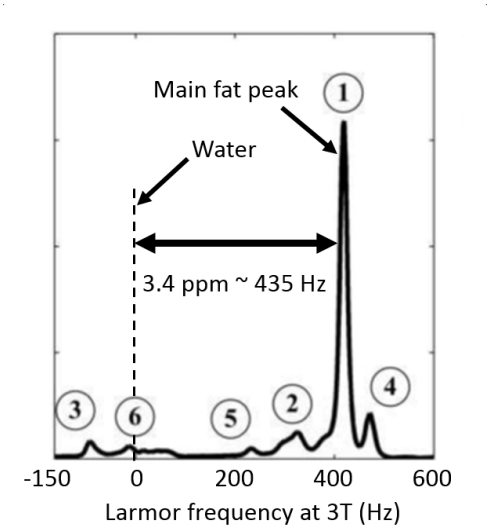

Figure 2.2: MRI fat spectrum (with the six peaks numbered) measured in knee subcutaneous fat at 3T. Image courtesy of Yu et al. [72].

In reality, we are dealing with protons located in various parts of different molecules that can be found in fatty tissue resulting in a multi-peak fat spectrum (Figure 2.2). The difference between the Larmor frequency of water and the main fat peak is about 3.4 ppm, however, several smaller peaks also contribute to the overall signal. All of these can have their own corresponding frequency (f_j), proton density (F_j), and $T^*_{2,j}$ values. Therefore, the overall signal can be described by:

$$S = W \cdot e^{\left(i2\pi f_{water} - 1/T^*_{2,water}\right)\cdot \mathrm{TE}} + \sum_j F_j \cdot e^{\left(i2\pi f_j - 1/T^*_{2,j}\right)\cdot \mathrm{TE}} \tag{2.3}$$

For accurate susceptibility mapping, the fat-water chemical shift effect needs to be overcome. Otherwise, chemical shift-induced phase variations might be interpreted as susceptibility-induced phase contributions leading to errors. The existing strategies for fat correction can be categorised into: (i) acquisition-based, and (ii) post-acquisition techniques. In this section, I review current methods in both categories.

2.1.1 Acqusition-based techniques

Acquisition-based fat-correction strategies take advantage of the chemical shift-induced Larmor frequency difference (Figure 2.2) to suppress the fat signal (second term in Equation 2.3) or the chemical shift-induced phase difference ($e^{i2\pi\Delta f\cdot \mathrm{TE}}$ in Equation 2.2). Here I discuss current acquisition features that achieve either of these.

2.1.1.1 Fat suppression

There are a number of ways to suppress the MRI fat signal [73]. The most obvious option is the use of *selective water excitation*, where the excitation pulse applied to displace the magnetic moments is tuned to the Larmor frequency of water (Figure 2.3a). Therefore, protons in fatty tissue that have substantially different Larmor frequencies are not excited and, consequently, are absent from the measured MRI signal. However, for this method, the excited frequency range needs to contain the entire water peak without overlapping the fat spectrum at all. This might be challenging as Figure 2.2 shows that there are smaller fat peaks very close to the water peak. Moreover, due to the susceptibility-induced field perturbations, the centre of the water peak varies spatially, which is the basis of QSM. In the head and neck, these variations can easily be on the order of a few ppm due to the

large susceptibility difference between tissue and air (around -9.4 ppm [16]). Therefore, whatever water frequency we set, there are likely to be regions of the image where not all water protons are excited, or where fat protons are excited instead.

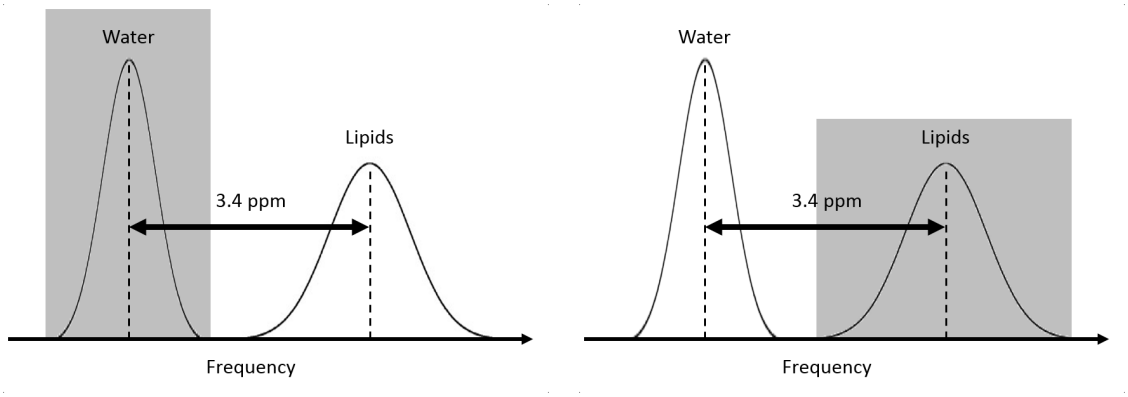

(a) Selective excitation of protons in water. (b) Selective excitation of protons in fat.

Figure 2.3: Frequency range of pulses for selective excitation (a) and fat suppression (b). The frequency range of the excitation pulse is highlighted in gray.

A similar technique called *fat saturation* first applies a 90° excitation pulse to fat protons only (Figure 2.3b) followed by a set of spoiler gradients to dephase the fat signal. The desired sequence (including a radiofrequency excitation pulse) is then applied to acquire only the water signal as the fat signal has been destroyed by the 90° preparation pulse and spoiler gradients. However, this concept has similar problems to *selective water excitation*. Due to the spatially varying Larmor frequencies, fat suppression might be partial in some regions, or the water signal could be suppressed instead.

Short T_1 Inversion Recovery (STIR) first applies a 180° inversion pulse to all protons. Since protons in fat and water have different T_1 relaxation rates (Figure 2.4), at a specific inversion time, $TI = \ln(2) \cdot T_{1,fat}$ the fat signal completely disappears, while the water protons still have a component parallel to B_0 (M_{water} in Figure 2.4). Therefore, starting the desired sequence at TI achieves efficient fat suppression. This technique does not suffer from the aforementioned problems with susceptibility-induced field inhomogeneities. However, it substantially increases the specific absorption rate (SAR, section 1.2.1) due to the extra 180° pulse, reduces SNR as the excited magnetisation vector (M_{water}) is much smaller than the original, fully relaxed signal, and increases scan time because of the extra TI necessary for a fully fat suppressed image. T_1 of fat is about 210 ms at 3T which leads to a TI = 145 ms. Overall, this increases the scan time by at least a few minutes which is not feasible in clinical practice where the length of a sequence has to be around 5 minutes

so that multiple sequences can be acquired within a single protocol. Moreover, the extra time increases the probability of motion artifacts occurring in the acquired images.

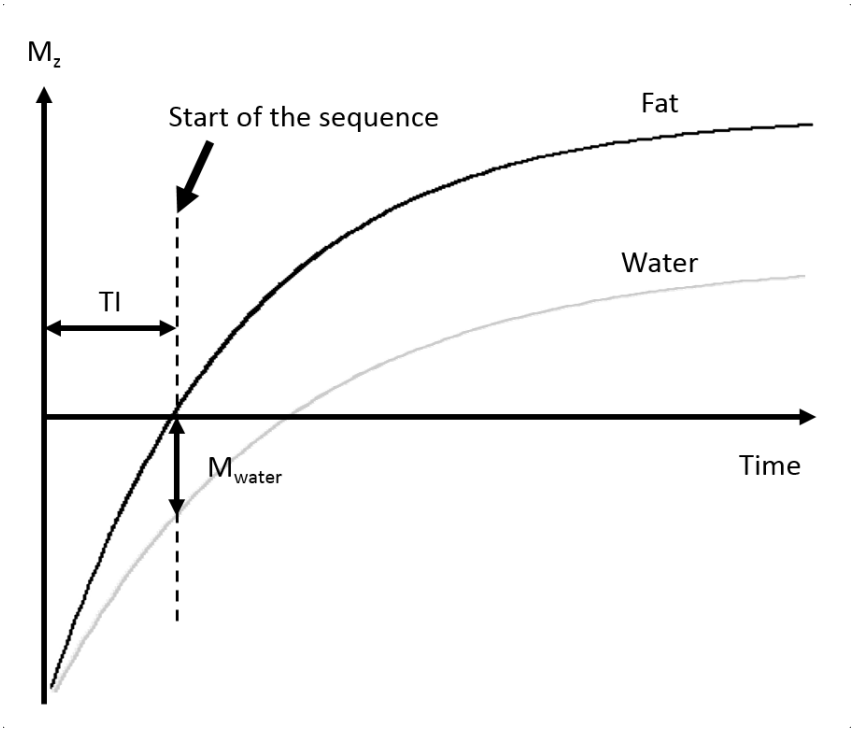

Figure 2.4: Fat suppression using STIR. The sequence starts when the fat signal has completely disappeared.

In general, suppressing all the fat signal might be preferred for a number of clinical applications. However, QSM relies on phase perturbations induced by the structure of interest (section 1.3.1) to calculate its susceptibility. These phase or field perturbations extend beyond the structure of interest. By suppressing the entire fat signal, we remove not only the chemical shift-induced, but also the susceptibility-induced phase variations from fatty tissue which might be a problem e.g. if the structure of interest is completely surrounded by fatty tissue. Unfortunately, cancerous lymph nodes of the head and neck, which are among the primary structures of interest for this study, are often located within fatty fascia which suggests that fat suppression might not be well suited for this application.

2.1.1.2 In-phase acquisition

In-phase acquisition is a method that reduces the chemical shift-induced phase difference between water and fat without suppressing the entire fat signal. We can achieve this by

setting all echo times (TEs) to instances where the fat and water signals are parallel, i.e. $2\pi\Delta f \cdot \mathrm{TE} = \mathrm{k} \cdot 2\pi$, where k is an integer. Therefore:

$$\begin{aligned} S &\propto \left(W + Fe^{i2\pi\Delta f \cdot \mathrm{TE}}\right) \cdot e^{i2\pi f_{water} \cdot \mathrm{TE}} \\ &\propto \left(W + Fe^{i2\pi \cdot k}\right) \cdot e^{i2\pi f_{water} \cdot \mathrm{TE}} \\ &\propto (W + F) \cdot e^{i2\pi f_{water} \cdot \mathrm{TE}} \end{aligned} \tag{2.4}$$

This way the fat magnitude (F) is preserved while the chemical shift-induced phase difference is eliminated. Another advantage of this technique is that, though the Larmor frequencies vary across the image volume due to the large susceptibility difference between tissue and air, the fat-water chemical shift remains unaffected. This method also does not cause substantially increased SAR or decreased SNR, and the difference in scan time is also minimal. However, it can only eliminate the effect of the main fat peak (Figure 2.2) which contains only about 70% of all protons [72] in a fatty environment. Whether or not this is enough to achieve sufficient fat correction is to be investigated using in-vivo experiments.

2.1.2 Post-acquisition techniques

There are a number of different techniques developed for separating water-based and fatty voxels post acquisition. Most of these also provide the water field map (f_{water}, i.e. the field map needed to calculate an accurate susceptibility map) as this is estimated during the procedure for a more accurate fat-water separation. Here I review some of the existing post-acquisition techniques for separating water and fat.

2.1.2.1 The 2012 ISMRM Fat-Water Separation Challenge

Many of the current techniques were compared in 2012 during the fat-water separation challenge of the International Society for Magnetic Resonance in Medicine (ISMRM) [74, 75]. Methods were tested in different parts of the body including images of the knee, head and neck, liver, and brain acquired at either 1.5 T or 3 T. Various techniques using single- or multipeak models (Equations 2.2 and 2.3 respectively), ignoring or accounting for the T_2^* relaxation, and incorporating 2, 3 or more echoes were entered to be the most robust and accurate fat-water separation method.

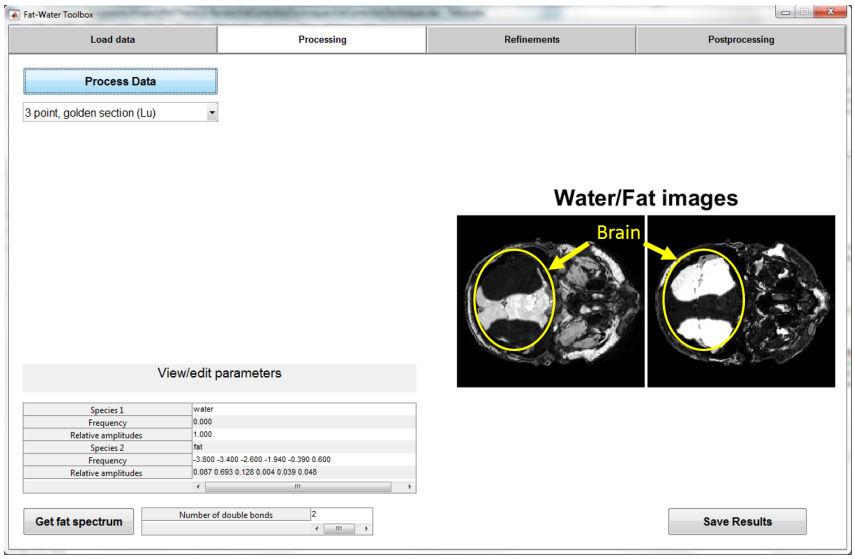

Figure 2.5: The fat-water separation toolbox released after the ISMRM challenge. This example showcases how most of the techniques based on slice-by-slice separation fail (left image: water magnitude, right image: fat magnitude). The yellow cirle highlights the brain that generally has low fat and high water content. This is not reflected by the results shown here.

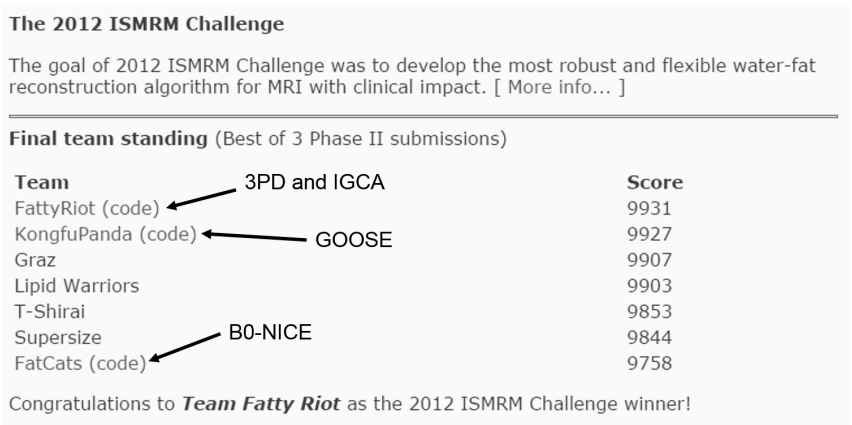

Figure 2.6: The winning teams of the 2012 ISMRM Fat-Water Separation Challenge (screenshot from http://challenge.ismrm.org/node/18). The few techniques published and advertised outside of the challenge are also displayed next to the corresponding teams.

A MATLAB-based toolbox with a user-friendly interface (Figure 2.5) was released containing some of these methods. Most of these techniques were dealing with 2D slices instead of a 3D volume which increased inaccuracies as information was not retained from neighbouring slices. One example of errors appearing in the calculated water and fat maps is shown in Figure 2.5. Moreover, many of the methods took a few minutes to process even a single slice making them clinically unfeasible in 3D volumes of the head and neck with potentially 200 or more slices. Finally, only a few of the teams achieving the highest scores disseminated their code separately from the challenge (Figure 2.6, arrows). These are the

techniques I tested and compared using in-vivo head-and-neck images in section 6.1. In the next few sections, I discuss the theory and implementation behind these methods.

2.1.2.2 Three-Point Dixon method (3PD)

3PD is a technique by Berglund et al. [76] based on the original Dixon method for obtaining the water and fat signals [77]. It is also one of the winning techniques of the 2012 ISMRM Fat-Water Separation Challenge (Figure 2.6).

In the original version, a single peak model is adopted (Equation 2.2) and the field dependence of the water frequency (f_{water}) is neglected:

$$S = W + Fe^{i2\pi\Delta f \cdot \mathrm{TE}} \tag{2.5}$$

Acquiring two echoes, one where $2\pi\Delta f \cdot \mathrm{TE} = 0$ (S_0) and one where $2\pi\Delta f \cdot \mathrm{TE} = \pi$ (S_π):

$$\begin{aligned} S_0 &= W + F \\ S_\pi &= W - F \end{aligned} \tag{2.6}$$

enables us to calculate the water and fat maps:

$$\begin{aligned} W &= 0.5 \cdot |S_0 + S_\pi| \\ F &= 0.5 \cdot |S_0 - S_\pi| \end{aligned} \tag{2.7}$$

3PD is an improvement over this method as it also incorporates the field dependence and uses a multipeak model:

$$S = \left(W + F \cdot \sum_j \alpha_j e^{i2\pi\Delta f_j \cdot \mathrm{TE}} \right) \cdot e^{i2\pi f_{water} \cdot \mathrm{TE}} \tag{2.8}$$

Here $\alpha_j = F_j/F$ from Equation 2.3, while $\sum_j \alpha_j = 1$, and $\Delta f_j = f_j - f_{water}$. For a multi-echo acquisition with 3 equally spaced echoes, the signal at each echo time is given by:

$$\begin{aligned} S_1 &= (W + a_1 F) \\ S_2 &= (W + a_2 F) \cdot b \\ S_3 &= (W + a_3 F) \cdot b^2 \end{aligned} \tag{2.9}$$

where:

$$a_i = \sum_j \alpha_j e^{i2\pi\Delta f_j \cdot \mathrm{TE}_i} \tag{2.10}$$

$$b = e^{i2\pi f_{water} \cdot \Delta\mathrm{TE}} \tag{2.11}$$

The following equation always holds in such a scenario:

$$S_1(a_3 - a_2) \cdot b^2 - S_2(a_3 - a_1) \cdot b + S_3(a_2 - a_1) = 0 \tag{2.12}$$

In 3PD, two candidate b values are calculated in each voxel from the above quadratic expression. Then, a region-growing scheme is used to decide which b corresponds to the actual water field map (instead of the fat field map) assuming that f_{water} is spatially smooth. Finally, W and F are estimated as the least-squares solutions of the aforementioned system (Equations 2.9):

$$\underbrace{\begin{bmatrix} S_1 \\ S_2 \\ S_3 \end{bmatrix}}_{\boldsymbol{S}} = \underbrace{\begin{bmatrix} 1 & a_1 \\ b & a_2 b \\ b^2 & a_3 b^2 \end{bmatrix}}_{A_b} \cdot \underbrace{\begin{bmatrix} W \\ F \end{bmatrix}}_{\mathbf{g}} \tag{2.13}$$

$$\mathbf{g} = \left(A_b^T A_b\right)^{-1} A_b^T \cdot \boldsymbol{S} \tag{2.14}$$

This technique is simple, robust, fast, and implemented for 3D volumes. The fat spectrum (α_j and f_j values) needs to be determined in advance, but the default settings generally work well in all regions of the body. Though in theory, any three equally spaced echoes are suitable for this method, it fails for some echo timings. For example, it cannot differentiate between b_{fat} and b_{water} at the region-growing stage if these two are always in phase (or rather the water signal and the main fat peak are in phase) resulting in water-fat *swaps*. Therefore, optimising TEs is necessary for accurate water, fat, and field estimation. According to Berglund et al. [76] the condition:

$$\mathrm{Re}(a + a_0 \cdot a) < 0 \tag{2.15}$$

$$a = exp(i2\pi\Delta f \cdot \Delta\mathrm{TE}) \tag{2.16}$$

$$a_0 = exp(i2\pi\Delta f \cdot \mathrm{TE}_1) \tag{2.17}$$

where Δf is the frequency difference between the water and the main fat peak, TE_1 is the first echo time, and $\Delta\mathrm{TE}$ is the echo spacing, needs to be fullfilled to avoid water-fat swaps. Furthermore, the noise level is optimal when $\angle(a) \approx 120°$ and $\angle(a_0) \approx 150°$ or $330°$, where $\angle$ denotes the phase angle. See Figure 6.6 for optimal (i) and non-optimal (v) timing with an assumed fat-water frequency difference of 434.52 Hz.

Another disadvantage of this technique is that it only uses the first three echoes and does not take T_2^* relaxation into account. The latter is generally not expected to become a problem for three, closely-packed echoes.

2.1.2.3 Iterative Graph Cut Algortihm (IGCA)

IGCA by Hernando et al. [78] is the other fat-water separation technique submitted by the winning team of the 2012 ISMRM Challenge.

Using the notation from the previous section, IGCA aims to solve the following minimisation problem:

$$W, F, b = \text{argmin}_{W,F,b} \, ||A_b \mathbf{g} - \boldsymbol{S}||^2 \tag{2.18}$$

This technique is not restricted to three echoes, therefore, $\boldsymbol{S}$ and A_b have rows for each echo. For a given water field map (i.e., a fixed b), W and F can be calculated as the least-squares solution (Equation 2.14) which simplifies the problem:

$$b = \text{argmin}_b \underbrace{\left|\left| A_b \left(A_b^T A_b\right)^{-1} A_b^T \cdot \boldsymbol{S} - \boldsymbol{S} \right|\right|^2}_{\mathcal{D}(\mathbf{r},b)} \tag{2.19}$$

Note that $b = b(\mathbf{r})$ and $S = S(\mathbf{r})$ are spatially varying. Hernando et al. also used an extra term to impose spatial smoothness on the water field map. This term has a similar role to the region growing scheme in 3PD:

$$b = \text{argmin}_b \left\{ \sum_{\mathbf{r}} \mathcal{D}(\mathbf{r}, b) + \mu \sum_{\mathbf{r}} \sum_{\mathbf{r'} \in \mathcal{N}(\mathbf{r})} w_{\mathbf{r},\mathbf{r'}} \left| f(\mathbf{r}) - f(\mathbf{r'}) \right|^2 \right\} \tag{2.20}$$

Here we replaced f_{water} with f, therefore $b = e^{i2\pi f \Delta \text{TE}}$. $\mathcal{N}(\mathbf{r})$ denotes the neighbourhood of the voxel at position $\mathbf{r}$. μ is a regularisation parameter, $w_{\mathbf{rr'}}$ are spatially dependent weights, and $\mathcal{D}(\mathbf{r}, b)$ is defined in Equation 2.19. This problem is solved on a discretised grid of potential field values using a graphcut algorithm that consists of a series of binary decisions. At each step of the iteration, for each voxel, the algorithm chooses between the field value of the previous iteration and a new, slightly different field value. Once the field is estimated, W and F are computed using 2.14 (where A_b and $\boldsymbol{S}$ incorporate all echoes).

This technique uses all the echoes, and is therefore expected to have an improved field estimation over 3PD. However, the graphcut scheme of a series of binary decisions is not guaranteed to converge to a global minimum. Moreover, even with the simplification of the optimisation using discretisation and the graphcut scheme, it is computationally feasible only in 2D slices instead of the 3D volume. Fortunately, processing a single slice only takes a few seconds, so applying this technique slice-by-slice is feasible.

2.1.2.4 GlObally Optimal Surface Estimation (GOOSE)

GOOSE by Cui et al. [79] is a variation of the IGCA technique described above. Instead of using an extra, regularisation term to ensure the smoothness of the estimated field map (Equation 2.20), the problem is reformulated as a constrained optimisation:

$$b = \text{argmin}_b \sum_{\mathbf{r}} \mathcal{D}(\mathbf{r}, b)$$
$$\text{such that}$$
$$|f(\mathbf{r}) - f(\mathbf{r'})| \leq \epsilon \tag{2.21}$$

where $\mathbf{r'} \in \mathcal{N}(\mathbf{r})$ and ϵ denotes the maximum field difference between adjacent voxels. Similarly to IGCA, this is solved on a discretised grid of potential field values using a graphcut scheme. Since there is a constraint on the difference between neighbouring field values, this problem is equivalent to fitting a smooth surface to $\mathcal{D}(\mathbf{r}, b)$, where the height of the surface at location $\mathbf{r}$ is $b = b(\mathbf{r})$, hence its name.

Note that GOOSE also takes into account the T_2^* decay as:

$$\mathcal{D}(\mathbf{r}, b) = \min_{T_2^*} \left|\left| A_\beta \left(A_\beta^T A_\beta\right)^{-1} A_\beta^T \cdot \boldsymbol{S} - \boldsymbol{S} \right|\right|^2 \tag{2.22}$$

where $\beta = e^{(i2\pi f - 1/T_2^*)\cdot \Delta TE}$.

This is another 2D method that requires slice-by-slice processing. However, the computation time of GOOSE can reach several minutes for a single slice, therefore it is not feasible for clinical application in 3D head-and-neck images.

2.1.2.5 B0 off-resonance mapping by Non-Iterative Correction of phase-Errors (B0-NICE)

B0-NICE by Liu et al. [80] aims to provide more accurate water field estimations instead of solely focusing on the separation of water and fat. It uses a multipeak model also incorporating the T_2^* decay:

$$S = \left(W + F \sum_j \alpha_j \cdot e^{i2\pi \Delta f_j \cdot TE} \right) \cdot e^{\left(i2\pi f - 1/T_2^*\right)\cdot TE} \tag{2.23}$$

This is the expression for the complex MRI signal. Its magnitude and phase components at different echoes (i) can be written as:

$$S_{magnitude,i} = \left| W + F \sum_j \alpha_j \cdot e^{i2\pi\Delta f_j \cdot \mathrm{TE}_i} \right| \cdot e^{-\mathrm{TE}_i/T_2^*} \tag{2.24}$$

$$S_{phase,i} = \angle \left(W + F \sum_j \alpha_j \cdot e^{i2\pi\Delta f_j \cdot \mathrm{TE}_i} \right) + 2\pi f \cdot \mathrm{TE}_i \tag{2.25}$$

Note that the latter corresponds to the unwrapped phase image. The measured values are expected to contain wraps. Also note that the magnitude is independent of f, while the expression for the phase does not contain T_2^*. However, both the magnitude and the phase components depend on W and F. B0-NICE takes advantage of this by estimating initial W, F, and f values by fitting S_{phase} to the unwrapped phase values across echoes in each voxel. This estimate for the field map contains errors both from inaccurate phase unwrapping and chemical shift effects. The W and F maps derived from a fit to the magnitude component are used to correct these errors, i.e. water masks calculated from the phase and magnitude images are matched. Here the fitting is performed by minimising the residual on a discretised grid of W, F, and T_2^* values. Once a corrected field map is obtained, W and F are calculated from all echoes using the least squares approximation (Equation 2.14).

This is another 2D method requiring slice-by-slice processing. It is much faster than GOOSE (about 30 seconds per slice) and has been reported to provide more accurate field estimations [80].

2.1.2.6 N-Point Dixon method (NPD)

3PD is an excellent candidate technique for fat-water separation and field estimation. However, it only uses three equally spaced echoes. It is reasonable to assume that taking advantage of all echoes would provide more accurate field estimation and improved signal-to-noise ratio in the results. Therefore, I modified the code of Berglund et al. [76] to include all echoes.

For example, in a 4-echo dataset with equally spaced echoes, we could use either the first three echoes or the last three echoes to perform 3PD as both satisfy Equation 2.12:

$$\begin{aligned} S_1 &= (W + a_1 F) \\ S_2 &= (W + a_2 F) \cdot b \\ S_3 &= (W + a_3 F) \cdot b^2 \\ S_1(a_3 - a_2) \cdot b^2 - S_2(a_3 - a_1) \cdot b + S_3(a_2 - a_1) &= 0 \end{aligned} \tag{2.26}$$

and

$$\begin{aligned} S_2 &= (W' + a_2 F') \\ S_3 &= (W' + a_3 F') \cdot b \\ S_4 &= (W' + a_4 F') \cdot b^2 \\ S_2(a_4 - a_3) \cdot b^2 - S_3(a_4 - a_2) \cdot b + S_4(a_3 - a_2) &= 0 \end{aligned} \tag{2.27}$$

In the second set of equations $W' = W \cdot b$ and $F' = F \cdot b$. Since both quadratic expressions equal zero, it follows that their sum is also zero:

$$\begin{aligned} &(S_1(a_3 - a_2) + S_2(a_4 - a_3)) \cdot b^2 - \\ &- (S_2(a_3 - a_1) + S_3(a_4 - a_2)) \cdot b + \\ &+ (S_3(a_2 - a_1) + S_4(a_3 - a_2)) = 0 \end{aligned} \tag{2.28}$$

Therefore, for four echoes, the candidate b values are calculated using Equation 2.28 instead of Equation 2.12. For N echoes, the sum of N-2 equations is used to calculate the quadratic expression. After estimating the water field map (b), the least squares solution of the following system is used to estimate W and F:

$$\begin{aligned} S_1 &= (W + a_1 F) \\ S_2 &= (W + a_2 F) \cdot b \\ &\vdots \\ S_N &= (W + a_N F) \cdot b^{N-1} \end{aligned} \tag{2.29}$$

This approach overcomes the limitation of 3PD that it only uses three echoes. However, this implementation still neglects the T_2^* relaxation which could easily become a problem as the number of echoes increases.

2.1.2.7 Simultaneous Phase Unwrapping and Removal of chemical Shift (SPURS)

SPURS is a recent technique developed by Dong et al. [81] to perform water field estimation designed specifically to perform susceptibility mapping. It builds on the technique of

T_2^*-IDEAL (Iterative Decomposition of water and fat with Echo Asymmetry and Least-squares estimation) [82]. T_2^*-IDEAL is an iterative scheme that requires an initial field map estimate. Using this estimate, the method applies Equation 2.14 to estimate initial W and F maps. Fixing these for every voxel, the new field map is estimated from:

$$S_i = (W + a_i F)e^{\beta \cdot \mathrm{TE}_i} \tag{2.30}$$

where $\beta = i2\pi f - 1/T_2^*$. This process continues until convergence. T_2^*-IDEAL requires a good initial field estimation.

In SPURS, non-linear fitting (section 2.2.1.3) is performed to estimate wrapped field values (f') with chemical shift components. The following minimisation problem is solved using a graphcut scheme to obtain the unwrapped chemical-shift-free field map:

$$k^*, m^* = \mathrm{argmin}_{k,m} \, ||\nabla(f' + k\Delta\mathrm{TE} - m\Delta f)|| \tag{2.31}$$

where ∇ is the differentiation operator, k and m are integers, and Δf is the chemical shift between water and the main fat peak. This step is meant to perform unwrapping (the $k\Delta$TE term) and "unfatting" (the $m\Delta f$ term) at the same time to enforce the smoothness of the field map: $f'' = f' + k^*\Delta\mathrm{TE} - m^*\Delta f$, where each voxel has its own optimal k^* and m^* values. f'' is used as the initial guess for the subsequent T_2^*-IDEAL step that incorporates a multipeak model.

SPURS is a promising technique for fat correction in head-and-neck images as it performs 3D field estimation with a multipeak fat model using all available echoes. It is much slower than 3PD, but its speed is still clinically feasible as it only takes a few minutes to process a 3D head-and-neck image.

2.1.3 Conclusions

Most acquisition-based strategies are either corrupted by the varying Larmor frequency of water protons due to the large susceptibility gradients at the air/tissue interfaces (e.g. selective excitation or fat saturation, section 2.1.1.1), or increase SAR and scan time, and decrease SNR (STIR, section 2.1.1.1). These techniques also tend to suppress the entire fat signal including the susceptibility-induced phase variations in fatty tissue. Healthy lymph nodes are often embedded in fatty fascia and capturing these susceptibility-induced phase variations is crucial for calculating accurate susceptibility values in these structures. In-phase imaging (section 2.1.1.2) is not affected by any of the above problems. Therefore, using in-phase acquisitions is the only acquisition-based strategy I tested in in-vivo head-and-neck images in section 6.1.

3PD, IGCA, GOOSE, and B0-NICE (sections 2.1.2.2, 2.1.2.3, 2.1.2.4, and 2.1.2.5 respectively) are post-acquisition techniques that performed well at the 2012 ISMRM Fat-Water Separation Challenge. Though GOOSE is much slower than the other techniques, I still included it in the comparison in section 6.1 because the team submitting it achieved second place at the Challenge. B0-NICE was ranked lower than the other techniques in terms of water-fat separation in the Challenge, but since it was specifically designed to produce accurate field maps (i.e. the field maps used to calculate susceptibility maps), I included this technique in section 6.1 too. NPD (section 2.1.2.6) is a modified version of 3PD I implemented to overcome the limitations of the original method, and SPURS (section 2.1.2.7) was specifically designed for susceptibility mapping, therefore these two methods were also part of the comparison in in-vivo head-and-neck images in section 6.1).

2.2 Field fitting and Phase unwrapping: Estimation of the total field map

The first step of the QSM pipeline is the calculation of the total field map (Figure 2.1). To achieve this, two different problems need to be resolved: (i) wraps have to be eliminated from the phase images and (ii) the field has to be estimated from multi-echo data using Equation 1.6. In this section, I review current field fitting and phase unwrapping techniques.

2.2.1 Field fitting

Field fitting techniques are based on the known magnitude and phase evolution within a voxel with a local magnetic field of ΔB. These methods require multi-echo data.

2.2.1.1 Linear fit

The MR phase evolves linearly over time (Equation 1.6). The magnetic field (ΔB) at a voxel can be easily determined by fitting a straight line to the unwrapped phase, φ.

Linear fitting can be performed quickly using the so-called pseudoinverse. For N echoes, the problem is defined by the following linear system (equivalent to Equation 1.6):

$$\underbrace{\begin{bmatrix} \varphi_1 \\ \vdots \\ \varphi_N \end{bmatrix}}_{\boldsymbol{\varphi}} = \underbrace{\begin{bmatrix} 1 & \mathrm{TE}_1 \\ \vdots & \vdots \\ 1 & \mathrm{TE}_N \end{bmatrix}}_{A} \cdot \underbrace{\begin{bmatrix} \varphi_0 \\ \gamma \Delta B \end{bmatrix}}_{\mathbf{x}} \tag{2.32}$$

where TE_i and φ_i for $i = 1..N$ are the echo times and the corresponding phase values respectively while φ_0 and $\gamma \Delta B$ are the intercept and the slope of the fitted line. The least squares solution of the problem can be expressed using the pseudoinverse (C):

$$\mathbf{x} = \underbrace{\left(A^T A\right)^{-1} A^T}_{C} \boldsymbol{\varphi} \tag{2.33}$$

where $\boldsymbol{\varphi}$, A and $\mathbf{x}$ are defined in Equation 2.32.

This technique is straightforward and easy to implement. However, before it can be applied, phase images at each echo need to be unwrapped separately using a phase

unwrapping technique that preserves the linearity of the phase. This could become time consuming depending on the phase unwrapping method. Also, acquiring more echoes is likely to yield more accurate field estimates which means that there is a trade off between scan time ($\propto$ number of echoes) and field map accuracy.

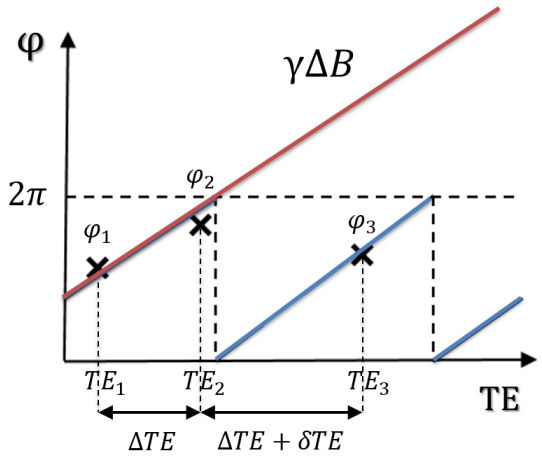

Figure 2.7: Illustration of the linear relationship (red line) between the phase of the signal (φ) and the echo time (TE). As the MRI device can not detect absolute phase values, the measured phase is rendered into the $[0, 2\pi]$ interval (blue line).

Robinson et al. proposed Unwrapping Multi-echo Phase Images with iRregular Echo spacings (UMPIRE), a field estimation method that requires the acquisition of exactly three echoes [83]. This method determines ΔB based on phase values φ_1, φ_2 and φ_3, measured at echo times TE_1, $\mathrm{TE}_2 = \mathrm{TE}_1 + \Delta\mathrm{TE}$ and $\mathrm{TE}_3 = \mathrm{TE}_2 + \Delta\mathrm{TE} + \delta\mathrm{TE}$ (Figure 2.7). It can be shown that if no wraps occur during δTE, in other words δTE is sufficiently small, the following equations hold and ΔB can be easily estimated:

$$\theta_{2,1} = \angle\left(\frac{e^{i\varphi_2}}{e^{i\varphi_1}}\right) = \gamma\Delta B \cdot \Delta\mathrm{TE} - 2\pi \cdot n \tag{2.34}$$

$$\theta_{3,2} = \angle\left(\frac{e^{i\varphi_3}}{e^{i\varphi_2}}\right) = \gamma\Delta B \cdot (\Delta\mathrm{TE} + \delta\mathrm{TE}) - 2\pi \cdot n \tag{2.35}$$

$$\theta_{3,2,2,1} = \theta_{3,2} - \theta_{2,1} = \gamma\Delta B \cdot \delta\mathrm{TE} \tag{2.36}$$

where $\angle$ denotes the operator that returns the angle of a complex number and n is an integer. UMPIRE has been shown to be robust to geometrical complexity, but sensitive to high noise [83, 93]. Unequal echo spacings are not straight-forward to set on all MRI systems, and using UMPIRE for field fitting limits the options for choosing optimal echo timings (e.g. in-phase imaging cannot be applied to overcome fat-water chemical shift effects, section 2.1.1.2).

2.2.1.2 Magnitude-weighted linear fit

In theory, more echoes acquired over a large range of potential TE values should provide more accurate field estimations. However, as the signal magnitude decays over time, the measured phase becomes more noisy and unreliable [84] which could result in inaccurate field estimations. A simple way of overcoming this problem is by using magnitude-weighted fitting:

$$M \cdot \varphi = M \cdot (\gamma \Delta B \cdot \mathrm{TE} + \varphi_0) \tag{2.37}$$

This formula is basically the same as Equation 1.6, but both sides are multiplied by the magnitude (M). The pseudoinverse from Equation 2.33 can be used to estimate ΔB with:

$$\boldsymbol{\varphi} = \begin{bmatrix} M_1 \cdot \varphi_1 \\ \vdots \\ M_N \cdot \varphi_N \end{bmatrix} \tag{2.38}$$

$$A = \begin{bmatrix} M_1 & M_1 \cdot \mathrm{TE}_1 \\ \vdots & \vdots \\ M_N & M_N \cdot \mathrm{TE}_N \end{bmatrix} \tag{2.39}$$

This magnitude-weighted version of the aforementioned linear fit ensures that unreliable phase values at later echoes have a smaller weight in the overall fit, because of their decreased magnitude due to T_2^* decay.

2.2.1.3 Non-linear fit

Liu et al. [85] proposed another method which exploits the phase evolution of both phase and magnitude images (Figure 2.8 a and b respectively) by fitting the following model to the complex data:

$$S = M_0 \cdot e^{-\frac{\mathrm{TE}}{T_2^*}} \cdot e^{i(\varphi_0 + \gamma \Delta B \cdot \mathrm{TE})} \tag{2.40}$$

where S is the complex MR signal and M_0 is the magnitude at TE = 0 ms. The combination of the exponentially decaying magnitude and the linearly evolving phase is a spiral curve in the complex plane (Figure 2.8 c). This concept is very similar to using the magnitude-weighted linear fit.

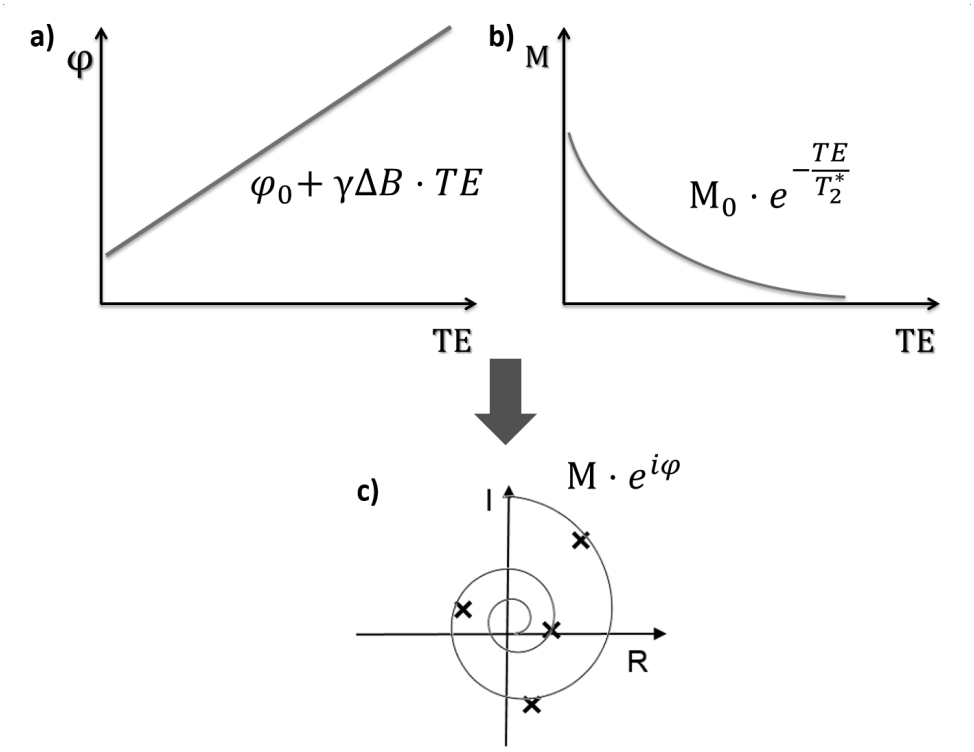

Figure 2.8: The complex MR signal as a function of TE (c) is a combination of the linear phase evolution (a) and exponential magnitude decay (b).

Similarly to the magnitude-weighted linear fit, non-linear fitting has a 'self-weighting' property originating from the fact that complex data is used instead of only phase images. The phase becomes unreliable as the magnitude decays to 0 and as the echo time increases [84]. The difference between complex vectors with different phase values becomes insignificant approaching the origin. Therefore, as opposed to linear fitting, this method is not sensitive to the increasing noise level of the phase as a function of TE.

In voxels with large ΔB, wraps can occur between two consecutive echoes. Even a noise-free multi-echo image could be fitted perfectly by an infinite number of field estimates: $\Delta B = \Delta B_{true} + 2\pi \cdot \frac{n}{\gamma \Delta \mathrm{TE}}$ where ΔB_{true} is the true field value, n is an arbitrary integer and ΔTE is the echo spacing. The implementation of Liu et al. [85] always prefers the ΔB with the lowest absolute value, resulting in residual wraps appearing in the estimated field maps which have to be removed by one of the phase unwrapping algorithms. However, in this case, unwrapping is performed only on one image and the unwrapping technique does not have to preserve the linearity of the phase as opposed to when using linear fitting.

A MATLAB implementation of non-linear fitting is available for download as part of the MEDI toolbox [86]. The function also provides an estimate of the noise map calculated

from the magnitude images across echo times [87]. This expression is deduced in chapter 3 (see Equation 3.21).

2.2.2 Phase unwrapping

Spatial unwrapping methods are based on the assumption that the phase is spatially smooth therefore only small phase variations are expected between neighbouring voxels. As a consequence, these techniques do not deal well with large, voxel-scale phase gradients induced by large susceptibility variations.

2.2.2.1 Region-growing techniques (FSL PRELUDE)

Region-growing techniques unwrap the image by adding integer multiples of 2π to connected regions or individual voxels while enforcing spatial smoothness, or minimal phase difference between neighbouring voxels. Many of these methods start the unwrapping from one or more seed points selected randomly or using some kind of quality function [88–91] (e.g. seed points can be voxels with the lowest estimated noise level [91]). The next voxel/region to be unwrapped can be a voxel/region neighbouring the already unwrapped part of the image [88, 89], or might be determined using another quality function [90–92] (e.g. the largest of the regions to be unwrapped). These techniques can often be time consuming, but they preserve the linearity of the phase.

One of the most popular region-growing methods is the Phase Region Expanding Labeller for Unwrapping Discrete Estimates (PRELUDE, [92]) which is also considered the gold standard method for phase unwrapping [93] and is available for download as part of the FSL software package [94]. In PRELUDE, the phase map is partitioned into connected regions by dividing the $[0, 2\pi]$ interval into 6 smaller intervals. These regions are then merged by adding integer multiples of 2π to one of two neighbouring regions assuming spatial smoothness of the phase. This process continues until all the regions are unwrapped and merged. More details on PRELUDE and a new, accelerated technique called SEGUE that I developed based on similar principles can be found in chapter 4.

2.2.2.2 Laplacian phase unwrapping (LPU)

This method exploits the fact that the Laplacian of the unwrapped phase image ($\nabla^2\varphi$) can be expressed in terms of the wrapped or measured phase image (φ^{meas}) [95]:

$$\nabla^2\varphi = \cos(\varphi^{meas}) \cdot \nabla^2 \sin(\varphi^{meas}) - \sin(\varphi^{meas}) \cdot \nabla^2 \cos(\varphi^{meas}) \tag{2.41}$$

Therefore, φ can be estimated by calculating the above expression and applying the inverse Laplacian (∇^{-2}) to the result in a series of convolutions and deconvolutions with the Laplacian kernel [96]:

$$\nabla^2_{3D} = \begin{bmatrix} 0 & 0 & 0 \\ 0 & 1 & 0 \\ 0 & 0 & 0 \end{bmatrix}, \begin{bmatrix} 0 & 1 & 0 \\ 1 & -6 & 1 \\ 0 & 1 & 0 \end{bmatrix}, \begin{bmatrix} 0 & 0 & 0 \\ 0 & 1 & 0 \\ 0 & 0 & 0 \end{bmatrix} \tag{2.42}$$

Note that the above kernel is only applicable for images of isotropic resolution. In any other case, anisotropy has to be accounted for using the forward distance discrete gradients to estimate the second derivatives [86]:

$$\begin{aligned} \nabla^2 f(x,y,z) &= \frac{\partial^2 f}{\partial x^2} + \frac{\partial^2 f}{\partial y^2} + \frac{\partial^2 f}{\partial z^2} \\ \frac{\partial^2 f(x,y,z)}{\partial x^2} &= \frac{\frac{f(x+dx,y,z)-f(x,y,z)}{dx} - \frac{f(x,y,z)-f(x-dx,y,z)}{dx}}{dx} \\ &= \frac{f(x+dx,y,z) + f(x-dx,y,z) - 2f(x,y,z)}{dx^2} \end{aligned} \tag{2.43}$$

where dx, dy and dz are the spacing values (voxel size + any gap between voxels) in each dimension. The anisotropic Laplacian kernel can be expressed as:

$$\nabla^2_{3D} = \begin{bmatrix} 0 & 0 & 0 \\ 0 & \frac{1}{dz^2} & 0 \\ 0 & 0 & 0 \end{bmatrix}, \begin{bmatrix} 0 & \frac{1}{dy^2} & 0 \\ \frac{1}{dx^2} & -\frac{2}{dx^2} - \frac{2}{dy^2} - \frac{2}{dz^2} & \frac{1}{dx^2} \\ 0 & \frac{1}{dy^2} & 0 \end{bmatrix}, \begin{bmatrix} 0 & 0 & 0 \\ 0 & \frac{1}{dz^2} & 0 \\ 0 & 0 & 0 \end{bmatrix} \tag{2.44}$$

Note that for $dx = dy = dz = 1$, this is equal to the isotropic Laplacian kernel from Equation 2.42.

Performing a convolution in the image domain is impractical as it is very time-consuming. However, using the Fourier convolution theorem, the Laplacian and the inverse Laplacian of an arbitrary function f can be calculated using Equations 2.45 and 2.46 respectively:

$$\nabla^2 f = \mathcal{F}^{-1}\left\{\mathcal{F}\left[\nabla^2_{3D}\right] \cdot \mathcal{F}\left[f\right]\right\} \tag{2.45}$$

$$\nabla^{-2} f = \mathcal{F}^{-1}\left\{T\left(\frac{1}{\mathcal{F}\left[\nabla^2_{3D}\right]}\right) \cdot \mathcal{F}\left[f\right]\right\} \tag{2.46}$$

where $\mathcal{F}$ denotes the Fourier transform. For the inverse calculation, a thresholding operator (T) has to be applied to the kernel, $\frac{1}{\mathcal{F}[\nabla^2_{3D}]}$, in the Fourier-domain to avoid artifacts induced where $\mathcal{F}[\nabla^2_{3D}] = 0$ by values in k-space that are too large:

$$T\left(\frac{1}{f}\right) = \begin{cases} \frac{1}{f} & |f| > \sigma \\ 0 & \text{otherwise} \end{cases} \tag{2.47}$$

where σ is the threshold value. The threshold has to be adjusted according to the image resolution as the values in ∇^2_{3D} (Equation 2.44), and consequently in its Fourier transform, are higher for an image of higher resolution. In practice, a modified threshold value ($\frac{\sigma}{dx^2}$) can be applied to account for the resolution and obtain results that are comparable across different resolutions [97].

Note that LPU tends to reduce components of the background fields as well, because most of these are harmonic within the region of interest, in other words $\nabla^2 B_{ext} = 0$ or $\nabla^2 \varphi_{ext} = 0$ (section 2.3). A higher σ provides unwrapped images with less background field contributions. Therefore, a very low σ has to be used to preserve the phase unwrapping feature of the technique but minimise its background field removal. It has been shown that LPU does not preserve the linearity of the phase [98], but it is a very fast technique and has been shown to be able to resolve open-ended fringe lines [4, 96]. A MATLAB implementation of LPU is available for download as part of the MEDI toolbox with $\sigma = 10^{-10}$ [86].

2.2.3 Conclusions

There are two conceptually different strategies to calculate total field maps. One solution is to unwrap phase images acquired at multiple echo times individually followed by a (magnitude-weighted) linear fit (sections 2.2.1.1 and 2.2.1.2). This can be time consuming as each phase image needs to be unwrapped separately. Moreover, a region-growing technique (section 2.2.2.1) needs to be used at this stage to preserve the linearity of the phase and these can be very slow in general. The other possible strategy for field estimation is to apply the non-linear fitting technique (section 2.2.1.3) to the multi-echo complex data and then use any phase unwrapping technique to eliminate residual wraps. This is a much quicker option, especially if Laplacian Phase Unwrapping (LPU, section 2.2.2.2) is used for phase unwrapping. However, LPU also reduces the background fields (even using a very small σ) which could affect the performance of the subsequent background field removal technique. Both options are compared using in-vivo head-and-neck images acquired in a healthy volunteer in section 6.4.

2.3 Background field removal

Since the term *background fields* refers to magnetic fields from many different sources (eg. fields induced by susceptibility sources outside the region of interest (ROI), hardware related magnetic field inhomogeneities), it is very hard to identify background fields in general. Therefore, background field removal (BFR) techniques make some basic assumptions about the background fields they are designed to eliminate. The two main assumptions are: (i) the local field variations we are interested in are of high spatial frequency whereas the background fields contain only low spatial frequency components, or (ii) the background fields within the ROI are induced by susceptibility sources outside the ROI. The vast majority of current BFR methods are based on the second assumption:

$$\begin{aligned} \Delta B &= B_{int} + B_{ext} \\ &= B_0 \cdot d * \chi_{int} + B_0 \cdot d * \chi_{ext} \end{aligned} \tag{2.48}$$

$$B_{ext} = B_0 \cdot d * \chi_{ext} \tag{2.49}$$

where d denotes the field of a unit magnetic dipole (Equation 1.17). In other words, d describes the field induced by a point susceptibility source. The total field map is a superposition of many dipole fields at different locations. The external part (i.e. $r > 0$) of the dipole field can be expressed as follows (section 1.3.1):

$$b_{ext} = \frac{3\cos^2\vartheta - 1}{4\pi r^3} \text{ for } r > 0 \tag{2.50}$$

It can be easily shown that the Laplacian of the external part of the dipole field is 0, or that B_{ext} is harmonic throughout the ROI:

$$\begin{aligned} \nabla^2 b_{ext} &= \frac{1}{r^2}\frac{\partial}{\partial r}\left(r^2\frac{\partial b_{ext}}{\partial r}\right) + \frac{1}{r^2\sin\vartheta}\frac{\partial}{\partial\vartheta}\left(\sin\vartheta\frac{\partial b_{ext}}{\partial\vartheta}\right) + \frac{1}{r^2\sin^2\vartheta}\frac{\partial^2 b_{ext}}{\partial\varphi^2} \\ &= \frac{1}{r^2}\frac{\partial}{\partial r}\left(r^2\frac{3-9\cos^2\vartheta}{4\pi r^4}\right) + \frac{1}{r^2\sin\vartheta}\frac{\partial}{\partial\vartheta}\left(\sin\vartheta\frac{-6\cos\vartheta\sin\vartheta}{4\pi r^3}\right) + \frac{1}{r^2\sin^2\vartheta}\cdot 0 \\ &= \frac{1}{r^2}\frac{\partial}{\partial r}\left(\frac{3-9\cos^2\vartheta}{4\pi r^2}\right) + \frac{1}{r^2\sin\vartheta}\frac{\partial}{\partial\vartheta}\left(\frac{-6\cos\vartheta\sin^2\vartheta}{4\pi r^3}\right) \\ &= \frac{1}{r^2}\frac{18\cos^2\vartheta - 6}{4\pi r^3} + \frac{1}{r^2\sin\vartheta}\frac{6\sin^3\vartheta - 12\cos^2\sin\vartheta\vartheta}{4\pi r^3} \\ &= \frac{18\cos^2\vartheta - 6}{4\pi r^5} + \frac{6\sin^2\vartheta - 12\cos^2\vartheta}{4\pi r^5} \\ &= \frac{6\left(\cos^2\vartheta + \sin^2\vartheta\right) - 6}{4\pi r^5} \\ \nabla^2 b_{ext} &= 0 \text{ for } r > 0 \end{aligned} \tag{2.51}$$

Internal and external susceptibility sources can be separated by a binary tissue mask. All BFR methods use some kind of tissue mask at some point in the algorithm. However,

while B_{ext} in Equation 2.48 is a smooth, continuous function, in practice, only discrete data points are measured at each voxel. Consequently, strong outside susceptibility sources very close to the mask boundary can have large contributions to the background fields which can be difficult to describe in a discrete coordinate system. Therefore, Schweser et al. classified BFR methods based on what additional assumptions they make about local and background field contributions near the boundary [99].

In the next few sections, I review current BFR techniques using the classification of Schweser et al. [99].

2.3.1 Homodyne filtering

Homodyne filtering [100–102] is the only technique I discuss that uses assumption (i), i.e. the background is of low spatial frequency while the local field variations are of high spatial frequency components. A high-pass filter (HPF) is applied to the image to retrieve the local field map. However, in practice, it is very difficult to construct a high-pass filter which does not introduce additional artifacts to the image while low-pass filtering (LPF) is relatively easy. Therefore, direct application of a HPF is avoided using the following algorithm.

1. Compute the Fourier transform of the image: $M(\mathbf{r})e^{i(\phi_{low}(\mathbf{r})+\phi_{high}(\mathbf{r}))} \Rightarrow M(\mathbf{k})e^{i(\phi_{low}(\mathbf{k})+\phi_{high}(\mathbf{k}))}$. $M(\mathbf{r})$ and $M(\mathbf{k})$ are the magnitude components in the image domain and in k-space respectively. ϕ_{low} and ϕ_{high} are the phase components corresponding to the low and high spatial frequency parts of the image.

2. Apply a low-pass filter (LPF) to the image: LPF $\left\{M(\mathbf{k})e^{i(\phi_{low}(\mathbf{k})+\phi_{high}(\mathbf{k}))}\right\} = M^*(\mathbf{k})e^{i\phi_{low}(\mathbf{k})}$. $M^*(\mathbf{k})$ is the modified magnitude in k-space after the filter has been applied. The LPF filters out the high frequency phase components.

3. Transform back to the image domain: $M^*(\mathbf{k})e^{i\phi_{low}(\mathbf{k})} \Rightarrow M^*(\mathbf{r})e^{i\phi_{low}(\mathbf{r})}$.

4. Complex division of the original by the filtered image: $\frac{M(\mathbf{r})e^{i(\phi_{low}(\mathbf{r})+\phi_{high}(\mathbf{r}))}}{M^*(\mathbf{r})e^{i\phi_{low}(\mathbf{r})}} = M^{**}(\mathbf{r})e^{i\phi_{high}(\mathbf{r})}$. $M^{**}(\mathbf{r}) = \frac{M(\mathbf{r})}{M^*(\mathbf{r})}$ is the modified magnitude in the image domain after complex division.

5. Take the phase of the result: $\angle\left(M^{**}(\mathbf{r})e^{i\phi_{high}(\mathbf{r})}\right) = \phi_{high}(\mathbf{r})$.

Complex division is preferred to subtraction in the case of phase images as direct subtraction would render the values into the $[-2\pi, 2\pi]$ interval instead of the $[-\pi, \pi]$

interval. Note that subtraction can also be used, but an additional correction is needed to ensure valid phase values.

This technique simultaneously eliminates the background fields and removes most of the wraps as the large phase variations inducing the wraps are usually of low spatial frequency.

Various window functions can be used as LPF (i.e. rectangular, Gaussian, cosine, Hamming, von Hann). The larger the width of the LPF is, the higher portion of the background field is eliminated. However, simultaneously the larger part of the middle of k-space, which contains the contrast information, is removed. In conclusion, there is always a trade-off between the amount of background field eliminated (and consequent phase unwrapping) and image contrast.

Homodyne filtering is a technique that is fast and easy to implement. However, it is very hard to establish an optimal LPF width that removes all background field components, but leaves the local field variations intact. Therefore, while it is a popular method for combined phase unwrapping and BFR in Susceptibility Weighted Imaging, where e.g. veins are visually enhanced in gradient-echo images using the phase variations induced by their low susceptibility, homodyne filtering is rarely used in Quantitative Susceptibility Mapping.

2.3.2 Assumption of no sources close to the boundary

The following methods assume (ii) (i.e. that the background fields are induced by susceptibility sources outside the tissue mask) and that the binary tissue mask is defined in such a way that no susceptibility sources can be found close to the boundary. This assumption usually holds for brain masks as susceptibility varies very slowly ($\sim$0.05 ppm) around brain edges. The assumption is violated close to the tissue/air interface where the susceptibility difference is around -9.4 ppm [16].

2.3.2.1 Inverse Laplacian Filter (iLF)

As mentioned in section 2.2.2.2, Laplacian phase unwrapping tends to also reduce the background fields due to their harmonic property. By choosing a higher σ threshold, iLF can perform the phase unwrapping and background field removal steps simultaneously. Therefore, this method can be applied directly to the field map estimated by non-linear

fitting. Note that since iLF first calculates the Laplacian of unwrapped phase images from wrapped phase images (Equation 2.52), the estimated field map needs to be rescaled to phase values before iLF, and scaled back to field units after. The overall process is described by the following equation [96]:

$$\varphi = M \cdot \nabla^{-2} \left\{ M \cdot \left(\cos(\varphi^{meas}) \cdot \nabla^2 \sin(\varphi^{meas}) - \sin(\varphi^{meas}) \cdot \nabla^2 \cos(\varphi^{meas}) \right) \right\} \tag{2.52}$$

where M is a 3D binary tissue mask appropriately eroded to eliminate the convolution artifacts caused by unreliable, noisy phase data outside the tissue. The values within the width of the Laplacian kernel from the edges affect the internal region, therefore it is important to erode the mask accordingly. For a kernel defined by Equation 2.42, an erosion by one or two voxels should be enough [96], but in practice, more erosions tend to improve the quality of the results. iLF is quick and very easy to implement.

2.3.2.2 Sophisticated Harmonic Artifact Reduction for Phase data (SHARP)

This algorithm utilises an extension of the harmonic mean value theorem, namely that for a harmonic function B_{ext}:

$$B_{ext} = \rho * B_{ext} \tag{2.53}$$

if ρ is a non-negative, symmetric, normalised function [103]. In SHARP, ρ is a spherical kernel of radius r. An interim field map, $\Delta\hat{B}$ can be derived:

$$\begin{aligned} \Delta\hat{B} &= \Delta B - \rho * \Delta B \\ &= B_{int} + B_{ext} - \rho * B_{int} - \underbrace{\rho * B_{ext}}_{B_{ext}} \\ &= B_{int} - \rho * B_{int} \\ &= (\delta - \rho) * B_{int} \end{aligned} \tag{2.54}$$

where δ is the delta function and $\Delta B = B_{int} + B_{ext}$.

The algorithm consists of the following steps:

1. Construct the spherical kernel ρ.
2. Compute the interim field distribution: $\Delta\hat{B} = \Delta B - \rho * \Delta B$. This can be implemented by taking advantage of the Fourier convolution theorem (section 1.3.1):

$$\begin{aligned} \Delta\hat{B} &= \mathcal{F}^{-1} \left\{ \mathcal{F}(\delta - \rho) \cdot \mathcal{F}(\Delta B) \right\} \\ &= \mathcal{F}^{-1} \left\{ (1 - \mathcal{F}(\rho)) \cdot \mathcal{F}(\Delta B) \right\} \end{aligned} \tag{2.55}$$

3. Compute the field variations due to internal susceptibility sources using Equation 2.54: $B_{int} = (\delta - \rho) *^{-1} \Delta\hat{B}$. Again using the Fourier convolution theorem:

$$B_{int} = \mathcal{F}^{-1}\left\{\frac{1}{1-\mathcal{F}(\rho)} \cdot \mathcal{F}(\Delta\hat{B})\right\} \tag{2.56}$$

Note that the kernel, $\frac{1}{1-\mathcal{F}(\rho)}$, has to be thresholded (as in Equation 2.47) and a suitable mask has to be applied to avoid convolution artifacts similarly to iLF (section 2.3.2.1). In general, SHARP tends to provide more accurate local field maps with less boundary-related artifacts when using larger kernels. However, for a kernel of radius r, a mask erosion width of at least r is necessary. Therefore, there is a trade-off between loss of information at the boundary and field accuracy. SHARP is available for download as part of the MEDI toolbox [86].

2.3.2.3 Variable-radius SHARP (VSHARP)

The main drawback of SHARP is the trade-off between the accuracy of the local field map and the loss of field information at the edges of the mask. To overcome this, Wu et al. proposed a method [104] that calculates the convolution in Equation 2.55 using large spherical kernels for voxels far away from the boundary, and kernels with gradually decreasing radii towards the mask edges. The deconvolution of Equation 2.56 is performed with the largest of the kernels used in the convolution step. This method provides accurate local field values within the tissue while simultaneously reducing boundary-related artifacts. However, due to the varying kernel radii, this technique has a high numerical complexity. A MATLAB implementation of VSHARP is available for download as part of the STI Suite software package [105].

2.3.2.4 Joint 2D and 3D phase processing

As mentioned in section 1.2.2.1, images acquired with a 2D gradient echo sequence are often corrupted by stripes due to patient motion. This becomes even more pronounced once the background fields are eliminated. Wei et al. [106] proposed a technique that can reduce the effect of striping in the susceptibility maps by combining 2D and 3D phase unwrapping and background field removal techniques:

1. First, a 2D version of the Laplacian phase unwrapping (section 2.2.2.2) is used to unwrap each slice separately.

2. Then, a modified, 2D version of VSHARP is applied to each slice to remove the in-plane harmonic background fields.

3. Finally, the through-plane harmonic components of the background are removed using 3D VSHARP described in section 2.3.2.3.

The main drawback of this method is that it uses VSHARP for the background field removal step making it unsuitable for applications where VSHARP is not the optimal technique for BFR. Also, applying BFR twice (first slice-by-slice and then in 3D) might result in overattenuation of the field values. The joint phase processing method is available for download as part of the STI Suite software package [105].

2.3.3 Assumption of constant-zero internal fields at the boundary

These techniques are based on the assumption that the contribution of internal susceptibility sources to the total field map is zero throughout the boundary of the tissue mask and (ii) (i.e. that the background fields are induced by susceptibility sources outside the tissue mask). Similarly to the no sources close to the boundary assumption, this usually holds when the mask edges are within the tissue, next to regions with low susceptibility variations (e.g. at the brain edges). However, the assumption is violated close to the tissue/air interface.

2.3.3.1 Laplacian Boundary Value (LBV) method

This technique [107] simply applies a numerical solver to the Poisson equation of the local magnetic field variations:

$$\begin{aligned} \nabla^2 B_{int} &= \nabla^2 (B_{tot} - B_{ext}) \\ &= \nabla^2 B_{tot} - \underbrace{\nabla^2 B_{ext}}_{0} \\ &= \nabla^2 B_{tot} \end{aligned} \tag{2.57}$$

where $B_{tot} = \Delta B = B_{int} + B_{ext}$. LBV assumes that magnetic field variations due to internal sources become insignificant at the tissue boundary. Therefore, the boundary condition of the above partial differential equation is set to $B_{int}|_{\partial M} = 0$, where ∂M denotes the edges of the binary tissue mask M.

In [107], Jacobi's method is described as a possible way to solve the above equation. The three-point finite difference is used to approximate the second derivatives:

$$\begin{aligned} \nabla^2 u &= \rho \\ (\nabla^2 u)_{i,j,k} &= \rho_{i,j,k} \\ \frac{u_{i+1,j,k} + u_{i-1,j,k} - 2 \cdot u_{i,j,k}}{dx^2} + & \\ \frac{u_{i,j+1,k} + u_{i,j-1,k} - 2 \cdot u_{i,j,k}}{dy^2} + & \\ + \frac{u_{i,j,k+1} + u_{i,j,k-1} - 2 \cdot u_{i,j,k}}{dz^2} &= \rho_{i,j,k} \end{aligned} \tag{2.58}$$

$u_{i,j,k}$ can be expressed from the above equation and used as an iteration scheme:

$$u_{i,j,k}^{(n+1)} = \frac{1}{\frac{2}{dx^2} + \frac{2}{dy^2} + \frac{2}{dz^2}} \left(\frac{u_{i+1,j,k}^{(n)} + u_{i-1,j,k}^{(n)}}{dx^2} + \frac{u_{i,j+1,k}^{(n)} + u_{i,j-1,k}^{(n)}}{dy^2} + \frac{u_{i,j,k+1}^{(n)} + u_{i,j,k-1}^{(n)}}{dz^2} - \rho_{i,j,k} \right) \tag{2.59}$$

The LBV algorithm consists of the following steps:

1. First, the Laplacian of the total field map $\rho = \nabla^2 B_{tot}$ is calculated and $u^{(0)} = B_{int}^{(0)}$ is set to an initial estimate (e.g. an array of zeros). The local field estimates at the boundary are set to 0: $B_{int}^{(0)}|_{\partial M} = 0$.
2. Then, the next estimate of $u^{(n+1)} = B_{int}^{(n+1)}$ is calculated using Jacobi's solver from Equation 2.59 for all internal voxels.
3. The previous step is repeated until convergence: $\frac{\overline{|B_{int}^{(n)} - B_{int}^{(n-1)}|}}{\overline{|B_{int}^{(n)}|}} < \epsilon$ where ϵ is the iteration termination threshold.

LBV does not introduce kernel threshold or radius parameters, which limits the ambiguity of the results compared to e.g. SHARP or iLF. However, the $B_{int}|_{\partial M} = 0$ assumption might be violated in some cases (e.g. near the tissue/air interfaces). This could be resolved by somehow estimating B_{int} at the mask edges, but it is very difficult to do so. LBV is available for download as part of the MEDI toolbox [86].

2.3.3.2 Iterative Spherical Mean Value (iSMV)

This method proposed by Wen et al. [108] also assumes constant-zero internal fields at the boundary while exploiting the harmonic mean value property of the background fields

from Equation 2.53. If ρ is a spherical kernel, this expression means that the background field remains intact upon averaging it across spheres.

In [108], the authors define the following operation, S:

$$S(\Delta B) = \begin{cases} \rho * \Delta B & \text{inside the mask} \\ \Delta B & \text{at the boundary} \end{cases} \tag{2.60}$$

where $\Delta B = B_{int} + B_{ext}$. Assuming that B_{int} is constant-zero at the boundary:

$$S(\Delta B) = \begin{cases} \rho * \Delta B & \text{inside the mask} \\ B_{ext} & \text{at the boundary} \end{cases} \tag{2.61}$$

Now let us consider the result of applying S to ΔB an infinite amount of times: $\hat{B} = S^{\infty}(\Delta B)$. S does not effect the values at the boundary, therefore $\hat{B} = B_{ext}$ near the edges. Also, $\hat{B}$ is harmonic *inside the mask*:

$$\begin{aligned} \rho * \hat{B} &= \rho * (S^{\infty}(\Delta B)) \\ &= \rho * (\rho *^{\infty} \Delta B) \\ &= \rho *^{\infty} \Delta B \\ &= \hat{B} \end{aligned} \tag{2.62}$$

Therefore, $\hat{B} = B_{ext}$. B_{int} can be calculated by applying S to ΔB until it converges to B_{ext} and then subtracting it from ΔB.

The implementation of the algorithm consists of the following steps:

1. Identify the ROI (tissue mask M) and its boundary (∂M).
2. Create a spherical kernel (ρ_r) of radius r for the S_r operation. Note that the weights assigned to each voxel in the kernel are proportional to the volume of the part of the sphere within the voxel (Figure 2.9 A). Also note that the spherical mean value theorem assumes a spherical kernel in the real domain, therefore the kernel has to be adjusted for voxel geometry (Figure 2.9 B).
3. Set $B^{(0)} = \Delta B$.
4. Calculate $B^{(n+1)} = S_r(B^{(n)})$:
   (a) Inside ROI: Convolve $B^{(n)}$ with the spherical kernel: $B^{(n+1)} = \rho_r * B^{(n)}$.
   (b) On the boundary: Set the values on the boundary to the total field on the boundary: $B^{(n+1)}|_{\partial M} = \Delta B|_{\partial M}$.

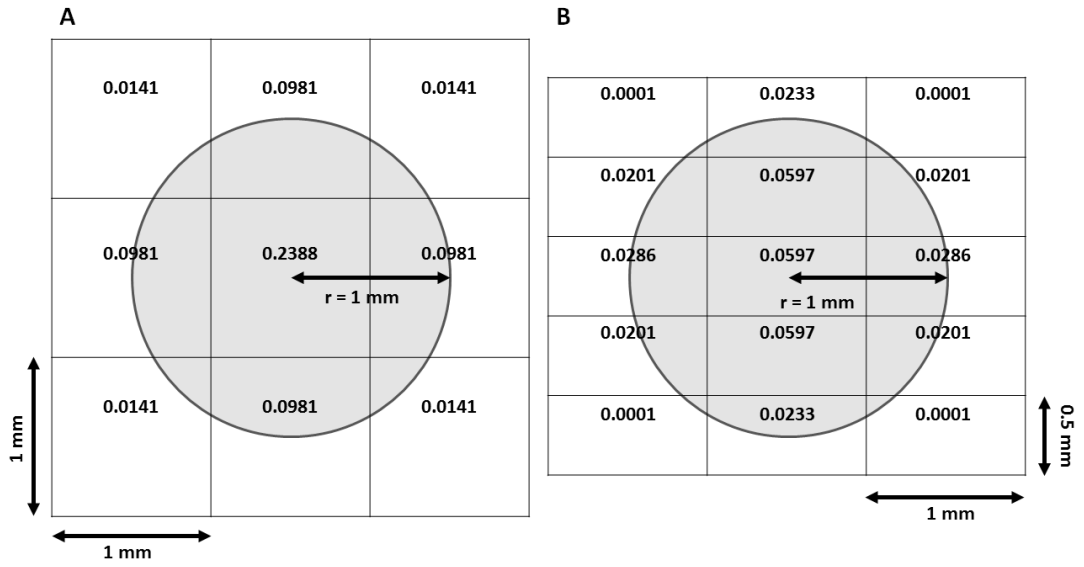

Figure 2.9: Central slices of 3D spherical kernels with radii of 1 mm and image resolutions of 1 mm × 1 mm × 1 mm (A) and 1 mm × 0.5 mm × 1 mm (B).

5. Repeat step 4 until convergence: $\frac{\overline{|B^{(n)}-B^{(n-1)}|}}{\overline{|B^{(n)}|}} < \epsilon$

6. Compute $B_{int} = B_{tot} - B^{(n)}$.

Wen et al. [108] have also shown that kernels (ρ) of radii 1 and 6 voxels yielded almost identical results. Therefore, this technique is suitable for background field removal near the edges of the brain. However, since iSMV makes the same assumptions as LBV, only using a different corollary of the harmonic property of the background fields for the implementation, it also has the same advantages and drawbacks.

2.3.4 Assuming a local field map with small Euclidean norm

These methods are also based on (ii) (i.e. that the background fields are induced by susceptibility sources outside the tissue mask). However, they avoid employing an explicit boundary condition by implicitly assuming that the local field map, B_{int}, has a small Euclidean norm compared to that of the background fields, B_{ext}. This is a valid assumption if most of the background originates from the susceptibility difference between tissue and air (∼-9.4 ppm [16]), while the internal fields are induced by the smaller susceptibility variations within the tissue (≤1 ppm).

2.3.4.1 Projection onto Dipole Field (PDF)

This method, proposed by Liu et al. [109], aims to explain the internal field variations of ΔB with a susceptibility distribution outside the tissue mask by solving the following minimisation problem:

$$\chi_{ext} = \arg\min_{\chi} \|MW(\Delta B - B_0 \cdot d * ((I - M)\chi))\|_2 \tag{2.63}$$

where $I - M$ is the inverse tissue mask (0 within the ROI and 1 outside) and W is a weighting matrix. The solution, χ_{ext} is a susceptibility distribution which is 0 within the mask ($\chi_{ext} = (I - M)\chi_{ext}$) and induces a field map, $B_0 \cdot (d * \chi_{ext})$, within the mask that is closest to the measured total field map ΔB. W assigns higher weights to the fit where ΔB is more reliable. This method implicitly assumes that the local field contributions are much smaller than the background fields, therefore $\Delta B \sim B_{ext}$ and, consequently, $B_0 \cdot (d * \chi_{ext}) = B_{ext}$.

The above minimisation problem is equivalent to the following linear system which can be solved using the pseudo inverse:

$$\begin{aligned} MW(B - \mathcal{D}(I - M)\chi) &= 0 \\ \underbrace{MW\mathcal{D}(I - M)}_{A}\chi &= \underbrace{MWB}_{b} \\ A\chi &= b \\ A^H A\chi &= A^H b \end{aligned} \tag{2.64}$$

where $B = \Delta B$ and $\mathcal{D} = B_0 \cdot d*$. Equation 2.64 can be solved using the conjugate gradient method [109]. Once χ_{ext} is obtained, the local field map can be calculated as $B_{int} = \Delta B - B_0 \cdot (d * \chi_{ext})$.

Due to the fact that the total field map is measured on a discrete, Cartesian coordinate system, fields induced by strong susceptibility sources at the boundary might be difficult to deal with (as mentioned in the introduction of this section). However, the advantage of PDF is that due to the lack of explicit boundary conditions, boundary-related effects do not propagate into the ROI, but only manifest as local artifacts that can be reduced by mask erosion. A MATLAB implementation of PDF is available for download as part of the MEDI toolbox [86].

Note that Wharton et al. [110] proposed a similar method called dipole fitting. They model the unwanted background field contributions using only a few dipole point sources (instead of using a susceptibility distribution) positioned outside the ROI. The model parameters are the strengths and locations of these sources.

2.3.4.2 Regularisation-enabled SHARP (RESHARP)

The main drawback of the methods based on the harmonic assumption (Equation 2.49) is that they do not eliminate background field contributions that are non-harmonic (such as phase offsets induced by spatially inhomogeneous excitation). Sun and Wilman proposed a background field removal method [111] that overcomes this issue by solving the minimisation problem below:

$$\arg\min_{B_{int}} \left(\| M(\delta - \rho) * (\Delta B - B_{int}) \|_2^2 + \lambda \| B_{int} \|_2^2 \right) \tag{2.65}$$

where ρ is the spherical kernel from section 2.3.2.2 and λ is the regularisation parameter. $(\delta - \rho) * (\Delta B - B_{int}) = (\delta - \rho) * B_{ext} = 0$, since both $\delta * B_{ext} = \rho * B_{ext} = B_{ext}$. The above minimisation problem can be solved with conjugate gradient optimisation [111]. The second term is called the Tikhonov regularisation term which forces B_{int} to have a small Euclidean norm. This essentially means that we want to model background fields as harmonic functions (first term), but not at the cost of generating unrealistically large local field variations (second term). By choosing a large λ, non-harmonic contributions of the background are suppressed along with the harmonic components. However, some components of the local field variations are reduced as these are also non-harmonic [99]. It has been shown that by choosing a reasonable λ, RESHARP produces more accurate local field maps near the boundary than SHARP [111].

2.3.5 Conclusions

Accurate background field removal is an essential and very challenging part of the QSM pipeline. A variety of different current techniques based on different underlying assumptions have been proposed to eliminate background fields. Schweser et al. [99] previously compared many of these methods using a detailed numerical phantom of the human brain. However, a similar comparison in the head and neck is still required. In section 6.3, I first compared some of the state-of-the-art techniques in a numerical brain phantom to verify that my results are in accordance with those of Schweser et al. and then compared the two most promising techniques (PDF and LBV, sections 2.3.4.1 and 2.3.3.1 respectively) in a head-and-neck phantom. In section 6.4, I investigated the properties of these two techniques in in-vivo images of the head and neck.

2.4 Susceptibility calculation

The local field map (B_{int}) can be expressed as a convolution between the unit dipole field (d, Equation 1.17) and the underlying tissue susceptibility distribution (χ_{int}):

$$B_{int}(\mathbf{r}) = B_0 \cdot d(\mathbf{r}) * \chi_{int}(\mathbf{r}) \tag{2.66}$$

Susceptibility calculation techniques aim to solve the inverse problem and infer χ_{int} from (B_{int}) either by taking advantage of the Fourier convolution theorem:

$$\mathcal{F}\{B_{int}(\mathbf{r})\} = B_0 \cdot D(\mathbf{k}) \cdot \mathcal{F}\{\chi_{int}(\mathbf{r})\} \tag{2.67}$$

where $D(\mathbf{k})$ is the Fourier transform of the unit dipole field from Equation 1.19, or by simply fitting the model described by Equation 2.66 to the local field map.

In the following section, I review current susceptibility calculation techniques.

2.4.1 Solving the inverse problem in the Fourier domain

Based on Equation 2.67, the susceptibility map should be easy to calculate by division in the Fourier domain:

$$\chi_{int}(\mathbf{r}) = \mathcal{F}^{-1}\left\{\frac{1}{B_0} \cdot \frac{1}{D(\mathbf{k})}\mathcal{F}\{B_{int}(\mathbf{r})\}\right\} \tag{2.68}$$

However, the denominator, $D(\mathbf{k})$ equals 0 on a conical surface where $k^2 = 3k_z^2$ (Equation 1.19). Furthermore, values of $D(\mathbf{k})$ close to this conical surface are very small, introducing high intensity points in $\chi_{int}(\mathbf{k})$, the estimated Fourier transform of the susceptibility map. These may amplify the noise in B_{int} and lead to streaking artifacts in the calculated susceptibility map. The following methods are designed to deal with zeros in $D(\mathbf{k})$ and the small values of $D(\mathbf{k})$ near the conical surface.

2.4.1.1 Truncated K-space Division (TKD)

The technique of Shmueli et al. [21] uses a regularised version of the k-space kernel, $\frac{1}{D(\mathbf{k})}$, to solve Equation 2.68:

$$\frac{1}{D_{TKD}(\mathbf{k})} = \begin{cases} \left(\frac{1}{3} - \frac{k_z^2}{k^2}\right)^{-1} & \text{if } \left|\frac{1}{3} - \frac{k_z^2}{k^2}\right| > \delta \\ \text{sign}\left(\frac{1}{3} - \frac{k_z^2}{k^2}\right) \cdot \frac{1}{\delta} & \text{otherwise} \end{cases} \tag{2.69}$$

where δ is a pre-defined threshold (or truncation) value[1].

One of the problems with this approach is that the susceptibility values are systematically underestimated due to the truncation of the kernel, $\frac{1}{D(\mathbf{k})}$. In [96], Schweser et al. addressed this problem by proposing a corrected version of the regularised dipole kernel:

$$\frac{1}{D_{TKD,corr}(\mathbf{k})} = \frac{1}{D_{TKD}(\mathbf{k})} \cdot \frac{1}{p(\mathbf{0},\delta)} \qquad (2.70)$$
$$p(\mathbf{r},\delta) = \mathcal{F}^{-1}\left\{\frac{D(\mathbf{k})}{D_{TKD}(\mathbf{k})}\right\}$$

where $p(\mathbf{r},\delta)$ is the point spread function (PSF) due to the dipole modification. The $\frac{1}{p(\mathbf{0},\delta)}$ term essentially corrects the DC offset of the kernel, enforcing $\int B_{int} \cdot d\mathbf{r} = \int (d * \chi_{int}) \cdot d\mathbf{r}$.

Figure 2.10 shows $D_{TKD}(\mathbf{k})$, and $\frac{1}{D_{TKD}(\mathbf{k})}$ along the red lines for different truncation values. The choice of δ determines the extent of regularisation. A small threshold maintains the shape of the dipole kernel, but does not attenuate the high-frequency noise in the images or the streaking artifacts that corrupt susceptibility maps. Susceptibility maps obtained with higher threshold values are more regularised with less noise and streaking. In practice, the maximum $\delta = 2/3$ tends to work well if combined with the PSF correction mentioned above to compensate for the underestimation of susceptibility values. TKD is a fast method that is easy to implement.

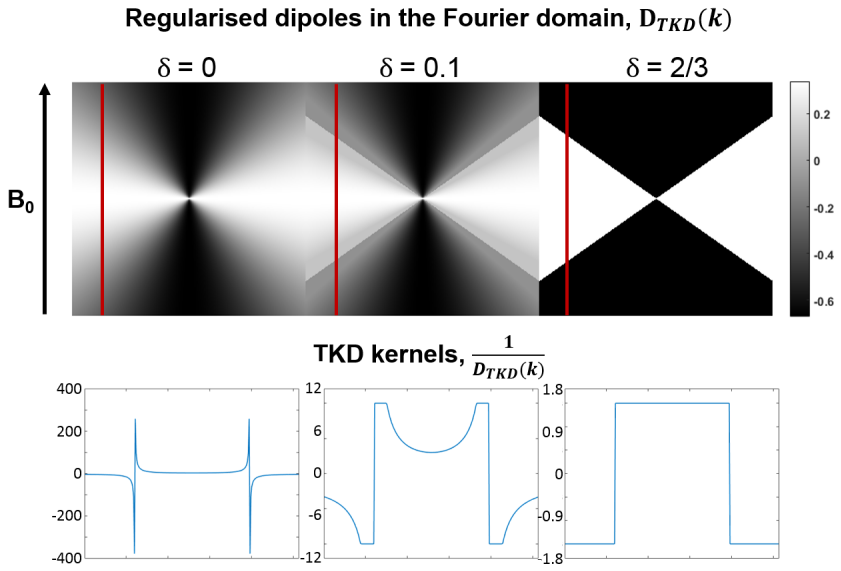

Figure 2.10: Regularised dipoles in the Fourier domain for different δ truncation values (top row). TKD kernels corresponding to each δ along the red lines are also plotted (bottom row).

[1]Not the delta function that it denoted earlier.

2.4.1.2 Calculation Of Susceptibility through Multiple Orientation Sampling (COSMOS)

The method of Liu et al. [112] is a multiple orientation technique based on the acquisition of multiple images with the object (e.g. head of the patient) rotated at different angles with respect to the direction of the main magnetic field (B_0). For an object rotated by an angle of ψ about the x axis, the relationship between the susceptibility map and the resulting field variations can be expressed by the following equation in the Fourier domain:

$$\begin{aligned} B_{int,\psi}(\mathbf{k}) &= B_0 \left(\frac{1}{3} - \frac{k_{zp}^2}{k^2} \right) \cdot \chi_{int}(\mathbf{k}) \\ &= B_0 \left(\frac{1}{3} - \frac{(k_z \cos\psi + k_y \sin\psi)^2}{k^2} \right) \cdot \chi_{int}(\mathbf{k}) \end{aligned} \tag{2.71}$$

In the case of N different orientations $(\psi_1, \psi_2 \dots \psi_N)$, $\chi(\mathbf{k})$ can be estimated from N different formulas:

$$B_0 \cdot \underbrace{\begin{bmatrix} D_{\psi_1}(\mathbf{k}) \\ \vdots \\ D_{\psi_N}(\mathbf{k}) \end{bmatrix}}_{\mathbf{D}} \cdot \chi_{int}(\mathbf{k}) = \underbrace{\begin{bmatrix} B_{int,\psi_1} \\ \vdots \\ B_{int,\psi_N} \end{bmatrix}}_{\mathbf{B}} \tag{2.72}$$

$$D_{\psi_i}(\mathbf{k}) = \frac{1}{3} - \frac{(k_z \cos\psi_i + k_y \sin\psi_i)^2}{k^2}$$

As long as for every $\mathbf{k}$, there exists a ψ_i, so that $D_{\psi_i}(\mathbf{k}) > 0$, the problem is well-posed. Intuitively, this means that there can not be a point in k-space where all the cones ($3k_z^2 = k^2$) intersect. $N \geq 3$ is a necessary condition.

The least squares solution of the above problem is given by:

$$\chi_{int}(\mathbf{k}) = \frac{\sum_{i=1}^{N} D_{\psi_i}(\mathbf{k}) \cdot B_{int,\psi_1}(\mathbf{k})}{B_0 \cdot \sum_{i=1}^{N} D_{\psi_i}(\mathbf{k})^2} \tag{2.73}$$

However, for noise considerations, Liu et al. introduced a weighting operator into the equation and turned it into a minimisation problem:

$$\arg\min_{\chi_{int}} \left\| W \cdot \mathcal{F}^{-1}(\mathbf{B} - B_0 \cdot \mathbf{D}\chi_{int}) \right\|_2 \tag{2.74}$$

COSMOS produces high quality susceptibility maps, but requires the acquisition of multiple images which reduces patient throughput. Also, subjects have to keep their heads at unnatural angles for 5-10 minutes which is uncomfortable, increasing the possibility of motion artifacts. Not to mention that rotating their heads in a tight-fitting RF coil

might be difficult. Furthermore, the exact angle of their heads needs to be measured or estimated and images acquired with the subject's head rotated at different angles have to be co-registered. In conclusion, COSMOS is not clinically applicable, but has been considered a gold standard method in the research community against which other methods are compared [113].

2.4.2 Regularisation-based fitting methods

Each of these methods is a fitting algorithm that tries to find the underlying susceptibility distribution by solving the following minimisation problem [114]:

$$\arg\min_{\chi_{int}} \|M(B_{int} - B_0 \cdot (d * \chi_{int}))\|_2^2 \tag{2.75}$$

where M denotes the binary tissue mask. This expression is usually completed with a weighting operator (W) that accounts for the inhomogeneous noise variance of the phase across the field of view:

$$\arg\min_{\chi_{int}} \|MW(B_{int} - B_0 \cdot (d * \chi_{int}))\|_2^2 \tag{2.76}$$

As B_{int} contains noise, the problem is subject to over-fitting, meaning that a χ_{int} corresponding to a perfect fit is very far from the real susceptibility distribution. Therefore, regularisation is needed to obtain a χ_{int} that is meaningful. The following techniques apply different regularisation strategies to the problem described by Equations 2.75 and 2.76.

2.4.2.1 Improved Sparse Linear Equation and Least Squares (iLSQR)

It would be straightforward to solve Equation 2.75 by applying the conjugate gradient method to:

$$\mathcal{D}\chi_{int} = B_{int} \tag{2.77}$$

$$\mathcal{D}^T\mathcal{D}\chi_{int} = \mathcal{D}^T B_{int} \tag{2.78}$$

where $\mathcal{D} = B_0 \cdot d*$ denotes the convolution with the dipole kernel. However, this method does not perform well for ill-conditioned problems.

Li et al. proposed to solve Equation 2.75 [115] using the LSQR method [116]. LSQR is a technique designed to solve linear systems such as $Ax = b$. It is similar to the conjugate gradient method in style, i.e. instead of calculating A^{-1}, A is only used to

compute products of the form Av where v is a vector. However, LSQR applies an algebraic rearrangement to reduce the original problem to a series of linear systems with tridiagonal system matrices. This makes the algorithm more numerically stable [116] and better suited for ill-conditioned problems.

Li et al. later proposed to further improve this technique [117] by subtracting the "streaky" part of the susceptibility map ($\chi_{streaks}$):

$$\chi_{iLSQR} = \chi_{LSQR} - \chi_{streaks} \tag{2.79}$$

where χ_{LSQR} is the LSQR solution of Equation 2.76. They proposed to estimate $\chi_{streaks}$, by solving the following minimisation problem using the LSQR method again:

$$\underset{\chi_{streaks}}{\arg\min} \left\| W_b \cdot \nabla(\chi_{LSQR}(\mathbf{r}) - \mathcal{F}^{-1}\left(\chi_{streaks}(\mathbf{k}) \cdot M_{IC}\right)) \right\|_2 \tag{2.80}$$

where M_{IC} is a binary mask of the ill-conditioned k-space regions and W_b is a weighting term that assigns higher weights to regions with low expected susceptibility gradients. In other words, $\chi_{streaks}$ tries to explain high susceptibility gradients in χ_{LSQR} in regions without susceptibility boundaries (i.e. streaks) using only the ill-conditioned part of k-space which is supposedly the origin of the streaking.

iLSQR is available as part of the STI Suite software package [105].

2.4.2.2 Tikhonov regularisation

In general, over-fitting leads to unrealistically large susceptibility values in χ_{int}. Therefore, it is sensible to introduce a regularisation term that keeps the Euclidean norm of χ_{int} small [114]:

$$\underset{\chi_{int}}{\arg\min} \left\| MW(B_{int} - B_0 \cdot (d * \chi_{int})) \right\|_2^2 + \alpha \left\| \chi_{int} \right\|_2^2 \tag{2.81}$$

where the second term is the so-called Tikhonov term and α is the regularisation parameter. The above minimisation problem is equivalent to solving the following linear system [87]:

$$(\mathcal{D}^T W^T M W \mathcal{D} + \alpha I) \cdot \chi_{int} = \mathcal{D}^T W^T M W \cdot B_{int} \tag{2.82}$$

where $\mathcal{D} = B_0 \cdot d*$ and I is the identity operator. Considering that $\mathcal{D}^T = \mathcal{D}$ and $W^T = W$, this can be solved using conjugate gradient optimisation. From now on, I refer to this method as **iterative Tikhonov**.

If neither a weighting matrix (W) nor a mask (M) are used, the above expression simplifies to:

$$(\mathcal{D}^2 + \alpha I) \cdot \chi_{int} = \mathcal{D} \cdot B_{int} \tag{2.83}$$

$$B_0^2 \cdot d * (d * \chi_{int}) + \alpha \cdot \chi_{int} = B_0 \cdot d * B_{int} \tag{2.84}$$

which is straight-forward to solve in the Fourier domain[2], which makes this implementation a direct k-space inversion method [118]:

$$D(\mathbf{k})^2 \cdot \mathcal{F}\{\chi_{int}(\mathbf{r})\} + \alpha \cdot \mathcal{F}\{\chi_{int}(\mathbf{r})\} = D(\mathbf{k}) \cdot \mathcal{F}\{B_{int}(\mathbf{r})\} \tag{2.85}$$

$$\chi_{int}(\mathbf{r}) = \mathcal{F}^{-1}\left\{\frac{B_0 \cdot D(\mathbf{k})}{B_0^2 \cdot D(\mathbf{k})^2 + \alpha} \cdot \mathcal{F}\{B_{int}(\mathbf{r})\}\right\} \tag{2.86}$$

Exchanging $\alpha \rightarrow B_0^2 \cdot \alpha$:

$$\chi_{int}(\mathbf{r}) = \mathcal{F}^{-1}\left\{\frac{1}{B_0} \cdot \frac{D(\mathbf{k})}{D(\mathbf{k})^2 + \alpha} \cdot \mathcal{F}\{B_{int}(\mathbf{r})\}\right\} \tag{2.87}$$

$$\chi_{int}(\mathbf{r}) = \mathcal{F}^{-1}\left\{\frac{1}{B_0} \cdot \frac{1}{D_{Tik}(\mathbf{k})} \cdot \mathcal{F}\{B_{int}(\mathbf{r})\}\right\} \tag{2.88}$$

where $\frac{1}{D_{Tik}(\mathbf{k})}$ is the Tikhonov kernel, similarly to $\frac{1}{D_{TKD}(\mathbf{k})}$ in the TKD inversion (section 2.4.1.1). PSF correction can be incorporated into the calculation similarly to section 2.4.1.1 as this technique also tends to underestimate susceptibility values due to the regularised dipole kernel. In this work, this implementation of the Tikhonov regularisation is referred to as **direct Tikhonov**. Note that the same PSF correction factor, estimated from the direct Tikhonov kernel, can be applied to the iterative Tikhonov result as well to obtain more comparable results.

[2]Note that $D(\mathbf{k})$ is the dipole kernel in k-space, different from $\mathcal{D} = B_0 \cdot d*$ which is an operator in the image domain.

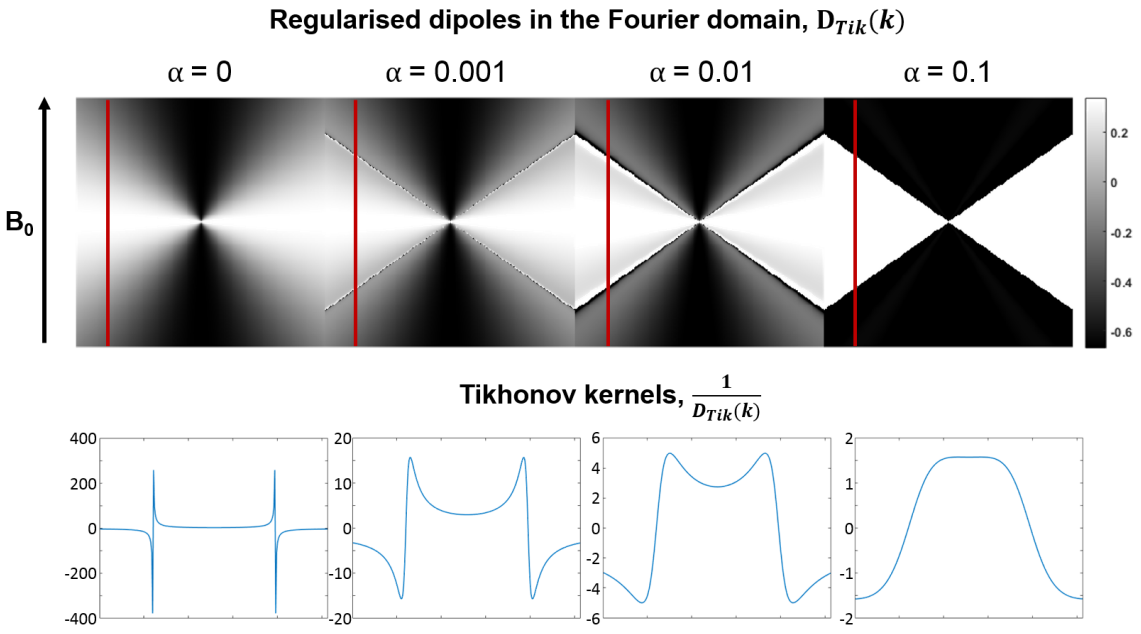

Figure 2.11: Regularised dipoles in the Fourier domain for different α values (top row). Tikhonov kernels corresponding to each α along the red lines are also plotted (bottom row).

Figure 2.11 shows $D_{Tik}(\mathbf{k})$, and $\frac{1}{D_{Tik}(\mathbf{k})}$ along the red lines for different α regularisation parameters. The kernels for $\alpha = 0$ and 0.1 are very similar to the TKD kernels at $\delta = 0$ and 2/3 (Figure 2.10), but the transition is much smoother. Since TKD tends to work well with $\delta = 2/3$ and PSF correction, it is sensible to use direct Tikhonov with $\alpha = 0.1$, also combined with PSF correction.

I implemented both the direct and iterative Tikhonov methods in MATLAB.

2.4.2.3 Total variation (TV) regularisation and Morphology Enabled Dipole Inversion (MEDI)

Total variation regularisation uses the total variation (L1-norm) of the gradient of the susceptibility map ($\nabla\chi_{int}$) as the regularisation term [119]:

$$\arg\min_{\chi_{int}} \|MW(B_{int} - B_0 \cdot (d * \chi_{int}))\|_2^2 + \lambda \|\nabla\chi_{int}\|_1 \tag{2.89}$$

In general, TV-regularisation prefers piece-wise constant solutions which is the reason for its popularity as it provides susceptibility maps that are easy to interpret visually. However, the true susceptibility distribution is likely to be heterogeneous even within structures such as the red nucleus or the globus pallidus.

MEDI is a modified version of the TV-regularisation method proposed by Liu et al. [120]:

$$\arg\min_{\chi_{int}} \|MW(B_{int} - B_0 \cdot (d * \chi_{int}))\|_2^2 + \lambda \|M_G \cdot \nabla\chi_{int}\|_1 \tag{2.90}$$

where M_G is a binary tissue mask of regions with small gradients in the magnitude image. This additional element ensures that the piece-wise constant property of the susceptibility map is enforced only where the magnitude image is nearly homogeneous. In other words, this technique assumes structural consistency between the susceptibility map and the magnitude image. However, there is no one-to-one correspondence between magnitude and susceptibility, therefore relying too heavily on this assumption could lead to inaccurate results.

An implementation of the MEDI algorithm is available as part of the MEDI toolbox [86].

2.4.2.4 Choice of the regularisation parameter

Most of the above fitting methods are based on the minimisation of RN + λ· RT where RN and RT are the residual norm and the regularisation term respectively, while λ is called the regularisation parameter. RN is either $\|B_{int} - B_0 \cdot (d * \chi_{int})\|_2^2$ (for the direct Tikhonov method) or $\|MW(B_{int} - B_0 \cdot (d * \chi_{int}))\|_2^2$ (for the iterative Tikhonov and MEDI algortihms). RT is $\|\chi_{int}\|_2^2$ for the Tikhonov methods and $\|M_G \cdot \nabla\chi_{int}\|_1$ for MEDI.

The regularisation parameter, λ, controls how much weight is given to the minimisation of RT relative to the minimisation of the RN term. If λ is too small, the regularisation term has almost no weight and the solution will be one that minimises $\|B_{int} - B_0 \cdot (d * \chi_{int})\|_2^2$. Due to the aforementioned noise in B_{int}, this often leads to over-fitting. On the other hand, if λ is too small, most of the weight is given to the regularisation term resulting in over-regularisation errors. The effect of this depends on the type of regularisation. For example, for the Tikhonov methods, this would lead to a severely attenuated solution that minimises the norm of the solution (Tikhonov regularisation term).

The L-curve method [121] is a widely used technique that optimises the regularisation parameter. Both terms are estimated for a range of different λ values: RN(λ), RT(λ). The parametric plot of (RN(λ), RT(λ)) is called the L-curve (Figure 2.12). For low λ values, RN is expected to be very small, while RT is generally high due to the aforementioned over-fitting effects. For high λ values, RT is expected to be small, and RN tends to be

high because the residual norm is barely considered when calculating the solution. If these assumptions are fulfilled, the (RN(λ), RT(λ)) plot has a characteristic L-shape:

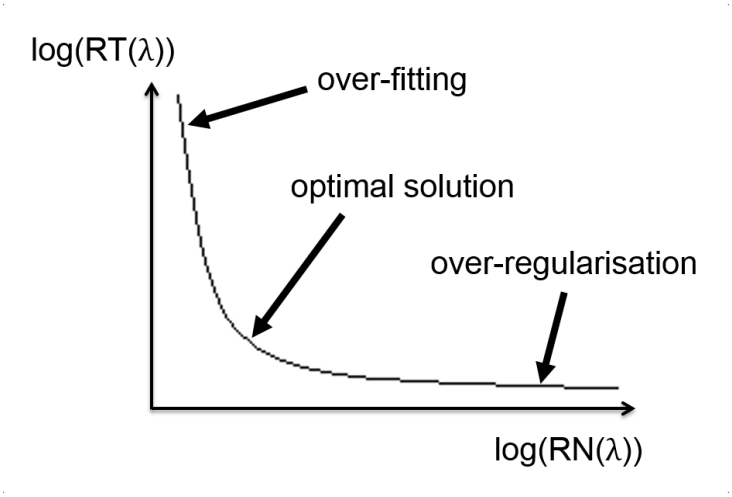

Figure 2.12: Characteristic L-shape of the parametric (RN(λ), RT(λ)) plot.

The optimal regularisation parameter corresponds to a point between over-fitting and over-regularisation where the curvature is maximal [121]. Note that many optimisation problems do not produce an L-shape for the (RN(λ), RT(λ)) plot. However, the maximum curvature point is still widely considered to be a very good estimate for the optimised regularisation parameter.

2.4.3 Conclusions

Susceptibility maps can be calculated from local field maps either using direct k-space inversion methods based on Equation 2.67 (e.g. TKD or direct Tikhonov) or iterative fitting of Equation 2.66 to the local field map in image space (e.g. iterative Tikhonov or MEDI). Though there is a wide variety of susceptibility calculation techniques developed in the past few years, there is no ground truth method even for brain images [113]. Therefore, in section 6.4, I compared clinically feasible susceptibility calculation methods using in-vivo images of the head and neck.

Chapter 3

Noise propagation in susceptibility mapping

Signal-to-noise ratio (SNR) is one of the most important features of MR images, as higher SNR corresponds to better image quality and higher measurement precision in quantitative MRI in general. SNR is a sensible measure of image quality and, therefore, a potentially straight-forward way to compare different acquisition parameters and post-acquisition processing pipelines in head-and-neck images. The signal in this context is defined as the MRI signal (S) that is proportional to the net magnetisation vector (section 1.2.1) in a given voxel:

$$S_m = S + N(\sigma) \tag{3.1}$$

The superimposed noise ($N(\sigma)$ in Equation 3.1) is a random value of Gaussian distribution:

$$P(N(\sigma) = x) = \frac{1}{\sqrt{2\pi\sigma^2}} e^{-\frac{x^2}{2\sigma^2}} \tag{3.2}$$

where $P(N = x)$ denotes the probability that $N(\sigma)$ is any given, real x value. The measured signal is S_m in Equation 3.1. The noise can be characterised by the standard deviation (σ) of the corresponding Gaussian distribution, and SNR can be defined as S/σ.

SNR can be measured, for example, using repeated measures of the same subject using the same acquisition parameters. Since in theory, the signal should not vary across acquisitions[1], the distribution of the measured values at any voxel is expected to be

[1] I am ignoring physiological effects in this demonstration.

Gaussian:

$$P(S_m = x) = \frac{1}{\sqrt{2\pi\sigma^2}} e^{-\frac{(x-S)^2}{2\sigma^2}} \tag{3.3}$$

Therefore, S and σ can be estimated as the mean and standard deviation of the repeated measures. However, this approach requires multiple acquisitions and, consequently, is very time-consuming.

A similar way of approximating the SNR relies on the assumption that the signal is homogeneous in a given region. Therefore, calculating the mean and standard deviation of the values measured in that region should provide a reasonable estimate [13]. However, this assumption is often violated.

In any case, the signal in a given voxel can usually be approximated by $S \sim S_m$ as $N(\sigma) << S$ is a reasonable assumption for most MR images. However, in QSM, the resulting susceptibility map is the final processed image that is meant to be used to aid the solution of the clinical problem. Therefore, SNR of the susceptibility map is the relevant quantity. Thus, it is essential to assess the propagation of the measurement uncertainty along the susceptibility mapping pipeline in order to properly characterise the effect of different QSM pipeline elements on susceptibility SNR and, consequently, susceptibility image quality. Here I use a theoretical approach to estimate and in-vivo brain data to demonstrate the evolution of the uncertainty at different stages of the QSM pipeline.

3.1 Propagation of measurement uncertainty

In order to calculate how measurement uncertainty at one stage of the QSM pipeline affects uncertainty in the next stage, I use the formula for the propagation of measurement uncertainty for Gaussian distributions [123]. For any function $f(a_1, a_2 \dots a_N)$, the measurement uncertainty of f ($\sigma(f)$) can be expressed as a function of the uncertainty of the dependent variables:

$$\sigma(f)^2 = \sum_{i=1}^{N} \left(\frac{\partial f}{\partial a_i} \right)^2 \cdot \sigma(a_i)^2 \tag{3.4}$$

Note that this formula is only valid for Gaussian noise distributions which is generally a reasonable approximation in MR images. Also, the above function needs to be completed with a covariance term, $Cov(a_i, a_j)$, if there is a correlation between the noise of a_i and a_j for any i, j pair of indices. Here I neglect this term as it is expected to be very small for gradient-echo MRI experiments used for susceptibility mapping [87].

3.2 Measurement uncertainty of the magnitude and phase

Note that even though in QSM, we mostly think in terms of magnitude (M) and phase (φ), in reality, the real (R) and imaginary (I) components of the complex MRI are the measured quantities. Therefore, these have Gaussian noise distributions:

$$P(R_m = x) = \frac{1}{\sqrt{2\pi\sigma_R^2}} e^{-\frac{(x-R)^2}{2\sigma_R^2}} \tag{3.5}$$

$$P(I_m = x) = \frac{1}{\sqrt{2\pi\sigma_I^2}} e^{-\frac{(x-I)^2}{2\sigma_I^2}} \tag{3.6}$$

The magnitude and phase can be calculated as follows:

$$M = \sqrt{R^2 + I^2} \tag{3.7}$$

$$\varphi = \arctan\left(\frac{I}{R}\right) \tag{3.8}$$

Therefore, the corresponding signal distributions can be calculated as:

$$P(M_m = z) = \int_{x^2+y^2=z^2} P(R_m = x) \cdot P(I_m = y) \tag{3.9}$$

$$P(\varphi_m = z) = \int_{y/x=\tan z} P(R_m = x) \cdot P(I_m = y) \tag{3.10}$$

$P(M_m = z)$ is the so-called Rician distribution that was shown to be close to Gaussian for high SNR [84]:

$$P(M_m = z) \approx \frac{1}{\sqrt{2\pi\sigma^2}} e^{-\frac{(z-\sqrt{M^2+\sigma^2})^2}{2\sigma^2}} \tag{3.11}$$

Another assumption here is that $\sigma_R = \sigma_I = \sigma$ which also happens to coincide with the measurement uncertainty of the magnitude. $P(\varphi_m = z)$ can also be approximated by a Gaussian for very high SNR [84]:

$$P(\varphi_m = z) \approx \frac{1}{\sqrt{2\pi(\sigma/M)^2}} e^{-\frac{z^2}{2(\sigma/M)^2}} \tag{3.12}$$

Here, the uncertainty of the phase equals: $\sigma_\varphi = \sigma/M$. σ_φ can also be calculated using the error propagation approach from Equation 3.4:

$$\begin{aligned}
\sigma_\varphi^2 &= \left(\frac{\partial\varphi}{\partial R}\right)^2 \cdot \sigma^2 + \left(\frac{\partial\varphi}{\partial I}\right)^2 \cdot \sigma^2 \\
&= \left(\frac{-I/R^2}{1+(I/R)^2}\right)^2 \cdot \sigma^2 + \left(\frac{1/R}{1+(I/R)^2}\right)^2 \cdot \sigma^2 \\
&= \frac{1/R^2 + I^2/R^4}{(1+(I/R)^2)^2} \cdot \sigma^2 \\
&= \frac{R^2+I^2}{(R^2+I^2)^2} \cdot \sigma(R)^2 \\
&= \frac{\sigma^2}{R^2+I^2} \\
\sigma_\varphi^2 &= \frac{\sigma^2}{M^2}
\end{aligned} \tag{3.13}$$

Note that I reached the same result. In conclusion, the SNR for the phase image can be estimated as:

$$\mathrm{SNR}_\varphi = \frac{\varphi}{\sigma/M} \tag{3.14}$$

M and φ are the measured magnitude and phase images at each voxel. σ can be estimated by calculating the standard deviation (SD) of the magnitude, or alternatively the real or imaginary images, in regions with homogeneous signal. For a more accurate estimation, SD can be calculated in five different regions of a few hundred voxels and σ can be estimated as the mean of these five measures (see section 1.2.2.2). Note that this approach assumes that σ is spatially homogeneous.

Here I demonstrate the process of estimating the noise in the phase maps using multi-echo brain images acquired in a healthy volunteer on a 3-Tesla scanner (Achieva, Philips Healthcare, NL) using a 3D gradient-echo sequence and a 32-channel head coil, with matrix size = 240×240×144, SENSE factors = 1×2×1.5, 1 mm isotropic resolution, TE_1 = 3 ms, ΔTE = 5.4 ms, 5 echoes, TR = 29 ms, and flip angle = 20°. Five 400-voxel (20-by-20) white matter regions were manually segmented in the central sagittal slice (Figure 3.1). The magnitude is expected to be homogeneous within these regions, therefore the Gaussian shapes of the histograms (Figure 3.1) can be used to estimate the magnitude noise. Note that this single-scan approach for calculating the SNR is only a simple demonstration of the noise evolution across the QSM pipeline using brain images acquired for a different study (chapter 5). It has been shown that the two-scan approach (section 1.2.2.2) yields more accurate results in images acquired using multiple channels and SENSE acceleration [124].

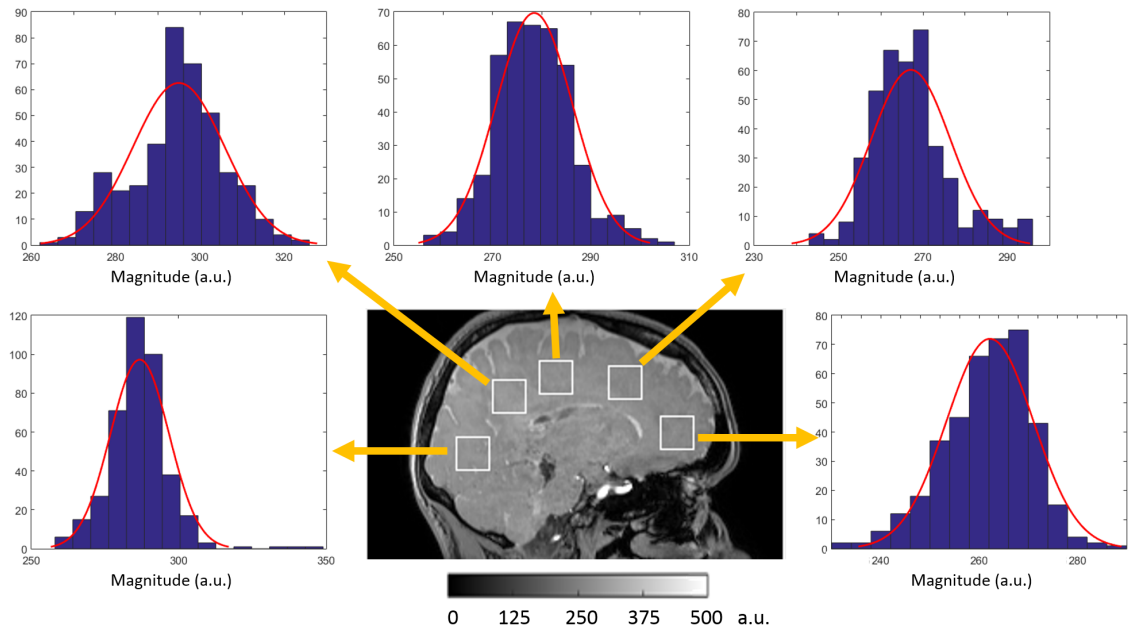

Figure 3.1: Manually segmented, 400-voxel regions in the central sagittal slice of the first-echo magnitude image. The corresponding histograms of these regions are also shown along with fitted Gaussian functions.

The magnitude noise was estimated in each region as the standard deviation of the magnitude signal. The process was repeated for each echo. In Figure 3.2 a, the magnitude noise is shown across echo times. There is a slight increase in noise level towards later echoes which is in keeping with previous studies [125]. Figure 3.2 also shows that the spatial variation in the magnitude noise increases with echo time. This is probably caused by the fact that contrast increases with echo time in gradient-echo images and the manually segmented white matter regions are less homogeneous at later echoes (not shown). It is debatable at this point whether the noise can be approximated to be independent of the echo time. Figure 3.2 also shows the spatial variations in SNR in the first-echo magnitude image calculated as M/σ, where σ is the mean of the noise in the five regions from the first echo.

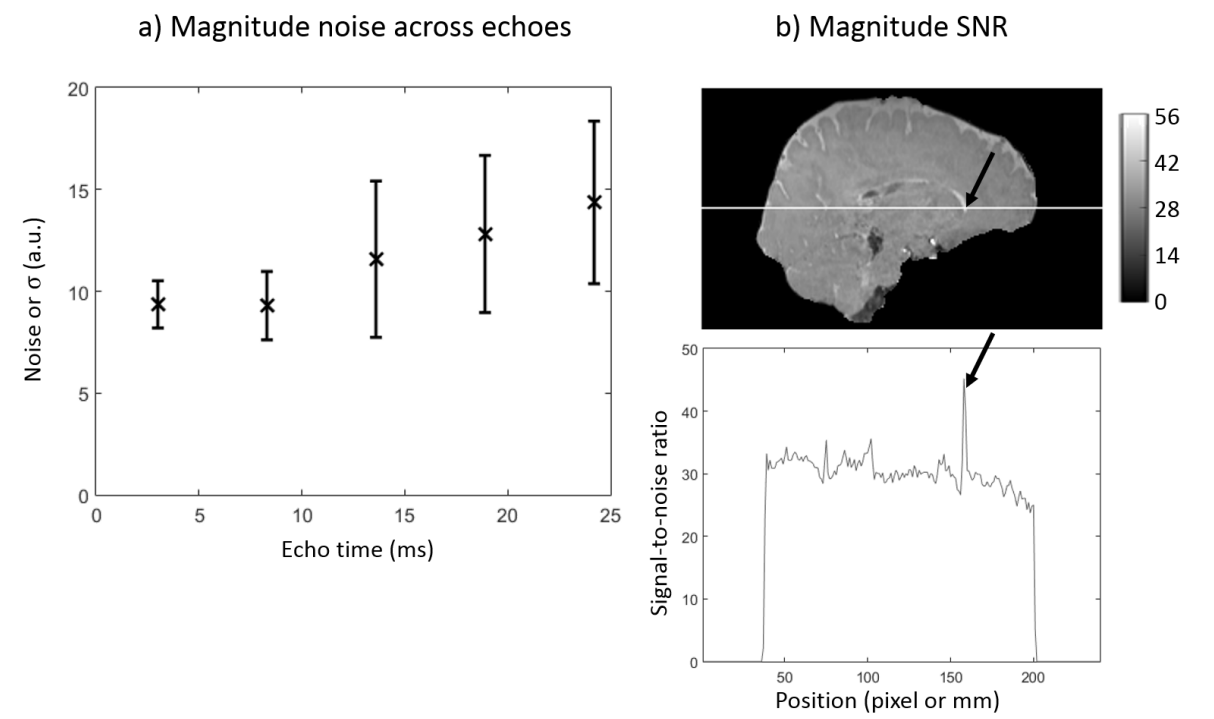

Figure 3.2: Variations in the magnitude noise across echo times (a) and SNR in the magnitude image (b). The scatter plot in (a) shows the mean noise across the five, 400-voxel regions with error bars equal to their standard deviation. The plotted line in (b) shows the variations in magnitude SNR across the brain along the white line in the first echo. The arrows indicate the elevated SNR due to the high signal of the cerebrospinal fluid in the lateral ventricle of the brain.

Figure 3.3 shows the phase (a) and SNR (b) profiles of the first-echo phase image. The SNR was calculated using Equation 3.14, where M/σ is shown in Figure 3.2 b. Note that the phase was unwrapped using SEGUE (chapter 4). Since this is a region growing technique (section 2.2.2.1), it is not expected to affect the noise distribution (section 3.3). However, the unwrapped phase map is more representative of the actual phase signal. Another important feature here is that the phase has a large variation across the volume (Figure 3.3 a) due to the background fields (section 1.3). Therefore, the phase cannot be expected to be homogeneous in otherwise structurally homogeneous regions. This is why it is easier to estimate the noise in the phase maps by measuring the noise level in the magnitude. Note the unrealistically large phase values towards the edges (Figure 3.3 a, arrows) probably generated by incorrect phase unwrapping around noisy voxels (section 4). This, however, is attenuated in the SNR (Figure 3.3 b, arrows) by the high noise level near the brain edges.

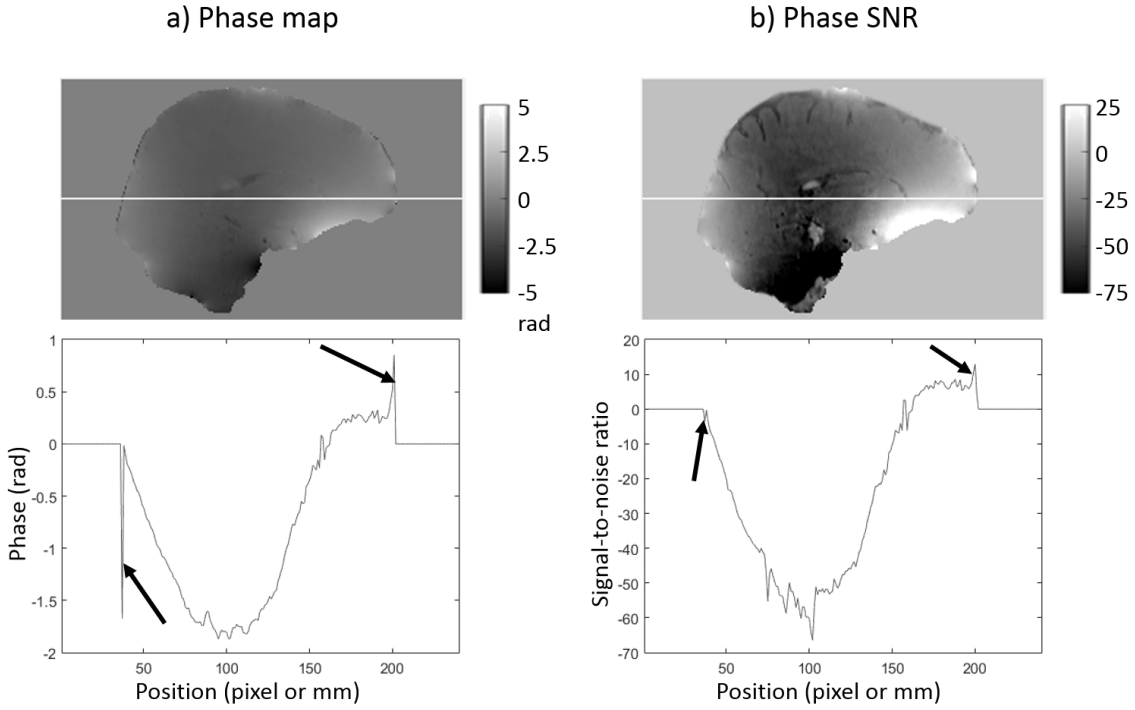

Figure 3.3: Unwrapped phase map (a) and spatial distribution of the phase SNR (b). The plotted lines show the phase and phase SNR profiles along the white lines in the images. The arrows in (a) indicate unrealistically high phase values close to the mask edges induced by unwrapping errors in noisy voxels. The arrows in (b) indicate how these are attenuated by the high noise in the same voxels.

3.3 Measurement uncertainty of the total field map

The first step in the susceptibility mapping pipeline is the estimation of the total field map. This can be done by either spatially unwrapping each echo separately followed by a linear fit to the phase, or applying the non-linear fitting approach to the complex data (section 2.2). In both cases, the relationship between the total field map (ΔB) and the phase is assumed to be linear (Equation 1.6):

$$\varphi_i = \gamma \Delta B \cdot \mathrm{TE}_i + \varphi_0 \tag{3.15}$$

A magnitude-weighted fit ($W_i = M_i$) is expected to provide total field maps with higher SNR as the high noise in later echoes is suppressed using the small magnitude weights (section 2.2.1.2). Moreover, non-linear fitting can also be approximated as a magnitude-weighted fit (section 2.2.1.3):

$$W_i \cdot \varphi_i = W_i \cdot (\gamma \Delta B \cdot \mathrm{TE}_i + \varphi_0) \tag{3.16}$$

The problem is defined by the following linear system:

$$\underbrace{\begin{bmatrix} W_1 \cdot \varphi_1 \\ \vdots \\ W_N \cdot \varphi_N \end{bmatrix}}_{\boldsymbol{\varphi}} = \underbrace{\begin{bmatrix} W_1 & W_1 \cdot \mathrm{TE}_1 \\ \vdots & \vdots \\ W_N & W_N \cdot \mathrm{TE}_N \end{bmatrix}}_{A} \cdot \underbrace{\begin{bmatrix} \varphi_0 \\ \gamma \Delta B \end{bmatrix}}_{\mathbf{x}} \tag{3.17}$$

The least squares solution can be calculated using the pseudoinverse (section 2.2.1.1): $\mathbf{x} = (A^T A)^{-1} A^T \boldsymbol{\varphi}$. Thus the total field map is estimated by the following expression:

$$\gamma \Delta B = \frac{\sum_i W_i^2 \sum_i W_i^2 \mathrm{TE}_i \varphi_i - \sum_i W_i^2 \mathrm{TE}_i \sum_i W_i^2 \varphi_i}{\sum_i W_i^2 \sum_i W_i^2 \mathrm{TE}_i^2 - (\sum_i W_i^2 \mathrm{TE}_i)^2} \tag{3.18}$$

Using Equation 3.4, the measurement uncertainty of the total field map can be calculated as:

$$\sigma(\gamma \Delta B)^2 = \sum_k \left(\frac{\partial(\gamma \Delta B)}{\partial \varphi_k} \right)^2 \sigma(\varphi_k)^2 \tag{3.19}$$

Substituting Equations 3.18 and 3.13 and performing the differentiation:

$$\sigma(\gamma \Delta B)^2 = \sum_k \left(\frac{\sum_i W_i^2 W_k^2 \mathrm{TE}_k - \sum_i W_i^2 \mathrm{TE}_i W_k^2}{\sum_i W_i^2 \sum_i W_i^2 \mathrm{TE}_i^2 - (\sum_i W_i^2 \mathrm{TE}_i)^2} \right)^2 \frac{\sigma_k^2}{M_k^2} \tag{3.20}$$

Assuming $W_k = M_k$ (magnitude weighting) and $\sigma_k = \sigma$ (echo time independent measurement uncertainty), expanding the square and simplifying the formula:

$$\begin{aligned}
\sigma(\gamma \Delta B)^2 &= \sum_k \frac{(\sum_i M_i^2)^2 M_k^4 \mathrm{TE}_k^2 + (\sum_i M_i^2 \mathrm{TE}_i)^2 M_k^4 - 2 \sum_i M_i^2 \sum_i M_i^2 \mathrm{TE}_i M_k^4 \mathrm{TE}_k}{\left(\sum_i M_i^2 \sum_i M_i^2 \mathrm{TE}_i^2 - (\sum_i M_i^2 \mathrm{TE}_i)^2 \right)^2} \frac{\sigma^2}{M_k^2} \\
&= \sum_k \frac{(\sum_i M_i^2)^2 M_k^2 \mathrm{TE}_k^2 + (\sum_i M_i^2 \mathrm{TE}_i)^2 M_k^2 - 2 \sum_i M_i^2 \sum_i M_i^2 \mathrm{TE}_i M_k^2 \mathrm{TE}_k}{\left(\sum_i M_i^2 \sum_i M_i^2 \mathrm{TE}_i^2 - (\sum_i M_i^2 \mathrm{TE}_i)^2 \right)^2} \sigma^2 \\
&= \frac{(\sum_i M_i^2)^2 \sum_k M_k^2 \mathrm{TE}_k^2 + (\sum_i M_i^2 \mathrm{TE}_i)^2 \sum_k M_k^2 - 2 \sum_i M_i^2 \sum_i M_i^2 \mathrm{TE}_i \sum_k M_k^2 \mathrm{TE}_k}{\left(\sum_i M_i^2 \sum_i M_i^2 \mathrm{TE}_i^2 - (\sum_i M_i^2 \mathrm{TE}_i)^2 \right)^2} \sigma^2 \\
&= \frac{(\sum_i M_i^2)^2 \sum_i M_i^2 \mathrm{TE}_i^2 - (\sum_i M_i^2 \mathrm{TE}_i)^2 \sum_i M_i^2}{\left(\sum_i M_i^2 \sum_i M_i^2 \mathrm{TE}_i^2 - (\sum_i M_i^2 \mathrm{TE}_i)^2 \right)^2} \sigma^2
\end{aligned}$$

$$\sigma(\gamma \Delta B)^2 = \frac{\sigma^2 \sum_i M_i^2}{\sum_i M_i^2 \sum_i M_i^2 \mathrm{TE}_i^2 - (\sum_i M_i^2 \mathrm{TE}_i)^2} \tag{3.21}$$

Note that Equation 3.21 is in accordance with the formula of Kressler et al. [87]. Also, in the last few steps, it was assumed that σ is independent of the echo time and that a magnitude-weighted fit is performed. If any of these assumptions is violated, Equation 3.20 should be used to calculate the measurement uncertainty of the total field map instead.

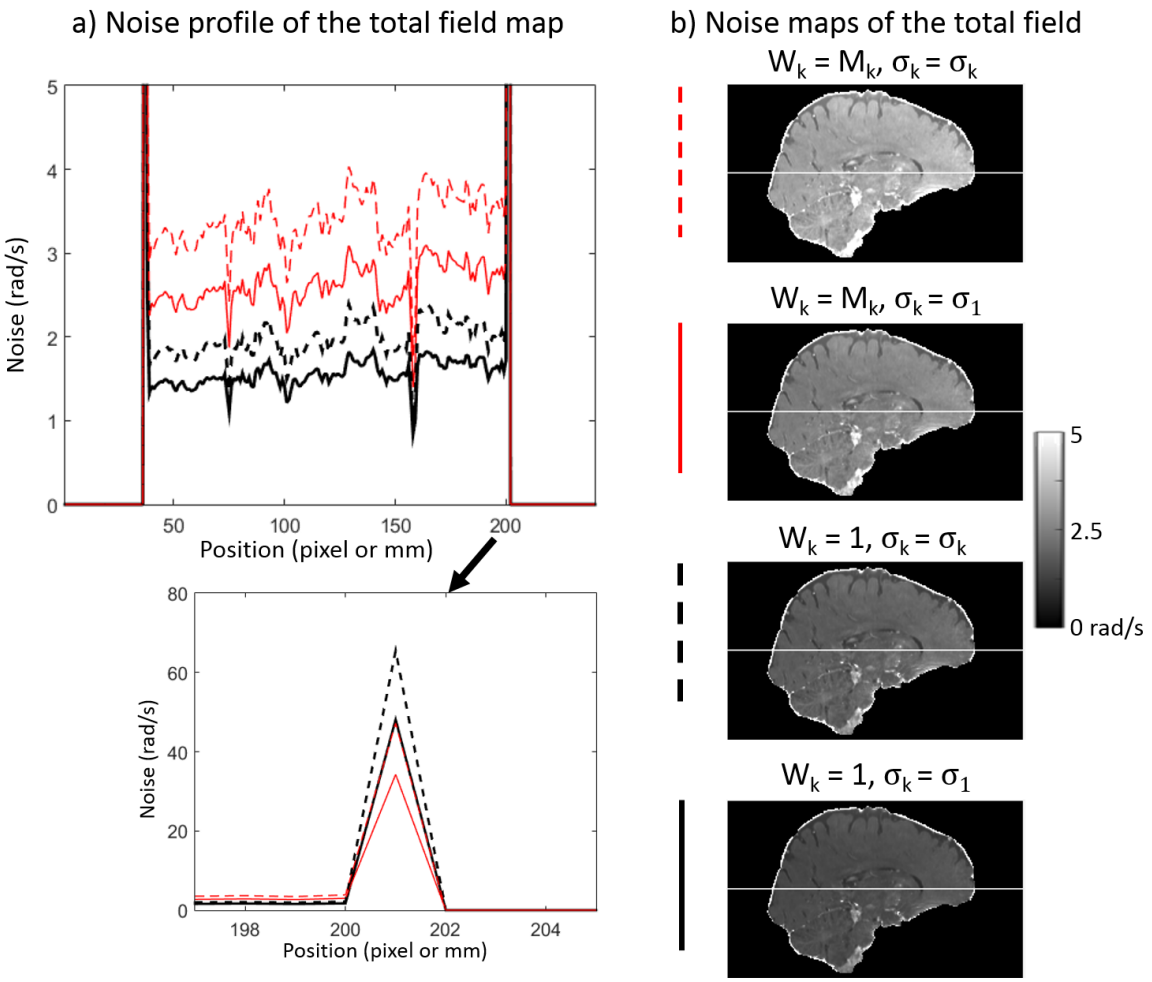

Figure 3.4: Noise profiles (a) and noise maps (b) of the total field map calculated with or without magnitude weighting (red and black lines respectively), and with or without accounting for the echo time-dependent magnitude noise (dashed and solid lines respectively).

The measurement uncertainty distribution of the total field map was estimated using Equation 3.20 both with or without magnitude weighting ($W_k = M_k$ or $W_k = 1$ respectively), and with or without taking into account the echo time dependence of the magnitude noise ($\sigma_k = \sigma_k$ or $\sigma_k = \sigma_1$ respectively). The resulting noise maps are shown in Figure 3.4 b along with the noise profiles across the white lines in each image (Figure 3.4 a, top). Magnitude-weighted fits provided higher noise within the brain (Figure 3.4 a, red lines). This seems counter-intuitive as the low magnitude is expected to attenuate the errors induced by high noise in the phase at later echoes (section 2.2.1.2). However, note that measurement uncertainty values within the brain are generally between 1 and 4 rad/s which is very low compared to the $\approx\pm100$ rad/s field values in a typical total field map. Therefore, regardless of the weighting, the total field SNR in the brain is at least 20-25. Zooming in on one of the voxels at the brain edges (Figure 3.4 a, bottom)

reveals that the ordering changes towards high-noise voxels. This is further demonstrated in Figure 3.5 where the magnitude-weighted noise maps are more consistently low in the circled areas. This result is in accordance with the comparison in section 6.4. In conclusion, magnitude weighting provides slightly higher noise levels in the brain, but also more consistently lower noise in regions with low signal and high magnitude noise outside the brain. Therefore, it is expected to improve the total field noise profiles of head-and-neck images.

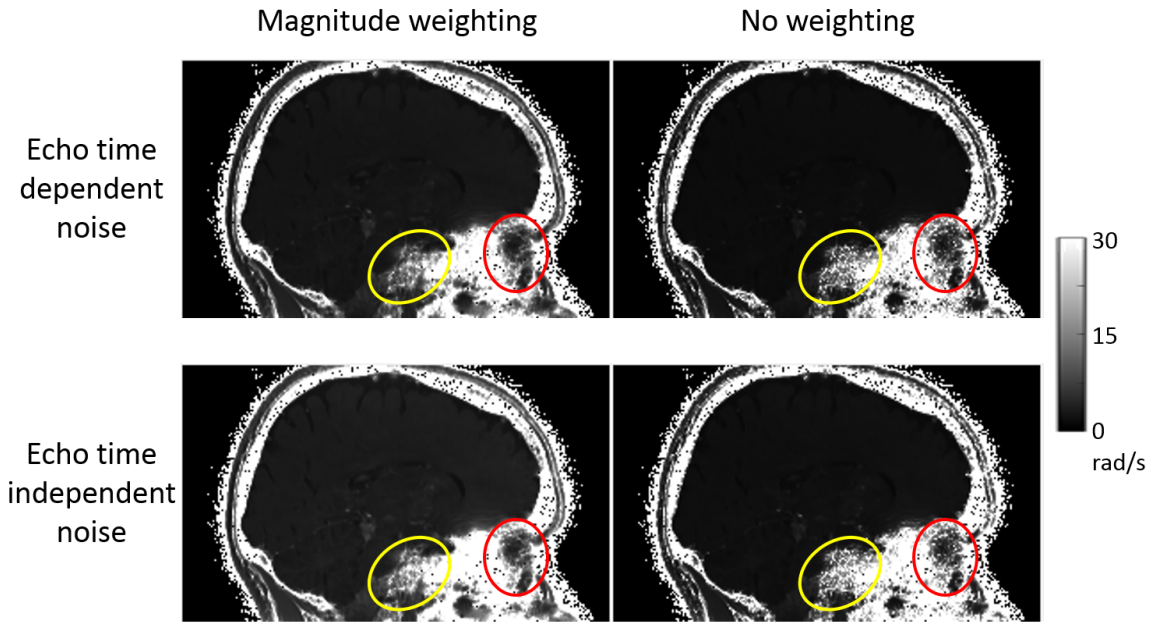

Figure 3.5: Total field noise maps in the head with (left column) or without (right column) magnitude weighting, and with (top row) or without (bottom row) accounting for the echo time-dependent magnitude noise. The red and yellow circles indicate high-noise regions where the magnitude-weighted fit provides overall lower noise.

Another important feature here is that accounting for the echo time-dependent magnitude noise resulted in higher noise within the brain (Figure 3.4, dashed lines). However, it is generally accepted within the QSM community to calculate the total field noise using Equation 3.21 instead of Equation 3.20 [85]. The inverse of this noise map is then used as a weighting term in many iterative susceptibility calculation methods (section 2.4.2). However, if the magnitude noise does in fact increase with echo time (Figure 3.2 a), neglecting this dependence might lead to additional errors later in the pipeline. However, it looks like the discrepancies between the dashed and solid lines in Figure 3.4 could be resolved using a constant factor. Figure 3.6 shows the total field noise maps, but the ones calculated without accounting for the echo time-dependent magnitude noise (middle column) were multiplied by 1.29 and 1.25 for the magnitude-weighted fit (top) and the

simple linear fit (bottom) respectively. This provided visually identical images to the ones where the echo time dependence is accounted for (left column). Moreover, the residual differences are only visible on a very small scale (right column). The mean absolute differences in the brain were 0.06 rad/s and 0.11 rad/s for the magnitude-weighted and simple linear fits respectively which correspond to about 1-2% of the dynamic range of the noise map. We can conclude that though the estimated total field noise is affected by the echo time-dependent magnitude noise, the relative uncertainties are less than 2% off using the simpler formula. Therefore, using Equation 3.21 to calculate the weighting term in iterative susceptibility calculation techniques is justified. Another advantage of applying Equation 3.21 over Equation 3.20 is that in the former, $\sigma = 1$ can be substituted and the relative errors are not affected. Therefore, there is no need to estimate the magnitude noise (σ) to perform QSM which removes a very cumbersome step from the processing pipeline.

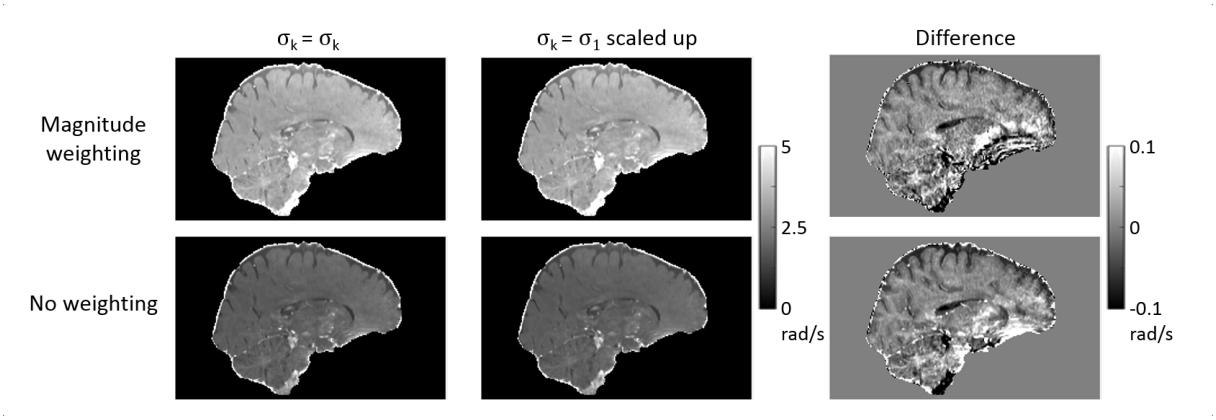

Figure 3.6: Total field noise maps in the brain with (top row) or without (bottom row) magnitude weighting, and with (left column) or without (middle column) accounting for the echo time-dependent magnitude noise. Noise maps in the middle column were scaled up to more closely resemble the images in the left column. The difference maps are also shown (right column). Note the reduced scale of the difference images.

Note that in this section, I discussed only the *noise distribution* of the different approaches. Linear fitting, magnitude-weighted linear fitting, and non-linear fitting can all result in different total field maps which also affects the SNR of the total field map.

In some cases (e.g. for non-linear fitting), an additional spatial unwrapping step is necessary after the field fitting to remove residual wraps. This can be achieved by some kind on region growing algorithm, like FSL PRELUDE (section 2.2.2.1). Since one of the features of these techniques is that they only add integer multiples of 2π to each measured phase value, they are not expected to affect the noise distribution within the field map. Another possibility for example is the Laplacian phase unwrapping (LPU) method (section

2.2.2.2). This technique has two different effects on phase/field maps: phase unwrapping and partial background field removal. Similarly to region-growing techniques, the phase unwrapping feature is not expected to affect the noise distribution. The measurement uncertainty propagation of background field removal techniques is discussed in the next section.

3.4 Measurement uncertainty of the local field map

The next step in the QSM processing pipeline is the elimination of the background field components. These are generally defined as all field components that were not induced by the susceptibility variations within the tissue mask (section 2.3). Because of this, the background (B_{ext}) and local (B_{int}) field contributions are independent (except near the mask edges [109], section 2.3). Therefore, a corollary of the measurement uncertainty propagation for Gaussian distributions applies here:

$$\begin{aligned} \Delta B &= B_{int} + B_{ext} \\ \sigma(\Delta B)^2 &= \sigma(B_{int})^2 + \sigma(B_{ext})^2 \end{aligned} \tag{3.22}$$

The first conclusion to draw here is that $\sigma(B_{int}) \leq \sigma(\Delta B)$ provides an upper limit for the noise in the local field maps [125]. Secondly, the estimated background fields are generally slowly varying, smooth functions that are subtracted from the total field map (ΔB) to obtain the local field variations (B_{int}). Therefore, the calculated B_{ext} is not expected to contain any noise ($\sigma(B_{ext}) = 0$). This does not mean that a total field map consisting of only background field elements (e.g. if the susceptibility is perfectly homogeneous within the mask) is noise-free, but implies that the background field removal step does not eliminate the noise of the local field components.

This argument is important for two reasons. First, most of the background field removal methods are iterative algorithms, where calculating the propagation of measurement uncertainty based on Equation 3.4 becomes extremely complicated. Secondly, many iterative susceptibility calculation methods use a weighting matrix to improve the fit (section 2.4.2). These weights are usually calculated using the inverse of Equation 3.21 if the total field was estimated from a multi-echo fit, or the inverse of 3.13 if a single-echo phase map is used for QSM. This only makes sense if the noise distribution is not altered by the background field removal step, otherwise $1/\sigma(B_{int})$ should be used as the weighting term.

Note that, though many background field removal techniques apply an iterative scheme, some simply perform a series of multiplications in k-space (section 2.3). This is similar to

the k-space inversion methods used for susceptibility calculation (section 2.4.1), therefore a similar approach could be adapted as in the next section to estimate the measurement uncertainty of the result. However, these techniques (including Laplacian phase unwrapping) apply some kind of threshold to their kernels which means that the high frequency components of the total field map are left intact. This further supports the argument that background field removal methods do not affect the noise distribution, since noise is generally of high frequency.

Finally, though background field removal is expected to leave the noise intact:

$$\sigma(B_{int}) = \sigma(\Delta B) \tag{3.23}$$

it definitely reduces SNR as $B_{int} << \Delta B$. Note that, as a consequence, higher SNR in the resulting local field map does not necessarily correspond to better background field removal as SNR is more likely to be large due to large residual background fields. Therefore SNR in the local field map is not a reliable way of assessing image quality.

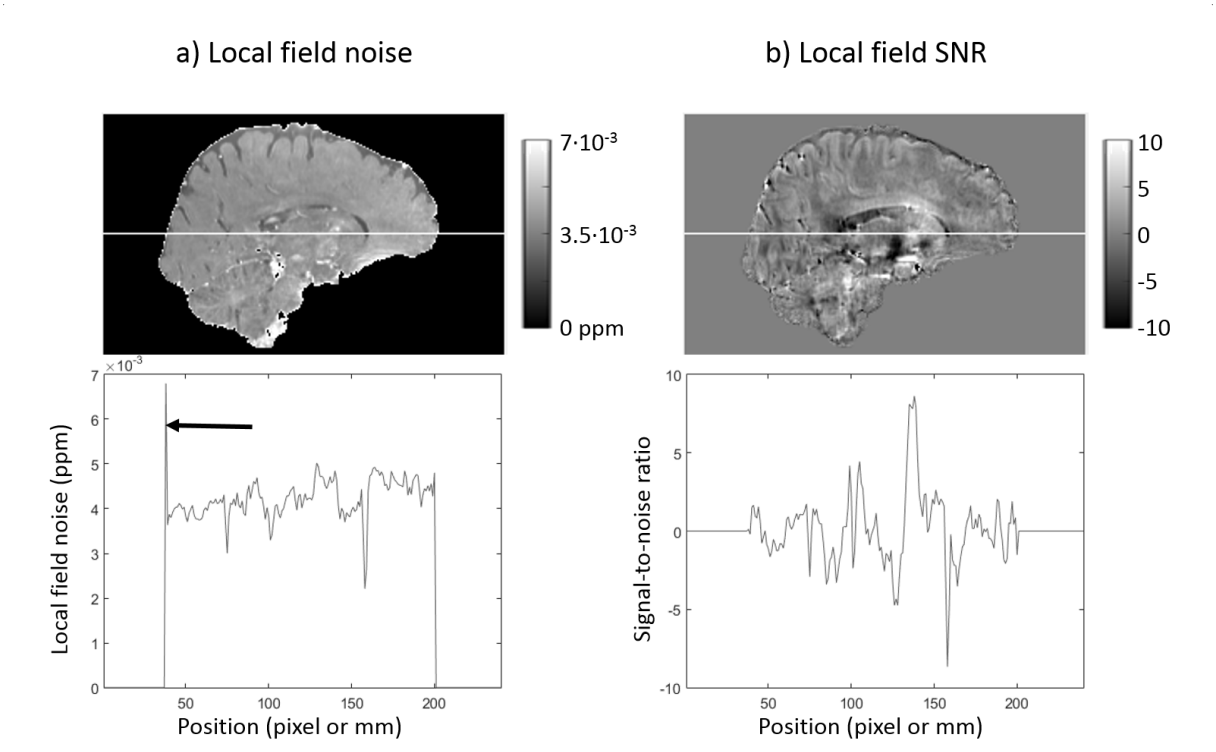

Figure 3.7: Spatial distribution of the local field noise (a) and SNR (b). The plotted lines show the noise and SNR profiles along the white lines in the images. The arrow in (a) indicates a voxel with very high noise close to the mask edge.

I calculated the local field map from the acquired multi-echo, complex images using: 1. Non-linear field fitting (section 2.2.1.3), 2. Laplacian phase unwrapping (section 2.2.2.2),

3. Projection onto Dipole Fields (section 2.3.4.1) to remove the background fields. Figure 3.7 a shows the calculated noise map in the local field assuming Equation 3.23, i.e. background field removal does not affect the noise distribution. The noise map was estimated using Equation 3.20 with $W_k = M_k$, as non-linear fitting is similar to a magnitude weighted fit in principle, and $\sigma_k = \sigma_k$, as this provides a more accurate estimation. The signal-to-noise ratio (SNR) in the local field map is displayed in Figure 3.7 b. Note that the SNR has large spatial variations because of the varying local field values. Also note that the rad/s field values were converted to ppm.

With the large, background field contributions eliminated, the local field (Figure 3.8) is expected to be mostly homogeneous in the aforementioned, manually selected, rectangular regions from Figure 3.1. This is further confirmed by the fact that the histograms in Figure 3.8 are mostly of Gaussian shapes. The local field map still has a non-local feature (section 1.3), but susceptibility sources inducing large field variations are not directly near these 400-voxel areas. Therefore, it is feasible to measure the noise in these five regions and compare them with values estimated using the propagation of measurement uncertainty.

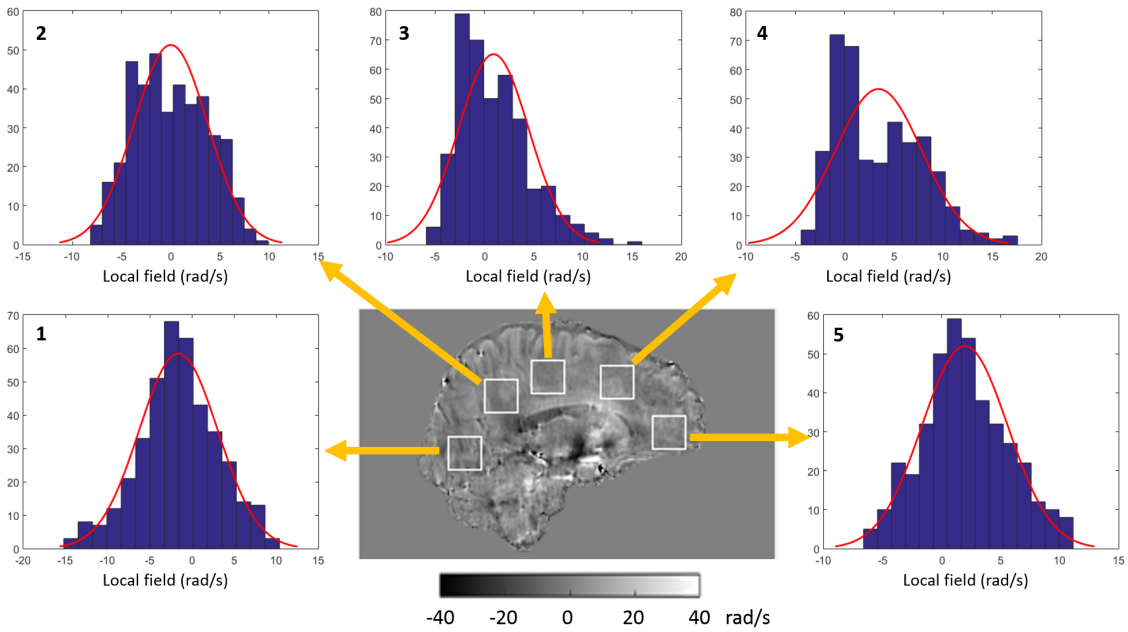

Figure 3.8: Manually segmented, 400-voxel regions in the central sagittal slice (same as in Figure 3.1) of the local field map. The corresponding histograms within these regions are also shown along with fitted Gaussian functions.

The measured noise was estimated as the standard deviation of the local field values in the five regions. The calculated noise was estimated as the mean of the noise values (Figure 3.7 a) in the same five, 400-voxel regions. Figure 3.9 shows the measured and

calculated noise in each region. There was good agreement between these values which shows that our calculation using the propagation of measurement uncertainty can accurately characterise the actual noise in the local field map. Moreover, this result also confirms the assumption that the background field removal does not have a substantial effect on the noise distribution.

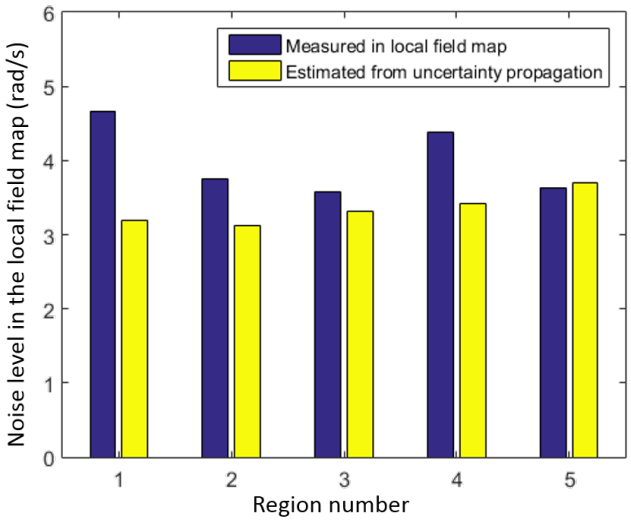

Figure 3.9: Measured and calculated noise in the local field map in five, manually selected, 400-voxel regions. Note that the region numbers correspond to the ones in the upper-left corners in the histograms of Figure 3.8.

3.5 Measurement uncertainty of the susceptibility map

The final step of the QSM pipeline is the susceptibility calculation step. Some susceptibility calculation techniques apply iterative fitting algorithms with various regularisation terms to estimate the underlying susceptibility distribution responsible for the induced field variations (section 2.4.2). As mentioned in the previous section, estimation of the measurement uncertainty propagation is extremely complicated for iterative methods. However, there is a way to perform the calculations for another popular class of susceptibility calculation methods, i.e. kernel-based k-space inversion techniques. Here I derive a simple formula describing the noise distribution in susceptibility maps calculated using kernel-based k-space inversion.

For kernel based methods, susceptibility is calculated using the following expression, where K is the applied k-space kernel:

$$\chi = \mathcal{F}^{-1}\left\{\frac{1}{B_0}K \cdot \mathcal{F}\left(B_{int}\right)\right\} \tag{3.24}$$

K is a regularised version of $1/D$, where D is the dipole kernel in k-space. The specific form of K depends on the type of regularisation (e.g. TKD or direct Tikhonov methods, sections 2.4.1.1 or 2.4.2.2).

The above expression can be expanded as follows:

$$\chi(\mathbf{r}) = \frac{1}{B_0}\int_{\mathbf{k}} K(\mathbf{k})\left\{\int_{\mathbf{r\prime}} B_{int}(\mathbf{r\prime})e^{-2\pi i\mathbf{kr\prime}}\mathbf{dr\prime}\right\}e^{+2\pi i\mathbf{kr}}\mathbf{dk} \tag{3.25}$$

Each point (j) in the susceptibility map is expressed using all points (k) in the local field map. Therefore, according to Equation 3.4:

$$\sigma(\chi_j)^2 = \sum_k \left(\frac{\partial\chi_j}{\partial B_{int,k}}\right)^2 \sigma(B_{int,k}^2) \tag{3.26}$$

The continuous version of the above can be expressed as:

$$\sigma(\chi(\mathbf{r}))^2 = \int_{\mathbf{r\prime\prime}} \left(\frac{\partial\chi(\mathbf{r})}{\partial B_{int}(\mathbf{r\prime\prime})}\right)^2 \sigma(B_{int}(\mathbf{r\prime\prime}))^2\mathbf{dr\prime\prime} \tag{3.27}$$

To calculate this integral, first we need to calculate the derivatives of Equation 3.25:

$$\begin{aligned}
\frac{\partial\chi(\mathbf{r})}{\partial B_{int}(\mathbf{r\prime\prime})} &= \frac{\partial}{\partial B_{int}(\mathbf{r\prime\prime})}\left(\frac{1}{B_0}\int_{\mathbf{k}} K(\mathbf{k})\left\{\int_{\mathbf{r\prime}} B_{int}(\mathbf{r\prime})e^{-2\pi i\mathbf{kr\prime}}\mathbf{dr\prime}\right\}e^{+2\pi i\mathbf{kr}}\mathbf{dk}\right) \\
&= \frac{1}{B_0}\int_{\mathbf{k}} K(\mathbf{k})\left\{\frac{\partial}{\partial B_{int}(\mathbf{r\prime\prime})}\int_{\mathbf{r\prime}} B_{int}(\mathbf{r\prime})e^{-2\pi i\mathbf{kr\prime}}\mathbf{dr\prime}\right\}e^{+2\pi i\mathbf{kr}}\mathbf{dk} \\
&= \frac{1}{B_0}\int_{\mathbf{k}} K(\mathbf{k})\cdot e^{-2\pi i\mathbf{kr\prime\prime}}\cdot e^{+2\pi i\mathbf{kr}}\mathbf{dk} \\
&= \frac{1}{B_0}\int_{\mathbf{k}} K(\mathbf{k})e^{2\pi i\mathbf{k(r\text{-}r\prime\prime)}}\mathbf{dk} \\
\frac{\partial\chi(\mathbf{r})}{\partial B_{int}(\mathbf{r\prime\prime})} &= \frac{1}{B_0}K_r(\mathbf{r\text{-}r\prime\prime})
\end{aligned} \tag{3.28}$$

where K_r is the inverse Fourier transform of K, i.e. the kernel in image space.

Substituting this result into Equation 3.27:

$$\begin{aligned}
\sigma(\chi(\mathbf{r}))^2 &= \int_{\mathbf{r\prime\prime}} \left(\frac{\partial\chi(\mathbf{r})}{\partial B_{int}(\mathbf{r\prime\prime})}\right)^2 \sigma(B_{int}(\mathbf{r\prime\prime}))^2\mathbf{dr\prime\prime} \\
&= \int_{\mathbf{r\prime\prime}} \frac{1}{B_0^2}K_r(\mathbf{r\text{-}r\prime\prime})^2\sigma(B_{int}(\mathbf{r\prime\prime}))^2\mathbf{dr\prime\prime} \\
\sigma(\chi)^2 &= \frac{1}{B_0^2}\cdot K_r^2 * \sigma(B_{int})^2
\end{aligned} \tag{3.29}$$

This final expression is in line with the corollary of the measurement uncertainty propagation, i.e. that the variances (σ^2) are additive.

As mentioned in section 2.4, the susceptibility calculation step recovers the underlying susceptibility distribution that induces the various field patterns. It is local and (mostly) orientation independent (section 1.3.1). Similarly to the local field map, the susceptibility map is expected to be mostly homogeneous in the five, manually drawn regions of Figure 3.1. Therefore, we can compare the measured and calculated noise in the susceptibility map too.

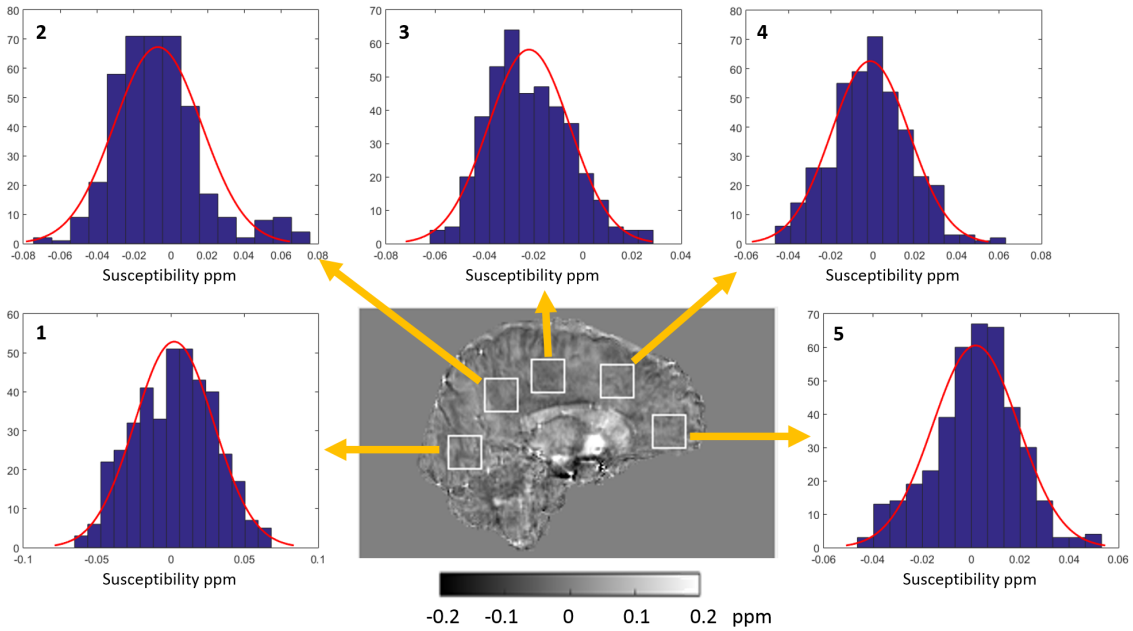

Figure 3.10: Manually segmented, 400-voxel regions in the central sagittal slice (same as in Figures 3.1 and 3.8) of the susceptibility map. The corresponding histograms within these regions are also shown along with fitted Gaussian functions.

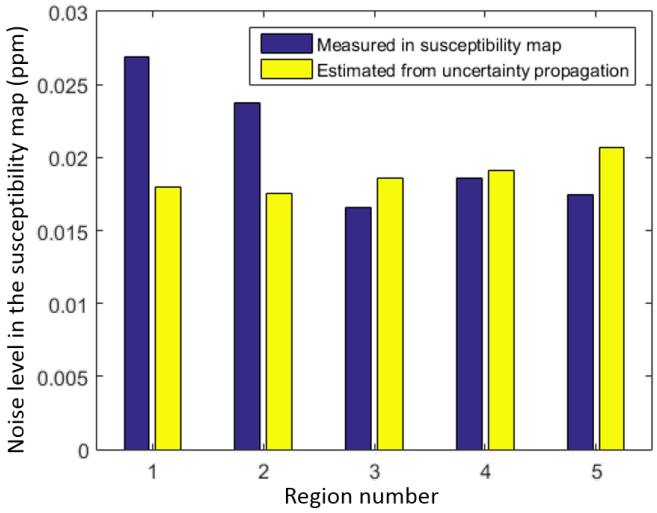

Figure 3.11: Measured and calculated noise in the susceptibility map in five, manually selected, 400-voxel regions. Note that the region numbers correspond to the ones in the upper-left corners in the histograms of Figure 3.10.

For this comparison, Truncated K-space Division (TKD, section 2.4.1.1) was applied to the aforementioned local field map to calculate the susceptibility map (Figure 3.10). The standard deviation in each of the five regions was used as the measured noise. The map of the susceptibility measurement uncertainty was computed using Equation 3.29. The calculated noise was estimated as the mean of the measurement uncertainty within the five, rectangular regions. Figure 3.11 shows the measured and calculated noise in each region. Again, there was good agreement between the measured and calculated values which underlines the fact that my calculations are able to predict the noise distribution in the susceptibility maps.

Another susceptibility map was also calculated using the direct k-space inversion method with Tikhonov regularisation (section 2.4.2.2). TKD and the direct Tikhonov method apply different k-space kernels (K). Here I compared how the susceptibility noise and SNR maps are affected by each kernel (Figure 3.12). Using the TKD kernel seems to provide susceptibility maps with slightly higher noise. However, due to the differences in the two kernels, the resulting susceptibility maps are also expected to be slightly different. Figure 3.12 b shows that none of the two techniques provided a consistently better SNR across the profile indicated by the white line. Note that both the noise and SNR profiles have similar shapes for the two techniques.

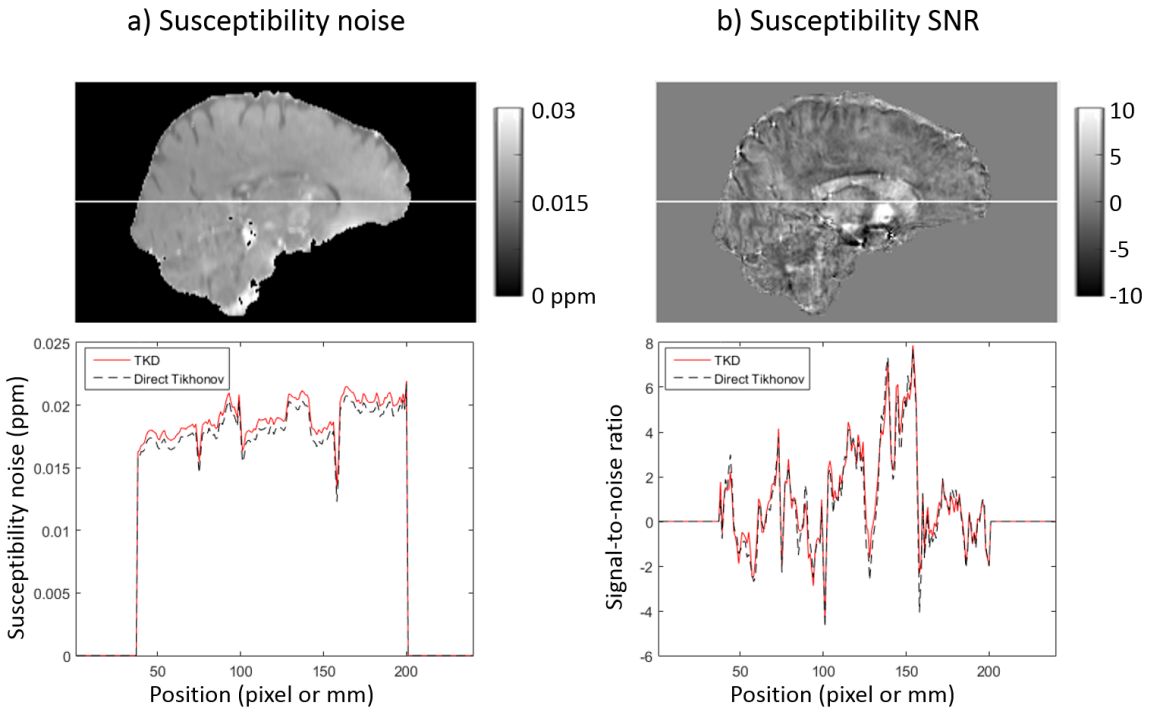

Figure 3.12: Spatial distribution of the susceptibility noise (a) and SNR (b) using either TKD (solid red line) or the direct Tikhonov method (dashed black line). The maps in both (a) and (b) correspond to the TKD results which were visually similar to the Tikhonov results.

3.6 Discussion and Conclusions

Figure 3.13 shows the evolution of the (calculated) measurement uncertainty across the QSM pipeline. All profiles are displayed in ppm. For the first-echo phase image (top), the conversion from rad to ppm was performed using:

$$\sigma(\varphi)_{\text{rad}} = \sigma(\varphi)_{\text{ppm}} \cdot 2\pi \cdot \text{TE}_1 \cdot \gamma B_0 \tag{3.30}$$

All noise profiles have very similar features. The measurement uncertainty profile of the susceptibility maps looks proportional to that of the local field map, albeit smoothed by the convolution with K_r^2. Even though the phase, field, and susceptibility values are expected to show large spatial variations, the noise in all three seems consistent across the volume. An $13 \cdot 10^{-3}$ ppm noise level of the phase map corresponds to a noise level of approximately $4 \cdot 10^{-3}$ ppm in the total and local field maps. This reduction in noise is probably due to the fitting step that is very resistant to noise. The final noise level

of around $17 \cdot 10^{-3}$ ppm in the susceptibility map is very close to the original phase noise. However, most of the phase signal comes from background sources and the range of susceptibilities measured in the brain is between $-100 \cdot 10^{-3}$ and $300 \cdot 10^{-3}$ ppm. Therefore, to achieve an acceptable susceptibility SNR, the acquired phase map needs to have a considerably larger signal-to-noise ratio than the final desired susceptibility SNR.

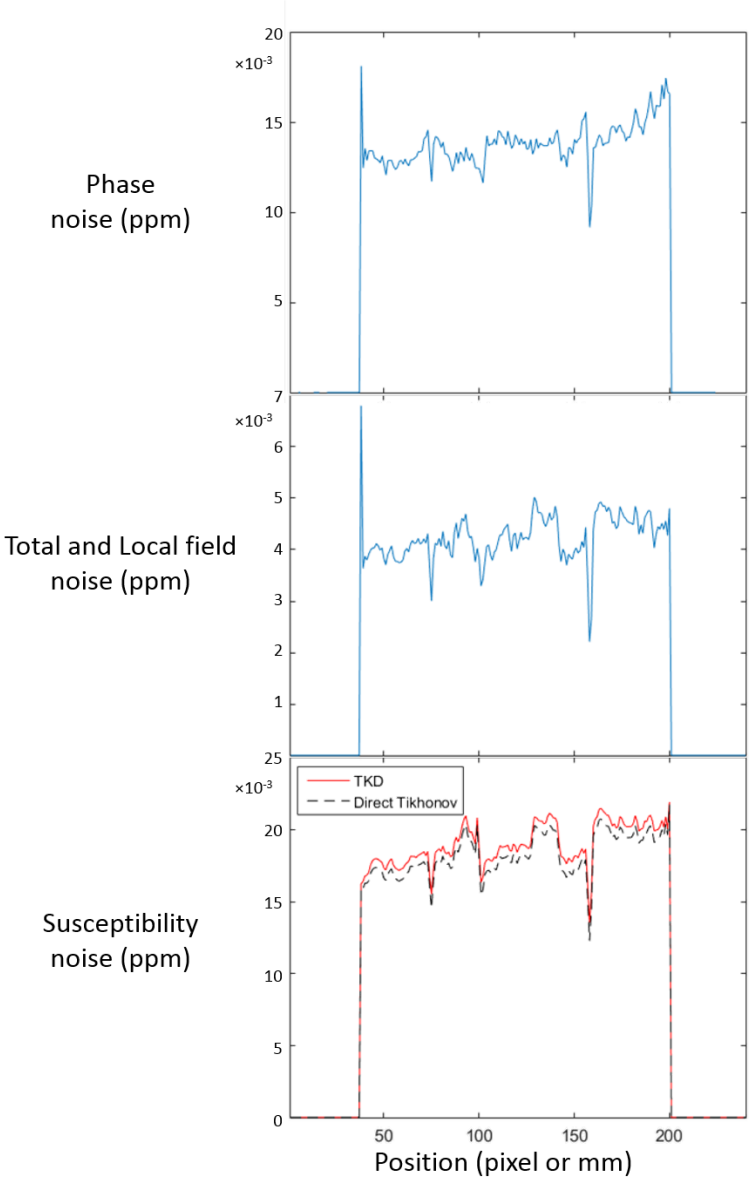

Figure 3.13: The evolution of the noise across the QSM pipeline. All plots show noise profiles along the white line from previous figures. The noise profile of the first-echo phase image is displayed at the top. The values were converted from rad to ppm for ease of comparison.

Here, I have demonstrated how the noise distribution is affected by each step of the susceptibility mapping pipeline using a simple demonstration and brain images acquired

in a healthy volunteer. Note that for a more accurate validation, the two-scan approach should be adopted (section 1.2.2.2). However, the goal of this chapter was to investigate if and where SNR can be used as a measure of image quality in the QSM pipeline. It could be a viable measure of image quality for the field fitting step or the susceptibility calculation step. However, it is not suitable for comparing background field removal techniques as these do not affect the noise but substantially reduce the signal, so a higher SNR could easily correspond to poorer background field removal and large residual background fields. Also, it is imperative to consider other features as well when comparing field fitting and susceptibility calculation strategies. For example, I have shown that magnitude-weighted field fitting provides slightly higher noise in the estimated field map in high SNR regions, but it substantially improves the noise distribution in low SNR areas. Therefore, a full visual assessment of the result and its noise map instead of measuring SNR in one or two carefully selected regions is crucial. Moreover, the measurement uncertainty only gives us information about the precision of the result. Wherever possible, it would be beneficial to also assess the accuracy of different methods. Finally, potential QSM pipeline elements have other important characteristics that could affect clinical feasibility, such as speed or robustness.

Chapter 4

SEGUE: a Speedy rEgion-Growing algorithm for Unwrapping Estimated phase

4.1 Motivation

While optimising the QSM pipeline for susceptibility mapping in the head-and-neck region, I was frustrated by the extremely long computation time of the gold standard 3D phase unwrapping technique, FSL PRELUDE (section 2.2.2.1). To overcome this, I developed SEGUE, a phase unwrapping technique based on similar principles to PRELUDE but with much shorter computation time. The following chapter has been accepted as a full paper to IEEE Transactions in Medical Imaging on 25 November 2018.

4.2 Introduction

The phase component of the complex Magnetic Resonance Imaging (MRI) signal acquired with a T_2^*-weighted gradient-echo sequence is proportional to the magnetic field inhomogeneities [118]. A range of techniques have recently been developed that exploit this property of the MRI phase including Susceptibility Weighted Imaging [101,102]. Furthermore, the recent increase in the use of high-field MRI systems has reinvigorated interest in phase imaging including the increasingly important field of Quantitative magnetic Susceptibility Mapping (QSM) [21,118,126–129]. Moreover, phase images are routinely used for

distortion correction in functional MRI [130–134], diffusion MRI [135–138], and recently in MRI-based radiation therapy planning [139].

As the phase in MRI is defined as the angle of the magnetisation vector in the complex (or transverse) plane, the measured MRI phase can only take values between 0 and 2π, introducing wraps (or 2π phase discontinuities) into the measured phase images (Fig. 4.1 a). At longer echo times, these phase images contain more spatial wraps (Figs. 4.5, 4.6, and 4.7 a).

Many algorithms have been developed to overcome this problem [93], but Phase Region Expanding Labeller for Unwrapping Discrete Estimates (PRELUDE, [92]) in the FMRIB Software Library (FSL, [140]) is considered the gold standard method [93] for robust, spatial phase unwrapping in three dimensions (3D). PRELUDE has been repeatedly shown to be able to unwrap standard brain images in a reasonable amount of time. However, depending on the image resolution, and field of view, at later echoes, the computation time (T_c) of PRELUDE can reach 15 minutes to unwrap a whole brain image on a 64-bit Ubuntu Virtual Machine with a 3.5 GHz Processor and 16 GB RAM. Therefore, large-scale studies requiring distortion correction in the brain (e.g. for functional or diffusion MRI) would greatly benefit from accelerated phase unwrapping.

PRELUDE has been developed and optimised primarily for brain images, but recently, QSM has been increasingly applied in parts of the body other than the brain [64, 81, 106, 141, 142]. It can take up to 17 minutes for PRELUDE to unwrap a pelvic image and nearly 10 hours for a head-and-neck image using a standard PC with the aforementioned specifications. Faster phase unwrapping would accelerate state-of-the-art research investigating a wide range of QSM applications. Moreover, these anatomical regions contain fatty as well as water-based tissue. The fatty areas have an additional, chemical-shift-induced phase component [81]. This could lead to errors in PRELUDE phase unwrapping that are yet to be addressed.

Here we develop a Speedy rEgion-Growing algorithm for Unwrapping Estimated phase (SEGUE) based on similar principles to PRELUDE, but with 1.5 to 70 times shorter T_c depending on the echo time and anatomical region. We also propose and investigate a simple, effective strategy for overcoming the chemical-shift-induced errors in the results of both PRELUDE and SEGUE. A MATLAB (Mathworks, Natick, MA, USA) implementation of SEGUE is downloadable from https://xip.uclb.com/i/software/SEGUE.html.

4.3 Theory

4.3.1 PRELUDE

The PRELUDE algorithm [92] consists of two main steps: 1) partitioning and 2) unwrapping and merging. First, the phase map is partitioned into connected regions by dividing the [0, 2π] interval into 6 smaller equal intervals (see e.g. Fig. 4.1 a and b). It is assumed that these regions do not contain any phase wraps. The wraps between these regions are unwrapped by adding an integer multiple of 2π to one of two neighbouring regions assuming spatial smoothness of the phase and these neighbouring regions are then merged. This process starts with the pair of neighbouring regions in which the wrong phase shift would introduce the most error in the unwrapped phase image (e.g. a pair of regions with a large number of interfacing voxels on the border), and it continues until all the regions have been unwrapped and merged. The computation time is expected to be proportional to the number of initial regions.

In high resolution images, an initial region can erroneously contain a wrap if it consists of areas with a phase difference more than 2π connected by a few noisy voxels (see Fig. 4.1 a and b, red arrows). Moreover, the process of creating initial regions (see Fig. 4.9 a, dashed line) may result in an apparent wrap between two points within a region (see Fig. 4.9 a, A and B). A large, 3D initial region containing a wrap can have global, unpredictable effects on the resulting unwrapped phase map. To avoid this, PRELUDE limits the initial regions to be two dimensional (2D) for high-resolution images with a voxel size of 1 mm $\times$ 1 mm $\times$ 1 mm or smaller. However, slicing all the large, connected, 3D regions into smaller, 2D regions results in a greatly increased number of initial regions (that scales linearly with the number of slices in the 3D volume) and, consequently, very long computation time.

4.3.2 SEGUE

SEGUE provides an alternative way of unwrapping high-resolution phase images more rapidly than PRELUDE [143]. The process is accelerated by: 1) always using 3D regions to reduce the number of initial regions, 2) unwrapping and merging multiple regions at the same time.

4.3.2.1 Partitioning

Similarly to PRELUDE, the [0, 2π] interval is first divided into 6 smaller intervals (Fig. 4.1 b). At this stage, areas having a phase difference more than 2π (Fig. 1 b, green arrows) might be connected by a few noisy voxels (Fig. 4.1 a and b, red arrows). Instead of restricting the regions to 2D as in PRELUDE, these small bridges between larger regions (Fig. 4.1 b, red arrow) are excluded before the connected regions are determined (Fig. 4.1 c, green arrows). The excluded voxels are: i) located at the edges of the mask in Fig. 4.1 b, and ii) have zero-valued first, second, or third neighbours in at least two of the three (x, y, and z) directions. Finally, the connected, 3D regions are identified and the excluded voxels are assigned to the initial regions that are closest to them (Fig. 4.1 d).

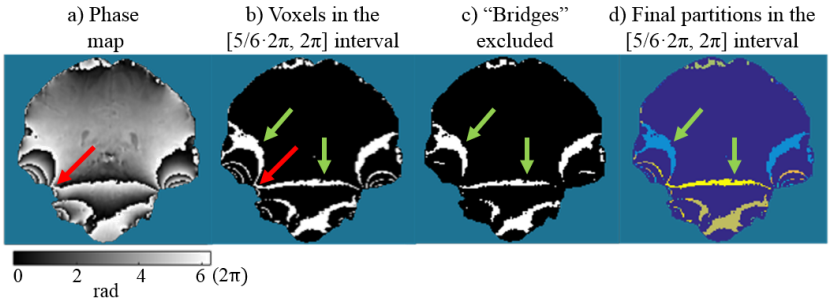

Figure 4.1: Partitioning in SEGUE. First, voxels with phase values within one of the smaller phase intervals are identified (b). Then, the small bridges connecting larger regions (a, b, red arrows) are excluded (c). Finally, the connected regions (colours) are identified and the excluded voxels are assigned to the closest region (d).

4.3.2.2 Unwrapping and Merging

Instead of comparing each adjacent pair of regions as in PRELUDE, the merging process in SEGUE starts by selecting the region with the largest border (Fig. 4.2, main region) and then gradually enlarging it by unwrapping all neighbouring regions at the same time and merging these with the main region.

Phase values in the adjacent voxels (Fig. 4.2, highlighted in yellow) in neighbouring regions, are estimated using linear extrapolation from two adjacent voxels (Fig. 4.2, red arrow), instead of nearest neighbour approximation as in PRELUDE. In theory, extrapolation should provide more accurate unwrapped phase maps near high susceptibility gradients. The extrapolated and measured phase values in these voxels are denoted by

φ and Φ respectively. Phase values in the adjacent voxels are extrapolated from every possible direction in 3D (Fig. 4.2, blue arrows).

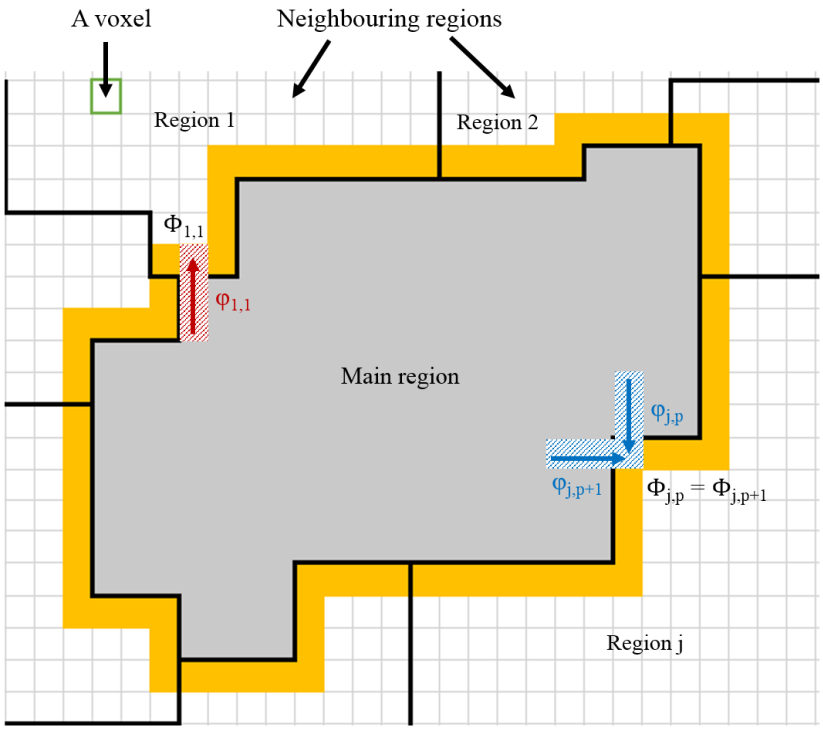

Figure 4.2: Unwrapping and merging in SEGUE. Phase values in the voxels adjacent to the main region (yellow) are estimated using linear extrapolation (red arrow) from every possible direction (blue arrows). The phase shift is calculated from the differences between the extrapolated (φ) and the measured (Φ) phase values in the adjacent voxels.

The necessary phase shift for region j is calculated for each pair (p) of extrapolated and measured phase values by:

$$\Delta\varphi_{j,p} = 2\pi \cdot round\left(\frac{\varphi_{j,p} - \Phi_{j,p}}{2\pi}\right) \tag{4.1}$$

The final phase shift for a given neighbouring region j, $\Delta\varphi_j$, is determined by majority voting among all $\Delta\varphi_{j,p}$ values. This phase shift ($\Delta\varphi_j$) is applied to region j only if a substantial proportion ($P_{agree,j}$ from Eq. 4.2) of $\Delta\varphi_{j,p}$ values agree on the final phase shift and the unwrapped neighbouring regions are then merged with the main region. Eq. 4.2 describes a balance between the proportion of agreeing extrapolated and measured pairs ($P_{agree,j}$) and the amount of information we have about the neighbouring region j ($P_{border,j}$).

$$(1 - P_{limit}) \cdot P_{agree,j} \geq 1 - P_{border,j} \tag{4.2}$$

$P_{agree,j}$ is the ratio of the number of p extrapolated and measured pairs where $\Delta\varphi_{j,p} = \Delta\varphi_j$ to the total number of all $\Delta\varphi_{j,p}$ values for a given neighbouring region j. $P_{border,j}$ is the

ratio of the number of voxels on the border between region j and the main region, and the total number of voxels on the border of region j. P_{limit} is a preset value between 0 and 1. At one extreme, if all pairs agree (i.e. $P_{agree,j} = 1$), we need a substantial proportion of the border of region j to be shared with the main region (i.e. $P_{border,j} \geq P_{limit}$) to accept the phase shift. Therefore, if the regions are only connected by a few interfacing voxel pairs, unwrapping and merging is not performed even if all $\Delta\varphi_{j,p}$ values are the same. At the other extreme, if the main region completely surrounds region j (i.e. $P_{border,j} = 100\%$), we already have all the obtainable information about the border of region j, so unwrapping and merging is performed regardless of the value of $P_{agree,j}$. $P_{limit} = 30\%$ was found to yield good results for most cases.

This process is repeated using the same enlarged main region until no more regions can be unwrapped and merged with it. Then, this main region is excluded from the unwrapping and the region with the second largest border is chosen as the next main region and the unwrapping and merging process continues. When at least $P_{req} = 70\%$ of the total volume in the tissue mask has been merged with one of the previous main regions, all of these are included in the unwrapping again and the merging process is repeated two more times with P_{limit} set to first 10% and then 0%.

Note that at the last stage ($P_{limit} = 0\%$), all regions where $P_{agree,j} = 100\%$ are unwrapped and merged with the main region regardless of the size of the shared border. Also, this repetition of the merging while decreasing P_{limit} is included only to ensure robust unwrapping in complicated anatomical regions (e.g. head-and-neck). In most brain images, more than 99% of the volume is merged with the first main region during the first cycle of the algorithm.

P_{req} can be set by the user. In general, a higher P_{req} provides more accurate phase maps, while a lower P_{req} results in faster unwrapping.

4.4 Methods

SEGUE was developed in MATLAB R2015a, but it runs in all versions released between 2013 and 2017. To test SEGUE, we compared its performance with PRELUDE in terms of unwrapping and computation time (T_c) by applying both techniques to simulated phase data and in-vivo MRI phase images of healthy volunteers.

4.4.1 Numerical phantoms

First, we tested SEGUE's ability to resolve complicated phase patterns in a digital phantom with no noise as described by Robinson et al. in [83] (complexity level = 4 and echo time = 10 ms).

To assess SEGUE's accuracy in noisy phase images, we used a 3D Gaussian distribution with varying noise levels as described in [93]. A 3D Gaussian (G) was embedded in a 256×256×256 matrix with an amplitude of 1, and a full width at half maximum (FWHM) of 128 in each direction. This phase pattern was scaled using the following expression:

$$\phi = \gamma B_0 \mathrm{TE} \cdot G \tag{4.3}$$

where γ is the proton gyromagnetic ratio, $B_0 = 7$ T is the magnetic field, and TE = 16 ms is the echo time. Gaussian-distributed noise was added to the real and imaginary components of $\exp(\mathrm{i}\phi)$ (i.e. the simulated complex MRI signal). Noise amplitudes of 0.1, 0.2, 0.3, and 0.4 were used. This gave similar phase maps to those in [93].

4.4.2 Volunteer images

To test SEGUE in a range of commonly scanned regions of the body, it was applied to phase images acquired in the brain, head-and-neck, or pelvis of healthy volunteers. While phase unwrapping is most commonly used in brain images, there has been increasing interest in phase imaging (e.g. QSM) in parts of the body outside of the brain. The acquired head-and-neck and pelvic images allowed us to test SEGUE in two different, but equally challenging anatomical regions and also investigate the performance of both SEGUE and PRELUDE in and around fatty tissue.

The local ethics committee approved this study and informed consent was obtained from all participants.

Brain images of 5 healthy volunteers were acquired at 3 Tesla (Philips, Achieva, Netherlands), using a 32-channel head coil, a 3D, T_2^*-weighted gradient-echo sequence, matrix size = 240×240×144, Sensitivity Encoding (SENSE) acceleration factors = 1×2×1.5, 1 mm isotropic resolution, TE_1 = 3.0 ms, ΔTE = 5.4 ms, 5 echoes, repetition time = 29 ms, and flip angle = 20°.

Head-and-neck images were also acquired in another 4 healthy volunteers using the same MRI system, a 16-channel head-and-neck coil and 3D gradient-echo sequence, matrix

size = 220×220×240, SENSE factors = 1.5×2×1, 1 mm isotropic resolution, TE_1 = 3.0 ms, ΔTE = 5.3 ms, 4 echoes, repetition time = 23 ms, and flip angle = 18°.

Images of the sacroiliac joint (pelvic images) acquired in 5 more healthy volunteers by Bray et al. [71] were also used to compare the two techniques. Multi-echo gradient-echo MRI was performed on a different 3-Tesla clinical system (Philips, Ingenia, Netherlands) using matrix size = 320×320×40, resolution = 1.56×1.56×2 mm, TE_1 = 1.17 ms, ΔTE = 1.6 ms, 6 echoes, repetition time = 25 ms, and flip angle = 3°.

4.4.3 Comparing PRELUDE and SEGUE

Both PRELUDE and SEGUE need tissue masks to identify the part of the image within which unwrapping needs to be performed. In the case of the complex phase topography, the entire 3D volume was unwrapped, while for the Gaussian phantoms, a sphere with a radius of 85 voxels was used. For the brain images, a mask was obtained using the FSL Brain Extraction Tool [144] on the last echo magnitude image. Masks for the head-and-neck and pelvic images were generated using a fixed threshold on the inverse noise maps calculated from the magnitude images across all the echoes [87].

All phase images were unwrapped using both PRELUDE and SEGUE and the results were evaluated using several metrics: 1. Computation time (T_c) on a 64-bit Ubuntu Virtual Machine with a 3.5 GHz Processor and 16 GB RAM, 2. Visual comparison of the unwrapped phase images, 3. Percentage of unwrapped voxels (UnVox), 4. Mean absolute error (ME) between the results and the ground truth for the numerical phantoms, and mean absolute difference (MD) between the PRELUDE and SEGUE results for the in-vivo images, 5. Percentage of voxels with different unwrapped phase (DiffVox) between the PRELUDE and SEGUE results (in the volunteer images only), 6. Maximum phase difference (MaxDiff) between the PRELUDE and SEGUE results (in the volunteer images only).

4.4.4 Removing the chemical shift-induced phase errors

In the head-and-neck and pelvic images, there is an additional, chemical-shift-induced phase difference between fatty and water-based voxels that could induce errors in both the PRELUDE and SEGUE unwrapped phase images. Here we tested a simple strategy for removing these errors; we tried applying both techniques separately in the fat and water

masks to prevent the chemical-shift-induced fat-water phase difference from affecting the unwrapping process. In the head-and-neck images, fat-water separation was performed using the 3-point Dixon method [76] from the ISMRM fat-water separation toolbox [75]. In the pelvis, fat and water magnitude images had already been created by the vendor-supplied software (Philips mDixon Quant; Philips Healthcare, Andover, Massachusetts, USA). Each voxel within the original tissue mask was assigned to either the water or the fat mask depending on whether the water or the fat magnitude was larger in that particular voxel.

4.5 Results

The phase phantom of complex topography is shown in Fig. 4.3 a and b. It was successfully unwrapped using SEGUE (Fig. 4.3 c) in less than 102 minutes while PRELUDE failed to terminate within 3 days and provided no results. The mean absolute error (ME) of the SEGUE result was very low (0.0002 rad, see Table 4.1) and differences between the unwrapped image and the ground truth were only visible at a very small scale (Fig. 4.3 d).

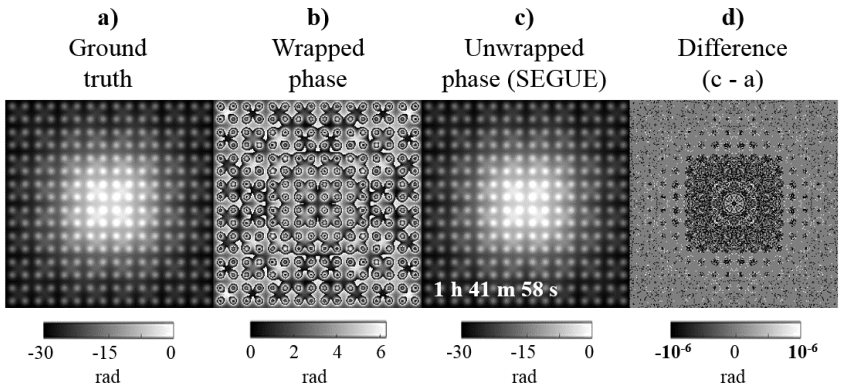

Figure 4.3: Unwrapping a phase phantom with complex topography. Both PRELUDE and SEGUE were applied to the complex topography phase map (b). While PRELUDE failed to terminate within 3 days, SEGUE was able to provide an unwrapped phase image (c) in less than 102 minutes (T_c is shown in the corner of the unwrapped image). The difference map (d) between the SEGUE result (c) and the ground truth phase map (a) shows discrepancies only on a very small scale. Slice 125 is shown in each case.

Fig. 4.4 shows the comparison between PRELUDE and SEGUE in the Gaussian phantom with different noise levels. All the unwrapped phase maps looked identical to the ground truth phase maps. The difference images became noisier as the noise level in the numerical phantom was increased. Table 4.1 shows that ME was the same for the two

techniques for all noise levels. PRELUDE was slightly faster than SEGUE in the phantom with the lowest noise. However, T_c of PRELUDE rapidly increased with increasing noise level (almost 12 hours for the phase map with the highest noise level), whereas SEGUE could unwrap even the phantom with the highest noise level in ≈1.5 minutes.

Table 4.1 shows that both techniques could unwrap 100% of the voxels in all numerical phantoms (except PRELUDE did not provide any results in the phantom of complex topography).

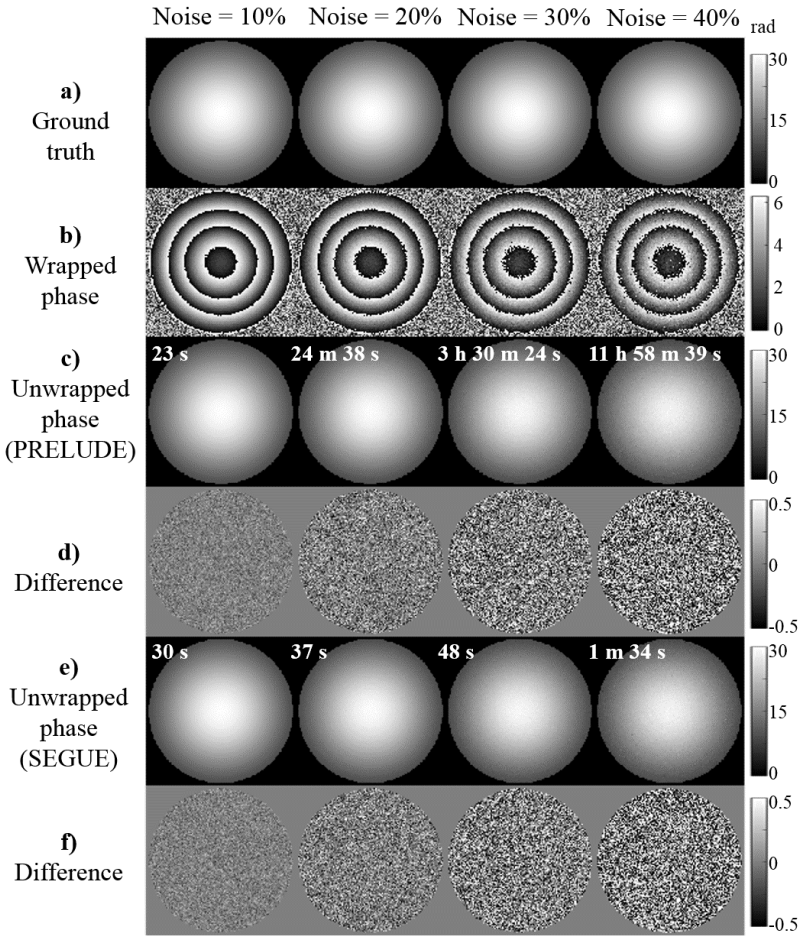

Figure 4.4: Unwrapping a Gaussian phantom. Phase maps of a Gaussian phantom with four different noise levels (a, b) were unwrapped using either PRELUDE (c) or SEGUE (e). T_c corresponding to each result is shown in the corner of the unwrapped phase maps. Difference images between the PRELUDE/SEGUE results and the ground truth phase maps (a) are also displayed (d and f respectively). All scales are in radians.

Figs. 4.5, 4.6, and 4.7 show the results of PRELUDE and SEGUE in the brain, head-and-neck, and pelvis of representative volunteers respectively. Example coronal slices are displayed for the brain and head-and-neck (Figs. 4.5 and 4.6 respectively) and the middle, axial slice is shown for the pelvic images (Fig. 4.7). Besides the wrapped (a) and

			PRELUDE		SEGUE	
	Noise level (%)	UnVox (%)	ME (rad)	T_c	ME (rad)	T_c
Complex	0	100	NA	> 3 days	0.0002	1 h 41 m 58 s
Gaussian	10	100	0.08	23 s	0.08	30 s
	20	100	0.16	24 m 38 s	0.16	37 s
	30	100	0.25	3 h 30 m 24 s	0.25	48 s
	40	100	0.34	11 h 58 m 39 s	0.34	1 m 34 s

Table 4.1: Summary of the results in numerical phantoms. Percentages of the unwrapped voxels (UnVox) using either PRELUDE or SEGUE and computation times (T_c) are shown as well as mean absolute errors (ME) calculated between the resulting unwrapped phase maps and the ground truth phase maps.

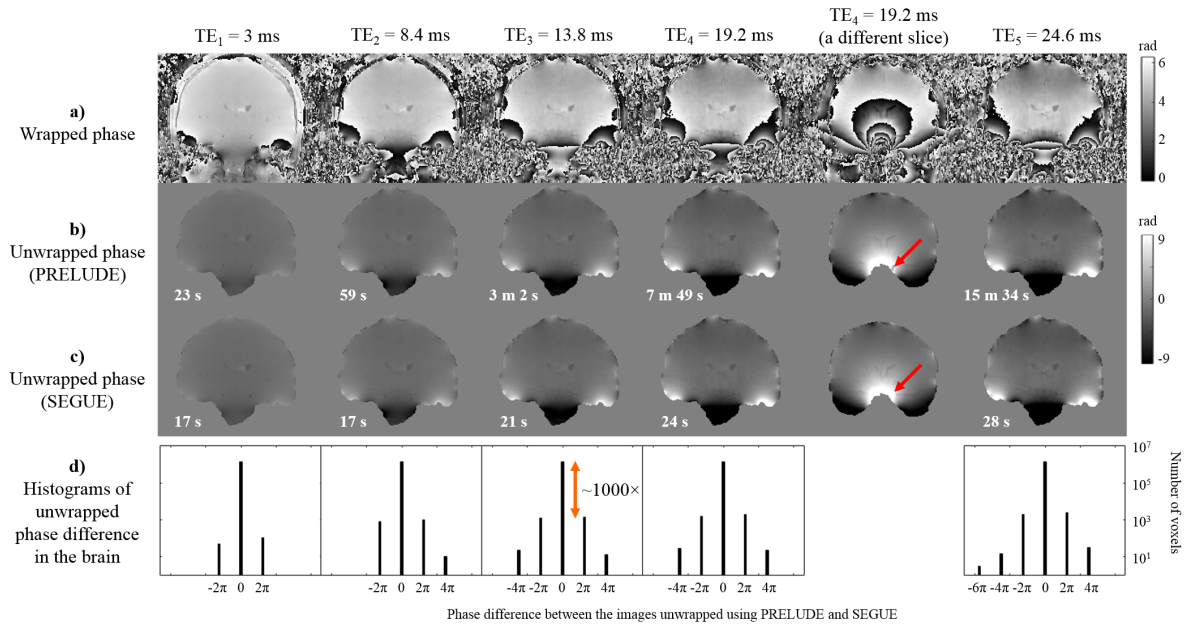

Figure 4.5: Unwrapping brain images. Phase maps acquired in the brain of a representative healthy volunteer at five different echo times (a) were unwrapped using either PRELUDE (b) or SEGUE (c). T_c corresponding to each result is shown in the corner of the unwrapped phase maps. Histograms of the difference images between the PRELUDE and SEGUE results are also displayed (d). The red arrows indicate where SEGUE appears to be more accurate than PRELUDE. There were at least 1000 times more voxels with identical unwrapped phase values in the PRELUDE and SEGUE results than voxels with a 2π phase difference (orange double arrow). Note the logarithmic scale in d.

unwrapped (b, c) phase maps, histograms of the unwrapped phase difference between the PRELUDE and SEGUE results (d) and computation times (T_c) are also shown.

In all brain images, the unwrapped phase maps calculated using PRELUDE and SEGUE (see Fig. 4.5 b and c) looked nearly identical. Fig. 4.5 d also shows that there were 1000 times more voxels with identical unwrapped phase values than voxels with a 2π phase difference between the PRELUDE and SEGUE results. Moreover, the red arrows indicate a small residual wrap (the phase difference was confirmed to be around 2π) in the PRELUDE result which was successfully resolved in the SEGUE result. Table 4.2

		PRELUDE		SEGUE				
	Echo time (ms)	UnVox (%)	T_c	UnVox (%)	T_c	DiffVox (%)	MD (rad)	MaxDiff (rad/2π)
Brain images (n = 5)	3	99.98±0.008	22 s ± 4 s	99.97±0.009	16 s ± 1 s	0.03±0.01	0.0019±0.0009	1.4±0.5
	8.4	99.97±0.007	55 s ± 6 s	99.97±0.009	18 s ± 1 s	0.11±0.02	0.007±0.001	1.8±0.5
	13.8	99.97±0.007	2 m 40 s ± 21 s	99.97±0.005	20 s ± 1 s	0.16±0.03	0.010±0.002	2.0±0.0
	19.2	99.98±0.002	6 m 19 s ± 52 s	99.96±0.004	23 s ± 1 s	0.22±0.03	0.014±0.002	3.0±1.0
	24.6	99.98±0.004	12 m 17 s ± 1 m 52 s	99.95±0.013	26 s ± 2 s	0.31±0.05	0.020±0.003	3.0±0.7
Head-and-neck images (n = 4)	3	99.8±0.05	16 m 19 s ± 11 m 35 s	99.6±0.20	36 s ± 3 s	0.11±0.20	0.03±0.01	3.0±0.8
	8.3	99.8±0.04	3 h 27 m 53 s ± 58 m 2 s	99.4±0.31	2 m 57 s ± 1 m 3 s	**7.1±5.6**	**0.46±0.36**	9.5±0.6
	13.6	99.8±0.04	6 h 9 m 21 s ± 57 m 54 s	99.3±0.26	6 m 59 s ± 1 m 35 s	**5.6±6.4**	**0.38±0.41**	15.5±2.4
	18.9	99.8±0.04	9 h 47 m 40 s ± 1 h 41 m 40 s	99.3±0.14	17 m 35 s ± 9 m 26 s	**6.1±4.2**	**0.50±0.36**	34.3±22.5
Pelvic images (n = 5)	1.17	96.0±5.9	7 m 24 s ± 3 m 52 s	95.8±5.8	18 s ± 6 s	0.74±0.18	0.05±0.01	2.6±0.9
	2.77	96.1±5.9	24 s ± 12 s	95.3±5.6	11 s ± 1 s	0.03±0.03	0.002±0.002	2.0±1.2
	4.37	96.1±5.9	2 m 0 s ± 1 m 12 s	95.9±6.0	13 s ± 3 s	0.74±1.49	0.047±0.094	2.4±0.5
	5.97	96.1±5.9	20 m 56 s ± 8 m 45 s	96.0±5.9	54 s ± 22 s	**4.84±1.79**	**0.35±0.16**	8.6±5.4
	7.57	96.1±5.9	9 m 53 s ± 6 m 17 s	95.7±5.8	19 s ± 8 s	1.04±1.44	0.12±0.21	12.6±18.7
	9.17	96.1±5.9	15 m 29 s ± 8 m 15 s	95.1±5.4	29 s ± 16 s	**3.57±16.41**	**0.23±0.45**	6.4±3.6

Table 4.2: Summary of the results in all healthy volunteers. Percentages of the unwrapped voxels (UnVox) using either PRELUDE or SEGUE and computation times (T_c) are shown as well as the percentages of differing voxels (DiffVox), mean absolute differences (MD), and the maximum differences (MaxDiff) between the PRELUDE and SEGUE results. In each cell, mean ± standard deviation across healthy volunteers are shown. The red numbers indicate high DiffVox and MD values in some or all of the healthy volunteers.

		PRELUDE		SEGUE				
	Echo time (ms)	UnVox (%)	T_c	UnVox (%)	T_c	DiffVox (%)	MD (rad)	MaxDiff (rad/2π)
Head-and-neck images (n = 3)	3	98.2±0.2	10 m 53 s ± 2 m 52 s	97.5±0.6	1 m 14 s ± 7 s	0.12±0.18	0.007±0.01	2.3±0.6
	8.3	98.2±0.2	1 h 40 m 22 s ± 30 m 52 s	96.6±1.1	8 m 1 s ± 6 m 4 s	**1.4±1.0**	**0.14±0.10**	24.7±25.4
	13.6	98.2±0.2	3 h 7 m 43 s ± 36 m 44 s	96.3±1.3	17 m 10 s ± 13 m 1 s	**1.7±2.1**	**0.14±0.18**	21.0±13.2
	18.9	98.2±0.2	5 h 33 m 26 s ± 58 m 13 s	96.4±1.1	41 m 17 s ± 15 m 47 s	**6.5±7.4**	**0.63±0.73**	39.3±27.5
Pelvic images (n = 5)	1.17	92.6±5.1	3 m 44 s ± 2 m 12 s	90.8±4.8	24 s ± 3 s	1.38±0.79	0.12±0.10	4.4±1.1
	2.77	92.6±5.1	27 s ± 10 s	92.2±5.1	20 s ± 2 s	0.03±0.03	0.002±0.002	2.8±0.4
	4.37	92.6±5.1	1 m 27 s ± 22 s	92.2±5.1	26 s ± 6 s	0.08±0.08	0.006±0.006	3.8±0.4
	5.97	92.5±5.1	8 m 44 s ± 3 m 23 s	91.6±4.9	43 s ± 16 s	**1.69±0.76**	**0.11±0.05**	7.0±1.6
	7.57	92.5±5.1	4 m 51 s ± 2 m 10 s	92.0±5.0	36 s ± 14 s	0.66±0.77	0.06±0.08	17.8±23.7
	9.17	92.5±5.1	7 m 44 s ± 2 m 49 s	92.0±5.2	52 s ± 28 s	**0.54±0.46**	**0.04±0.03**	9.8±4.1

Table 4.3: Summary of the head-and-neck and pelvic results when unwrapping separately in the water and fat masks. Percentages of the unwrapped voxels (UnVox) using either PRELUDE or SEGUE and computation times (T_c) are shown as well as the percentages of differing voxels (DiffVox), mean absolute differences (MD), and the maximum differences (MaxDiff) between the PRELUDE and SEGUE results. In each cell, mean ± standard deviation across healthy volunteers are shown. Note that the head-and-neck images of one healthy volunteer were excluded due to a failed fat-water separation. The red numbers indicate greatly improved DiffVox and MD values compared to Table 4.2, while the blue numbers indicate values that are still slightly high compared to the rest of the echoes.

shows that the low percentage of differing voxels ($< 0.4\%$ across all individuals), low mean absolute difference (< 0.03 rad), and low maximum difference ($< 5 \cdot 2\pi$) were consistent across the five healthy volunteers. Moreover, both techniques could unwrap more than

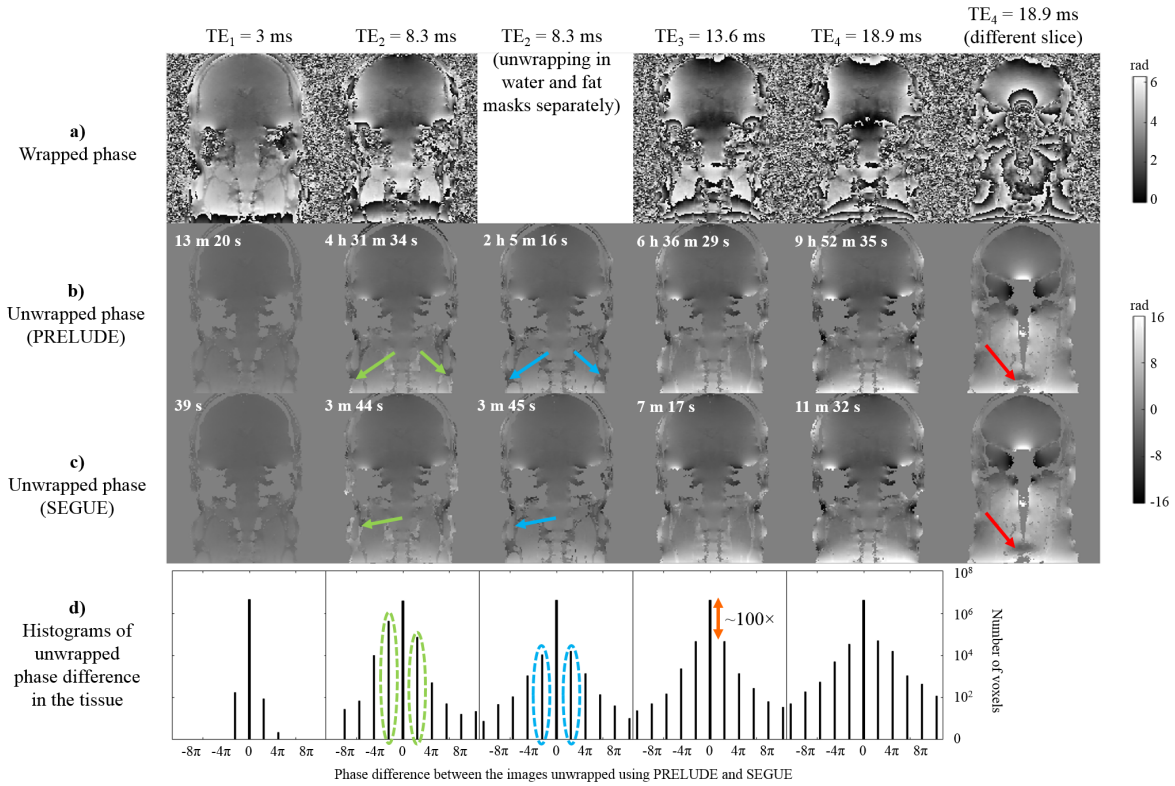

Figure 4.6: Unwrapping head-and-neck images. Phase maps acquired in the head-and-neck of a representative healthy volunteer at four different echo times (a) were unwrapped using either PRELUDE (b) or SEGUE (c). Both techniques were also applied separately in the water and fat masks (example shown in the third column). T_c corresponding to each result is shown in the corner of the unwrapped phase maps. Histograms of the difference images between the PRELUDE and SEGUE results are also displayed (d). The red arrows indicate where SEGUE seems to be more accurate than PRELUDE. The green arrows indicate residual wraps in fatty tissue. There were at least 100 times more voxels with identical unwrapped phase values in the PRELUDE and SEGUE results than voxels with a 2π phase difference (orange double arrow) except when residual wraps in fatty tissue were present (green dashed lines). Note the logarithmic scale in d. The blue arrows and blue dashed lines indicate how performing the unwrapping separately in the water and fat masks removed the residual wraps in the fatty fascia in both PRELUDE and SEGUE.

99.9% of the entire brain in each case. SEGUE was only slightly faster than PRELUDE at the first echo time, but the difference in T_c drastically increased towards later echoes. At TE_{max} = 24.6 ms, SEGUE was about 30 times faster. Note that T_cs were also consistent across volunteers.

In the more challenging head-and-neck and pelvic images (see Figs. 4.6 and 4.7) the unwrapped phase images of PRELUDE and SEGUE were still very similar visually. In Fig. 4.6, the red arrows indicate a residual wrap in the PRELUDE results that was successfully resolved by SEGUE. The histograms of the phase differences (see Figs. 4.6 and 4.7 d) indicate at least 100 times more voxels with identical unwrapped phase than

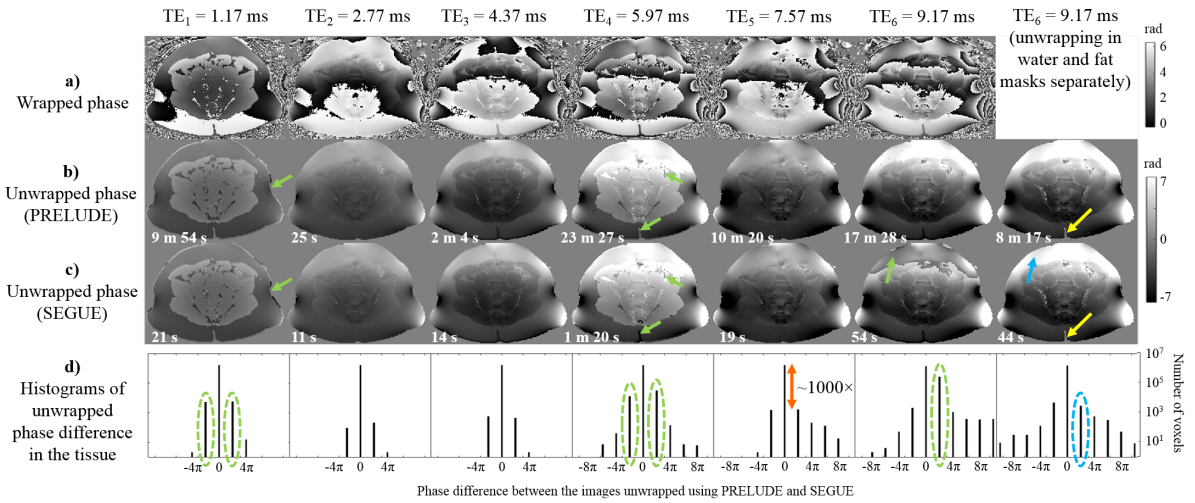

Figure 4.7: Unwrapping images of the pelvis. Phase maps acquired in the pelvis of a representative healthy volunteer at six different echo times (a) were unwrapped using either PRELUDE (b) or SEGUE (c). Both techniques were also applied separately in the water and fat masks (example shown in the last column). T_c corresponding to each result is shown in the corner of the unwrapped phase maps. Histograms of the difference images between the PRELUDE and SEGUE results are also displayed (d). The green arrows indicate residual wraps in fatty tissue. There were at least 1000 times more voxels with identical unwrapped phase values in the PRELUDE and SEGUE results than voxels with a 2π phase difference (orange double arrow) except when the results were visually different in fatty tissue (green dashed lines). Note the logarithmic scale in d. The blue arrows and blue dashed lines indicate how performing the unwrapping separately in the water and fat masks removed the residual wraps in subcutaneous fat. The yellow arrows indicate that the skin was excluded from the unwrapped phase images when PRELUDE or SEGUE were applied separately within the fat and water masks.

voxels with a 2π phase difference for the head-and-neck and pelvic images when the example slices appeared identical on visual comparison. There are more differing voxels (see Figs. 4.6 and 4.7 d, green dashed lines) where residual wraps are observed towards the tissue edges or in fatty tissue (see Figs. 4.6 and 4.7 b-c, green arrows). Residual wraps appearing within the subcutaneous fat or fatty fascia were a recurring problem for both PRELUDE and SEGUE. This is partly the reason for the relatively high DiffVox (5-20%) and MD (0.5-1 rad) values at certain echo times in Table 4.2 (highlighted in red). Since the head-and-neck and pelvic masks were generated by thresholding the inverse noise map, these masks include some small, noisy voxels outside of the tissue that are immediately excluded from the unwrapping by both phase unwrapping techniques as they are not connected to the largest region in the mask. Therefore the UnVox values are a bit lower than for brain images, but both PRELUDE and SEGUE unwrapped more than 99% of the head-and-neck images (across all individuals). For the pelvic images, sometimes the arms of the volunteer appeared next to the pelvis and are also similarly excluded by both PRELUDE and SEGUE, so the UnVox values were even lower (about 90% across

all individuals or about 96% on average), but they were similar for the two techniques for all images. In the head-and-neck and pelvic images, SEGUE was about 30 to 70, and 2 to 30 times faster than PRELUDE, respectively. Again, T_cs are reasonably consistent across volunteers.

All head-and-neck and pelvic images were also unwrapped separately within water and fat masks using both PRELUDE and SEGUE (see Fig. 4.6 third column, Fig. 4.7 last column, and Table 4.3). Note that the head-and-neck images of one volunteer were excluded from the results of Table 4.3 as the fat-water separation failed in this case. The simple strategy of unwrapping within water and fat masks separately successfully removed the residual wraps in fatty tissue (see Figs. 4.6 and 4.7 b-c, blue arrows) and resulted in a reduced number of differing voxels (see Figs. 4.6 and 4.7 d, blue dashed lines). It also reduced both DiffVox ($< 4\%$ across all volunteers) and MD (< 0.3 rad) for most echo times (see Table 4.3, highlighted in red). DiffVox and MD in the last-echo head-and-neck images were still high (see Table 4.3, highlighted in blue), because there was one volunteer where a large portion of the scalp was not properly unwrapped by SEGUE resulting in DiffVox $\approx$15% and MD $\approx$1.5. In the remaining volunteers, DiffVox was less than 2.5% and MD was below 0.25 rad, in line with the rest of the results in the head-and-neck. Similarly, the slightly higher DiffVox and MD in the fourth-echo pelvic images (compared to the rest of the echoes) originated from one volunteer where the unwrapping was inconsistent between SEGUE and PRELUDE in a small area of the subcutaneous fat due to imperfect fat-water separation. UnVox values were slightly reduced compared to when PRELUDE and SEGUE were applied in the entire tissue mask at once, because both techniques perform the unwrapping only in the largest connected region of the tissue mask. Therefore, for example the water-based skin was not unwrapped in many pelvic images (see Fig. 4.7, yellow arrows) as it was separated from the rest of the water-based tissue by the subcutaneous fat. However, the UnVox percentages were still similar for PRELUDE and SEGUE in all images. PRELUDE was usually about twice as fast when unwrapping in the fat and water masks separately, while SEGUE was slightly slower in each case. However, SEGUE was still about 10 times faster than PRELUDE in most cases (except in the second- and third-echo pelvic images, where it was only 1.3 and 3 times faster on average). Finally, note that MaxDiff was much higher in these challenging anatomical regions (head-and-neck and pelvis) than in brain images both with and without unwrapping separately within fat and water masks. In summary, applying PRELUDE or SEGUE separately within fat and water masks improves the unwrapped phase images with no great increase in computation time.

4.6 Discussion

We have developed SEGUE, a new, fast phase unwrapping algorithm based on similar principles to the state-of-the art method, PRELUDE. The unwrapping is accelerated in SEGUE by always using 3D partitioning and by simultaneous unwrapping and merging of several regions. We compared SEGUE with PRELUDE in numerical phantoms and using in-vivo images of the brain, head-and-neck, and pelvis. SEGUE provided almost identical results to PRELUDE in each case, but was up to 70 times faster depending on the echo time and anatomical region. We have also shown that applying either technique within water and fat masks separately successfully removed residual wraps in fatty tissue and resulted in more similar unwrapped phase maps between PRELUDE and SEGUE.

For images acquired at short echo times, PRELUDE [92, 140] and SEGUE often had similar computation times (T_c). However, with increasing echo time, the phase images became more wrapped which exponentially increased the number of initial, 2D regions and, consequently, T_c of PRELUDE. Since the increase in the number of the initial 3D regions with increasing echo time was much slower, SEGUE could unwrap severely wrapped phase images at later echoes very quickly compared to PRELUDE, while the resulting unwrapped phase images looked very similar. Both the histograms of the difference images and the measured DiffVox values confirmed that most voxels had identical unwrapped phase values in the PRELUDE and SEGUE results. In case of the brain images, this was the overwhelming majority of the voxels (differing voxels $< 0.4\%$) in every image.

Unwrapping the head-and-neck and pelvic images using either PRELUDE or SEGUE proved to be more challenging. One of the issues is the presence of fatty tissue (fascia and/or subcutaneous fat) that led to residual wraps in the unwrapped phase images. In most anatomical regions, the majority of voxels are water-based and the fatty tissue is usually completely surrounded by these water-filled voxels (e.g. fatty fascia between the muscle sheets). Therefore, the regions partitioned within the fatty tissue often have a larger border with the neighbouring water-based regions than with other fatty regions. Consequently, at the unwrapping and merging step of the algorithms, the phase within fatty regions is compared to the phase of the water-based regions rather than the phase in other fatty tissue. However, the phase in fatty regions has an additional, chemical-shift-induced component. If the chemical-shift-induced phase difference between fatty and water-based regions is close to π, the calculated phase shift (either 0 or 2π) is expected to be arbitrary and largely dependent on the local noise level. This is a recurring problem for both PRELUDE and SEGUE in anatomical regions containing fatty tissue. Here, we have shown that applying these techniques in the fat and water masks separately can resolve

this issue. A limitation of this approach is that fat-water separation is needed to generate separate fat and water masks. In addition, for most fat-water separation techniques, multi-echo data are needed and the quality of the separation might depend on the echo timing [76]. Furthermore, current fat-water separation strategies do not necessarily work in every image (e.g. the three-point Dixon method failed in one of the head-and-neck images even though it was acquired using the same sequence and parameters as the others). Moreover, the quality of the fat-water separation affects the quality of the phase unwrapping as seen in one of the pelvic images with imperfect fat-water separation.

Applying PRELUDE and SEGUE within fat and water masks separately substantially increased the number of identical voxels in both the head-and-neck and the pelvis. The percentage of differing voxels (DiffVox) is still slightly higher in general in the head-and-neck images than in the brain or pelvic images. This is due to some smaller regions in the head-and-neck (such as the tissue around the nasal septum, Fig. 4.8, arrows) being connected to the bulk of the tissue by only a few voxels within the tissue mask making it hard to estimate their corresponding phase shift. Therefore, sometimes these regions had different phase shifts in the PRELUDE and SEGUE results (Fig. 4.8, orange arrows). Based on the approximate shape of the phase variations expected to be induced by the susceptibility difference between tissue and air in the sinuses (Fig. 4.8, dipole field and dashed lines), it seems that only SEGUE could unwrap the tissue on the left side of the nasal septum (Fig. 4.8, orange arrows), while both PRELUDE and SEGUE failed on the right (Fig. 4.8, yellow arrows). The same problem occurred in one of the last-echo head-and-neck images when a large part of the scalp was unwrapped incorrectly as it was connected to the bulk of the tissue by only a few voxels in the water mask.

Identifying a more robust fat-water separation technique and creating more accurate tissue masks tailored for specfic clinical applications are beyond the scope of this study but these steps would definitely help mitigate these remaining issues with phase unwrapping in challenging areas of the body. Also, note that though the three-point Dixon method failed in one out of the four head-and-neck images, fat-water separation errors were present only in one pelvic image out of five and even these were restricted to a small area at the outer edges of the subcutaneous fat. Moreover, all the regions where PRELUDE and SEGUE provided different results, due to them being connected to the rest of the tissue by only a few voxels, were in areas that are not generally the focus of MRI studies (e.g. nasal septum, eyeballs, or scalp).

The large MaxDiff values in a few voxels towards the edges of the tissue (see Table 4.2, especially the head-and-neck results) are induced by noisy voxels. SEGUE estimates the

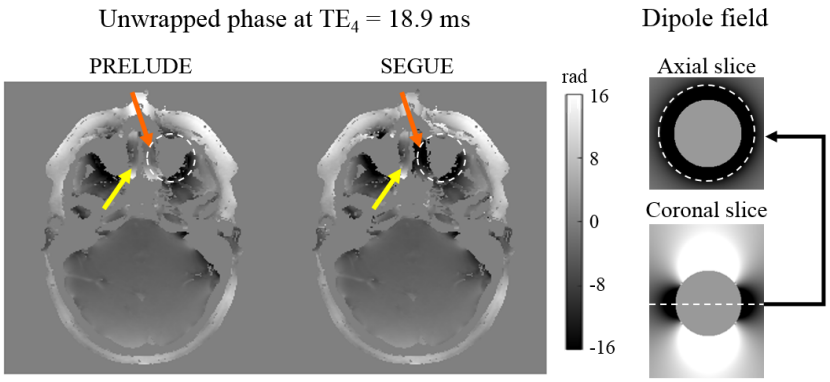

Figure 4.8: Unwrapped phase around the nasal septum in the last-echo head-and-neck image of the representative volunteer. The dashed lines indicate the expected shape of the dipolar phase variations induced by the susceptibility difference between tissue and the air in the nasal sinuses. The orange arrows indicate the tissue on the left side of the nasal septum that only SEGUE could unwrap successfully, while the yellow arrows indicate the right side where both techniques failed.

phase shift by linear extrapolation using phase values in two neighbouring voxels. If both of these voxels are noisy, the extrapolated, estimated phase is likely to be very inaccurate. PRELUDE uses a single nearest-neighbour extrapolation, which is less likely to induce extremely high unwrapped phase values. However, the linear approach is expected to be more accurate near large phase gradients where the real phase values of neighbouring voxels are not close to each other. The measured MaxDiff values are larger for head-and-neck images, because this anatomical region contains larger susceptibility gradients (e.g. at the tissue/air interfaces around the sinuses) inducing highly-variable phase. More careful masking of these noisy voxels towards the mask edges could eliminate these effects.

Note that due to the 3D partitioning, SEGUE is expected to be less robust than PRELUDE to open-ended fringe lines (OFs), i.e. wraps that do not reach the edge of the tissue [145], but suddenly stop within the tissue (Fig. 4.9 a, yellow arrow). At the partitioning step, the gray voxels in Fig. 10 a (highlighted by the dashed line) can form a single region when there should be a 2π difference between region A and region B due to the wrap indicated by the arrow. This situation can occur for several different reasons. Some MRI systems perform a coil combination technique after multi-channel acquisitions that results in incorrect phase values [93] and large OFs in the tissue (Fig. 4.9 a). Highly-variable phase due to large susceptibility gradients and/or motion can also induce OFs (Fig. 4.9 b). Small open-ended fringe lines can form when a voxel along a wrap contains spins with phases close to both $+\pi$ and $-\pi$. Since the measured phase is the phase of the complex sum of spins with these individual phase values, the voxel appears gray ($\approx$0 rad)

instead of black (+π) or white (-π) forming a partial volume open-ended fringe line (Fig. 4.9 c).

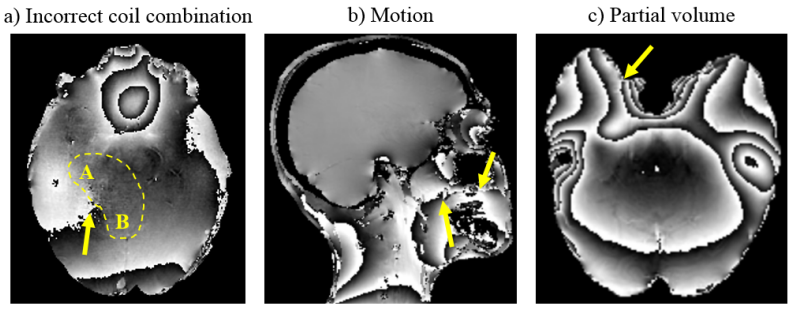

Figure 4.9: Open-ended fringe lines can occur e.g. due to incorrect coil combination in multi-channel imaging (a), highly-variable phase due to large susceptibility gradients and/or motion (b), or partial volume effects (c).

2D partitioning can mitigate the effects of all kinds of open-ended fringe lines, because the 2D regions tend to be very small. Incorrect unwrapping of one of the 2D regions does not necessarily propagate into other parts of the image. In contrast, 3D partitions can be large, connecting regions that are very far from each other, leading to long-ranging effects. However, using 2D partitioning greatly increases the number of initial regions everywhere, not just around open-ended fringe lines. Therefore this approach is very inefficient in dealing with this problem. Note that the approach SEGUE uses for partitioning (removing the small bridges between larger regions before identifying the initial, connected regions) seems to be able to deal with most types of OFs. OFs due to incorrect coil-combination are expected to cause more problems for SEGUE than for PRELUDE, but these can be avoided by combining the phase images from multiple coils correctly at the earlier image reconstruction step [93].

Finally, note that while testing SEGUE in phase images acquired using other modalities is beyond the scope of this study, the SEGUE algorithm is not specific to MR images and could be applied more broadly in future.

4.7 Conclusions

We have developed SEGUE, a spatial phase unwrapping technique that was found to be 1.5 to 70 times faster than the gold-standard, PRELUDE, and produced similarly accurate results. SEGUE could provide an alternative to PRELUDE, especially for highly wrapped, high-resolution images. We have also shown that performing phase unwrapping

separately within the fat and water masks in challenging anatomical regions led to more accurate results in both PRELUDE and SEGUE. Separate fat and water unwrapping is an option available within SEGUE. SEGUE (downloadable from https://xip.uclb.com/i/-software/SEGUE.html) promises to accelerate and improve phase unwrapping for a broad range of MR phase imaging applications from Quantitative Susceptibility Mapping to distortion correction in functional and diffusion MRI.

Chapter 5

The Effect of Low Resolution and Coverage on the Accuracy of Susceptibility Mapping

5.1 Motivation

The original aim of my PhD was to apply susceptibility mapping to pre-existing, clinical MRI data acquired in patients with head-and-neck squamous cell cancer (HNSCC). In 2014, Tudisca et al. [146] investigated T_2^* as a potential biomarker of HNSCC. They reported that the T_2^* of tumours significantly decreased when the patients were breathing 100% oxygen compared to breathing air. Inhaling 100% oxygen has been believed to increase oxygenation in tumours [147] which should decrease its susceptibility resulting in reduced field inhomogeneities and, consequently, an increase in T_2^*. Given this contradiction, they concluded that further work was needed to ascertain the exact mechanisms. Their data were provided to me to investigate this anomaly using QSM. Susceptibility maps from the phase images acquired while the patients were breathing air were calculated using the optimised pipeline (section 6.4): non-linear field fitting, Laplacian phase unwrapping, PDF, and iterative Tikhonov. Figure 5.1 shows the results in a representative case. There was barely any contrast in the calculated susceptibility maps either in the neck (left), in the brain (right), or in and around tumours (yellow arrows) apart from the strong residual background fields (blue arrows) and some residual wraps (red arrow).

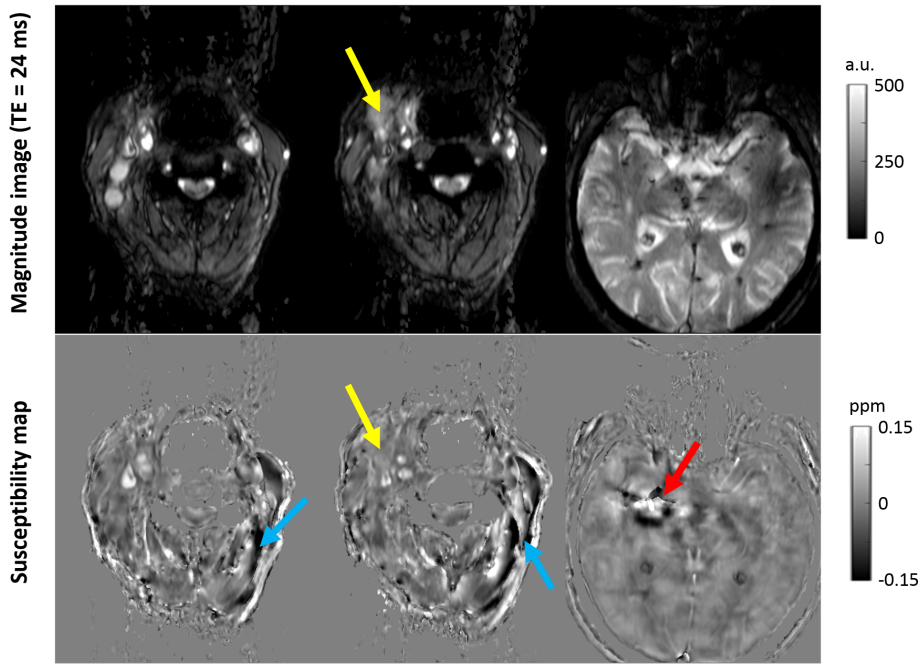

Figure 5.1: Magnitude (top) and susceptibility (bottom) maps in a patient with HNSCC. The arrows indicate the tumour (yellow), residual background fields (blue), and residual wraps (red).

QSM in the head and neck is challenging due to motion and large background fields among other factors (section 1.3.3). However, the aforementioned head-and-neck data was acquired with a very low resolution in the through-slice dimension (slice thickness = 5 mm, gap = 2.5 mm) and only 27 slices. We suspected that these parameters might not be sufficient for accurate susceptibility mapping meaning that the standard clinical acquisition of the head and neck is not suitable for QSM and, therefore, the acquisition protocol needed to be optimised for this anatomical region (section 6.2). To prove this, I investigated these effects in general using numerical simulations and in-vivo brain images. I describe this experiment in the following chapter which was published in Magnetic Resonance in Medicine on 19 October 2018.

5.2 Introduction

Quantitative Susceptibility Mapping (QSM) is an emerging MRI technique that can reveal disease-related changes in tissue iron, myelin and calcium content, and venous oxygenation. Therefore, QSM shows potential for an increasing range of clinical applications [129]. Magnetic susceptibility (χ) is an intrinsic tissue property relating the magnetic field in-

duced within the tissue to the applied magnetic field. The relationship of $\chi(\mathbf{r})$, the tissue susceptibility distribution over space ($\mathbf{r}$), to the resulting phase variations ($\varphi(\mathbf{r})$) can be expressed by the following convolution with the dipole field distribution ($d(\mathbf{r})$) where B_0 denotes the main magnetic field [21, 114]:

$$\varphi(\mathbf{r}) \propto B_0 \left(\chi(\mathbf{r}) * d(\mathbf{r})\right) \tag{5.1}$$

QSM recovers the inherent tissue susceptibility distribution from gradient-echo phase images in three conceptual steps: phase unwrapping, background field removal and susceptibility calculation [118, 126–128]. One advantage of QSM is that it does not require any additional, special hardware or sequences. In theory, susceptibility maps can be calculated from any MR image acquired with a T_2^*-weighted gradient-echo pulse sequence. Therefore QSM can provide additional information for clinicians when gradient-echo images are acquired as part of the diagnostic MRI protocol. However, clinical images are often acquired with large slice thickness [146, 148–153] and reduced coverage in the through-slice dimension [49, 146, 154–157] to shorten scans and increase patient throughput. As QSM techniques are increasingly applied in clinical imaging, it is imperative to understand the effect of low resolution and coverage on susceptibility maps.

Recent studies have begun to investigate the effect of resolution on the accuracy of QSM. In Li et al. [158], MR images of five healthy volunteers acquired with 1 mm isotropic resolution were downsampled in the through-slice dimension to simulate slice thicknesses of 2 and 4 mm, followed by QSM. The study found the error in susceptibility due to increased slice thickness to be negligible. However, Haacke et al. [128] found a 10-25% decrease in the susceptibility of iron-rich deep-brain structures (e.g. globus pallidus and caudate nucleus) when increasing the slice thickness from 0.5 to 3 mm in a numerical brain phantom. Zhou et al. [159] acquired images of gadolinium-filled balloon phantoms at four different isotropic resolutions (0.7 to 1.8 mm) and reported a decrease in the calculated susceptibility with decreasing resolution. In [160], Sun et al. acquired brain images of a healthy volunteer at different isotropic resolutions (2, 3 and 4 mm) using a sequence optimised for functional QSM. They reported a decrease in mean susceptibility in five iron-rich brain regions with increasing voxel size. These findings indicate that, at least over a narrow resolution range (0.5 —4 mm), there is a decrease in *absolute* susceptibility values with increasing voxel size.

One study has investigated the effect of spatial coverage on QSM. In Elkady et al. [161], five healthy volunteers were scanned with a resolution of $0.5\times0.75\times2$ mm and full coverage of the brain. Spatial coverage was incrementally truncated post-acquisition to a minimum through-slice FOV of 12 mm centered on the globus pallidus (GP). A susceptibility error of

more than 5% was found in the GP for FOVs smaller than 5.6 times its size in the through-slice dimension. This result implies that capturing the full extent of the susceptibility-induced phase or field variations is necessary for accurate QSM.

Based on the results of these studies we hypothesise that either low resolution or low coverage will result in reduced and erroneous *absolute* susceptibility values. We aimed to overcome the limitations of previous studies. For example, Haacke et al. [128] used a numerical brain phantom instead of acquired images, while Elkady et al. [161] simulated a decreased FOV by excluding slices post-acquisition. Here, in addition to performing simulations in a numerical phantom, we also acquired MR images at different resolutions and FOVs in healthy volunteers [162, 163]. Though Zhou et al. [159] did acquire images at different resolutions, balloon phantoms are not sufficient to model detailed human brain anatomy. Therefore, we collected in-vivo brain images to show that this effect is substantial in healthy volunteers. Finally, the brain acquisitions of Sun et al. [160] used EPI and were tailored for functional QSM, whereas we used a 3D gradient-echo sequence designed for structural QSM. We also used a broader range of slice thickness and coverage than any of the previous studies and explored the effect of slice spacing on QSM for the first time. Furthermore, we used 3D gradient-echo imaging instead of a 2D multi-slice sequence to acquire images at different resolutions as 3D imaging is becoming the sequence-of-choice for QSM. In addition, we included the white matter in the analysis instead of only investigating deep-brain structures as in all previous studies. Moreover, we compared images acquired in healthy volunteers with downsampled images of the same volunteers to test the applicability of post-acquisition downsampling. We also investigated the source of the error introduced by a reduced coverage by downsampling the acquired images at different stages of the QSM pipeline. Here, we created a new, high-resolution, anthropomorphic, head-and-neck numerical phantom and used it to compare simulated and acquired images. Simulations performed on the numerical phantom also enabled us to compare calculated susceptibility values against ground-truth values to allow quantitative measurement of QSM accuracy.

5.3 Methods

5.3.1 Data acquisition

The local ethics committee approved this study and informed consent was obtained from all participants.

To investigate the effect of reduced through-plane resolution (used in clinical practice) on QSM, multi-echo brain images were acquired in 5 healthy female volunteers (age range: 26-30 years) at 3T (Achieva, Philips Healthcare, NL) using a 3D gradient-echo pulse sequence tailored for structural QSM and a 32-channel receiver head coil, with matrix size = 240×240×144, SENSE factors = 1×2×1.5, 1 mm in-plane resolution, TE_1 = 3 ms, ΔTE = 5.4 ms, 5 echoes, TR = 29 ms, flip angle = 20° and slice thicknesses 1, 2, 4 and 6 mm. Multiple echoes were acquired rather than single echoes as these have been shown to provide more accurate field estimation [18, 128, 164].

To investigate the effect of reduced through-plane coverage (used in clinical practice) on QSM, the same volunteers were also scanned using a 2D gradient-echo pulse sequence to avoid aliasing in the through-slice (head-foot) direction. A 2D acquisition was also most appropriate here as clinical studies often use 2D multi-slice acquisitions. A 32-channel receiver head coil was used with matrix size = 240×240 in-plane, SENSE factors = 1×2, 1 mm isotropic resolution, TE_1 = 4.9 ms, ΔTE = 5.3 ms, 5 echoes, TR = 4549 ms, flip angle = 90° and a through-slice FOV of 144, 111, 78 and 44 mm centered around the middle of the brain. Post-acquisition downsampling in the first two volunteers predicted a sharp decrease in susceptibility contrast below a coverage of 44 mm. Therefore, the last three volunteers were also scanned with a 20 mm through-slice FOV.

The scanner-reconstructed, post-coil combination magnitude and phase images were used for all subsequent image processing in each case.

5.3.2 Designing a realistic numerical head-and-neck phantom

We compared the acquisitions with simulations performed on a numerical phantom to investigate whether the phantom could accurately model in-vivo brain images and to assess how the estimated susceptibilities compared to ground-truth values. A numerical phantom of 1 mm isotropic resolution was necessary to model the highest-resolution acquisitions. Also, to accurately model the background fields in the brain, the phantom needed to include the entire head-and-neck. As no such numerical phantom was available, we created our own realistic, high-resolution, numerical head-and-neck phantom based on the Zubal phantom [165].

The Zubal phantom is an anthropomorphic model of the human head and torso. It contains indexed regions designating anatomical structures in the brain and the body obtained by manual segmentation of (spoiled gradient-echo) MRI and CT images of two

human male volunteers. The head (Figure 5.2 a) and the torso (Figure 5.2 b) phantoms have initial isotropic resolutions of 1.5 mm and 2.5 mm respectively.

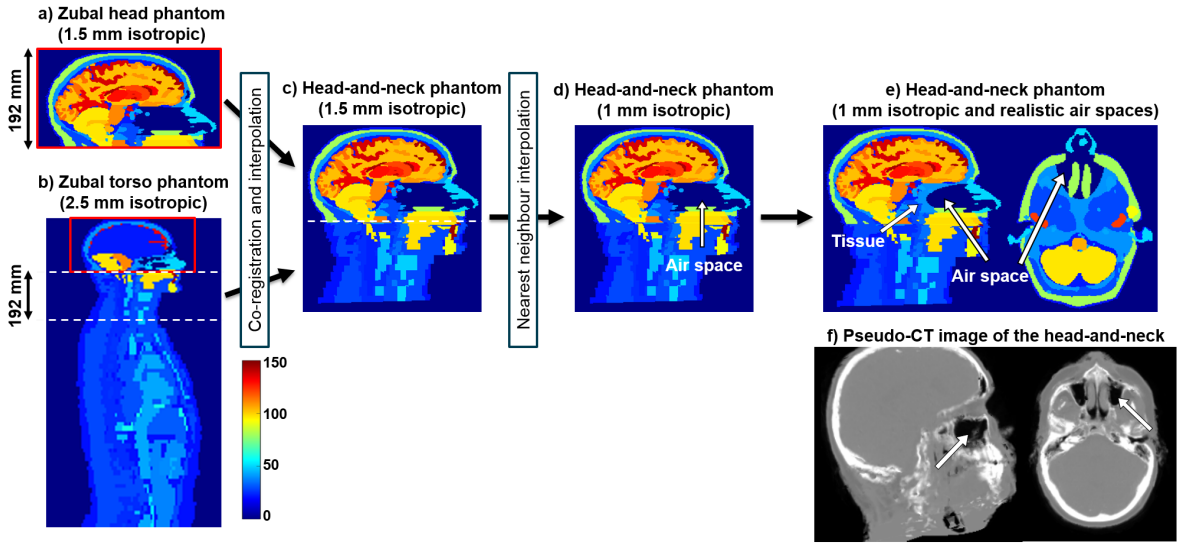

Figure 5.2: Creation of a realistic, numerical head-and-neck phantom. The Zubal head phantom (a) was modified to include the neck section (c) from the torso phantom (b), interpolated to achieve 1 mm isotropic resolution (d) and the oropharyngeal air space was made smaller and more realistic (e-f). The overlapping regions in a and b are outlined in red. Images a-e display the indices of different regions used in the original Zubal phantoms. Pseudo-CT images (f) were generated from a proton density map of a healthy volunteer using an online pseudo-CT synthesis tool [166–168].

A new, high-resolution, anthropomorphic head-and-neck phantom was created in 3 steps (Figure 5.2):

1. The overlapping torso and head phantoms (index maps) were rigidly co-registered in the overlapping region (outlined in red in Figure 5.2 a, b) using the NiftyReg toolbox [169] with default settings and nearest-neighbour interpolation. The co-registered and interpolated 192 mm neck section (Figure 5.2 b) of the torso phantom was then attached to the head phantom (Figure 5.2 c) to obtain a full head-and-neck phantom of 1.5 mm isotropic resolution and a matrix size of 256×256×256.

2. The resulting head-and-neck phantom was further improved by nearest-neighbour interpolation of the indices in MATLAB to achieve 1 mm isotropic resolution (Figure 5.2 d) and a matrix size of 384×384×384.

3. Preliminary simulations showed that the largest oropharyngeal air space in the numerical phantom (Figure 5.2 d) induced strong background fields in the brain that proved to be very difficult to remove completely using standard methods such as Projection onto Dipole Fields (PDF) [109] or the Laplacian Boundary Value method

(LBV) [107]. However, none of the acquired images contained such large background fields. Also, compared to a pseudo-CT image of the head-and-neck (Figure 5.2 f) [166–168], the air space in the numerical phantom seemed too large with unrealistically sharp edges perpendicular to B_0. Therefore, a simple ellipsoidal shape (centre = [195, 61, 248], axes = [25, 65, 18] in voxel units) was used to make the oropharyngeal air space in the numerical phantom smaller and more anatomically realistic (Figure 5.2 e).

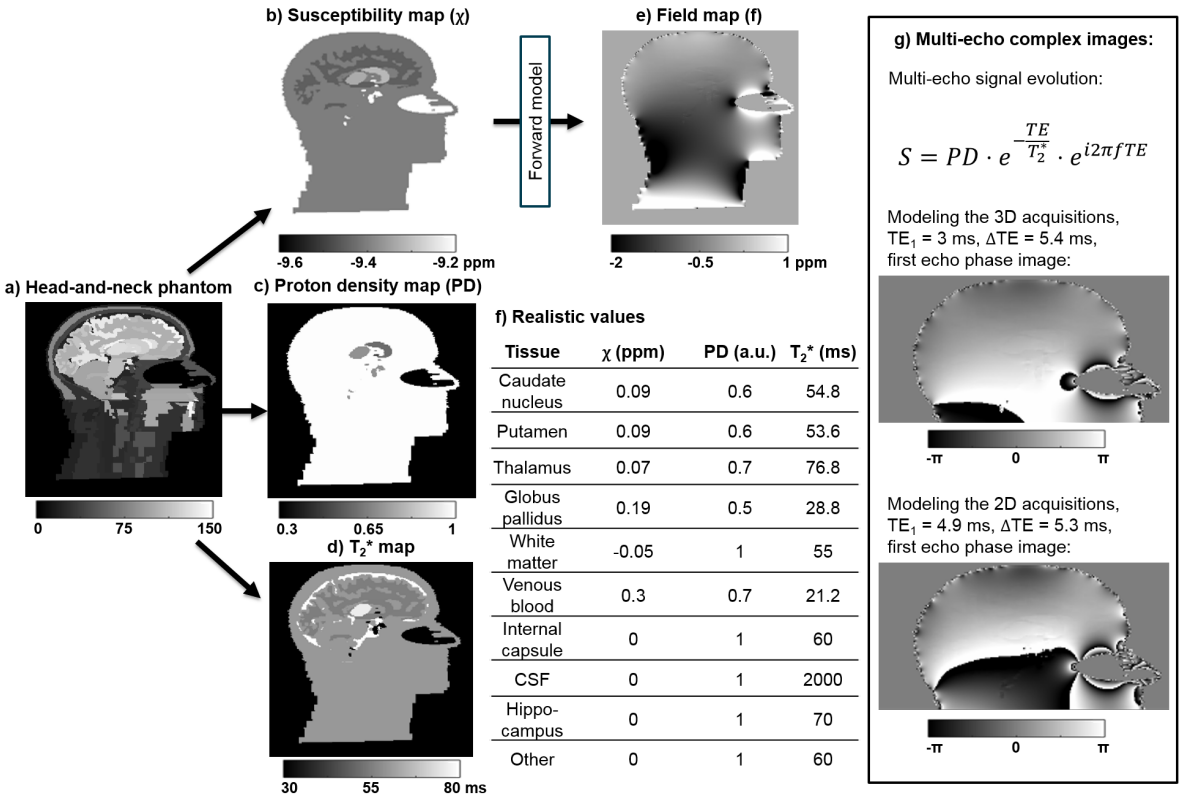

Tissue	χ (ppm)	PD (a.u.)	T_2^* (ms)
Caudate nucleus	0.09	0.6	54.8
Putamen	0.09	0.6	53.6
Thalamus	0.07	0.7	76.8
Globus pallidus	0.19	0.5	28.8
White matter	-0.05	1	55
Venous blood	0.3	0.7	21.2
Internal capsule	0	1	60
CSF	0	1	2000
Hippo-campus	0	1	70
Other	0	1	60

Figure 5.3: Multi-echo brain images of the numerical phantom. Realistic susceptibility (b), proton density (c) and T_2^* (d) values were assigned to several brain regions (f) based on previous literature [85,170–173]. The field map (e) was calculated from the susceptibility map using a Fourier-based forward model [174]. Multi-echo complex images (g) were calculated to model the 3D and 2D acquisitions.

Realistic proton density, susceptibility and T_2^* values, based on previous literature [85, 170–173], (Figure 5.3 f) were assigned to several brain regions in the numerical phantom (Figure 5.3 b-d). The susceptibility values in Figure 5.3 f are relative values referenced to 9.4 ppm, i.e. the susceptibility difference between tissue and air [16]. A Fourier-based forward model [174] was applied to estimate a field map (Figure 5.3 e) from the susceptibility distribution. Multi-echo complex images (Figure 5.3 g) were simulated in the head at 3T with:

- TE_1 = 3 ms, ΔTE = 5.4 ms, 5 echoes and
- TE_1 = 4.9 ms, ΔTE = 5.3 ms, 5 echoes

to model the 3D (varying resolution) and 2D (varying coverage) acquisitions respectively.

5.3.3 Simulations

To compare the volunteer acquisitions with simulations in healthy volunteers and the numerical head-and-neck phantom, both high-resolution, full-coverage images of all 5 healthy volunteers and the complex simulated images of the numerical phantom were downsampled to simulate increased slice thicknesses or decreased FOVs (Figure 5.4).

Low-resolution complex MRI images were simulated from the full-resolution 3D volunteer acquisitions (Figure 5.4 d) and the simulated multi-echo numerical phantom images (Figure 5.4 c) by averaging the complex image across each slab of m = 2 to 6 mm slices (Figure 5.4 h-i).

Low-coverage images were simulated from the full-coverage 2D volunteer acquisitions (Figure 5.4 a) and the simulated multi-echo numerical phantom images (Figure 5.4 b) by including only the central n = 89, 77, 66, 54, 21 and 14% of the slices (Figure 5.4 f-g). Full brain coverage corresponds to n = 100%.

Low-resolution images with isotropic voxels but large slice spacing were also simulated in the numerical phantom by including only every p = 2^{nd} to 6^{th} slice in the initial complex image.

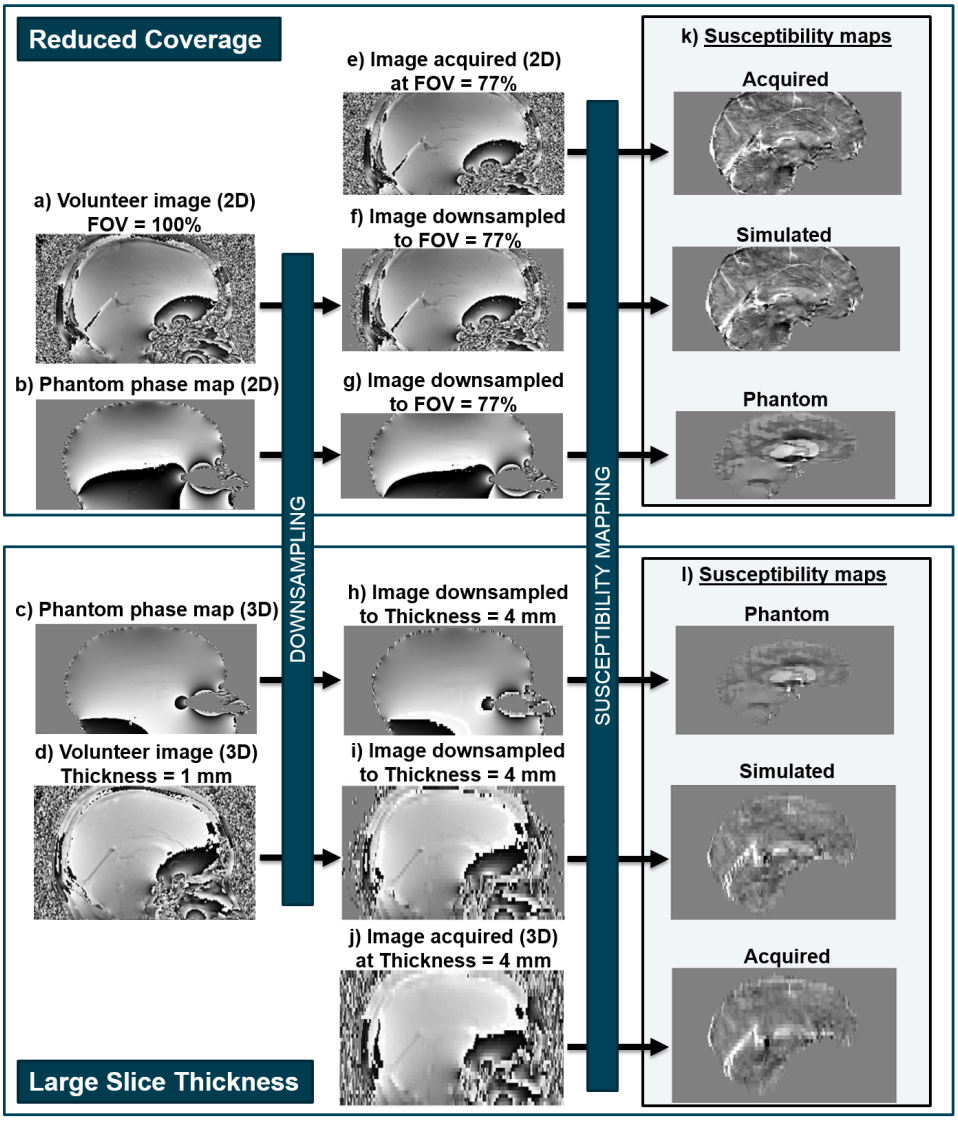

Figure 5.4: Flow chart to illustrate simulations of reduced coverage and resolution. Multi-echo brain complex image volumes were simulated from a numerical phantom (b, c) and acquired in healthy volunteers (a, d). The effect of a reduced FOV (f, g) and reduced through-slice resolution (h, i) were investigated by downsampling the images as well as acquiring low-coverage (e) and low-resolution (j) brain images. Susceptibility maps (k, l) were calculated and compared in each case.

5.3.4 Susceptibility mapping (QSM) pipeline

Susceptibility maps were calculated from all complex images (Figure 5.4 k, l) using the following susceptibility mapping pipeline:

1. Non-linear field fitting [85, 86]
2. Laplacian phase unwrapping [86, 96]

3. Background field removal using PDF [86, 109]

4. Susceptibility calculation using Truncated K-space Division (TKD with $\delta = 2/3$ [21] and correction for susceptibility underestimation using the point spread function from [96])

Zero padding, to matrix sizes of 256×256×256 and 384×384×256 for the volunteer and numerical phantom images respectively, was applied before steps 2 and 4. Brain masks were generated by combining (Figure 5.5 c) the results of the FSL Brain Extraction Tool [144] applied to the last-echo magnitude image (Figure 5.5 a), and thresholding of the inverse noise map [86, 87] (Figure 5.5 b). The first mask excluded voxels outside the brain (Figure 5.5 b, orange arrow) while the second mask ensured that only low-noise regions were included (Figure 5.5, blue arrows) in the susceptibility calculation reducing streaking artifacts from noisy voxels at the brain edges.

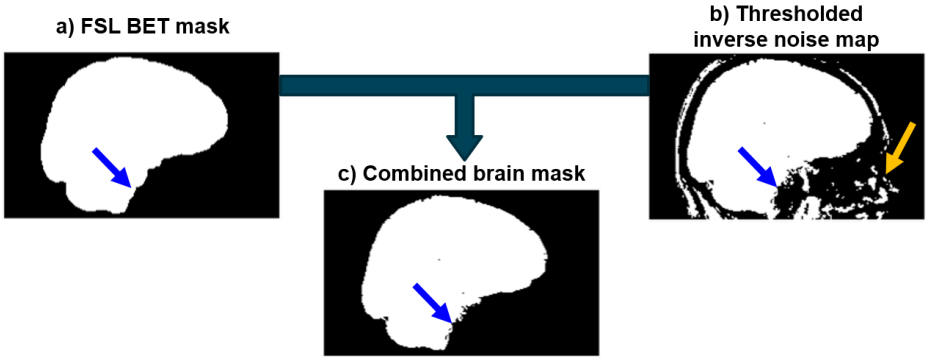

Figure 5.5: Brain mask creation. The final brain mask (c) is the intersection of an FSL BET mask (a) excluding all the tissue outside of the brain (orange arrow), and the thresholded inverse noise map (b) excluding all voxels with high noise (blue arrows).

It could be argued that direct k-space inversion methods, such as TKD, might reconstruct inaccurate susceptibility maps at low resolution and coverage because they implicitly assume that the field values outside the tissue mask are zero instead of noisy or unknown. In theory, susceptibility calculation (SC) techniques that perform fitting of the field map within the tissue mask in image space could overcome this problem. To test whether errors in the estimated susceptibility could be corrected using an image-space fitting technique, we applied the same QSM pipeline as described above but with Morphology Enabled Dipole Inversion (MEDI [86, 120]) as the final step instead of TKD, for all the acquired volunteer images and the numerical phantom.

To investigate the source of the error introduced by a reduced coverage, we performed the aforementioned post-acquisition downsampling (from n = 100% to 14%) not only

before the QSM pipeline, but after steps 2 or 3 as well. This was repeated with the above QSM pipeline but with LBV (31) as the background field removal (BFR) step to examine how the results are affected by different BFR techniques. LBV was chosen because it was shown to perform similarly well to PDF in the brain while introducing slightly different error patterns near the tissue edges [99].

5.3.5 Regions of interest (ROIs) in the brain

The mean and standard deviation of susceptibilities in several brain regions were used to compare the acquisitions and simulations, because the mean is the summary susceptibility measure used in the majority of studies applying QSM. Only regions that have been widely studied in the susceptibility mapping community due to their paramagnetic or diamagnetic nature were included. Regions that were not part of the Zubal segmentation (e.g. red nuclei) were excluded. Therefore, the five ROIs used in this study were: caudate nucleus, putamen, thalamus, globus pallidus and white matter.

Brain ROIs (Figure 5.7 g) in the full-resolution, full-coverage images were obtained via non-rigid registration of the Eve atlas magnitude image [175] and the last-echo magnitude images as these had the most similar echo times and image contrast. The registration was performed using NiftyReg [169] with 5 levels, a final grid spacing of 3 voxels and the weight of the bending energy term set to 0.03. This provided suitable segmentations of the ROIs in all five healthy volunteers as assessed by visual inspection [176]. The posterior corona radiata was used as a white matter ROI in the volunteer images as unlike other ROIs in the Eve atlas (e.g. superior corona radiata), it never had an overlap with the gray matter or any of the iron-rich deep-brain regions. The posterior limb of the internal capsule was also segmented in the volunteer images, because it has been found to be the best reference tissue for susceptibility maps [177].

To obtain the aforementioned ROIs for the low-resolution and low-coverage images, the full-resolution, full-coverage susceptibility maps were rigidly co-registered with all other susceptibility maps in the same volunteer using MATLAB's *imregister* function. The resulting transformations were then applied to the ROIs in the full-resolution, full-coverage image using MATLAB's *imwarp* function to obtain the same regions in the low-resolution or low-coverage images.

The mean and standard deviation of susceptibilities were calculated in the five brain ROIs and referenced to the posterior limb of the internal capsule for the volunteers and the whole internal capsule for the numerical phantom as the latter does not have subsegments

in the phantom. The average and standard deviation of the mean susceptibility in each ROI were calculated across subjects. To show that our results did not originate from edge effects at very low coverage, the same analysis was repeated in the images acquired with the lowest coverage, but the mean was calculated in the middle slice only.

Signal-to-noise ratio (SNR) was estimated in the first-echo magnitude images acquired at the highest resolution and at full coverage. The ratio between the mean and standard deviation of the signal magnitude in each ROI was used as a measure of SNR.

To compare our results with those of Elkady et al. [161], we estimated the coverage corresponding to a mean susceptibility in the globus pallidus (GP) that was 5% less than that in the full-coverage case for each healthy volunteer. We used the results of the downsampling instead of the acquisitions as these were very similar and we had more downsampled than acquired images. To determine the coverage corresponding to a 5% decrease ($\mathrm{Cov}_{5\%}$) in the mean susceptibility of the GP, we estimated the mean susceptibility in the GP as a function of coverage using linear interpolation of susceptibilities between the simulated coverage values. The size of the GP in the through-slice dimension for each healthy volunteer was also measured. We repeated this process for the rest of the ROIs.

5.4 Results

5.4.1 Comparison of acquisitions in volunteers and simulations

Figures 5.6 and 5.7 show the mean susceptibility in several brain regions over varying slice thickness and coverage respectively for the volunteers (a, both acquisitions (x) and simulations (triangles and square)) and the numerical phantom (b). For the numerical phantom, the effect of increasing slice spacing is also shown (Figure 5.6 f). Simulated susceptibility maps in both the volunteers (e) and the numerical phantom (d) showed similar behaviour to maps from acquired images (c).

In all cases, the susceptibility contrast between the five ROIs decreased with increasing slice thickness (Figure 5.6). The phantom simulations show that increased slice thickness also led to inaccurate susceptibility values (Figure 5.6 b where the ground-truth values are indicated by the horizontal lines). In some cases, anisotropic voxels provided results which were numerically closer to the ground-truth (e.g. white matter in Figure 5.6 b). The trends and the susceptibility maps were very similar for the slice thickness and slice

spacing simulations (Figure 5.6 b, f and Figure 5.6 d, g). The SNR in the first-echo magnitude images acquired at the highest resolution was 17±4 on average across all volunteers and ROIs.

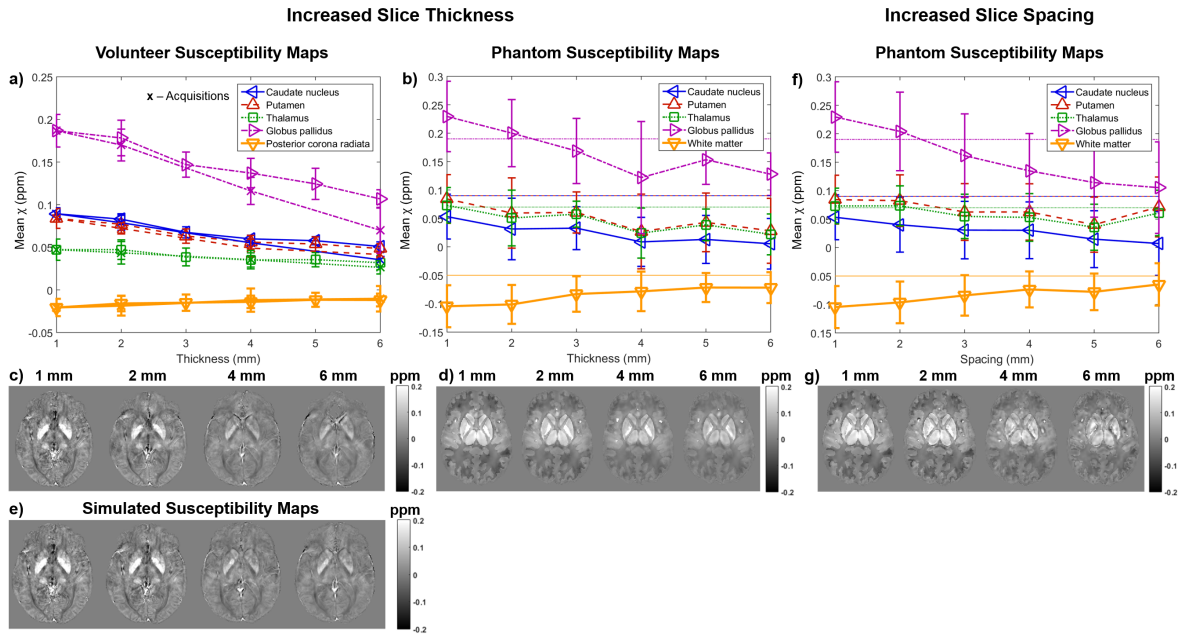

Figure 5.6: Susceptibility over varying slice thickness and slice spacing. Mean susceptibilities in five ROIs are plotted against slice thickness. Susceptibilities were averaged across five volunteers (a, x acquisitions, triangles and square simulations) and simulated in the numerical phantom (b, horizontal lines indicate the corresponding ground-truth susceptibility values). For the numerical phantom, the effect of increasing slice spacing is also shown (f). The data acquired in volunteers (a) have error bars equal to the standard deviation of the mean ROI values across the five volunteers. The error bars in the phantom results (b, f) correspond to the standard deviation within the ROIs. Axial slices of susceptibility maps calculated from images at different slice thicknesses or slice spacings acquired (c) or simulated (e) in a representative volunteer and simulated in the phantom (d, g) are also shown.

Figure 5.7 shows that the mean susceptibilities in the small deep-brain structures were roughly constant until the through-slice coverage reached 30% of the full FOV (44 mm), below which the susceptibility contrast between the five ROIs dropped drastically. However, in the white matter, the decrease in contrast and *absolute* mean susceptibility started at around 75% of the full FOV in both the volunteer images and the numerical phantom (Figure 5.7 a, b, orange lines). Again, the estimated susceptibility in some regions was closer to the ground-truth at the lowest coverage (e.g. globus pallidus and white matter in Figure 5.7 b). Mean susceptibilities calculated in the entire ROIs were very similar to those calculated in the middle slice only (Figure 5.7 a, arrow) in the images acquired with the lowest coverage.

On average, a coverage of at least 4.2±0.6 times the size of the globus pallidus was needed for its mean susceptibility to be within 5% of that at full coverage (Figure 5.7 f). The same measure for the rest of the ROIs was: 2.1±0.8 (caudate nucleus), 2.3±0.8 (putamen), 1.2±0.3 (thalamus), 5.8±0.4 (white matter). The SNR in the first-echo magnitude images acquired at full coverage was 18±4 on average across all volunteers and ROIs.

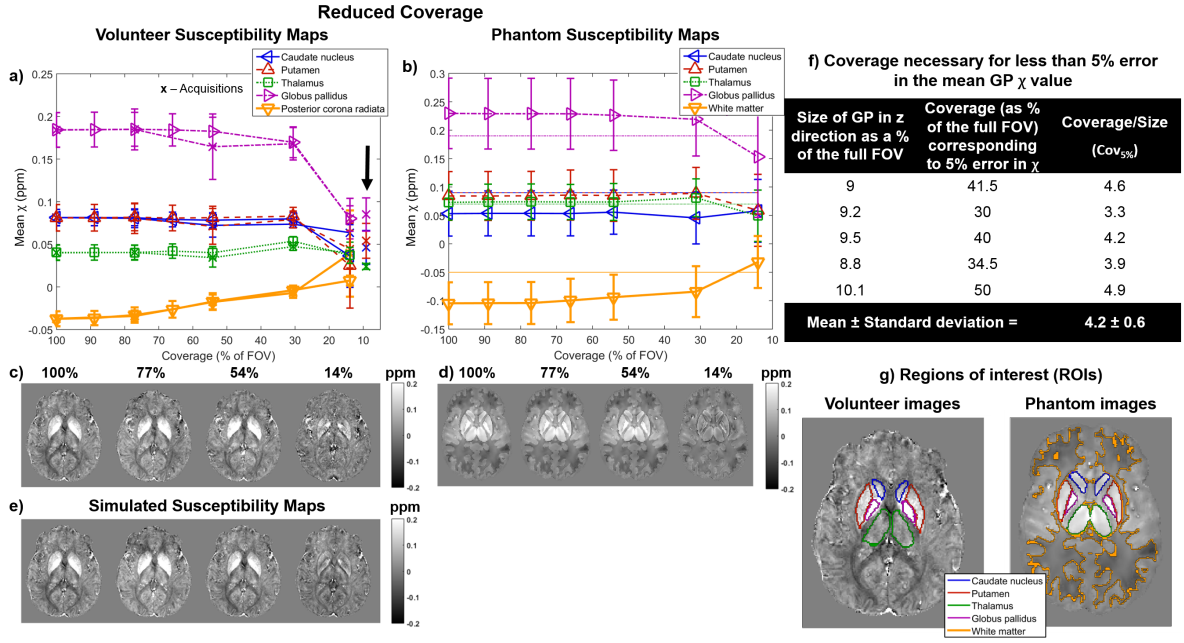

Figure 5.7: Susceptibility over varying coverage. Mean susceptibilities in five ROIs are plotted against coverage. Susceptibilities were averaged across five volunteers (a, x acquisitions, triangles and square simulations) and simulated in the numerical phantom (b, horizontal lines indicate the corresponding ground-truth susceptibility values). The arrow (a) indicates mean susceptibilities in the ROIs calculated in the middle slice only in case of the lowest coverage acquisitions. The data acquired in volunteers (a) have error bars equal to the standard deviation of the mean ROI values across the five volunteers. The error bars in the phantom results (b) correspond to the standard deviation within the ROIs. Axial slices of susceptibility maps calculated from images at different coverage acquired (c) or simulated (e) in a representative volunteer and simulated in the phantom (d) are also shown. We calculated the coverage necessary for less than 5% decrease ($Cov_{5\%}$) in the susceptibility of the globus pallidus in each healthy volunteer (f). Regions of interest are shown (g) on full-coverage susceptibility maps in a representative healthy volunteer and the numerical phantom. The white matter region of the healthy volunteer (posterior corona radiata) is not shown as it is not in this slice.

5.4.2 Results of different susceptibility calculation techniques

Figures 5.8 and 5.9 show the mean susceptibility in five ROIs over varying slice thickness and coverage respectively calculated using TKD (a-b, e-f) and MEDI (c-d, g-h) in a

representative volunteer (a-d) and the numerical phantom (e-h). The results were very similar for all volunteers (not shown). The trends and susceptibility maps look similar to those in Figure 5.6 for increasing slice thickness (Figure 5.8) and in Figure 5.7 for decreasing coverage (Figure 5.9) except when MEDI was applied to the numerical phantom (g and h). In this case, the results suggest that the MEDI algorithm was able to reproduce the susceptibility distribution at full resolution and coverage more accurately than TKD. Furthermore, the MEDI pipeline seems to be more robust against increased slice thickness (Figure 5.8 h) when applied to the numerical phantom even though a slight loss of contrast was still present at lower resolutions. However, TKD was more robust to decreased coverage (Figure 5.9 e).

In general, the MEDI results had slightly lower contrast than the TKD results in the high resolution case and, consequently, their decrease in susceptibility contrast at large slice thickness was less pronounced.

Note that the error bars now correspond to the standard deviation within each ROI. These are generally smaller in the numerical phantom than in the volunteer especially when MEDI was applied to the numerical phantom.

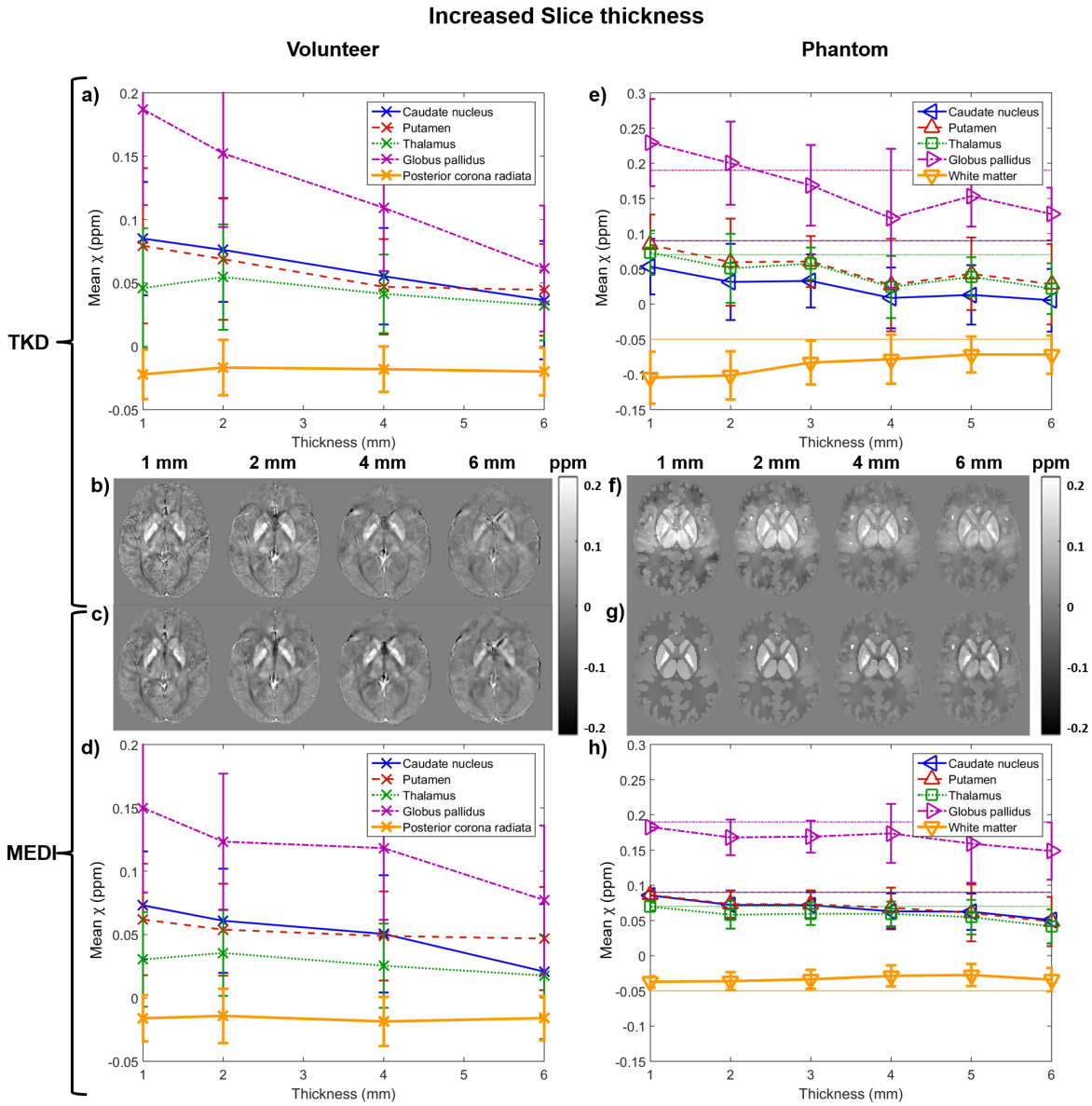

Figure 5.8: Susceptibility over varying slice thickness for different susceptibility calculation methods. Mean susceptibilities in five ROIs are plotted against slice thickness in a representative volunteer (a, d) and the numerical phantom (e, h) calculated using TKD (a-b, e-f) or MEDI (c-d, g-h). Note that here (unlike in Figures 5.6 and 5.7), the error bars in all graphs are equal to the standard deviation within the ROIs. Axial slices of susceptibility maps from images at different slice thicknesses (b-c, f-g) are also shown.

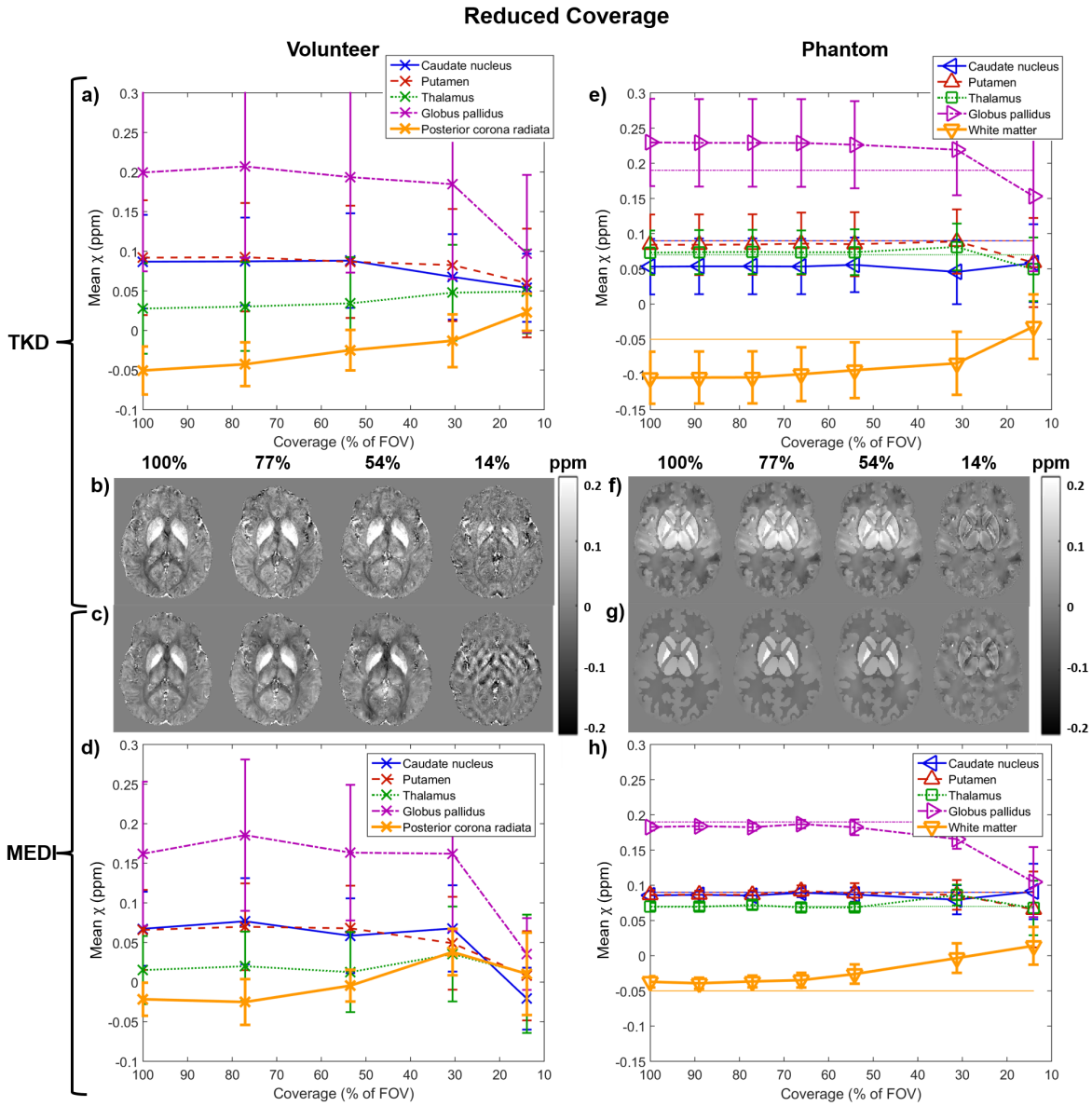

Figure 5.9: Susceptibility over varying coverage for different susceptibility calculation methods. Mean susceptibilities in five ROIs are plotted against coverage in a representative volunteer (a, d) and the numerical phantom (e, h) calculated using TKD (a-b, e-f) or MEDI (c-d, g-h). Note that here (unlike in Figures 5.6 and 5.7), the error bars in all graphs are equal to the standard deviation in the ROIs. Axial slices of susceptibility maps from images at different FOVs (b-c, f-g) are also shown.

5.4.3 The source of the error introduced by a very low coverage

Figure 5.10 a shows mean susceptibilities calculated in the GP in the images acquired at full coverage, downsampled from n = 100% to 14% after BFR, before BFR, or before applying the QSM pipeline, and acquired at 14%. Though the susceptibilities provided by the LBV pipeline were consistently higher, both pipelines showed similar trends.

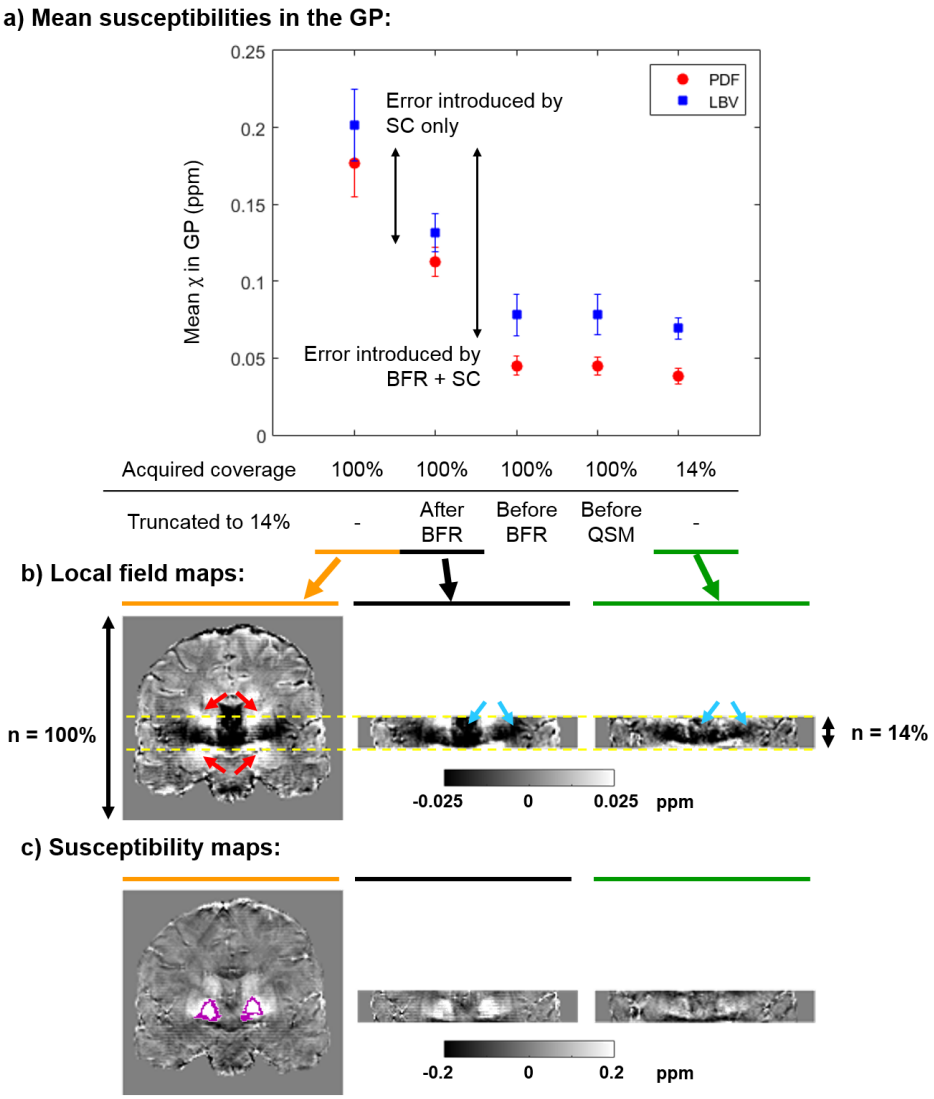

Figure 5.10: Investigating the source of the error introduced by a reduced coverage. Mean susceptibilities in the GP calculated in images acquired at n = 100%, downsampled from n = 100% to 14% after BFR, before BFR, or before QSM, and acquired at n = 14% are shown (a). The error bars correspond to the standard deviation across subjects. The same experiment was performed using two different BFR techniques (PDF and LBV). The double arrows indicate the amount of error introduced by BFR + SC and SC only. Coronal slices of the local field (b) and susceptibility (c) maps calculated as part of the QSM pipeline (after step 3 and step 4 respectively) are shown in a representative healthy volunteer acquired with FOVs 100% (left), 14% (right), and downsampled after BFR (middle). The GPs are outlined in pink. Regions of the induced field perturbations (indicated by red arrows) are cut off at 14% coverage. Moreover, the field variations are attenuated near the volume edges in the image acquired at n = 14% (blue arrows). These factors are the primary sources of the reduced susceptibility contrast at low coverage.

The susceptibilities calculated from the images acquired at n = 14% or downsampled before BFR or QSM were very similar, whereas the results obtained by downsampling after BFR were halfway between the susceptibilities from images acquired at n = 100% or

14%. The double arrows indicate the error induced by BFR + SC and SC only. Example local field and susceptibility maps are also shown (Figure 5.10 b, c respectively).

5.5 Discussion

We compared mean susceptibilities in five ROIs over varying slice thickness, slice spacing and coverage. Susceptibility maps were calculated from images acquired in five healthy volunteers, downsampled images of the same volunteers, and images simulated in a numerical phantom designed to mimic detailed human brain anatomy. We also compared the variation of mean susceptibilities over slice thickness and coverage using two fundamentally different SC techniques (TKD and MEDI), and investigated the source of the error introduced by a reduced FOV using two state-of-the-art BFR methods (PDF and LBV). Increased slice thickness and slice spacing as well as very low coverage all resulted in loss of contrast in the susceptibility maps. The error at very low coverage is introduced at the BFR and SC steps. The trends in mean susceptibilities were very similar for the acquired and downsampled volunteer images, and for the numerical phantom. Susceptibility maps obtained using the two different pipelines were also very similar in the images acquired in volunteers.

The ranges of susceptibilities for each ROI according to previous literature [22, 111, 119, 178, 179] are: caudate nucleus (0.04—0.11 ppm), putamen (0.04—0.13 ppm), thalamus (–0.02—0.05 ppm), globus pallidus (0.12—0.21 ppm) and white matter (–0.06—0.03 ppm). The susceptibility values measured in this work at high resolution and full coverage are all within these ranges. Moreover, the low standard deviation of the susceptibilities across volunteers confirms the reproducibility of QSM in the brain [44, 46, 47].

The results of the slice thickness experiments are in good agreement with the findings of Haacke et al. [128], Zhou et al. [159] and Sun et al. [160] who all reported decreasing *absolute* susceptibility with decreasing resolution for a numerical brain phantom, a balloon phantom and brain acquisitions tailored for functional imaging respectively. However, our results include a larger range of resolutions, volunteer acquisitions tailored for structural imaging as well as downsampled volunteer images and simulations using a numerical phantom. Furthermore, we also simulated increasing slice spacing in the numerical phantom. This showed a decrease in susceptibility contrast with increasing slice spacing similar to that seen with increasing slice thickness. This reduced contrast was probably caused by insufficient sampling of the susceptibility-induced field perturbations. As the slice thickness increased, the complex MRI signal was averaged across increasingly

anisotropic voxels and information about the field variations was lost. This is the VSF (voxel sensitivity function) mixing effect described by Zhou et al. [159]. Zhou et al. reported that the mixing effect at lower resolutions reduces phase contrast, i.e. attenuates the susceptibility-induced field variations, leading to a decrease in *absolute* susceptibility at lower resolutions. This means that the susceptibility of paramagnetic sources inducing positive field perturbations (such as the deep-brain nuclei) decreases, while the susceptibility of diamagnetic sources inducing negative field perturbations (such as white matter) increases with decreasing resolution. Noise-related effects are unlikely to contribute in our case because of the high SNR (around 17 even at the highest resolution).

In [161], Elkady et al. found a 5% error in the susceptibility of the globus pallidus (GP), compared to the susceptibility calculated at full-coverage, when the FOV decreased below 5.6 times the size of the GP which is higher than our result for a similar susceptibility error, i.e. $\text{Cov}_{5\%} = 4.2 \pm 0.6$. However, they also mention that the BFR technique they used eroded the brain by the kernel radius. Accounting for this renders their actual $\text{Cov}_{5\%}$ to approximately 4.7 which is comparable with our findings, even though we used a different QSM pipeline and did not center our FOV around the GP. In a study focusing on one deep-brain structure, the FOV is expected to be centered around the ROI. Therefore, reducing coverage symmetrically from the top and bottom of the brain is a limitation of this study. However, in this way we could include more regions in our analysis. In any case, the ROIs used in this study are very close to the center of the brain in the head-foot direction in our images (except the white matter region in the volunteers). Our results investigating the source of the errors caused by very low coverage indicates that the BFR and SC steps introduce about the same amount of error (Figure 5.10 a, double arrows). BFR attenuates the local field components close to the mask edges (Figure 5.10 b, blue arrows). More accurate BFR could potentially overcome this problem, however, here we used two state-of-the-art techniques with similar results, and it has been shown that all known BFR techniques lead to errors toward the mask edges [99]. The error introduced by the SC step is probably due to regions of the local field map being cut off at reduced coverage (Figure 5.10 b, red arrows). We have shown that neither TKD nor MEDI could fully recover the original susceptibility contrast (Figure 5.9 a-d). Both of these effects arise when the FOV is comparable to the extent of the susceptibility-induced field variations. Therefore, the small deep brain regions are only affected by a very low coverage, while the decrease in *absolute* mean susceptibility in the white matter region started at around 75% of the full FOV as it is a much larger ROI with more extensive field variations in the numerical phantom, and it is off-center in the volunteer images. The induced field variations which are attenuated or cut off are positive for paramagnetic (deep-brain nuclei) and negative for diamagnetic (white matter) susceptibility sources, therefore, similarly to

decreasing resolution, the *absolute* susceptibility decreases with decreasing through-plane coverage.

The numerical phantom experiments suggest that the susceptibility of some ROIs (e.g. white matter) were closer to the ground-truth at the lowest resolution or coverage (e.g. Figure 5.6 b, f and Figure 5.7 b). However, this is due to the fact that the susceptibility mapping pipeline (TKD) is imperfect and overestimated *absolute* susceptibility values (i.e. produced higher susceptibility for paramagnetic sources and lower susceptibility for diamagnetic sources than their ground truth susceptibility values) in some regions in the high-resolution, full-coverage images. Therefore, the mean susceptibilities in these regions became numerically closer to the ground-truth as the *absolute* susceptibility values decreased due to decreasing resolution or coverage. This effect is the reason for using mean susceptibilities in the ROIs instead of an error metric such as the root-mean-square error which can be misleading when a solution with more artifacts or lower quality happens to be numerically closer to the ground-truth. Note that this overestimation of the *absolute* susceptibility had a substantial effect at full resolution and coverage on the globus pallidus and white matter, but not on the caudate nucleus, putamen, and thalamus. This could be associated with the large size of the white matter and the high susceptibility of the globus pallidus in the phantom, but investigating this effect further is beyond the scope of this study. There is no known SC method that can accurately reconstruct susceptibility maps completely accurately in an entire brain in vivo [113]. Different susceptibility mapping pipelines over- or underestimate the susceptibilities of certain regions to variable extent. However, our experimental scheme aims to investigate the trends, i.e. to characterize the errors introduced by low resolution and coverage by varying only these two parameters.

In all cases, susceptibility maps calculated from downsampled images were very similar to maps calculated from images acquired with reduced resolution or coverage. This shows that downsampling of high-resolution and full-coverage MRI images modelled low-resolution and low-coverage acquisitions well. Moreover, simulations performed in our realistic, noise-free numerical phantom also yielded similar results to those in volunteers. This supports the hypothesis that the errors in the estimated susceptibility are primarily introduced by low resolution or coverage rather than by noise, microstructural, hardware-related or physiological effects which were not present in the numerical phantom. A notable example of this is the susceptibility anisotropy of white matter which has been shown to affect its measured susceptibility [24]. However, in this study the decreasing susceptibility contrast is similar for the volunteer (anisotropic white matter) and numerical phantom (isotropic white matter by design) images implying that susceptibility anisotropy does not contribute substantially to the error induced by low resolution and coverage.

The results of comparing the two different SC techniques suggest that MEDI could reconstruct the susceptibility maps in the numerical phantom with lower error than TKD, and did not overestimate the susceptibilities of the ROIs. The numerical susceptibility phantom used in this study consists of distinct regions with piece-wise constant susceptibilities. The regularisation term of MEDI penalises regions with high susceptibility gradient, therefore it is better suited to calculate piece-wise constant susceptibility maps where gradients are small within the regions. This is reflected in the fact that it provided more accurate susceptibility maps than TKD in the numerical phantom, though this same property of MEDI might lead to oversmoothing in in-vivo susceptibility maps. However, the fact that the volunteer results were very similar for the two techniques in both the slice thickness and the coverage experiments suggests that the numerical phantom simulations underestimated the errors introduced by MEDI. Susceptibility varies on a microstructural scale in vivo [4, 23, 24] which is also confirmed by the lower standard deviations within each ROI in the numerical phantom compared to volunteer images. In conclusion, the numerical phantom might not be suitable for investigating the effect of resolution and coverage on QSM when the MEDI pipeline is used. However, the fact that the susceptibility maps calculated using the two pipelines were very similar in the healthy volunteer suggests that even iterative fitting methods, such as MEDI, cannot recover the loss of susceptibility contrast caused by low resolution and coverage. Note that MEDI provided susceptibility maps with a slightly narrower dynamic range than TKD at full resolution and coverage in vivo. This is probably caused by the susceptibility overestimation of TKD at full resolution and coverage together with the oversmoothing of MEDI.

It should be noted that our results are only applicable to brain studies. Though we gave a general qualitative explanation for the source of the decreased contrast, it is possible that motion and fat-water chemical shift effects are the dominant factors in other parts of the body making the influence of resolution and coverage less pronounced.

In general, high resolution and large coverage provide more accurate susceptibility values. The fact that multiple studies using a variety of different QSM pipelines reported similar conclusions underlines the fact that currently the best way to avoid loss of susceptibility contrast is to carefully optimise these parameters. However, resolution and coverage are often constrained by the total scan time available. Moreover, very high resolution images acquired with a longer scan time are more likely to be corrupted by motion artifacts which could also introduce errors in the estimated susceptibility. Here we have shown that for accurate susceptibilities, high resolution is necessary and the FOV needs to exceed the structures of interest by a few times their size. The widespread clinical practice of imaging with large slice thickness, low coverage and gaps between slices leads

to loss of contrast and is not suitable for accurate QSM. The decrease in contrast may depend on various parameters such as the size, susceptibility and shape of the ROI as well as its location within the FOV. Our crude estimations imply a linear relationship between the susceptibility of an ROI and its corresponding $Cov_{5\%}$ (Figure 5.11) which is in accordance with the fact that sources of higher susceptibility induce more extensive field variations. More ROIs and a finer grid of simulated resolutions and coverages would be necessary to determine an over-arching relationship between the properties (e.g. size and susceptibility) of a susceptibility source, and the optimal resolution and coverage. Performing such experiments might be feasible using downsampling of in-vivo, complex images or simulations in our numerical phantom as we have shown that these model MRI acquisitions well. It might also be valuable to investigate the effect of low resolution and coverage in-plane. Finally, future studies could explore the trends in susceptibility accuracy at even higher resolutions where the reduced signal-to-noise ratio due to small voxels, motion issues due to long scan time, and microstructural effects are likely to influence and dominate the results.

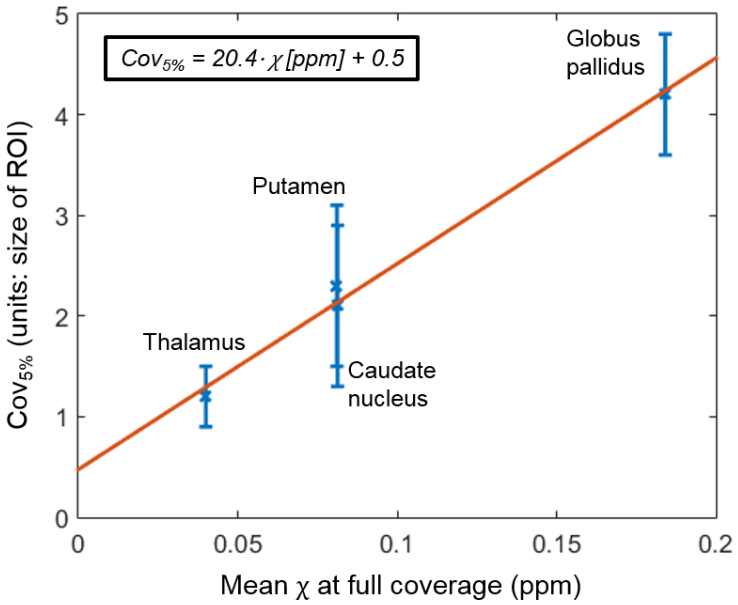

Figure 5.11: Linear relationship between the coverage necessary for a less than 5% decrease in susceptibility ($Cov_{5\%}$) and the mean susceptibility in 4 ROIs. The white matter region was excluded due to its high $Cov_{5\%}$ (5.8±0.4). This high value was caused by its off-center location which means that even a slightly reduced coverage affected its induced fields. The other 4 ROIs were all very close to the middle in the head-foot direction. The least squares linear equation is displayed in the top-left corner.

5.6 Conclusions

Low resolution and low coverage lead to loss of contrast and errors in susceptibility maps. The widespread clinical practice of imaging at low resolution and coverage is not suitable for accurate susceptibility mapping. The reduced accuracy is probably caused by insufficient sampling (i.e. VSF mixing effect and cut-off) and overattenuation (during background field removal near the mask edges) of the susceptibility-induced local field variations. Based on this and similar studies so far, carefully optimised acquisitions seem to be the best solution to this problem. Determining the optimal parameters could be feasible using simulations which were shown to model the acquired images well.

Chapter 6

Optimising the MRI acquisition and QSM pipeline for application in the head-and-neck

As explained in section 1.3.3, the ultimate aim of our research is to correlate the oxygenation measured in cancerous head-and-neck lymph nodes with their susceptibility calculated from MR images using magnetic susceptibility mapping (QSM). Considering that this is the first study using QSM in head-and-neck images, no gold standard protocol exists. In this chapter, I describe the optimisation of the MRI data acquisition and QSM processing pipeline for clinically applicable susceptibility maps in head-and-neck images. All images were acquired on a 3T scanner (Achieva, Philips Healthcare, NL) using a 3D gradient-echo sequence, a 16-channel head-and-neck coil (Figure 6.1).

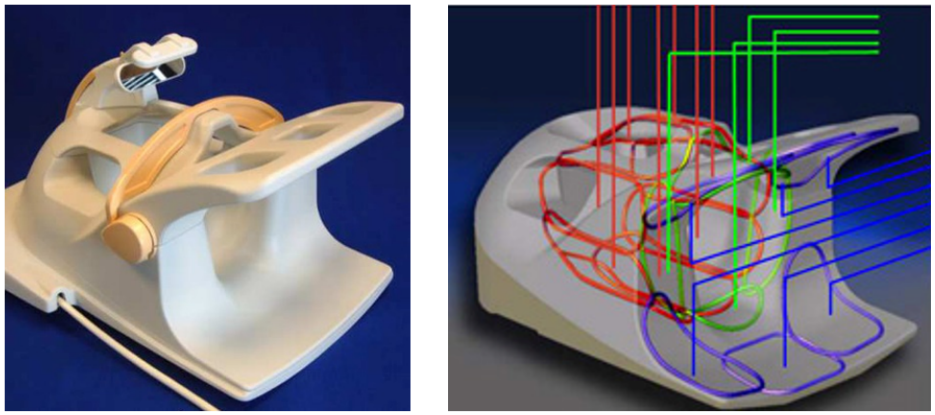

Figure 6.1: Picture (left) and diagram (right) of the 16-channel head-and-neck coil. The coils are highlighted in red, green, and blue in the diagram.

One of the main issues in head-and-neck imaging is the abundance of fatty tissue in this anatomical region which introduces echo time dependent susceptibility contrast (Type 2 chemical shift artifact, section 1.3.2). A range of fat correction strategies have been developed in the past decades (section 2.1), but there is no gold standard method for overcoming this issue. In section 6.1, I compared state-of-the-art fat correction methods (section 2.1.3) in in-vivo head-and-neck data acquired in healthy volunteers to identify the most accurate and robust technique (section 6.1.4).

In sections 6.2 and 6.4, I optimise the MRI acquisition and the QSM pipeline respectively for the head-and-neck region using in-vivo images. In practice, this is an iterative process, but here I present the final stage where I compare different MRI acquisitions in terms the quality of the resulting susceptibility maps calculated using the optimised pipeline from section 6.4, and I compare different QSM pipelines in head-and-neck images acquired with the optimised protocol from section 6.2.

In section 6.2, I decide on image orientation (section 6.2.3.1), resolution and SENSE acceleration factors (section 6.2.3.2), and whether flow compensation should be used (section 6.2.3.3). A summary chart of the optimisation process and the main conclusions can be found in section 6.2.4.

Background field removal (BFR) is one of the most important and challenging steps in the susceptibility mapping pipeline (Figure 2.1). Section 6.3 focuses on comparing current BFR methods in numerical phantoms of the brain and head and neck to inform the subsequent optimisation of the QSM pipeline in 6.4.

In section 6.4, I select the best field fitting and phase unwrapping (section 6.4.3.2), background field removal (section 6.4.3.3), and susceptibility calculation (section 6.4.3.4) methods for the head-and-neck region. Techniques are compared based on signal-to-noise ratio in the resulting field and susceptibility maps wherever applicable (section 3.6), computation time, and visual assessment (i.e. amount of visible artifacts). A summary chart of the optimisation process and the main conclusions can be found in section 6.4.4.

In chapter 7, I test the repeatability of the optimal MRI acquisition protocol (Figure 6.29) and subsequent QSM pipeline (Figure 6.50) developed in this chapter in healthy volunteers to assess the feasibility of detecting the estimated susceptibility difference between hypoxic and normoxic tissue (section 1.3.1).

6.1 Fat Correction of MR Phase Images for Accurate Susceptibility Mapping in the Head and Neck

6.1.1 Introduction

The chemical shift (CS) between fat and water appears as variations in the phase maps that are not susceptibility-induced (section 1.3.2). The phase difference between fat and water depends on the echo time (Equation 2.2). Therefore, CS effects can lead to different contrast between fat and water in the susceptibility map for images acquired with different echo-timing (Figure 6.2). For accurate QSM, it is essential to suppress CS-induced phase variations.

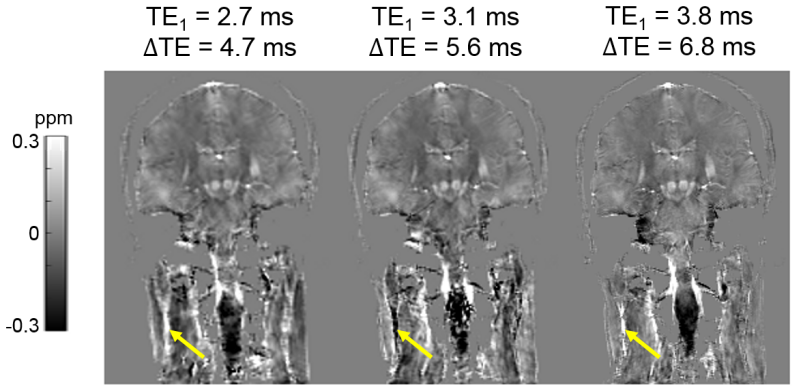

Figure 6.2: Coronal susceptibility maps of the head-and-neck region calculated from images acquired with different echo-timing (given above each image). The arrows indicate the fatty fascia.

There are a number of strategies for fat correction (FC) in phase images (section 2.1). However, there is no established value in the literature for the susceptibility of fatty fascia or subcutaneous fat in the head and neck. In the absence of such a reference value, I reviewed the results of QSM studies in other parts of the body containing fatty tissue.

In 2016, Sharma et al. [141] demonstrated the potential of susceptibility as a biomarker for liver iron overload. They acquired multi-echo images using a spoiled gradient-echo sequence and fit a multi-peak model (Equation 2.3) to their six echoes to calculate a fat-corrected field map. I estimated the susceptibility of fatty tissue from their published results (Figure 6.3) to be around 0.29 ppm.

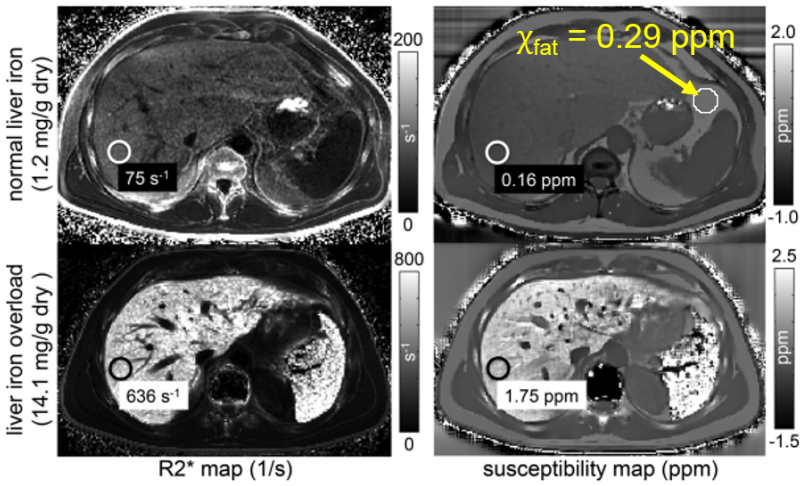

Figure 6.3: Susceptibility of fatty tissue (circle I have superimposed indicated by the arrow) estimated from an image published by Sharma et al. [141].

In 2015, Dong et al. [81] introduced SPURS (section 2.1.2.7), a new technique for fat correction specifically designed for accurate susceptibility mapping. They demonstrated the potential of SPURS in multi-echo images of the liver. Again, I estimated the susceptibility of subcutaneous fat from their published results (Figure 6.4) and found it to be around 0.57 ppm.

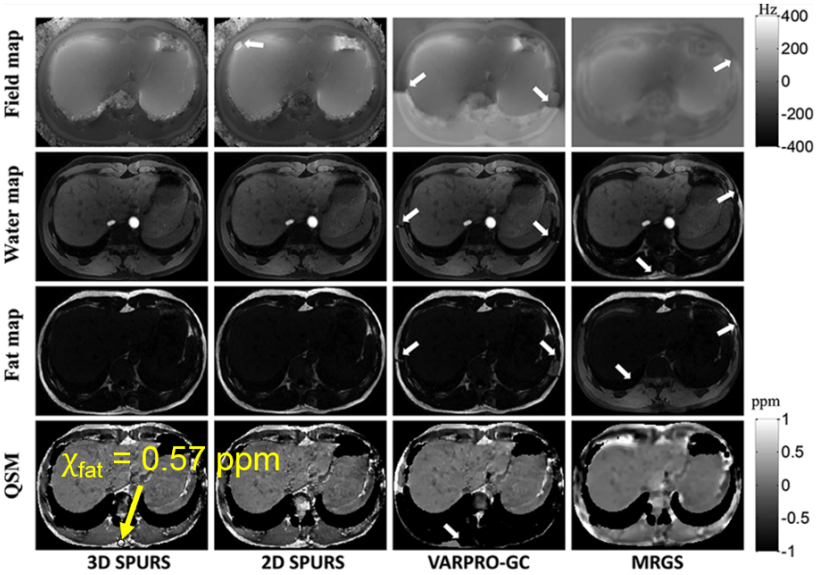

Figure 6.4: Susceptibility of subcutaneous fat (circle I have superimposed indicated by the arrow) estimated from an image published by Dong et al. [81].

In 2017, Wei et al. [180] investigated the magnetic susceptibility properties of the knee. They used a similar approach to Sharma et al. to eliminate the CS effects. I estimated the susceptibility of fatty tissue from their published results (Figure 6.5) to be around 0.19 ppm.

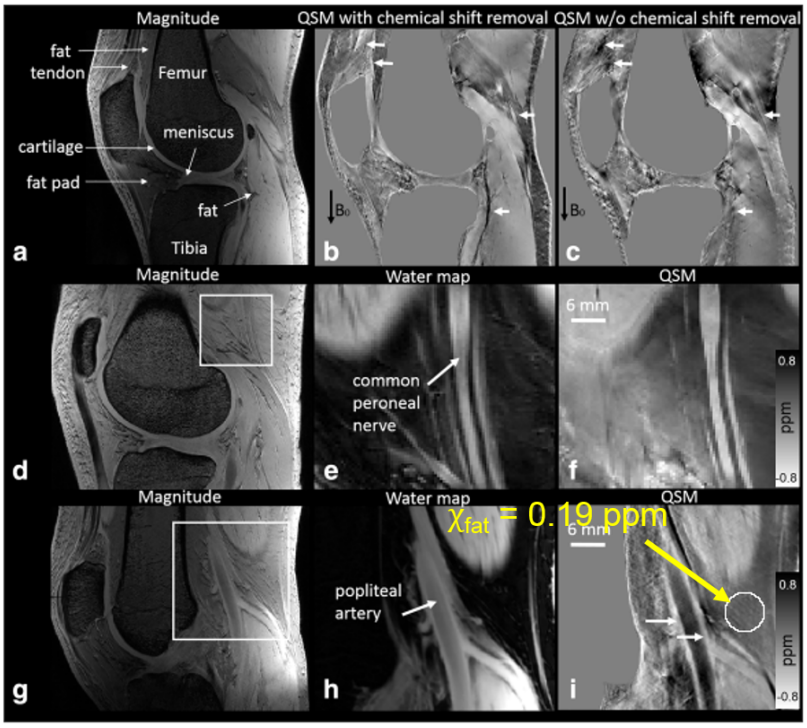

Figure 6.5: Susceptibility of fatty tissue (circle I have superimposed indicated by the arrow) estimated from an image published by Wei et al. [180].

In all three examples, fat was found to appear more paramagnetic than the surrounding water-based tissue. Large molecules, such as lipids, are expected to have diamagnetic features [16]. However, note that in susceptibility mapping, the susceptibility difference between water/tissue and air (≈-9 ppm) is removed by the background field removal step. Therefore, fat can still appear bright in the images.

In conclusion, there are a number of available techniques for post-acquisition fat-correction and previous QSM studies suggest that fat appears bright in the susceptibility maps. Here I investigate the options for fat-correction (section 2.1) in the head and neck for accurate susceptibility mapping. Due to the lack of a gold standard technique, I evaluated the fat fraction maps produced by the various methods based on the known anatomy of the head and neck, compared susceptibility values measured in fatty fascia using different fat-correction strategies, and assessed the robustness of these methods to echo-timing and across subjects.

6.1.2 Methods

6.1.2.1 Data acquisition

To evaluate and compare a range of fat-correction strategies, investigate the echo-time-dependence of fat-corrected susceptibility maps, and assess the robustness of the methods to echo-timing, images were acquired in the head and neck of five healthy volunteers using 8 different acquisition protocols.

The local ethics committee approved this study and informed consent was obtained from all participants. The key acquisition parameters for this study in five healthy volunteers are shown in Figure 6.6. Note that I mainly used retrospective data I acquired at earlier stages of my PhD for this comparison. Volunteer 3 was the only subject I scanned specifically for this experiment. *bw* was between 290 and 440 Hz/pixel for all acquisitions which translates to a 1-1.5 voxel shift between water and fat protons (section 1.3.2). This resulted in little to no visible artifacts presumably because most structures in the neck (subcutaneous fat, fascia, and even lymph nodes) are much larger in the frequency encoding (head-foot direction) than in the two phase encoding directions (note that 3D imaging was used in each case).

	Volunteer 1		Volunteer 2			Volunteer 3		Volunteer 4		Volunteer 5
Sequence	(i)	(ii)	(iii a)	(iii b)	(iii c)	(iv a)	(iv b)	(i)	(v)	(v)
Resolution	1 mm	1 mm	1 mm	1.25 mm	1.5 mm	1 mm	1 mm	1 mm	1.25 mm	1.25 mm
TE_1	3 ms	4.6 ms	3.8 ms	3.1 ms	2.7 ms	3.3 ms	5.6 ms	3 ms	2.8 ms	2.8 ms
ΔTE	5.3 ms	4.6 ms	6.8 ms	5.6 ms	4.7 ms	5.4 ms	7.7 ms	5.3 ms	5.1 ms	5.1 ms
Echoes	4	4	4	6	7	4	4	4	5	5
TR	23 ms	21 ms	29 ms	35 ms	34 ms	24 ms	33 ms	23 ms	27 ms	27 ms

Regular acquisition | In-phase acquisition | Acquisitions to look at echo time dependence of susceptibilities | Acquisitions to investigate robustness to echo-timing

Figure 6.6: MRI acquisition parameters used to acquire multi-echo head-and-neck images in five healthy volunteers to compare different fat-correction strategies, demonstrate the echo-time-independence of fat-corrected susceptibility maps, and investigate the robustness of methods to echo-timing.

6.1.2.1.1 Standard and in-phase acquisitions in the same volunteer

To test and compare a range of post-acquisition fat-correction techniques, multi-echo head-and-neck images were acquired in a healthy volunteer (Volunteer 1), with field of view = 24×24×22 cm (orientation = AP-RL-FH), SENSE factor = 2×1.5×1, 1 mm isotropic resolution, TE_1 = 3 ms, ΔTE = 5.3 ms, 4 echoes, and a flip angle of 18° (Figure

6.6, (i)). In-phase images were also acquired (Figure 6.6, (ii)) in the same volunteer to assess in-phase acquisitions as a fat correction strategy.

6.1.2.1.2 Varying echo-timing in the same volunteer

To show that the use of fat-correction resolves the echo-time-dependent contrast illustrated in Figure 6.2, I acquired a set of QSM-optimised multi-echo head-and-neck images in a healthy volunteer (Volunteer 2), with field of view = 20×24×24 cm (orientation = AP-RL-FH), SENSE factor = 1×2×1, and flip angle around 12°. The corresponding echo-timing, resolution and number of echoes are shown in Figure 6.6 (iii a-c).

Two more sets of images were acquired in a healthy volunteer (Volunteer 3), with field of view = 24×20×24 cm (orientation = AP-RL-FH), SENSE factor = 2×1.5×1, and flip angle 18°. In this case, both images had 1 mm isotropic resolutions, therefore, the only varying factor was the echo-timing. The corresponding parameters are shown in Figure 6.6 (iv a-b). For both images, the echo-timing was carefully selected to achieve optimal fat-water separation by the three-point Dixon method (section 2.1.2.2).

6.1.2.1.3 Additional acquisitions to test the robustness of fat-correction techniques to echo-timing

The best fat-correction techniques were tested in a few more acquisitions to investigate their robustness to echo-timing and across subjects (Figure 6.6, Volunteers 4 and 5). Volunteer 4 was scanned using (i) and another sequence (v) with similar parameters apart from the ones shown in Figure 6.6. Volunteer 5 was also scanned with (v).

6.1.2.2 Comparison of fat-fraction and field maps

Fat-fraction (FF) and field maps were estimated from acquisition (i) of Volunteer 1 using state-of-the-art methods from the 2012 ISMRM Fat-Water Separation Challenge [74]: 3PD (section 2.1.2.2), GOOSE (section 2.1.2.4), B0-NICE (section 2.1.2.5), and IGCA (section 2.1.2.3). The fat-correction algorithm developed for accurate susceptibility mapping (SPURS, section 2.1.2.7) was also used on these images. A field map was estimated from the in-phase acquisition (ii) of Volunteer 1 using non-linear field fitting (section 2.2.1.3). Note that FF maps cannot be calculated from in-phase acquisitions. Since all other techniques provided wrapped field map estimates, the SPURS and GOOSE results were manually rewrapped for ease of comparison.

6.1.2.3 The 3-point Dixon method at different echo-timings

To show that fat correction can resolve echo-time dependent susceptibility contrast (Figure 6.2), susceptibility maps were calculated from (iii a-b) both with and without fat correction using an optimised QSM pipeline (section 6.4):

1. 3PD or non-linear field fitting to estimate the field map with or without fat correction respectively
2. LPU (section 2.2.2.2) to unwrap the field maps
3. PDF (section 2.3.4.1) to calculate the local field variations
4. Iterative dipole fitting with Tikhonov regularisation (section 2.4.2.2)

An ROI of 629 voxels was manually drawn within the fatty fascia on the first echo magnitude image acquired with (iii a) in Volunteer 2. This ROI was segmented in the other two, lower resolution images by rigidly registering the magnitude images with the highest-resolution magnitude image in MATLAB and applying the transformation to the ROI. The mean and standard deviation (SD) of susceptibilities were calculated in these ROIs in all cases.

6.1.2.4 The extended 3-point Dixon method (N-point Dixon)

3PD is a promising fat-correction technique as it was one of the winning methods of the ISMRM Fat-Water Separation Challenge, and it is relatively simple and robust. However, it only uses the first three echoes in multi-echo image. I have expanded this technique to include all available echoes in the calculation (section 2.1.2.6) hoping to achieve better susceptibility SNR. I compared the resulting N-point Dixon method (NPD) I developed with 3PD by calculating susceptibility maps in Volunteers 2 (iii a-c) and 3 (iv a-b) using the above QSM pipeline both with either 3PD or NPD as the first step.

6.1.2.5 Comparison of 3PD, SPURS, and in-phase imaging

3PD, SPURS, and in-phase imaging proved to be the most accurate techniques for estimating the total field map in Volunteer 1 (section 6.1.3.1). To investigate whether these techniques gave similar results, I have calculated susceptibility maps using steps 2-4 of the

QSM pipeline above for the 3PD and in-phase field maps, and steps 3-4 for the SPURS result (as this field map did not require additional unwrapping). Two ROIs (1125 and 1740 voxels) were drawn manually in the fatty fascia on the first-echo magnitude image acquired with (i) in Volunteer 1. The same regions were segmented in the images acquired with (ii) by rigidly registering the first-echo magnitude images in MATLAB and applying the resulting transformation to the ROIs. The mean and SD of the susceptibility in the ROIs were calculated in each case.

FF maps were also calculated using SPURS and 3PD in additional head-and-neck images acquired in Volunteers 4 and 5 to test the robustness of these techniques to echo-timing and across subjects.

6.1.3 Results and Discussion

6.1.3.1 Comparison of different techniques

Figure 6.7 shows a comparison between six fat-correction strategies in Volunteer 1. GOOSE failed to provide an accurate fat-fraction map and the resulting unwrapped field map also looks erroneous. B0-NICE and IGCA estimated high fat-fraction (FF) in the water-based sternocleidomastoid muscle (red arrows), and low fat-fraction in parts of the subcutaneous fat (blue arrows). Fat-fraction maps provided by 3PD and SPURS were similar and looked reliable with high FF everywhere in subcutaneous fat and low FF in muscles. Moreover, the 3PD, SPURS, and in-phase acquisition field maps were also very similar (highlighted by yellow boxes). A more detailed comparison of these techniques can be found in section 6.1.3.4.

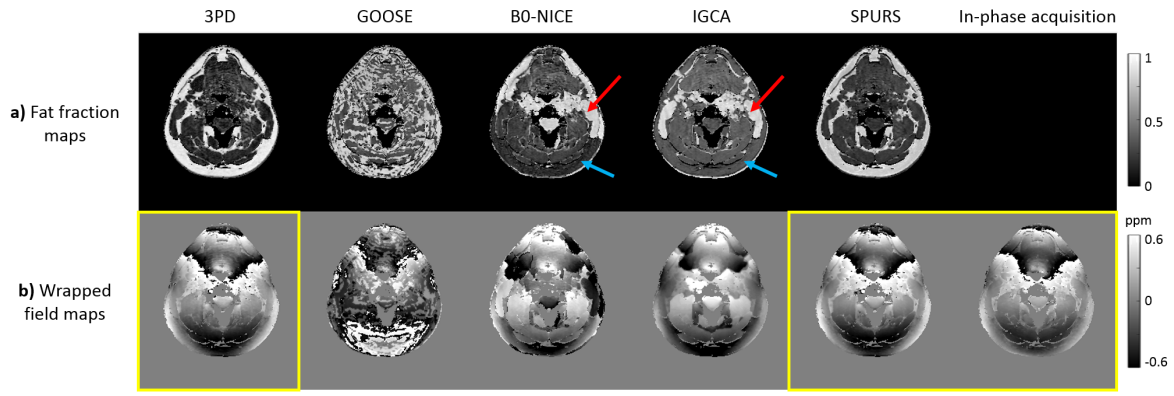

Figure 6.7: Comparison of six fat-correction strategies in Volunteer 1. Fat-fraction (a) and wrapped field maps (b) estimated using five different post-acquisition techniques and in-phase imaging are shown in the same transverse slice in the neck. The field maps output by SPURS and GOOSE were rewrapped for ease of comparison. Note that fat-fraction maps cannot be calculated when in-phase acquisition is used. The arrows indicate the water-based sternocleidomastoid muscle (red arrows), and the subcutaneous fat (blue arrows) in the B0-NICE and IGCA fat-fraction maps.

6.1.3.2 The 3-point Dixon method at different echo-timings

Figure 6.8 shows susceptibility maps calculated with 3PD and without fat correction (FC) in images acquired at three different resolutions and, consequently, echo-timing (Figure 6.6, Volunteer 2 (iii a-c)). Fat correction provided susceptibility maps with very similar contrast for the three different echo-timings (top row, yellow arrows), while the contrast in the susceptibility maps calculated without correction largely depended on the timing (bottom row, yellow arrows). Susceptibility of fat was also similar for the three echo-timings after fat correction, but was very different for the uncorrected susceptibility maps (Figure 6.8, middle row). All these results demonstrate that fat correction (using 3PD) can overcome the problem of echo-time-dependent susceptibility contrast. Moreover, the echo-time independent contrast in the fat-corrected maps shows increased susceptibility in fatty tissue compared to water-based tissue, which is in line with the results of previous studies (section 6.1.1).

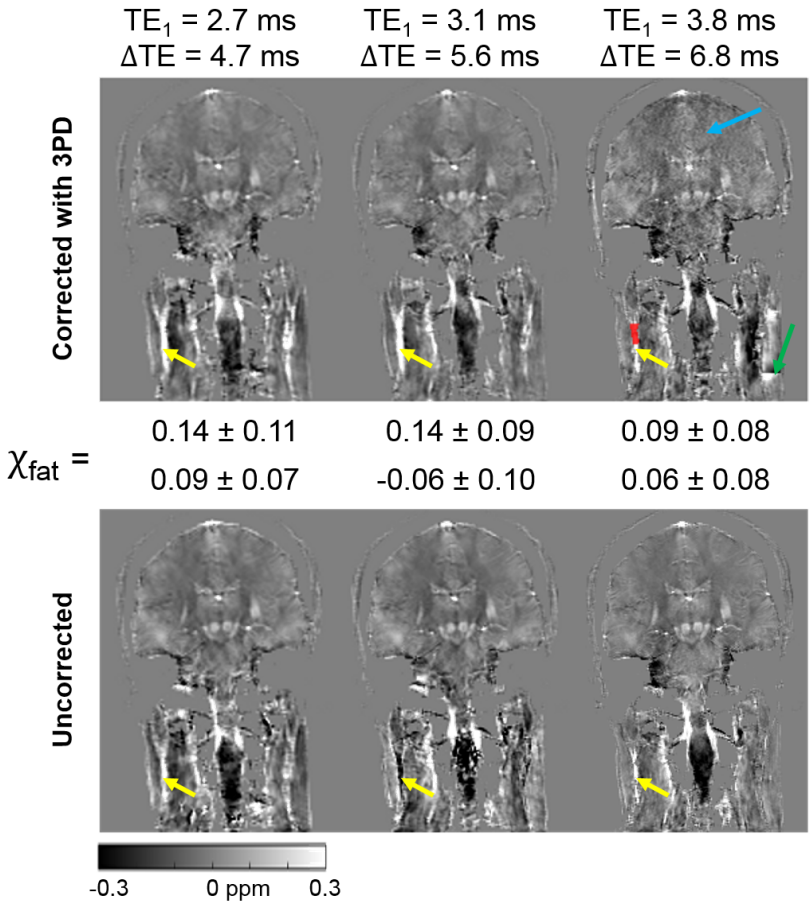

Figure 6.8: Susceptibility maps calculated with (top row) and without (bottom row) FC in images acquired with three different echo-timings in Volunteer 2. The manually segmented fatty region is highlighted in red, and the measured mean ± SD susceptibility values are displayed in the middle row. The yellow arrows indicate the fatty fascia that has echo-time-dependent contrast in the uncorrected case (bottom row), but echo-time-independent contrast after fat correction (top row). The blue and green arrows indicate noisy results and swapping artifacts respectively in the highest resolution, fat-corrected susceptibility map.

The susceptibility of fatty tissue in the highest-resolution image calculated after FC (Figure 6.8 top-right corner) was substantially lower than in the other two fat-corrected maps. Moreover, this susceptibility map was generally more noisy due to the small voxel size (blue arrow), and contained additional, swapping artifacts (section 2.1.2.2) introduced by 3PD because the echo-timings were not optimal for FC (green arrow). This implies that 3PD is sensitive to echo-timing, and it might amplify errors in the phase maps, i.e. low SNR is even more prominent in the susceptibility maps if 3PD is used (Figure 6.8, right).

6.1.3.3 The extended 3-point Dixon method (N-point Dixon)

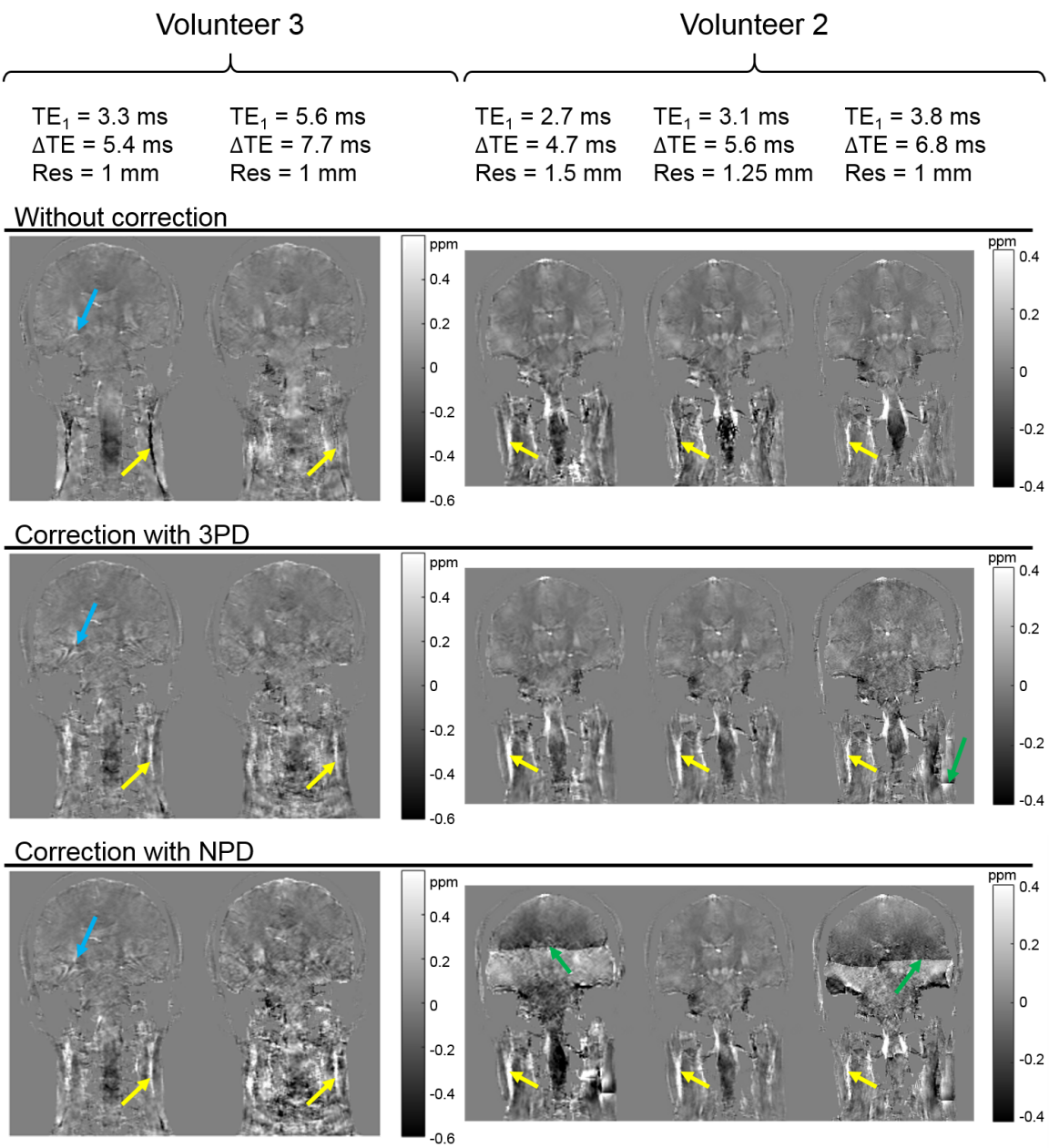

Figure 6.9: Susceptibility maps calculated without fat correction (top row), using 3PD (middle row), or NPD (bottom row) in images acquired in Volunteer 2 (right column) and Volunteer 3 (left column). The yellow arrows indicate the fatty fascia that has echo-time-dependent contrast in the uncorrected case (top row), but echo-time-independent contrast after fat correction (middle and bottom rows). The blue arrows indicate how fat correction amplified motion artifacts in Volunteer 3. The green arrows indicate swapping artifacts.

Figure 6.9 shows susceptibility maps calculated without fat correction (top row), using 3PD (middle row), or NPD (bottom row) in images acquired in Volunteer 2 (right column)

and Volunteer 3 (left column). The yellow arrows indicate the fatty fascia in each susceptibility map. The uncorrected maps had echo-time-dependent fat-water contrast in both Volunteer 2 (acquired at three different resolutions and, consequently, echo-timing) and Volunteer 3 (acquired at 1 mm isotropic resolution, but with two different echo-timings). Both 3PD and NPD provided susceptibility maps with echo-time-independent contrast with bright fatty tissue in both volunteers. However, while NPD works well around the optimal echo-timing (left column and middle image from the right column), its sensitivity to sub-optimal echo-timing resulted in more prominent swapping artifacts (green arrows). Note that while the echo-timing of both acquisitions in Volunteer 3 (left column) was nearly optimal for 3PD, the images on the right were generally very noisy and uninformative due to the unusually long echo times. Also note that the motion artifacts in the susceptibility maps of Volunteer 2 were amplified by both 3PD and NPD (blue arrows). In conclusion, NPD is substantially less robust to the echo-timing than 3PD, therefore it is not appropriate for clinical use.

6.1.3.4 Comparison of 3PD, SPURS, and in-phase imaging

Figure 6.10 shows susceptibility maps calculated from the 3PD, SPURS, and in-phase acquisition field maps of Volunteer 1 from Figure 6.7. All three susceptibility maps had very similar fat/muscle contrast (yellow/white arrows). The susceptibility values of fat measured in two ROIs containing fatty tissue (see magnitude image) are in good agreement for the three fat-correction strategies. The slightly higher susceptibility in the SPURS susceptibility map could be due to the lack of LPU in the pipeline (since SPURS performs unwrapping as well) which might attenuate the local field variations.

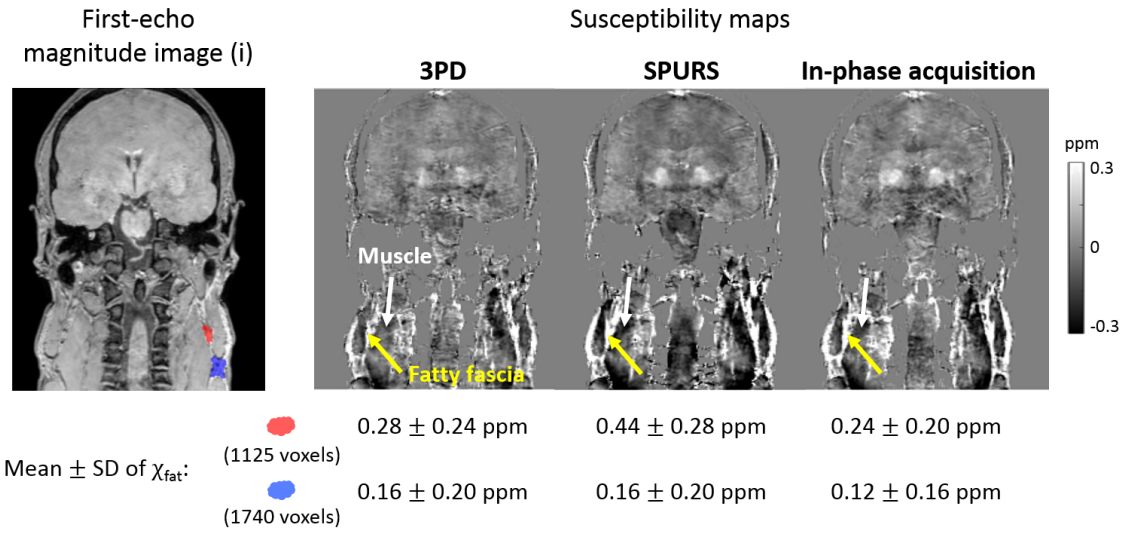

Figure 6.10: Susceptibility maps calculated from the 3PD, SPURS, and in-phase acquisition field maps of Volunteer 1 (Figure 6.7, yellow boxes). The arrows indicate the fatty fascia (yellow) and the surrounding muscle (white) in each map. Two fatty ROIs are shown in the magnitude image. The mean and standard deviation of susceptibility in these regions are displayed below each susceptibility map.

Figure 6.11 shows fat-fraction maps in four different volunteers, acquired with three different echo-timings (Figure 6.6), calculated using 3PD and SPURS. Both fat-correction techniques provided realistic fat-fraction maps in Volunteers 1 and 4 when the images were acquired with (i). However, these techniques failed for images of slightly different echo-timings ((v) and (iv)) resulting in swapping artifacts (green arrows). 3PD consistently failed for the (v) echo-timing, but performed well for (i) in both volunteers. According to the guidelines in Berglund et al. [76] (section 2.1.2.2), the echo-timing in (i) is slightly closer to the optimal timing than the timing in (v):

$$\begin{aligned}
\mathrm{Re}(a + a_0 \cdot a)_{(i)} &= \mathrm{Re}\left(e^{i2\pi\cdot\Delta f\cdot\Delta TE} + e^{i2\pi\cdot\Delta f\cdot TE_2}\right) \\
&= \mathrm{Re}\left(e^{i2\pi\cdot 434.52\ \mathrm{Hz}\cdot 5.3\ \mathrm{ms}} + e^{i2\pi\cdot 434.52\ \mathrm{Hz}\cdot 8.3\ \mathrm{ms}}\right) = -1.11 < 0 \\
\angle(a_0)_{(i)} &= \angle\left(e^{i2\pi\cdot\Delta f\cdot TE_1}\right) = \angle\left(e^{i2\pi\cdot 434.52\ \mathrm{Hz}\cdot 3\ \mathrm{ms}}\right) = 110^\circ \\
\angle(a)_{(i)} &= \angle\left(e^{i2\pi\cdot\Delta f\cdot\Delta TE}\right) = \angle\left(e^{i2\pi\cdot 434.52\ \mathrm{Hz}\cdot 5.3\ \mathrm{ms}}\right) = 110^\circ
\end{aligned} \tag{6.1}$$

$$\begin{aligned}
\mathrm{Re}(a + a_0 \cdot a)_{(v)} &= \mathrm{Re}\left(e^{i2\pi\cdot\Delta f\cdot\Delta TE} + e^{i2\pi\cdot\Delta f\cdot TE_2}\right) \\
&= \mathrm{Re}\left(e^{i2\pi\cdot 434.52\ \mathrm{Hz}\cdot 5.1\ \mathrm{ms}} + e^{i2\pi\cdot 434.52\ \mathrm{Hz}\cdot 7.9\ \mathrm{ms}}\right) = -0.69 < 0 \\
\angle(a_0)_{(v)} &= \angle\left(e^{i2\pi\cdot\Delta f\cdot TE_1}\right) = \angle\left(e^{i2\pi\cdot 434.52\ \mathrm{Hz}\cdot 2.8\ \mathrm{ms}}\right) = 90^\circ \\
\angle(a)_{(v)} &= \angle\left(e^{i2\pi\cdot\Delta f\cdot\Delta TE}\right) = \angle\left(e^{i2\pi\cdot 434.52\ \mathrm{Hz}\cdot 5.1\ \mathrm{ms}}\right) = 100^\circ
\end{aligned} \tag{6.2}$$

It is interesting to note that both (i) and (v) fulfill the $\mathrm{Re}(a + a_0 \cdot a) < 0$ criterion for avoiding water-fat swaps and 3PD still fails for images acquired with (v). This could be because this criterion was calculated for a single-peak model [76] and the latest implementation of 3PD uses a multi-peak fat spectrum for fat-water separation. Alternatively, my approximation for the chemical shift ($\Delta f = 3.4$ ppm $\cdot 3$ T $\cdot 42.6$ MHz/T $= 434.52$ Hz) may not be accurate.

In any case, there is only a 0.2 ms difference in both TE_1s and ΔTEs between (i) and (v). Consequently, a slightly different magnetic field or chemical shift could easily lead to similar errors. Note that in chapter 8, I applied 3PD to images of the sacroiliac joint acquired in healthy volunteers and patients with spondyloarthritis. While 3PD performed adequately in most cases, it failed in a few subjects even though all images were acquired with the same sequence. Therefore, 3PD cannot be expected to perform robustly in a multi-centre study. SPURS also failed for slightly suboptimal echo-timings ((iv) and (v)), therefore it is not robust to the echo-timing either.

In-phase imaging (ii) is a built-in option in most scanners. It suppresses CS effects on a voxel-by-voxel basis without performing any spatial, region-growing techniques which are the main source of the water-fat swaps appearing in both 3PD and SPURS results (Figure 6.11). Reducing chemical shift effects at the acquisition stage also avoids any potential, additional noise introduced by post-acquisition fat-correction techniques (Figure 6.8). Though in-phase imaging only corrects for the main fat peak, since it provided a similar susceptibility map to 3PD and SPURS (Figure 6.1.3.4), both of which use the multi-peak model, we can assume that the single-peak approximation is sufficient for performing QSM in the head and neck. In conclusion, in-phase imaging is a good candidate for robust fat-correction in head-and-neck images for accurate QSM.

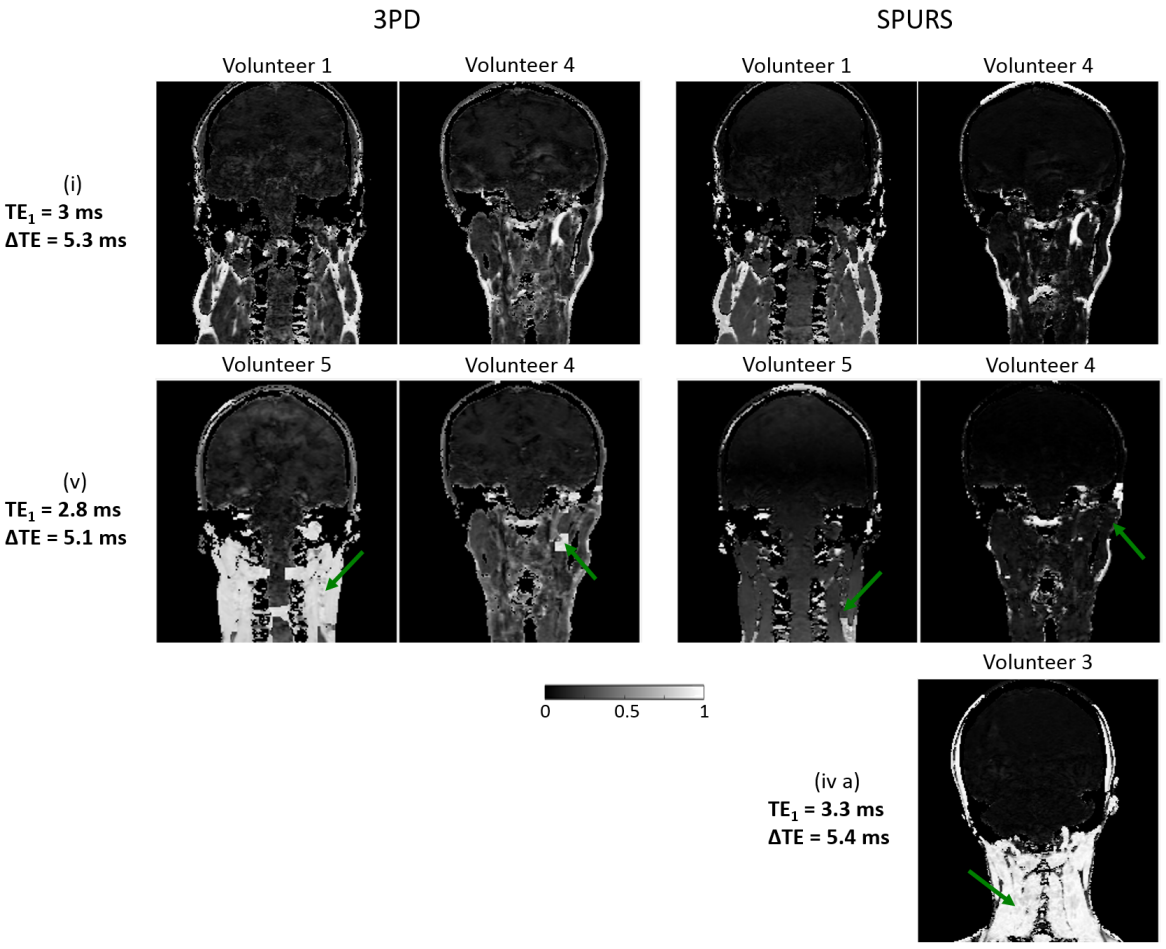

Figure 6.11: Fat-fraction maps calculated in similar coronal slices in four different healthy volunteers using 3PD and SPURS. The echo-timings are shown next to the images. The arrows indicate swapping artifacts.

6.1.4 Conclusions

Most of the available fat-water separation techniques do not identify fatty and water-based tissues accurately in the head and neck. The few strategies that provide reliable fat fraction maps, i.e. 3PD, SPURS, and in-phase acquisitions, predict similar susceptibilities in fatty ROIs, confirming their reliability. Furthermore, using fat correction results in echo-time-independent susceptibility contrast. Moreover, the resulting susceptibility maps indicate increased susceptibility in fatty tissue relative to water-based tissue which is in line with previous literature.

However, both post-acquisition techniques I tested here that had promising results in one healthy volunteer (3PD and SPURS) failed in images acquired with slightly different echo-timing or in different volunteers. This manifests as swapping artifacts due to the

failure of the region-growing steps in both techniques to accurately identify fatty and water-based voxels. Therefore, these techniques are not robust to the echo-timing or across subjects and, therefore, cannot be expected to perform well in a multi-centre study.

On the other hand, in-phase acquisitions provided susceptibility maps with reasonable quality, similar to the post-acquisition techniques based on the multi-peak model. It is also a built-in option on most clinical scanners and does not rely on a region-growing algorithm that is likely to introduce water-fat swaps into the images.

In conclusion, I propose in-phase imaging to be used as a fat correction strategy for accurate QSM in the head and neck. 3PD and SPURS may provide a feasible alternative for pre-existing data that were not acquired with in-phase echoes (chapter 8).

6.2 Optimising the MRI acquisition for susceptibility mapping in the head and neck

6.2.1 Introduction

For clinical applicability, accurate susceptibility maps are necessary with good contrast between anatomical structures to provide reliable estimation of oxygenation levels (section 1.1). In chapter 5, I have shown that high resolution and a reasonable coverage extending beyond the structures of interest is necessary to achieve adequate susceptibility contrast. Furthermore, short scan time is required to increase patient comfort and throughput, and reduce motion artifacts. In clinical practice, diagnostic MRI sequences are often part of a bigger protocol. Therefore, individual sequences have to be less than about 5 minutes long to be clinically feasible. These parameters (resolution, coverage, scan time, SNR, and contrast) are interdependent and improving one of them may constrain another. For example, in theory, higher resolution provides finer details and better susceptibility contrast, but it also leads to lower SNR and/or increased scan time.

There are other features of the data acquisition that specifically affect the phase contrast like (i) chemical shift effects, and (ii) flow artifacts (section 1.3.2). In section 6.1, I compared a range of state-of-the-art strategies for overcoming (i), of which in-phase imaging was found to be the most accurate and robust technique. The effects of a vendor-supplied flow compensation still need to be investigated.

Here, I assess and compare different acquisition features (e.g. image orientation, field-of-view, resolution, SENSE acceleration, and flow compensation) in the context of susceptibility mapping in the head and neck to determine the optimal acquisition sequence and parameters for QSM in the head and neck. A summary chart of the optimisation process and the main conclusions can be found in section 6.2.4.

6.2.2 Methods

To optimise the gradient-echo sequence (section 1.2.2) for clinically applicable susceptibility maps of the head and neck, I considered and compared different acquisition features. In some cases, I also acquired complex MR images of the head and neck in healthy volunteers using a range of sequence parameters followed by QSM for a direct comparison of the resulting susceptibility maps. These were calculated using the optimised pipeline

from section 6.4: non-linear field fitting (section 2.2.1.3), Laplacian phase unwrapping (section 2.2.2.2), Projection onto Dipole Fields (section 2.3.4.1), and iterative fitting in the image domain using Tikhonov regularisation with $\alpha = 0.04$ (section 2.4.2.2).

6.2.2.1 3D or 2D acquisition

In section 1.2.2.1, I compared the properties of 2D and 3D gradient-echo (GRE) acquisitions in theory. My simple calculations predicted similar total scan time for a multislice 2D acquisition and a 3D sequence, but higher SNR for the 3D sequence (section 1.2.2.2). The SNR and scan time estimates of the Philips Achieva 3 T system [181] for a 2D and 3D GRE brain scan with similar parameters (Figure 6.12) confirm these estimates.

	a) 3D GRE	b) 2D GRE
Matrix size	240×240×144	240×240×144
SENSE factor	2	2
Resolution	1 mm isotropic	1 mm isotropic
TE_1	3 ms	4.9 ms
ΔTE	5.4 ms	5.3 ms
Number of echoes	5	5
TR	28 ms	4549 ms
Flip angle	20°	90°
Total scan time	6 mins 10 secs	6 mins 54 secs
Relative SNR	1.168	0.604

Figure 6.12: Comparison of the 3D or 2D gradient echo acquisitions in terms of total scan time and SNR estimated by the Philips Achieva 3T system for a brain scan.

Due to subject motion, the susceptibility maps calculated from phase images acquired with 2D gradient-echo are corrupted by stripes in the through slice dimension (section 1.2.2.1). Though there exists a combined phase unwrapping and background field removal technique that can reduce striping in the susceptibility maps (section 2.3.2.4), the resulting local field maps often contain residual stripes. Moreover, using 2D acquisitions would require us to use methods which can reduce striping, thus limiting the range of potential QSM pipelines we could apply to the head-and-neck images. As a result, 3D imaging is rapidly becoming the sequence of choice for QSM. It is also much more SNR efficient (Equation 1.14 and Figure 6.12). Therefore, I decided to use 3D acquisitions for all the subsequent comparisons.

6.2.2.2 Image orientation and field-of-view (FOV)

Extended FOV in all phase encoding directions is necessary to avoid aliasing (section 1.2.2.1). In case of a 3D acquisition of the head and neck, both phase encoding directions (i.e. phase and slice encoding) need to be perpendicular to the head-foot (HF) direction where it is possible to increase the FOV beyond the size of the body and still avoid wrap-around artifacts. Therefore, in our optimised sequence, HF was selected as the readout or frequency encoding direction. This left us with two possible image orientations: sagittal (phase encoding = AP, slice encoding = RL) and coronal (phase encoding = RL, slice encoding = AP).

Motion along the phase encoding (or first phase encoding) direction can lead to severe inaccuracies in the phase manifesting in substantial artifacts in the susceptibility maps especially if SENSE acceleration is also used in the same direction. Here, I demonstrate this by visually comparing susceptibility maps calculated from retrospective data: images acquired using either sagittal or coronal orientations and a range of different SENSE acceleration factors. Two healthy volunteers (27 and 24 years, male and female respectively) were scanned with **coronal orientation** using: FOV = 24×24×22 cm^3 (FH-AP-RL), SENSE factors ranging from 1 to 2 in both phase and slice encoding directions, isotropic resolutions = 1 - 1.5 mm^3, TE_1 = 2.7 - 4.61 ms (in-phase imaging included), ΔTE = 4.61 - 6.8 ms (in-phase imaging included), 4 - 7 echoes, TR = 22 - 35 ms, flip angle = 11° - 13°. Another two healthy volunteers (both 29 years, both male) were scanned with **sagittal orientation** on the same scanner using similar parameters except: TE_1 = 3 - 4.92 ms (in-phase imaging included), ΔTE = 4.61 - 5.3 ms (in-phase imaging included), 4 echoes in all cases, TR = 21 - 23 ms, flip angle = 12° - 18°. Susceptibility maps were calculated in each case using the pipeline described above. Sagittal orientation led to strong motion artifacts in the susceptibility maps (section 6.2.3.1). Therefore, coronal orientation was used for all subsequent scans. The frequency encoding direction was kept strictly parallel to the main magnetic field, B_0, to avoid additional artifacts originating from the tilting or from correction for the tilting [182].

The large head-foot FOVs (24 cm) described above reflect my decision to include the entire head-and-neck region in my acquired images. This study focuses on head-and-neck cancer, so it is not crucial to collect data in the brain. However, since in our optimised sequence, frequency encoding is performed in the HF direction, excluding the brain would only marginally reduce the total scan time (section 1.2.2.1). Moreover, including the brain helped me appreciate the quality of the resulting images, since many studies use susceptibility mapping in the brain. Finally, including the brain in QSM provides a lot of

different regions that could potentially be used as reference tissues in a large-scale study. Therefore, all images were acquired covering the entire head and neck including the brain.

6.2.2.3 Resolution, SENSE acceleration, and number of echoes

In chapter 5, I showed that using small, isotropic voxels is very important for accurate susceptibility mapping. However, high resolution leads to increased scan time and reduced SNR. A scan time of about 5 minutes is the upper limit for a clinically applicable sequence. However, it can take several years to translate a new technique into clinical practice. During this time, new acceleration techniques are expected to appear as well as better hardware and reconstruction methods. Therefore, at an early stage, this criterion does not need to be very strict. Here I kept the total scan time of all potential sequences below around 6 minutes.

Scan time could be reduced for high-resolution images by acquiring fewer echoes. However, for accurate field fitting, a reasonable number of echoes are needed, especially at high resolution where the SNR is low. A strict minimum of three echoes is required to perform the non-linear fitting which is the first step of our QSM pipeline. For further acceleration, sensitivity encoding (SENSE, section 1.2.2.3) can be applied in both phase encoding directions (since I decided to use a 3D acquisition).

Here I compared a range of different resolutions (between 1.1 and 1.4 mm isotropic), and SENSE acceleration factors (1.5 or 2 in the first, and 1 or 1.5 in the second phase encoding direction to avoid wrap-around effects described in section 6.2.3.1). Acquiring images even at the lowest resolution (1.4 mm isotropic) required SENSE acceleration in at least one phase encoding direction to acquire four echoes in around 6 minutes. Increasing the number of echoes would necessitate a much lower resolution and/or unrealistically high SENSE factors to maintain a short scan time. Therefore, the number of echoes was fixed at four for all potential sequences. Some clinical protocols only allow for an even shorter total scan time than 5 minutes [183] in which case using only three echoes could be considered.

To compare these factors in terms of QSM, complex MR images were acquired in the head and neck of a healthy volunteer (24 years, female) using: FOV = 24×24×22 cm^3 (FH-AP-RL), coronal orientation, SENSE factors ranging from 1 to 2, isotropic resolutions = 1.1 - 1.4 mm^3, $TE_1 = \Delta TE = 4.61$ ms (for in-phase imaging), 4 echoes, $bw = 290$ Hz/pixel, TR = 22 ms, flip angle = 12°. The resolutions and SENSE factors for the individual scans are shown in Figure 6.13.

Resolution (isotropic)	SENSE factors (RL / AP)	Total scan time (min:sec)
1.1 mm	2 / 1.5	5:37
1.25 mm	2 / 1	6:04
1.25 mm	1.5 / 1.5	5:57
1.4 mm	1.5 / 1	6:13

Figure 6.13: Parameters of all four acquisitions used for optimisation of the image resolution and the SENSE acceleration factors.

Susceptibility maps were calculated in each case using the aforementioned QSM pipeline. Three healthy lymph nodes of sizes about 250 mm^3 (Node 1, Figure 6.14 orange), 300 mm^3 (Node 2, Figure 6.14 green), and 150 mm^3 (Node 3, Figure 6.14 pink) were manually delineated on all last-echo magnitude images using ITK-SNAP [184,185]. These were selected based on their visibility in the 1.1 mm isotropic image which was the most noisy one and contained a lot more motion artifacts than the other three. The red nucleus (RN, Figure 6.14 red) and substantia nigra (SN, Figure 6.14 blue) were also manually delineated in ITK-SNAP. This segmentation was performed on the susceptibility maps as these structures were not visible in the magnitude images of the highest resolution (1.1 mm isotropic). The four different sequences were compared based on visual assessment, and by calculating mean susceptibilities in all the manually segmented regions. The difficulty of identifying and segmenting the lymph nodes was also noted in each case. Signal-to-noise ratios were also calculated in all first-echo magnitude images by selecting five rectangular regions in the white matter in a sagittal slice similarly to section 3.2.

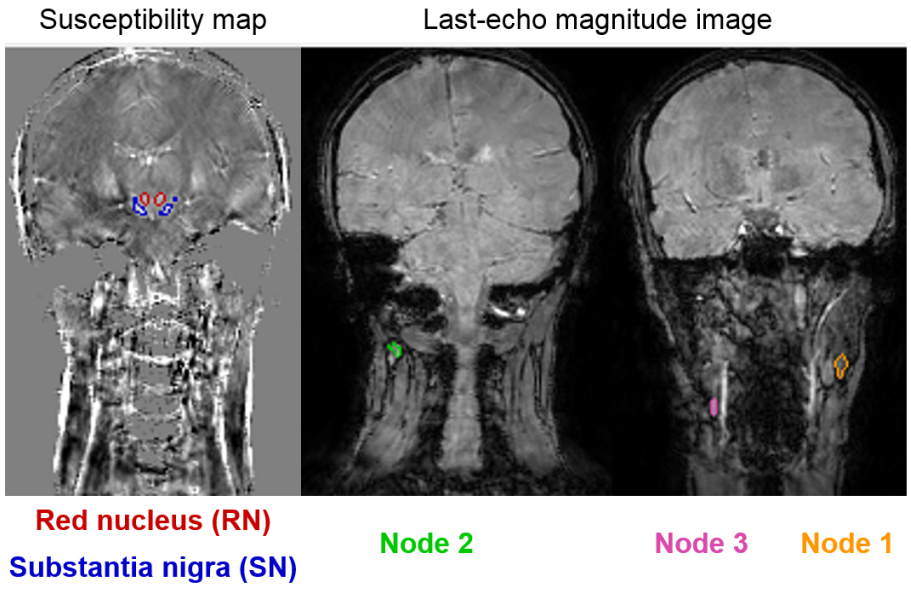

Figure 6.14: Manually segmented regions of interest (ROIs) in the images acquired with resolution = 1.25 mm isotropic and SENSE factors = 1.5 in both phase and slice encoding directions.

6.2.2.4 Flow compensation

In section 6.2.3.2, I selected the two sequences with 1.25 mm isotropic resolutions (Figure 6.13) as potential candidates for the optimised acquisition. Based on the data acquired for the previous section, a definitive choice could not be made between these two sequences with different SENSE acceleration factors. Therefore, here I acquired data with and without flow compensation using both sequences in another healthy volunteer (27 years, female). Note that all other parameters remained the same after switching on flow compensation.

The built-in flow compensation feature of the Philips Achieva scanner is designed to perform flow compensation on the first echo in the readout or frequency encoding direction (in which flowing particles induce the largest phase accumulation). To investigate how this affects the remaining three echoes, I observed the gradients to be applied (Figure 6.15) in the Philips Pulse Programming Environment (PPE), extracted the exact gradient pulse shapes and amplitudes, and calculated their integrals and first moments in MATLAB. I repeated the process with the built-in flow compensation on. Note that the gradient pulse shapes and amplitudes do not depend on the SENSE acceleration factors.

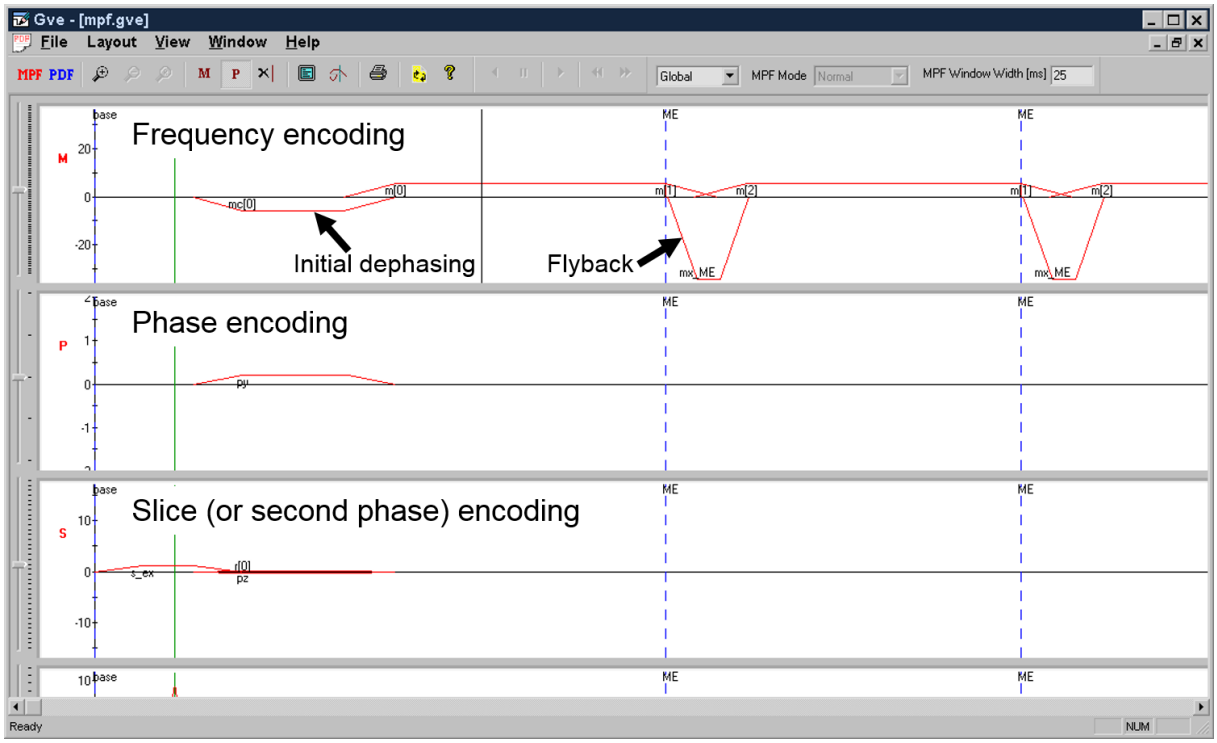

Figure 6.15: Gradients applied in the frequency, phase, and slice encoding directions according to the Philips Pulse Programming Environment.

Susceptibility maps were calculated in all four cases (with SENSE factors either 2×1 or 1.5×1.5, and with or without flow compensation) using the susceptibility mapping pipeline outlined in section 6.2.2. This time, the high SNR and the reduced motion artifacts enabled me to apply FSL FIRST [186] to all first-echo magnitude images for automatic segmentation of the caudate nucleus, putamen, globus pallidus, and thalamus. Additionally, the red nucleus and substantia nigra along with five different healthy lymph nodes (sizes: about 120, 930, 220, 250, and 190 mm^3) were also manually delineated on the last-echo magnitude images using ITK-SNAP [184, 185]. The four sequences were compared by visual examination, and by calculating mean susceptibilities in all aforementioned regions of interest (ROIs). Signal-to-noise ratios were also calculated in all first-echo magnitude images by selecting five, 20 pixels-by-20 pixels rectangular regions in the white matter in a sagittal slice similarly to section 3.2.

6.2.3 Results and Discussion

6.2.3.1 Image orientation

I acquired a total of 19 different images in the four healthy volunteers using the sequences described in section 6.2.2.2. Visual assessment of the magnitude and phase images, as well as the local field and susceptibility maps led to two main observations demonstrated here.

First of all, sagittal acquisitions were corrupted by strong artifacts extending into the brain. In Figure 6.16, the yellow double arrows indicate the (first) phase encoding directions in both sagittal and coronal images. Severe motion artifacts are present in the sagittal images behind the eye (red arrows) that are not present in the susceptibility maps calculated from the coronal orientation phase maps. These artifacts extend well into the brain leading to artifacts on both sides of the red nucleus and substantia nigra (red arrows). This is probably caused by motion-induced ghosting along the first phase encoding direction induced by eye motion. Note that though in Figure 6.16 images from only two volunteers are shown with SENSE factors = 1.5 in both directions, these artifacts were present in all sagittal images and were absent from all coronal images regardless of the resolution, volunteer, or SENSE factors. For example, Figure 6.17 shows two different acquisitions and again, the arifact was only present in the sagittal one (black arrow). The artifact was also present in sagittal images acquired without any SENSE acceleration (not shown).

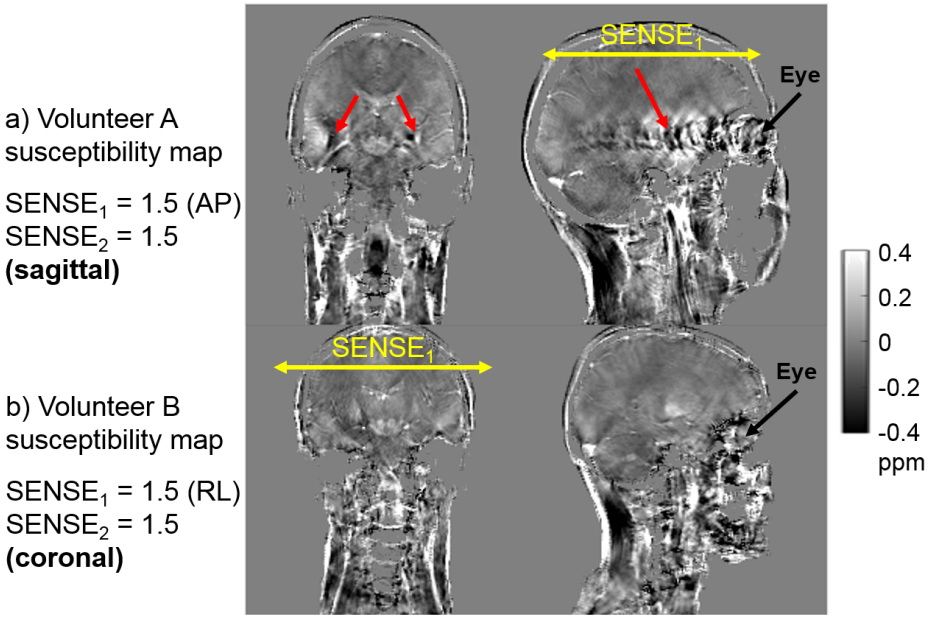

Figure 6.16: Artifact induced by eye motion in sagittal acquisitions.

The other conclusion is that a SENSE factor of 2 in the second phase encoding (or slice encoding) direction resulted in unusual artifacts in the phase images regardless of the orientation. In Figure 6.17, data from two volunteers are shown. The yellow double arrows indicate the direction of the slice encoding gradient (where SENSE = 2). Figure 6.17 c shows that the SENSE combined (section 1.2.2.3) phase map is not consistent on the two sides of the artifact (red arrow). This was probably caused by incorrect coil combination due to the large SENSE acceleration. The artifact was more prominent in the susceptibility maps of the sagittal orientation acquisitions since it affected more of the tissue in this case. This also confirms that a coronal orientation should be preferred. For this optimisation, I restricted the SENSE factor of the second phase encoding direction to 1.5 at most to avoid all artifacts induced by incorrect coil combination. However, for a coronal acquisition, using higher SENSE factors could be considered in cases of very limited scan time as the SENSE factor did not have a huge affect on the susceptibility maps in the brain and the neck. Again, note that this artifact was present in all images with $\text{SENSE}_2 = 2$ (along the slice encoding direction) and was absent from those acquired with $\text{SENSE}_2 < 2$ in the slice encoding direction regardless of the SENSE factor in the first phase encoding direction, orientation, resolution, or volunteer.

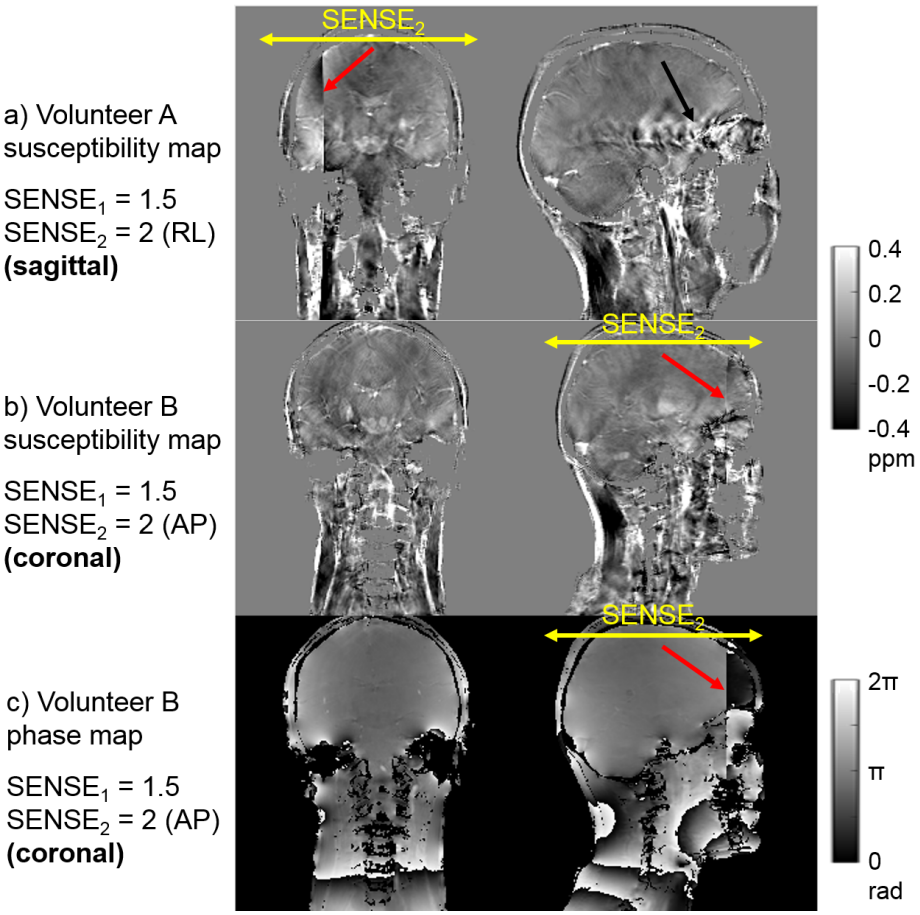

Figure 6.17: Artifact induced by a SENSE factor of 2 in the second phase encoding (or slice encoding) direction.

6.2.3.2 Resolution and SENSE acceleration factors

Figure 6.18 shows example coronal slices of the susceptibility maps for the different acquisition parameters described in section 6.2.2.3. The first thing to note is that the highest resolution images (first column) are corrupted by severe ghosting artifacts. This is probably caused by the interactions between subject motion and the large SENSE acceleration factors in both phase encoding directions. In addition, these images are expected to have much lower SNR due to the smaller voxel size. This is not reflected in the measured first-echo magnitude SNR (Figure 6.18, magnitude SNR values), but was noted during the manual segmentation on the last-echo magnitude images. The high noise level made the identification and delineation of the lymph nodes very difficult. To sum up, the high resolution (1.1 mm isotropic) images have lower SNR (visually) and are more sensitive to subject motion, therefore not suitable for large-scale head-and-neck studies.

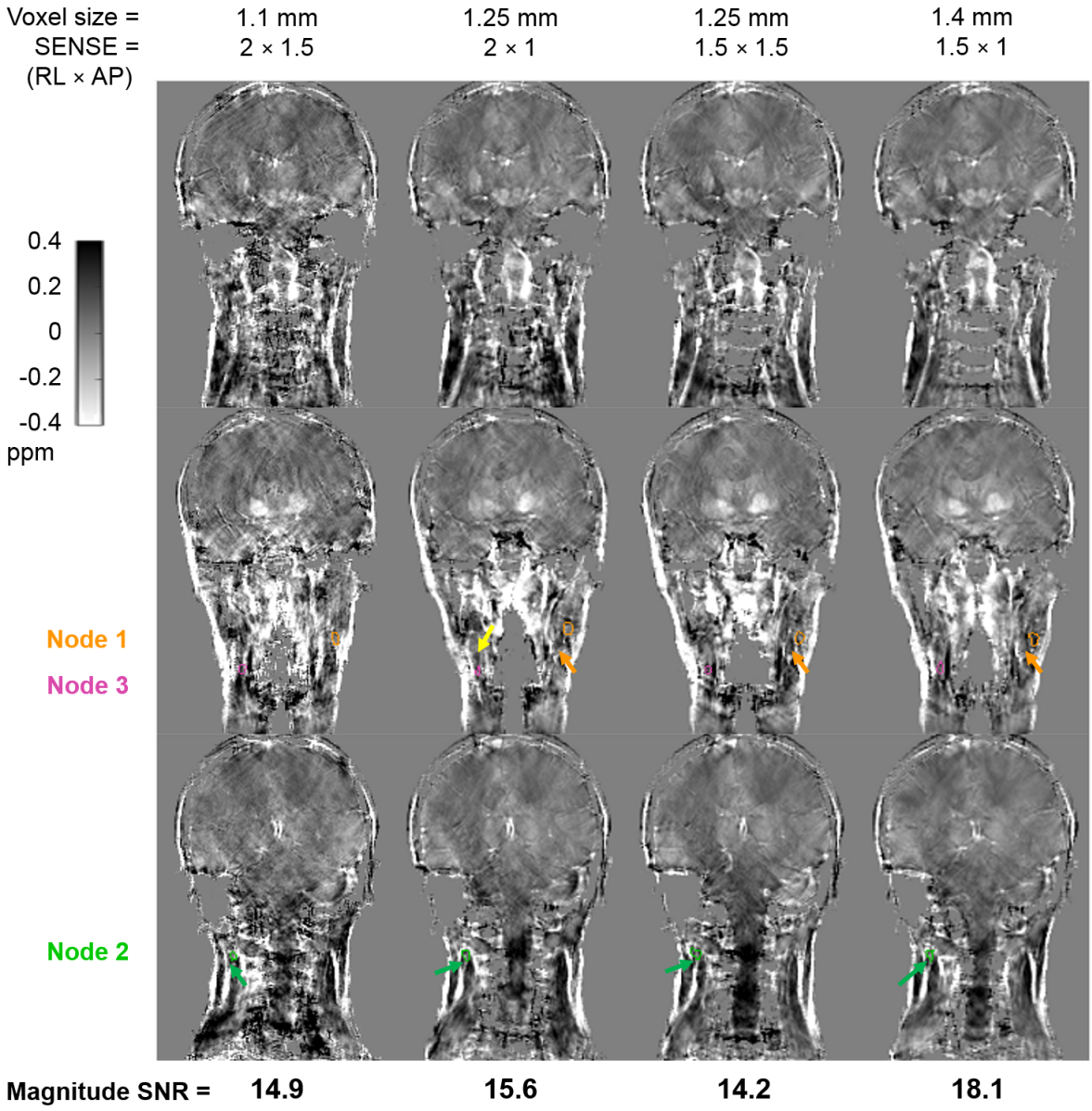

Figure 6.18: Optimising the resolution and the SENSE factors. Example coronal slices of the calculated susceptibility maps for the four different acquisition protocols (columns) used in the same volunteer are shown. The contours of the manually segmented healthy lymph nodes are shown in orange, green, and pink. The arrows indicate additional features of the susceptibility maps. The measured magnitude SNRs are displayed below the images.

The contours of the lymph nodes are also shown in Figure 6.18. Node 1 (orange) was visible in all susceptibility maps especially in the second column. It is interesting to note that an even larger node next to Node 1 was clearly visible in all susceptibility maps (orange arrows) expect the highest-resolution one (1.1 mm isotropic). It was not included in the analysis as it was not identifiable in the last-echo magnitude image of the highest-resolution data. Node 2 (green) is also easy to see in all susceptibility maps due to

the surrounding bright fatty tissue. Moreover, another node is again visible next to this one in all maps (green arrows) including the highest-resolution one. Again, this was not included in the analysis for similar reasons (i.e. it was not visible in the highest-resolution magnitude image).

The yellow arrow indicates a well-defined dark region in the susceptibility map in the second column which does not correspond to any visible structures in the magnitude images (not shown), but also does not look like an artifact. The susceptibility map calculated from the SENSE = 2×1 acquisition (second column) contained several apparent structures. In general, this susceptibility map looked crisper and less blurry than the others, therefore it was easier to visually identify similar structures.

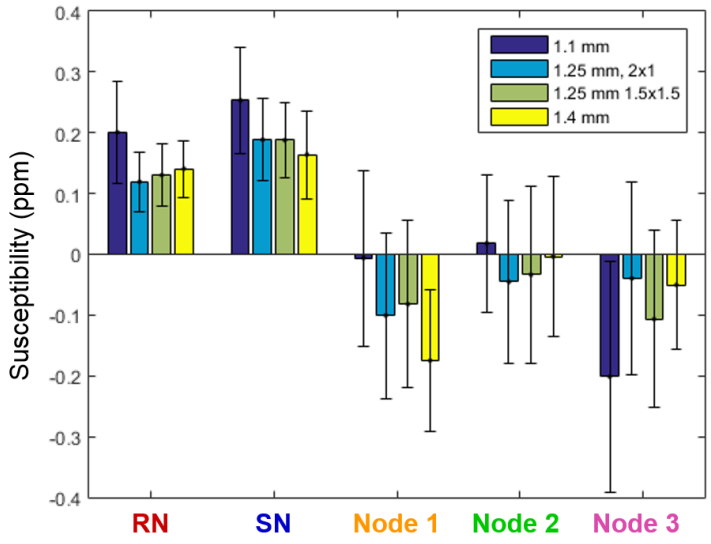

Size of ROIs (voxels)

	RN	SN	Node 1	Node 2	Node 3
	158	653	142	153	90
	219	440	139	158	73
	244	409	156	138	72
	167	388	82	133	54

Figure 6.19: Mean susceptibilities measured in the five manually segmented ROIs in the susceptibility maps corresponding to the four different acquisitions. The plot has error bars equal to the standard deviation of susceptibilities in each ROI. The sizes of the ROIs are also displayed in voxel units.

Figure 6.19 shows the measured mean susceptibilities in each manually segmented ROI. The sizes of the ROIs are also displayed in voxel units. Susceptibilities measured in the two brain regions (RN and SN) are very consistent across the three lower-resolution acquisitions. The higher measured susceptibilities in the highest-resolution image (1.1 mm, dark blue bars) could be partially due to the increased contrast of higher-resolution

susceptibility maps demonstrated in chapter 5. It could also be a result of performing the manual segmentation directly on the susceptibility maps. Only high-susceptibility voxels were selected and their noisy surroundings were mostly excluded. This is also reflected in the fact that, surprisingly, the RN region segmented in the highest-resolution image contains fewer voxels than the RN regions delineated in the rest of the images. RN and SN were delineated more consistently in the other three cases as these looked substantially less noisy.

The mean susceptibilities measured in the highest-resolution image (1.1 mm, dark blue bars) were also significantly different from the rest in the three healthy lymph nodes because the segmentation was difficult to perform on the very noisy last-echo magnitude image. Again, the values were somewhat consistent across the other three acquisitions. Node 3 is a particularly small node close to one of the main vessels in the neck (Figure 6.14, pink) and, therefore, suffered from flow artifacts. As a result, it is not surprising that even the two acquisitions of the same resolution (1.25 mm) provided slightly different measured susceptibilities (Node 3, light blue and green bars). It is important to note, however, that the measured values are very close for these two sequences in all other ROIs (light blue and green bars).

The lowest-resolution (1.4 mm isotropic) magnitude images were expected to have the highest SNR. However, due to the increased voxel size, these images were more sensitive to partial volume effects which made the segmentation process more complicated. Also, the selected lymph nodes were generally not spherical. They were larger in one or two dimensions and very thin in at least one direction. In some cases, a node could be identified in only three slices of the magnitude image at the lowest resolution which was shown to reduce susceptibility contrast and accuracy (chapter 5). Moreover, upon further inspection, Node 1 was not properly identified in the lowest-resolution image because it was less visible due to the partial volume effect. Instead, another node close to Node 1 was segmented that apparently had a lower mean susceptibility. This is also visible in Figure 6.18 where the node surrounded by the orange contours is much darker in the last column. To sum up, partial volume effects can have a significant influence on the susceptibility values measured in small structures such as healthy lymph nodes. In the acquisitions of 1.25 mm isotropic resolution, the advantage of the reduced partial voluming in comparison to the lowest-resolution (1.4 mm) case outweighs the drawback of a slightly lower SNR.

At this point, it would be hard to determine if asymmetric (2×1) or symmetric (1.5×1.5) SENSE acceleration provides more accurate susceptibility maps. Here I make a few observations based on detailed visual inspection. In general, the susceptibility map

obtained using symmetric SENSE acceleration looks a bit more blurry in the anterior-posterior direction than the one obtained with asymmetric SENSE factors. For example, the two lymph nodes in the yellow circles in Figure 6.20 are separated nicely in the susceptibility map on the left as opposed to the one on the right which looks more blurry. Note that the corresponding magnitude images are very similar. This could be explained by the fact that the asymmetric image was acquired with a lower SENSE factor in the AP direction.

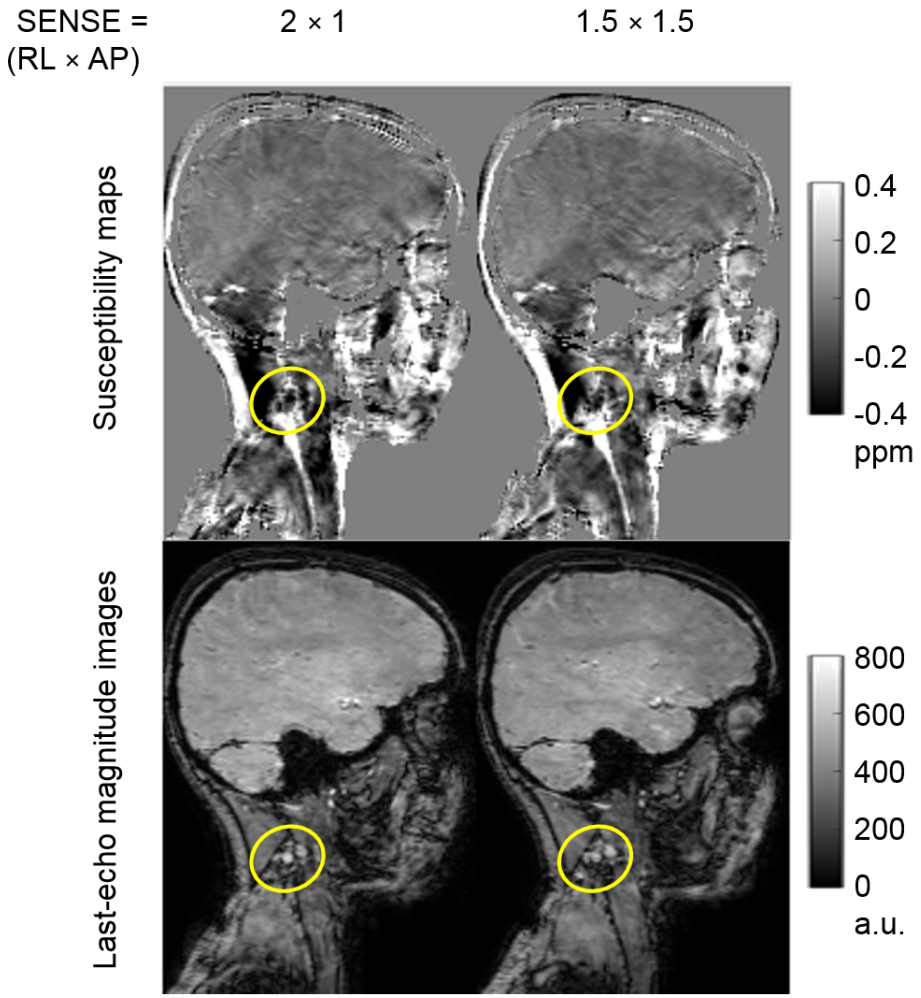

Figure 6.20: Sagittal slices of the last-echo magnitude images and corresponding susceptibility maps of the two acquisitions with 1.25 mm isotropic resolution and different SENSE acceleration factors.

There is no such difference between the two susceptibility maps in the right-left direction. On the contrary, in Figure 6.21, the structure indicated by the arrow seems a bit more separated from the node on its right in the susceptibility map obtained using asymmetric SENSE acceleration, even though this map was acquired with a higher SENSE factor in the RL direction. However, it must be noted that, in this case, the magnitude images are also slightly different. Given the arrangement of the individual coils within

the 16-channel head-and-neck coil (i.e. there are more coil elements in the RL direction, Figure 6.1), it is likely that the SENSE reconstruction is more robust to high SENSE factors in the RL than in the AP direction.

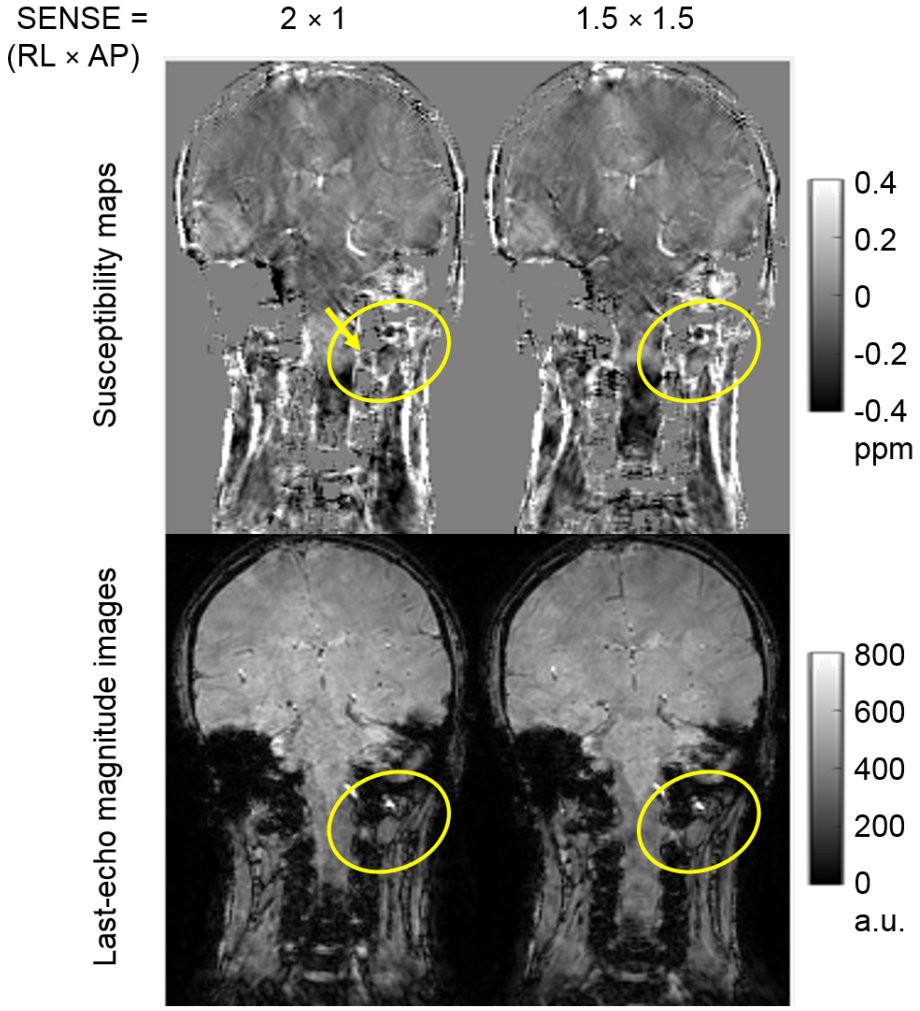

Figure 6.21: Coronal slices of the last-echo magnitude images and corresponding susceptibility maps of the two acquisitions with 1.25 mm isotropic resolution and different SENSE acceleration factors.

Figure 6.22 shows an additional, interesting structure that can only be seen in the susceptibility map obtained using asymmetric SENSE acceleration. Small, tightly-packed circular structures can be seen in the yellow circle in the top left image. This does not appear in any of the other susceptibility maps or any of the magnitude images. Based on the known anatomy of the head and neck, these regions could be part of the internal structure of the parotid gland, possibly lymph nodes within the gland. Figure 6.22 shows the potential of susceptibility mapping to reveal structures not visible in standard gradient-echo magnitude images.

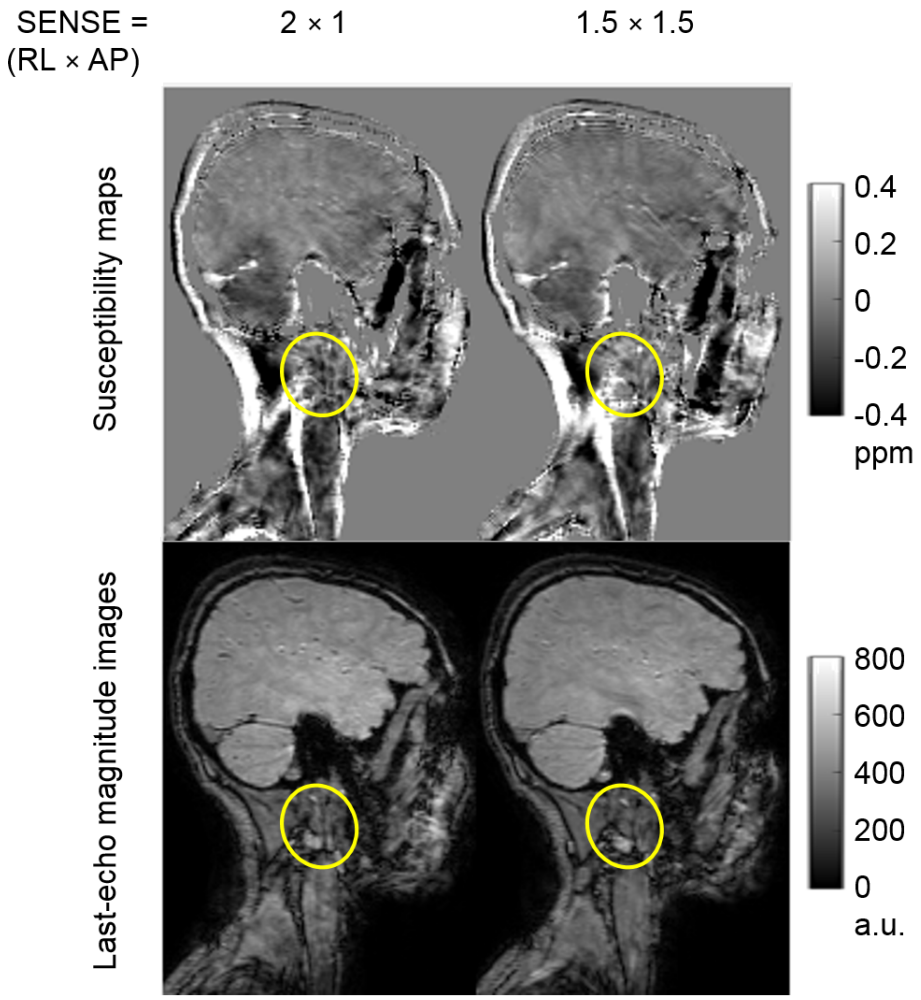

Figure 6.22: Sagittal slices of the last-echo magnitude images and corresponding susceptibility maps of the two acquisitions with 1.25 mm isotropic resolution and different SENSE acceleration factors.

In conclusion, images acquired with 1.1 mm isotropic resolution are too noisy for accurate identification and segmentation of lymph nodes. These also require very high SENSE acceleration factors in both phase encoding directions (to restrict the total scan time to a clinically feasible 6 minutes) which leads to severe ghosting when there is subject motion. Images obtained at a 1.4 mm isotropic resolution have high SNR, but in this case, the small structures of interest (such as lymph nodes) are affected by partial volume effects which makes it difficult to identify and segment them. Susceptibility maps calculated from the 1.25 mm isotropic acquisitions seem promising and very similar. Though using asymmetric SENSE acceleration appears to provide superior susceptibility map quality, the effect of flow compensation was investigated in the following section using both sequences.

6.2.3.3 Flow compensation

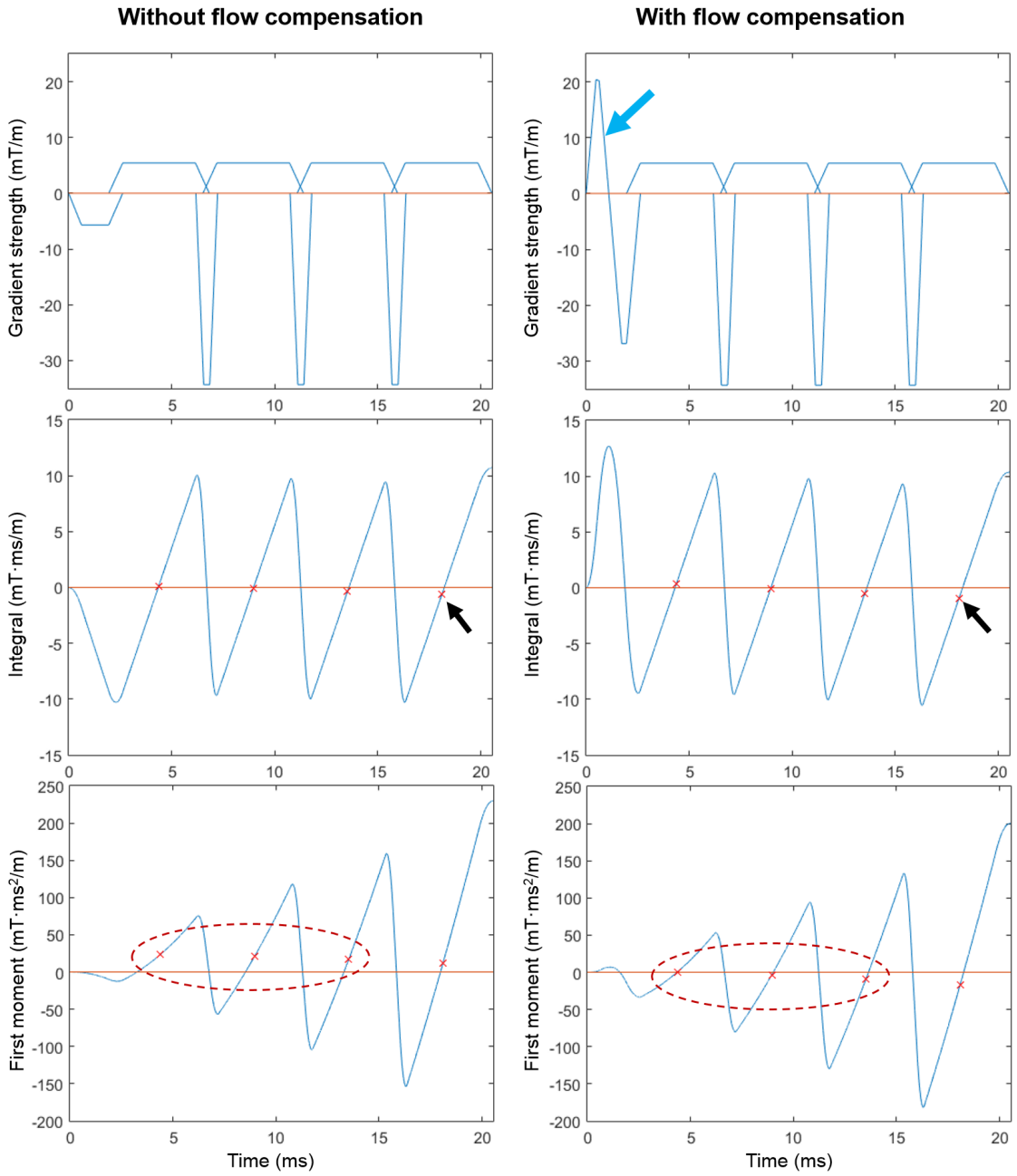

Figure 6.23: Comparison of the gradients (top row), their integrals (middle row) and the first moments (bottom row) with (right column) and without (left column) flow compensation on the first echo. The red crosses indicate the echo times. The red dashed ellipses indicate improved first-order gradient moment nulling at the first three echoes when using the manufacturer-provided flow compensation feature.

Figure 6.23 shows the difference between the gradients in the frequency encoding (or readout) direction with (right column) and without (left column) flow compensation on the first echo. The blue arrow in the top right plot indicates how the initial dephasing gradient is modified to achieve flow compensation at the first echo. The echo times are

indicated by the red crosses in the middle and bottom rows. The integrals (middle row) are very close to zero both with and without flow compensation (as expected for correct echo formation, section 1.3.2), though the gradient integral is a bit further from zero at the last echo when flow compensation is on (black arrows). Using flow compensation moved the first moments (bottom row) noticeably closer to zero as expected, especially at the first three echoes (red dashed ellipses). Since using the built-in, vendor-supplied flow compensation feature does not increase scan time, based on the gradient shapes and first moments, it would be beneficial to switch it on for our optimised protocol.

Figure 6.24 shows example susceptibility maps with and without flow compensation corresponding to the four different sequences (from section 6.2.2.4) used in the same volunteer. All four susceptibility maps look very similar and the corresponding magnitude SNRs are also in good agreement. The contours of the brain ROIs are also shown. The quality of the automatic segmentation (bottom row) is acceptable, though in some cases, the delineated regions look smaller than the actual anatomical region (e.g. globus pallidus, red arrows). It is worth noting that FSL FIRST was designed for T_1-weighted images with good contrast between white matter, gray matter, and the cerebrospinal fluid. Since our gradient-echo magnitude images have much lower contrast, it is possible that the regions were determined based on a fitted template and the general shape of the brain rather than the actual contrast within the brain. In any case, this method seems consistent across the four sequences. Whether FSL FIRST can be used in a large-scale repeatability study across volunteers remains to be investigated.

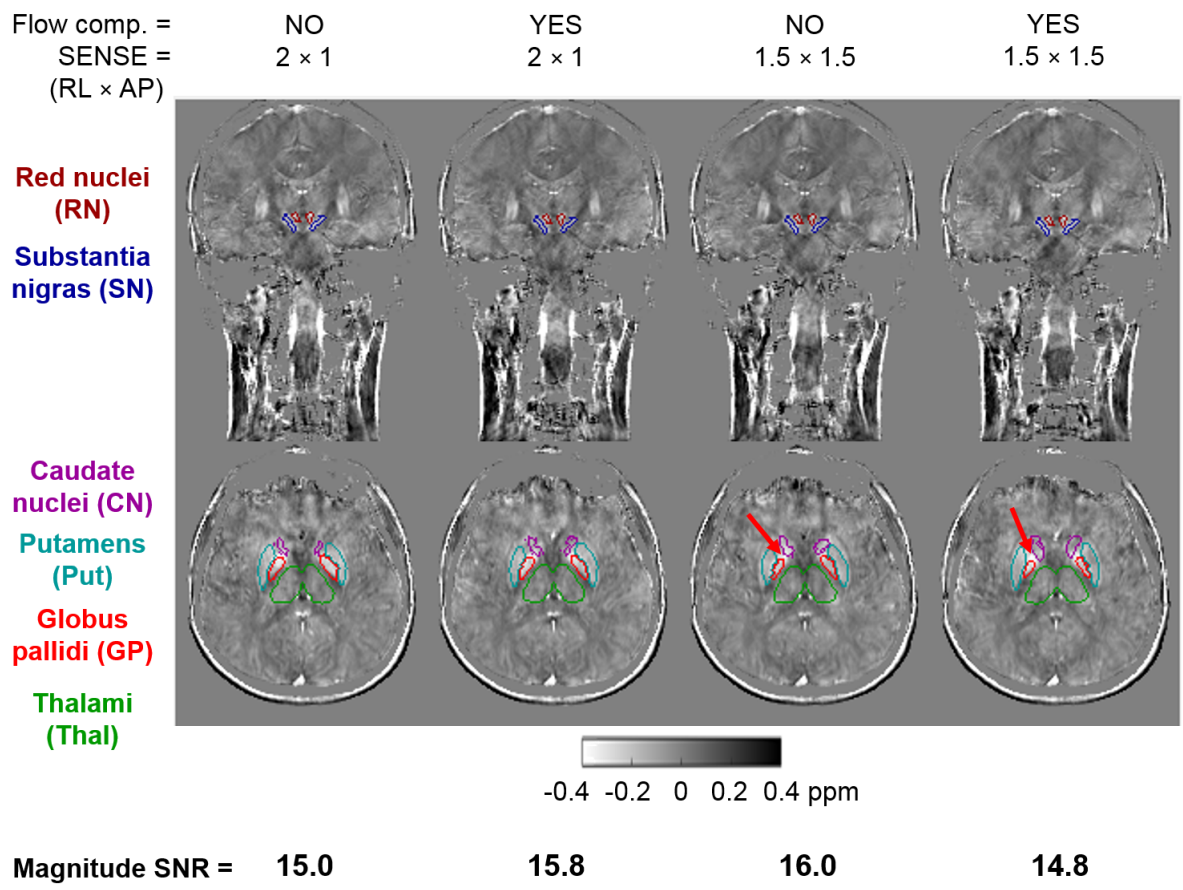

Figure 6.24: The effect of flow compensation and different SENSE acceleration factors on QSM in the head and neck. Example coronal (top row) and axial (bottom row) slices of the calculated susceptibility maps for the four different sequences (columns) used in the same volunteer are shown. The contours of the manually delineated red nucleus and substantia nigra, as well as the automatically segmented caudate nucleus, putamen, globus pallidus, and thalamus are also shown. The measured first-echo magnitude SNRs are displayed below the images.

Figure 6.25 shows example susceptibility maps corresponding to the four different sequences used in the same volunteer along with the contours of the five, manually segmented, healthy lymph nodes. Again, all four susceptibility maps are similar visually. Note that flow compensation did not have a substantial affect on the contrast of the large vessels in the neck such as the internal carotid artery and internal jugular vein (yellow arrows, dark and bright spots respectively). Since these vessels have different deoxyhemoglobin concentrations, the jugular vein is expected to be much brighter than the arteries, which is exactly the case. It is also possible that blood accelerates in these vessels in the neck instead of flowing steadily which could also contribute to the phase difference. This is not negated by the flow compensation as it only nulls the first moment which compensates for spins flowing at a constant velocity only (section 1.3.2).

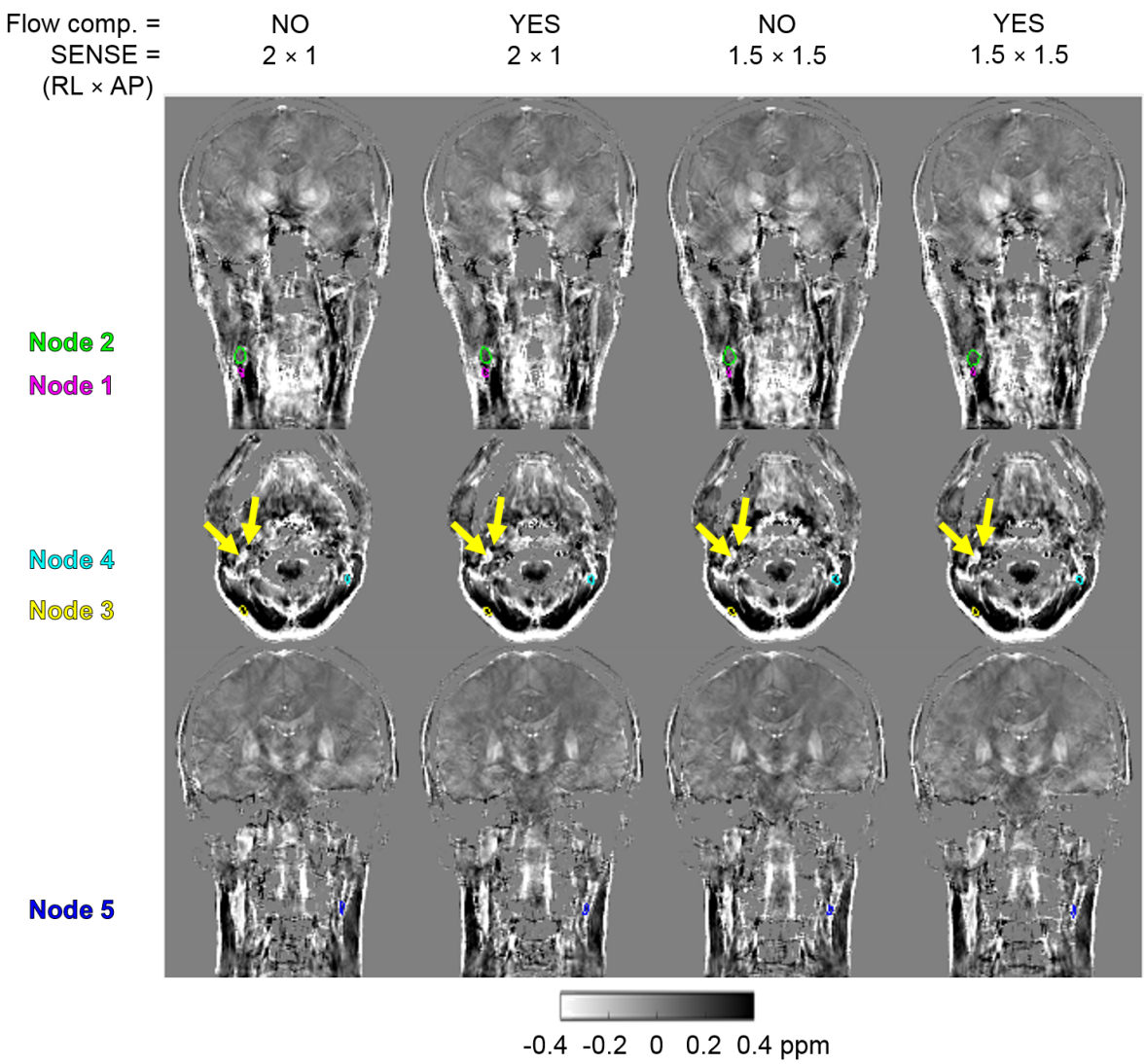

Figure 6.25: The effect of flow compensation and different SENSE acceleration factors on QSM in the head and neck. Example coronal (top and bottom rows) and axial (middle row) slices of the calculated susceptibility maps for the four different sequences (columns) used in the same volunteer are shown. The contours of the manually delineated healthy lymph nodes are also shown. The yellow arrows indicate the large internal carotid arteries (dark) and internal jugular veins (bright).

Figure 6.26 shows the measured mean susceptibilities in each ROI. The sizes of the ROIs are also displayed in voxel units. The mean susceptibilities as well as the standard deviations were very consistent across the four sequences. This shows that there is no substantial difference between the four potential protocols in terms of the measured values. Furthermore, this indicates that susceptibility mapping is repeatable (see also the boxplot in Figure 6.27) in the head and neck even when using different SENSE acceleration and flow compensation. The sizes of the segmented ROIs were also very consistent across the four images.

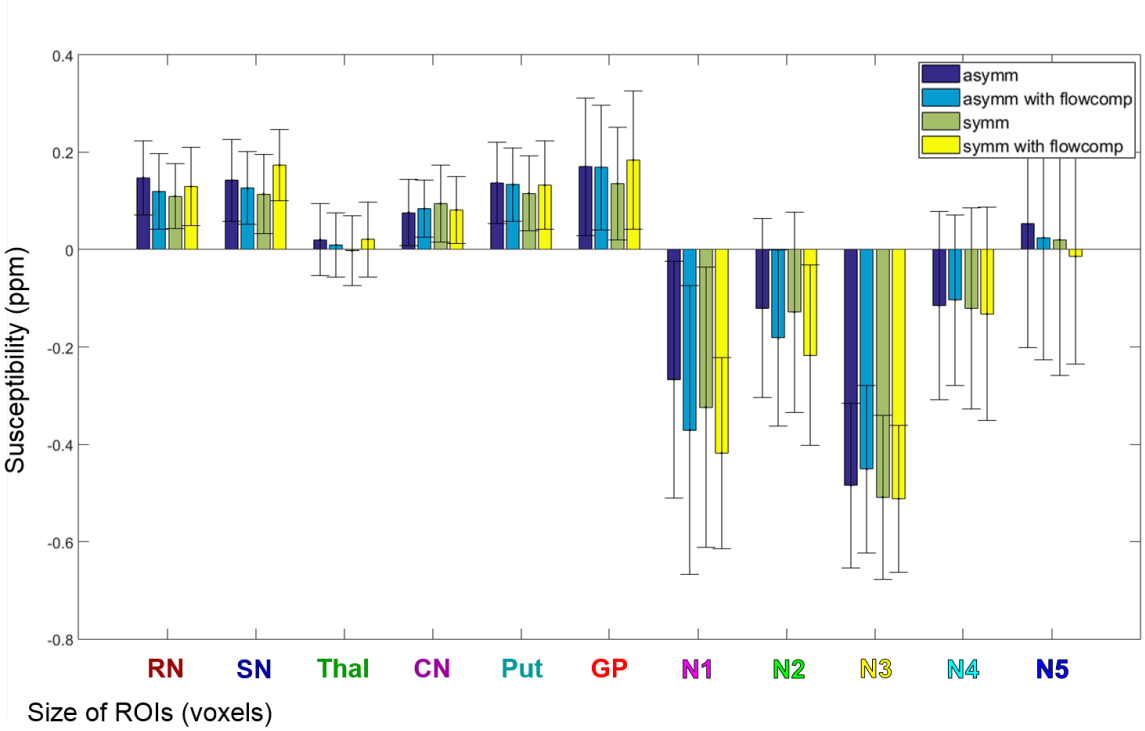

Size of ROIs (voxels)

	266	412	7295	2339	3611	1615	62	461	129	108	105
	273	414	7218	2587	3737	1681	66	493	117	130	118
	271	417	7296	2797	3506	1661	62	519	117	143	117
	273	409	7360	2837	4005	1578	52	450	95	126	73

Figure 6.26: Mean susceptibilities measured in all segmented ROIs in the susceptibility maps corresponding to the four different acquisitions with and without flow compensation and with symmetric and asymmetric SENSE factors. The plot has error bars equal to the standard deviation of susceptibilities within each ROI. The sizes of the ROIs are also displayed in voxel units.

Figure 6.27 shows a boxplot of the measured mean susceptibility values in each region pooled across all four acquisitions. Note that these values are not just highly repeatable in the brain, but the measured values are all within the ranges found in the literature [22, 111, 119, 178, 179]: red nucleus (0.09-0.15 ppm), substantia nigra (0.08-0.19 ppm), caudate nucleus (0.040.11 ppm), putamen (0.040.13 ppm), thalamus (0.020.05 ppm), globus pallidus (0.120.21 ppm). Another interesting thing to note here is that though the measured susceptibilities seem to be repeatable in the healthy lymph nodes, there is a large variation in susceptibility across the lymph nodes. Most of them look diamagnetic. Node 5 is the only one that was measured to be slightly more paramagnetic than water, but this could be because it is a small node surrounded by paramagnetic fat. Though it looks darker than the fatty fascia (Figure 6.25, bottom row, blue contours), slight errors in the segmentation or partial volume effect could have a large influence on the measured result. Node 1 has the highest variation in its measured susceptibility across

the four different sequences presumably due to its very small size. In general, the fact that these lymph nodes have susceptibilities similar to that of muscle could indicate that they are well oxygenated. This provides a basis for the future detection of low oxygenation in cancerous lymph nodes. However, the extent of the changes in nodal susceptibility due to lower oxygen levels is to be investigated in future studies.

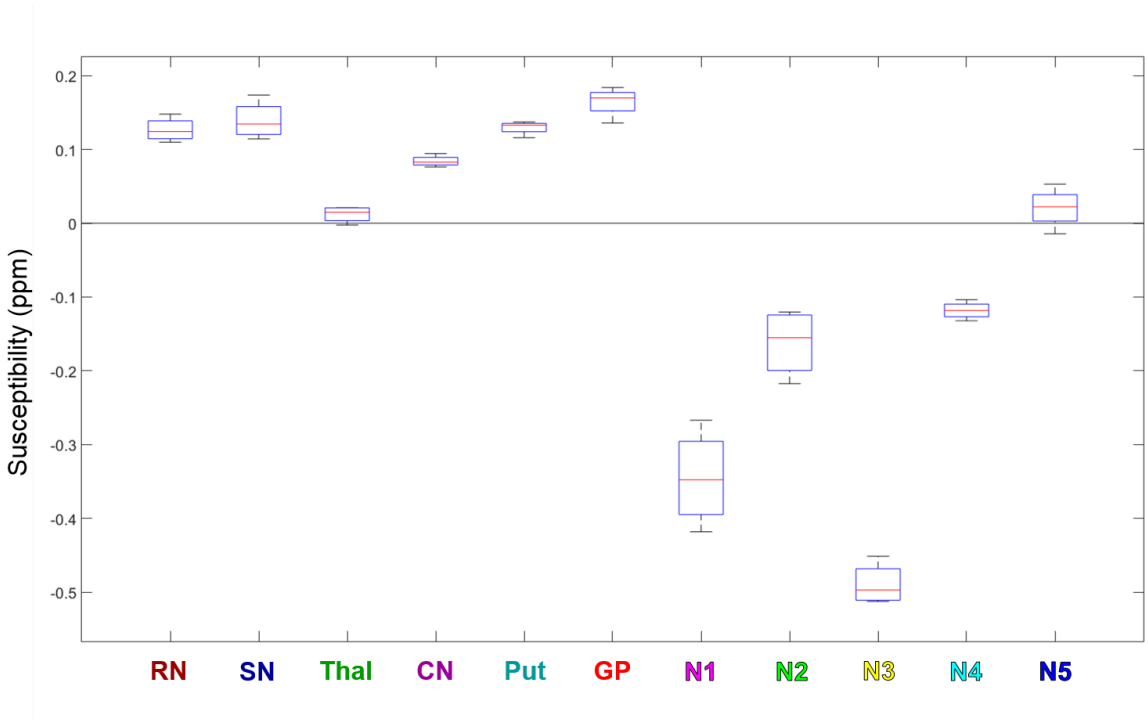

Figure 6.27: Boxplot of the mean susceptibilities measured in each ROI in the susceptibility maps using four different acquisitions.

The differences between images acquired using symmetric and asymmetric SENSE factors were not as apparent here as in the previous section probably due to the lack of subject motion. The two susceptibility maps in Figure 6.28 looked almost identical on a slice-by-slice, visual inspection. I could only find one instance where there was substantial visible difference between the two images. In Figure 6.28, the area indicated by the yellow arrow looks crisper and more detailed in the susceptibility map (top row) corresponding to a 2×1 SENSE acceleration even though the same regions looks identical in the last-echo magnitude images (bottom row).

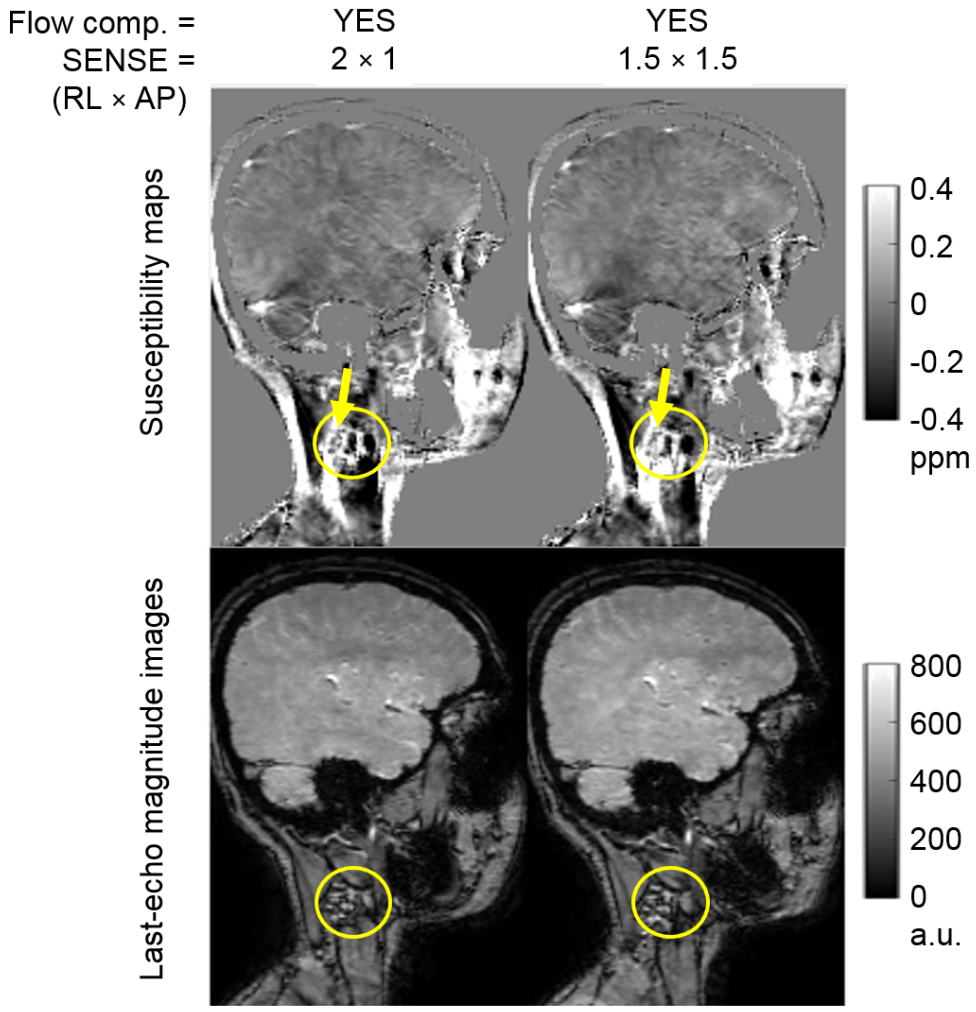

Figure 6.28: Comparison of asymmetric and symmetric SENSE factors in the head and neck in flow-compensated sequences. Sagittal slices of the last-echo magnitude images (bottom row) and corresponding susceptibility maps (top row) of the two acquisitions with 1.25 mm isotropic resolution and flow compensation are shown.

In conclusion, flow compensation does not seem to affect the appearance of the images or the measured mean susceptibilities. However, using the gradient shapes predicted by the PPE, I have shown that it does provide an improved first order gradient-moment nulling in the first three echoes. Since using the vendor-supplied flow compensation does not cost extra scan time, it will be used in our optimised protocol. The two sequences with 1.25 mm isotropic resolutions and different SENSE acceleration factors seem to provide very similar results in terms of visible susceptibility contrast and measured mean susceptibilities in brain regions and healthy lymph nodes. An asymmetric SENSE factor (2×1) provided infinitesimally better susceptibility maps and, based on the design of the head-and-neck coil, image quality is expected to be more robust to high SENSE acceleration factors in the RL direction. Therefore, asymmetric SENSE factors will be used in

the optimised protocol. However, symmetric SENSE factors could also be considered in case of any unforeseen problems with the asymmetric SENSE acceleration.

6.2.4 Conclusions

Here I have optimised the MRI acquisition for robust, artifact-free susceptibility mapping of the head and neck within clinically applicable scan times. Figure 6.29 summarises the methods and conclusions of this process. A 3D gradient echo sequence should be used as it is more SNR efficient than a 2D sequence and does not result in striping artifacts. The HF direction was chosen to be the readout or frequency encoding direction to minimise aliasing within the tissue. I decided to include the entire head and neck in the optimised protocol, but excluding the brain could be considered to slightly shorten the total acquisition time. Sagittal acquisitions were corrupted by severe, eye motion-induced artifacts, therefore, coronal orientation is preferred. 1.25 mm isotropic resolution provided sufficient signal-to-noise ratio and a low level of SENSE noise (as opposed to 1.1 mm isotropic resolution) while at the same time providing susceptibility maps that were not substantially influenced by partial volume effects (as opposed to susceptibility maps of 1.4 mm isotropic resolution). Four echoes can be acquired within the limited scan time (6 minutes), but a three-echo sequence could be considered for studies in which even less time is available. Flow compensation will be utilised in the optimised protocol as it was found to have little visible effect on the susceptibility maps, but was shown to improve the first order gradient-moment nulling at no additional scan time cost. A SENSE acceleration of 2×1 (RL and AP) is preferred, but SENSE factors of 1.5×1.5 (RL and AP) could be considered as an alternative in case of any unexpected problems since these parameters provided very similar results.

This optimised sequence is used in section 6.4 that focuses on optimising the QSM pipeline and in chapter 7 where I assess the repeatability of the combined optimal acquisition protocol and QSM pipeline.

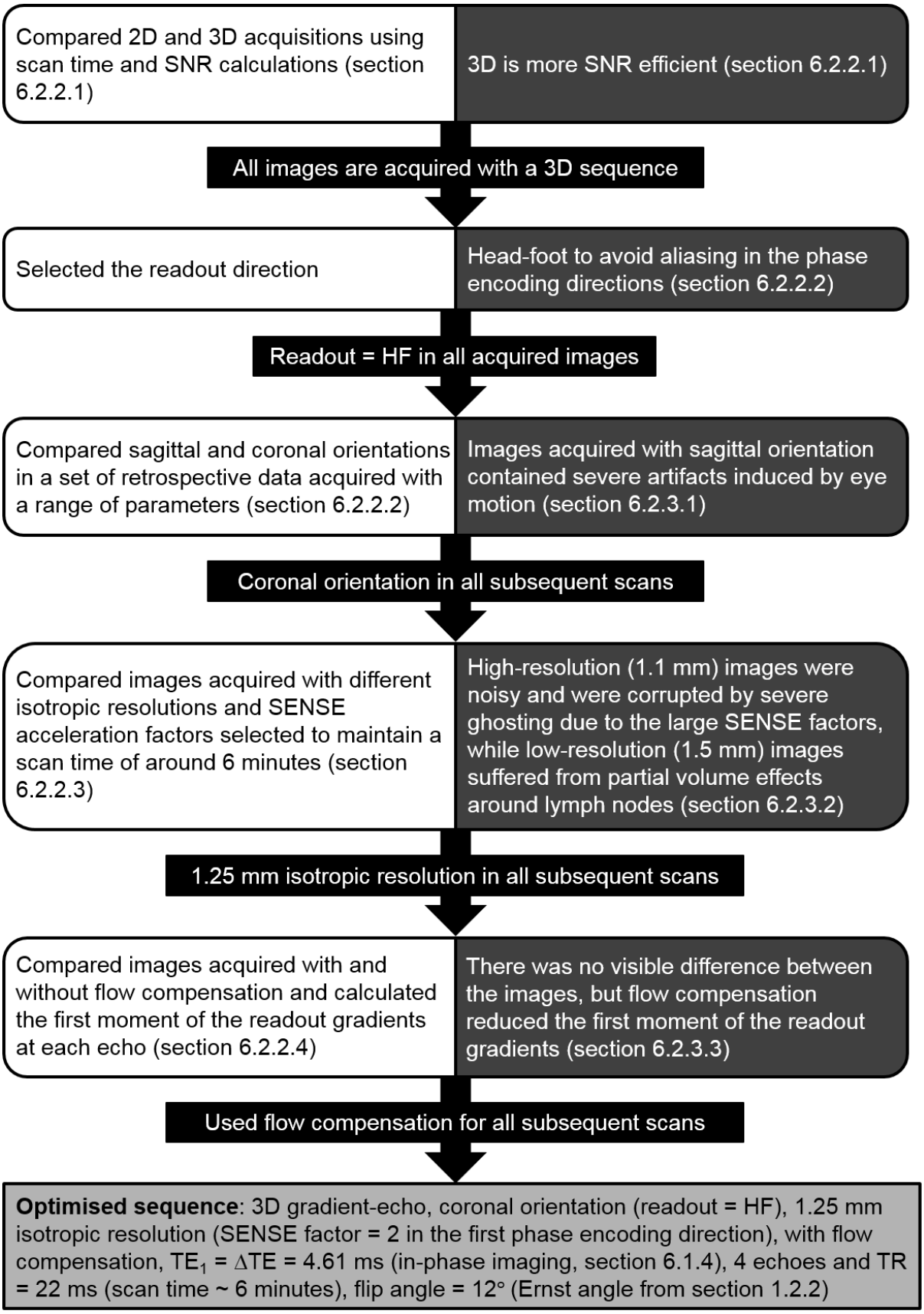

Figure 6.29: Summary chart of the MRI acquisition optimisation.

6.3 A comparison of background field removal techniques using ground truth evaluation

6.3.1 Introduction

Magnetic field contributions that do not originate from susceptibility sources inside the region of interest are called background fields (section 2.3). The main source of most of the background fields is the high susceptibility difference between tissue and air (-9.4 ppm [16]). In the past few years, a large variety of background field removal (BFR) techniques have been developed to reduce or eliminate these field contributions and avoid residual background fields propagating into the calculated susceptibility maps (section 2.3).

In 2016, Schweser et al. [99] compared 13 current BFR methods using a realistic numerical brain phantom. A field map was generated from the ground truth susceptibility map to which all 13 BFR techniques were applied with optimal parameters chosen by the respective authors of each original publication. The resulting local field maps were compared to the ground truth local field map obtained using the reference scan method (section 6.3.2.3). Normalised root mean square error (NRMSE) was calculated in each local field map as a function of the distance from the surface of the brain. As all techniques were applied on different computers, the computation times were not included in the comparison. The study concluded that only minor differences were present in the local field maps, mainly in the cortex of the brain. It is not clear to what degree these differences propagate into the susceptibility maps but the authors claimed that, in their experience, none of the residual background fields led to apparent susceptibility artifacts. They advised against the use of methods like SHARP (section 2.3.2.2) or VSHARP (section 2.3.2.3) for cortical studies as they either did not provide local field values in the cortex (SHARP) or these values were inaccurate (VSHARP).

In this work, I compared five cutting edge BFR techniques. I made sure to include at least one technique for all the different assumptions that BFR methods are based on (section 2.3). I used a realistic numerical head-and-neck phantom (from section 5.3.2) for the ground truth comparison. In our phantom, background fields coming from the body were simulated by the neck piece, whereas Schweser et al. used a whole body susceptibility phantom. They also assigned different susceptibility values to bone, vessels, and CSF, but not to the thalamus, globus pallidus and caudate nucleus as in this study. I simulated multi-echo complex images from the phantom and compared both phase unwrapping and

BFR in combination as opposed to Schweser et al. who only compared the background field removal techniques using a perfect, unwrapped total field map. In addition, I have also calculated susceptibility maps to assess how the errors in the field maps propagate into the susceptibility distribution. I have optimised each technique on the same computer, therefore I could include computation times in the comparison. Finally and most importantly, I have performed the comparison in the brain first to check if my results agree with those of Schweser et al., then I compared the most promising techniques in the head and neck as this region is the main focus of this thesis (section 1.1).

6.3.2 Methods

6.3.2.1 A realistic numerical head-and-neck phantom

The anthropomorphic head-and-neck phantom from section 5.3.2 was used to investigate the differences between several state-of-the-art BFR techniques. Using the susceptibility, magnitude and T_2^* maps from Figure 5.3, multi-echo complex images were simulated from the entire head and neck with $TE_1 = 3$ ms, $\Delta TE = 5.4$ ms, 5 echoes.

6.3.2.2 Calculating local field and susceptibility maps in the brain using different BFR techniques

As the following comparison was performed in the brain, the initial matrix size of the multi-echo complex images was reduced from 384×384×384 (containing the entire head-and-neck) to 384×384×192 (containing only the brain) as in this case, the neck piece only served to simulate the background fields in the brain.

Most BFR techniques require unwrapped field images as inputs. Therefore, non-linear field fitting (section 2.2.1.3) and Laplacian phase unwrapping (LPU, section 2.2.2.2) were applied to the simulated images as this is the simplest way of calculating unwrapped total field maps from complex multi-echo data acquired with a 3D gradient echo sequence (section 6.4). The following optimised BFR methods were applied to the unwrapped field map in the brain.

- **Inverse Laplacian Filtering (iLF)** (section 2.3.2.1) with $\sigma = 0.03$, zero filling to a matrix size of 384×384×256, and the brain mask eroded 5 times. This method

was applied to the wrapped field map (after non-linear fitting) as iLF is a technique capable of both phase unwrapping and background field removal.

- **Sophisticated Harmonic Artifact Reduction for Phase Data (SHARP)** (section 2.3.2.2) with $\sigma = 0.03$, a kernel radius of 5 mm, and zero filling to a matrix size of 384×384×256.
- **Variable-kernel SHARP (VSHARP)** (section 2.3.2.3) with a kernel radius of 25 mm, and zero filling to a matrix size of 384×384×256.
- **Laplacian Boundary Value (LBV)** (section 2.3.3.1) without mask erosion as erosion did not improve the results.
- **Projection onto Dipole Fields (PDF)** (section 2.3.4.1) without mask erosion as erosion did not improve the results.

Susceptibility maps were calculated from all local field maps using Truncated K-space Division (TKD with $\delta = 2/3$ and PSF correction, section 2.4.1.1).

6.3.2.3 Ground truth evaluation

In this numerical model, the background fields originate from the tissue/air interfaces around the head and neck as well as in the oropharyngeal air space. Therefore background field contributions were calculated using the forward model [174] (Equation 1.16) on the background susceptibility phantom (Figure 6.30 c, where the susceptibility of all internal regions were set to -9.4 ppm, the susceptibility of the tissue). The true (ground truth) local field map (Figure 6.30 e) was derived by subtracting the background fields (Figure 6.30 d) from the total field map (Figure 6.30 b). This is called the reference scan method [109] as it resembles the process of measuring the background fields in a physical phantom by removing the object of interest from the medium in which it is embedded [112, 187].

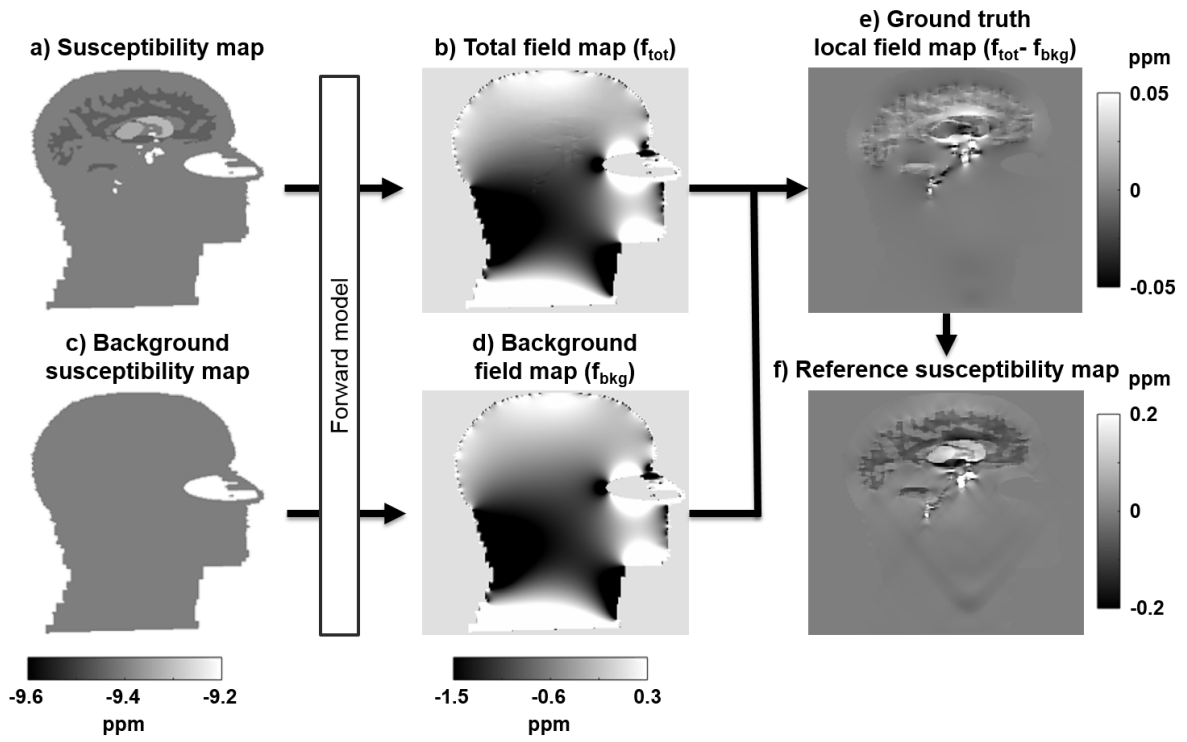

Figure 6.30: Reference scan method. Field maps (b, d) were calculated from the total susceptibility distribution (a) as well as a background susceptibility map (c) which does not contain any brain regions with different susceptibility values. The difference between the total (b) and the background (d) field maps is the true local field map (e). A reference susceptibility map (f) was calculated from the ground truth local field map using TKD.

A reference susceptibility map (Figure 6.30 f) was obtained by applying TKD to the ground truth local field map. There is no susceptibility calculation method in existence that can invert the local field map perfectly [113]. Preliminary results (not shown) suggested that the error introduced by susceptibility calculation can sometimes 'compensate' for the errors in the local field map resulting in the mean susceptibility of some regions to be numerically closer to the ground truth even when the susceptibility map contains more artifacts. Therefore, I used the reference susceptibility map instead of the ground truth susceptibility map to make a fair comparison between the BFR methods tested in this work.

All estimated local field maps and susceptibility maps were compared to the ground truth local field map and the reference susceptibility map respectively by visual inspection and NRMSE calculated in the brain. The mean and standard deviation of susceptibility values in five brain regions (caudate nucleus, putamen, thalamus, globus pallidus, white matter) were calculated and compared with those of the reference susceptibility map. Repeated measures ANOVA was used to evaluate whether the BFR method had a signif-

icant effect on the measured mean susceptibilities. BFR techniques were also compared in terms of computation time on a standard PC with an Intel Xeon processor and 32 GB RAM.

6.3.2.4 Comparison of LBV and PDF in the head and neck

As the ultimate goal is susceptibility mapping in the head and neck, I selected the methods that performed best in the brain (LBV and PDF, section 6.3.3.1) for further comparison in the whole head-and-neck phantom. Local field maps and susceptibility maps calculated from the multi-echo complex data (section 6.3.2.1) using non-linear fitting, LPU, LBV or PDF, and TKD were compared by visual inspection and NRMSE calculated in the head and neck.

While optimising these BFR methods for the head and neck, I observed that mask erosion is crucial for successful LBV in this region. Therefore, local field maps were estimated using a binary tissue mask eroded either 0 or 3 times for both LBV and PDF to compare their robustness to the number of mask erosions.

I also noted that these techniques, especially PDF, were not able to remove residual background fields around the elliptical air space of the numerical phantom. This may have been because of the interactions between the phase unwrapping (LPU) and background field removal (PDF) steps of the susceptibility mapping pipeline. To investigate this, LBV and PDF were also compared using FSL PRELUDE (section 2.2.2.1) instead of LPU as the phase unwrapping step.

6.3.3 Results and Discussion

6.3.3.1 Comparison of BFR techniques in the brain

Figure 6.31 shows coronal and axial slices of the ground truth local field map and local field maps estimated using five different BFR methods. All calculated local field maps were very similar to the ground truth except the result of iLF which had visibly lower contrast. Furthermore, the difference map between the local field map estimated by iLF and the true local field map contained large variations within the tissue and field values were not retrieved at the edges of the brain due to the large number of mask erosions. SHARP and VSHARP both seemed to perform well further away from the edges. However, due to the kernel size, SHARP did not produce results at the brain edges while VSHARP provided

inaccurate local field values at the boundaries of the brain and around the thalamus (dark arrows). PDF and LBV provided local field maps that appeared closest to the ground truth by visual inspection, though some residual background fields were still present at the brain edges which could not be removed by mask erosion (white arrows). LBV provided the field map with the lowest NRMSE.

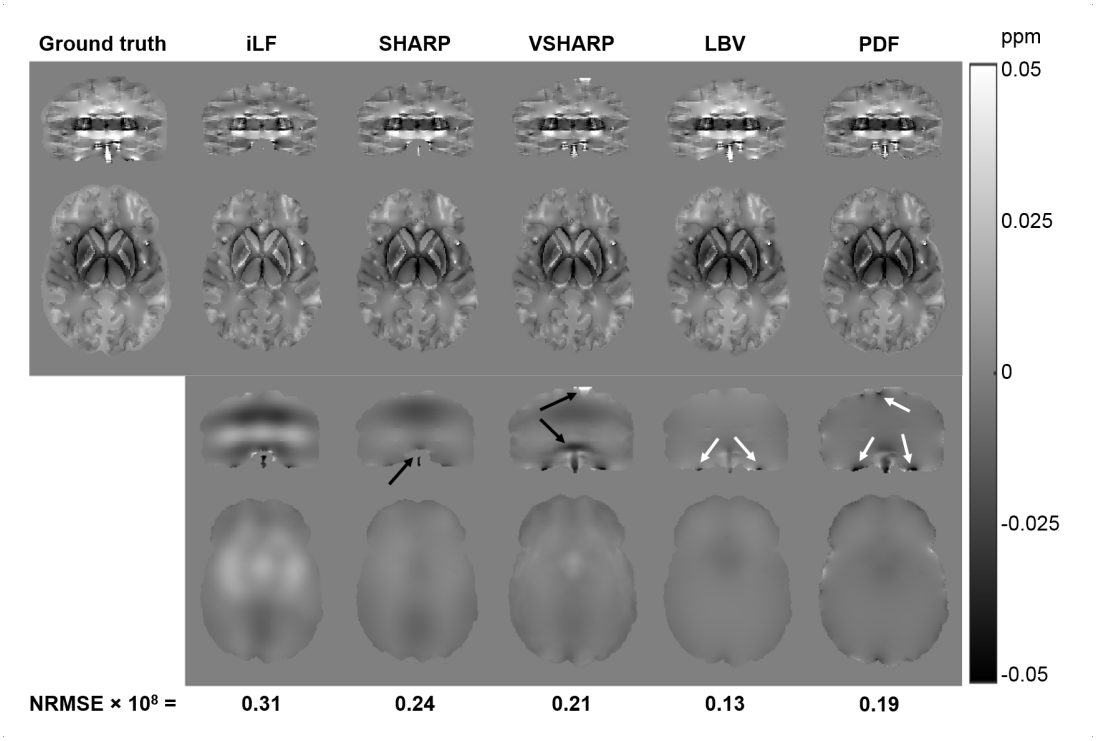

Figure 6.31: Comparison of background field removal techniques in the brain. Coronal and axial slices of the ground truth local field map and local field maps calculated using five different BFR methods (top row). Difference images between the estimated local field maps and the ground truth are also shown (bottom row) as well as NRMSE in the brain.

All the aforementioned local field maps were further processed using TKD to assess the effect of BFR on the susceptibility maps. Figure 6.32 shows coronal and axial slices of susceptibility maps calculated from the the ground truth local field map and local field maps estimated using five different BFR methods. All susceptibility maps were visually similar to the reference susceptibility map except the result of the iLF pipeline which had visibly lower contrast. The susceptibility maps calculated using iLF, SHARP and VSHARP had relatively large errors around the deep-brain structures (dark arrows). In addition, iLF and SHARP did not provide susceptibility values at the edges of the brain due to the mask erosions and VSHARP's estimates were erroneous at the brain edges. Susceptibility maps calculated from the LBV and PDF local field estimates seemed to be the closest to the reference susceptibility map with smaller errors around the iron-rich deep-brain structures. However, even these results contained errors at the edges of the

brain (white arrows). Susceptibility maps calculated from local field maps provided by LBV and PDF had the lowest NRMSE in the brain.

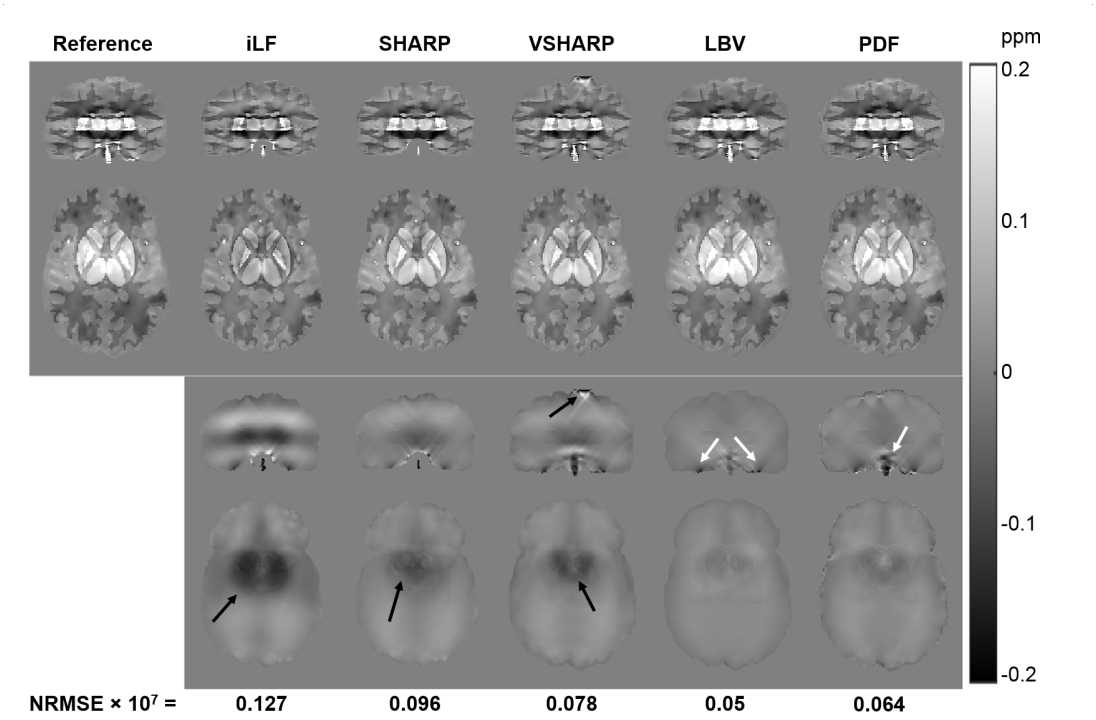

Figure 6.32: Comparison of susceptibility maps in the brain. Coronal and axial slices of susceptibility maps calculated from the ground truth local field map (reference) and local field maps estimated using five different BFR methods (top row). Difference images are also shown (bottom row) as well as NRMSE in the brain.

Figure 6.33 shows the mean and standard deviation of susceptibilities in the five brain regions in susceptibility maps calculated from the different local field estimates. It is apparent that the BFR method did not affect the results of TKD substantially except in the white matter where the iLF, SHARP and VSHARP pipelines estimated higher susceptibilities than the reference. In any case, the BFR method used had no significant effect on the measured susceptibility maps (p-value = 0.17 for repeated measures ANOVA).

Figure 6.34 shows computation times corresponding to each BFR method. While VSHARP and PDF were much slower than the other three techniques, their computation times were still below one minute for the whole brain.

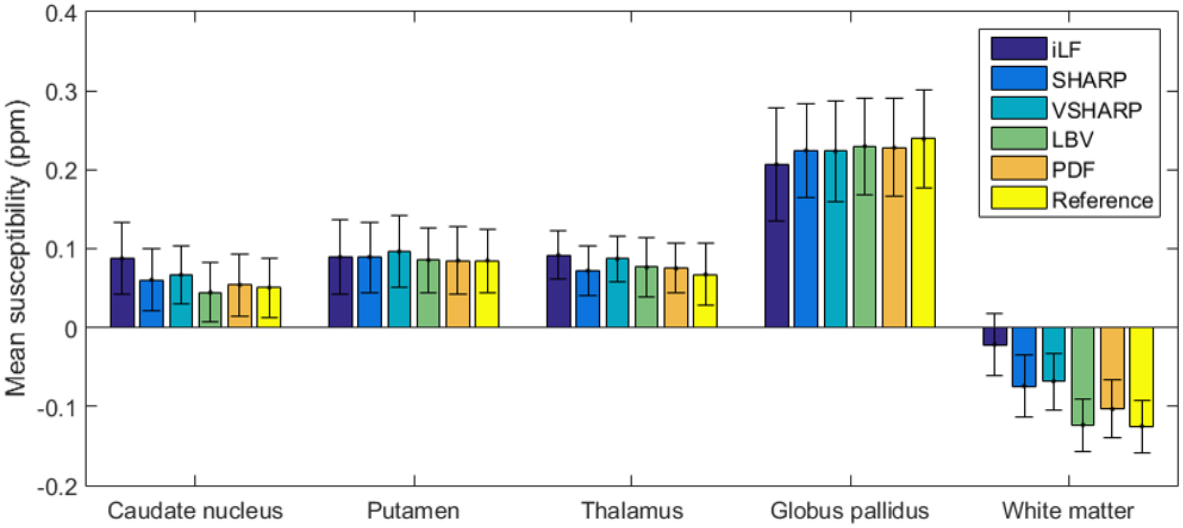

Figure 6.33: Mean susceptibilities in five brain regions in susceptibility maps calculated from local field maps estimated with five different BFR methods. Reference refers to the susceptibility map calculated from the ground truth local field map. The values have error bars equal to the standard deviation of the susceptibility in each region.

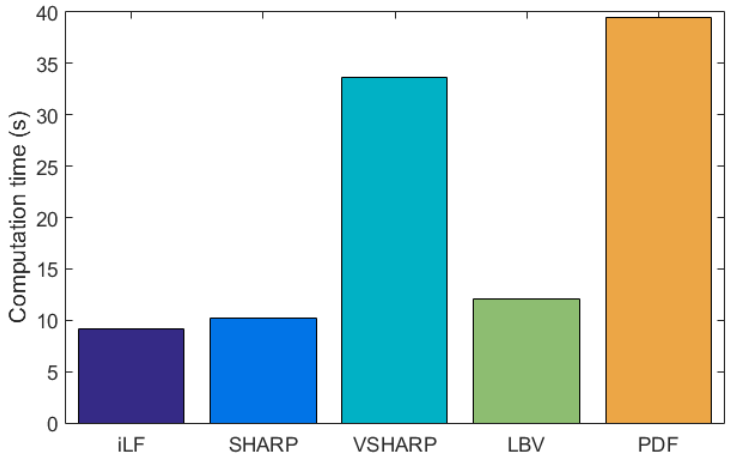

Figure 6.34: Computation times of the five BFR techniques in the brain.

The results of our comparison of different BFR methods in the brain are in accordance with the conclusions of Schweser et al. [99]. iLF, SHARP and VSHARP either did not provide local field and susceptibility values at the brain edges or these values were inaccurate. Though the local field and susceptibility map estimates of the LBV and PDF pipelines seemed to be the most similar to the ground truth local field and reference susceptibility maps, mean susceptibilities calculated in five brain regions were not significantly affected by the BFR method used.

6.3.3.2 Comparison of LBV and PDF in the head and neck

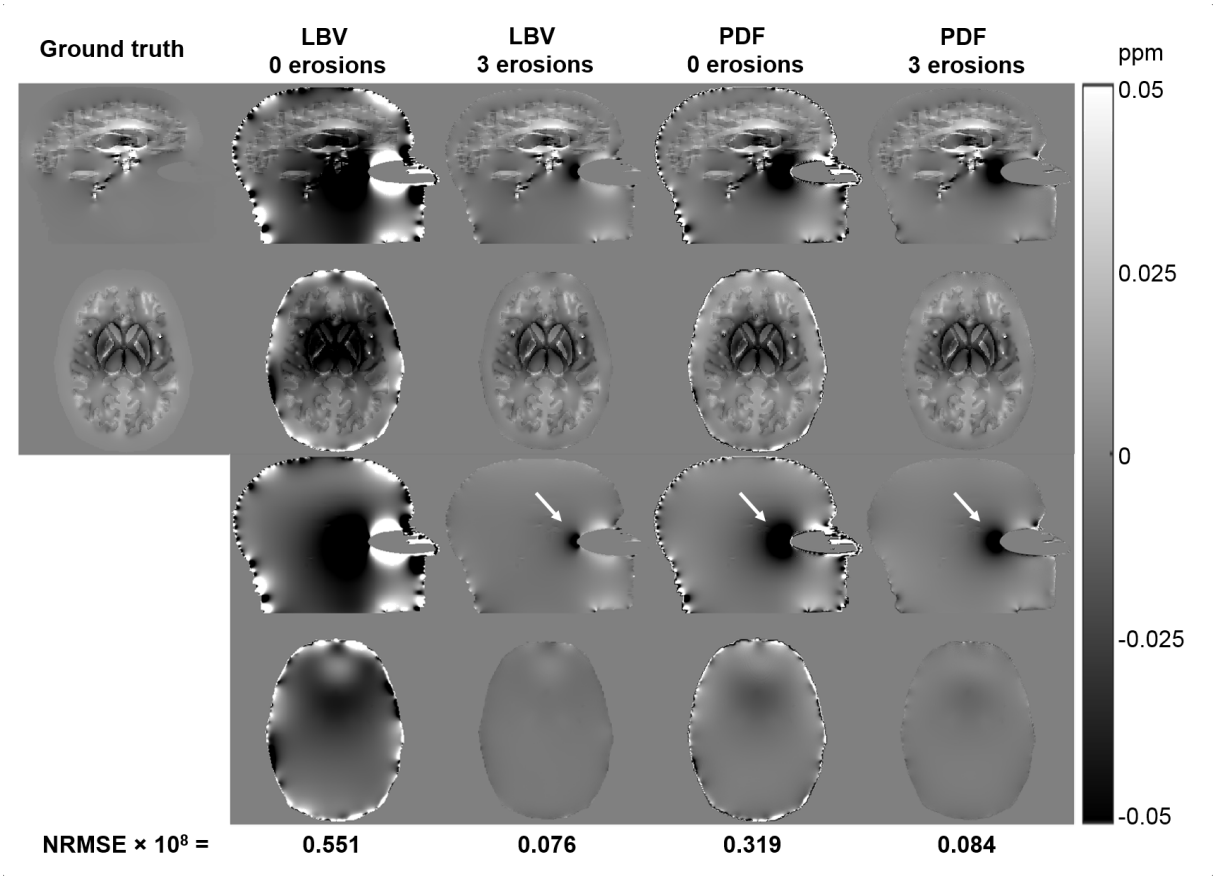

Figure 6.35: Comparison of LBV and PDF after LPU in the head and neck. Sagittal and axial slices of the ground truth local field map and local field maps calculated using LBV and PDF with 0 or 3 mask erosions in the head (top row). Difference images between the estimated local field maps and the ground truth are also shown (bottom row) as well as NRMSE in the head and neck.

In the last section, I concluded that LBV and PDF could reduce background fields in the brain similarly well. Here, I discuss how these techniques perform in the head and neck. Figure 6.35 shows sagittal and axial slices of the ground truth local field map and local field maps calculated using non-linear fitting, LPU, and LBV or PDF. The results LBV provided were strongly dependent on the number of mask erosions (Figure 6.35, LBV with 0 and 3 erosions). LBV assumes that the internal field contributions are constant zero at the tissue boundary (section 2.3.3.1). This might be a good approximation when the edges of the tissue mask are near regions with low susceptibility variations (Figure 6.36 a). In this case, field variations on the boundary induced by internal voxels near the boundary are negligible. Therefore, LBV performs well in the brain where the susceptibility variations at the edges are usually below 0.1 ppm. However, for whole head-and-neck images, this susceptibility difference is equal to that of the tissue/air interface which is around 9.4 ppm [16]. In this case, internal voxels near the boundary have a significant contribution

to the fields at the boundary (Figure 6.36 b) and LBV's assumption is violated. Since this assumption provides the boundary conditions for the differential equation that LBV solves, its violation has long-ranging effects (Figure 6.35, LBV with 0 erosions).

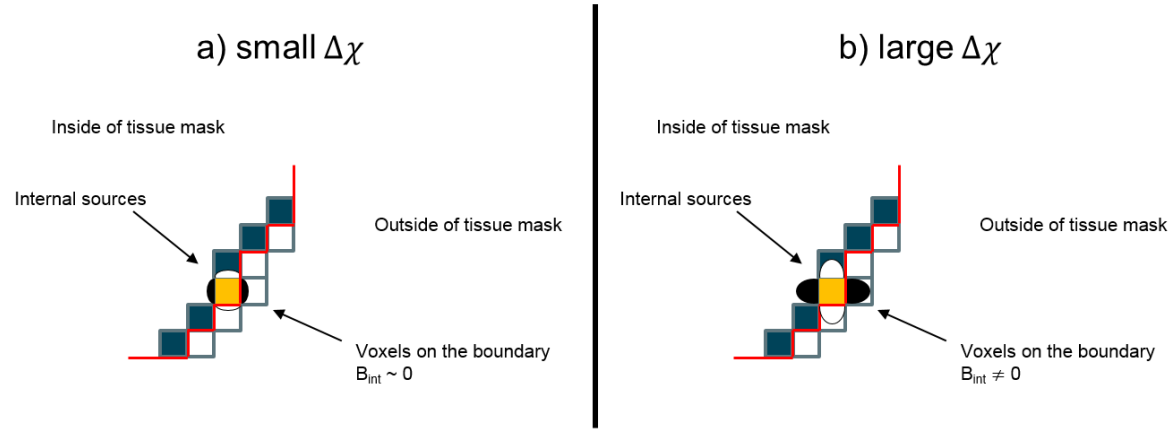

Figure 6.36: The validity of LBV's assumption. The black and white lobes (a and b) indicate the dipolar fields induced by the susceptibility difference between the orange internal voxel and its surroundings. LBV's assumption that the internal fields (B_{int}) are zero on the boundary only holds when the edges of the tissue mask are near regions with low susceptibility variations (a) and is violated when the susceptibility differences are large (b).

PDF was more robust to the number of mask erosions than LBV (Figure 6.35). PDF is a fitting method which estimates a susceptibility variation outside the tissue mask that can explain the field distribution within the tissue mask (section 2.3.4.1). Eroding the mask means that a few more voxels (at the boundary) are included in the candidate susceptibility distribution outside the mask instead of the field map to be fitted inside the tissue mask. Figure 6.35 confirms that mask erosion only affects the PDF results very close to the mask edges.

The arrows in figure 6.35 show that the two methods, especially PDF, failed to remove some background fields around the elliptical air space which propagated into the susceptibility maps in the form of very strong streaking artifacts (not shown). Both methods were applied to the images after non-linear fitting and LPU. Even with a very low kernel threshold, Laplacian based techniques (such as LPU) tend to also reduce the background fields (section 2.2.2.2). It is possible that some of the remaining background fields could not be modelled as contributions from outside susceptibility sources because some components have been removed, therefore PDF failed. Since both Laplacian techniques and LBV are based on the fact that field contributions of outside sources are harmonic inside the tissue mask ($\nabla^2 B_{ext} = 0$, section 2.3), even if LPU removes some of the background fields, the remaining background fields are expected to still be harmonic within the ROI.

Therefore, LBV was able reduce these fields more successfully than PDF (Figure 6.35, arrows).

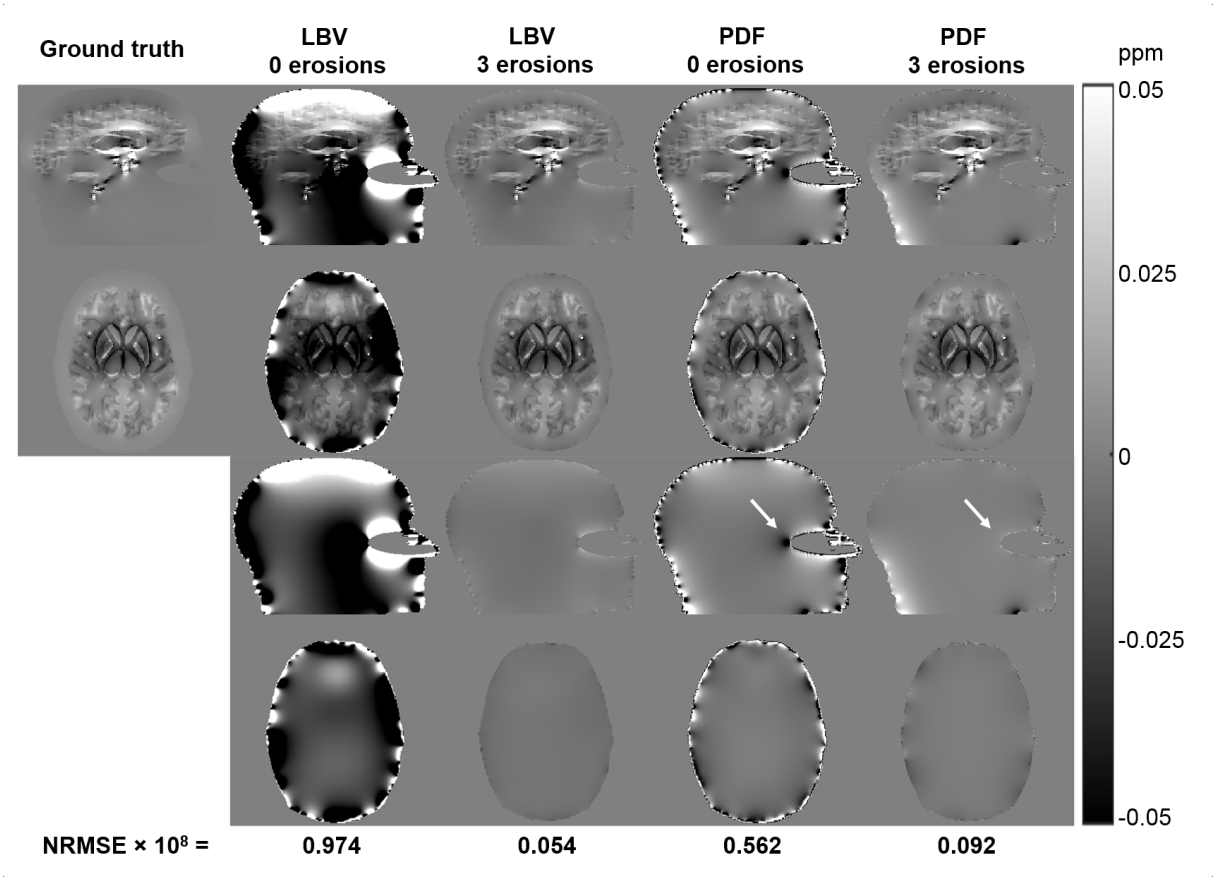

Figure 6.37: Comparison of LBV and PDF after FSL PRELUDE in the head and neck. Sagittal and axial slices of the ground truth local field map and local field maps calculated using LBV and PDF with 0 or 3 mask erosions in the head (top row). Difference images between the estimated local field maps and the ground truth are also shown (bottom row) as well as NRMSE in the head and neck.

To confirm the idea that residual background fields in the local field map calculated using PDF were caused by the interaction between the LPU step and PDF, the former was replaced by FSL PRELUDE in the pipeline and LBV and PDF were compared again. Figures 6.37 and 6.38 show sagittal and axial slices of the local field maps and susceptibility maps calculated using non-linear fitting, FSL PRELUDE, LBV or PDF, and TKD. Using FSL PRELUDE instead of LPU enabled PDF (and also LBV) to eliminate the background fields around the elliptical air space (arrows in Figure 6.37) confirming my explanation from the previous paragraph. Susceptibility maps in Figure 6.38 further demonstrate that PDF is more robust to the number of mask erosions than LBV.

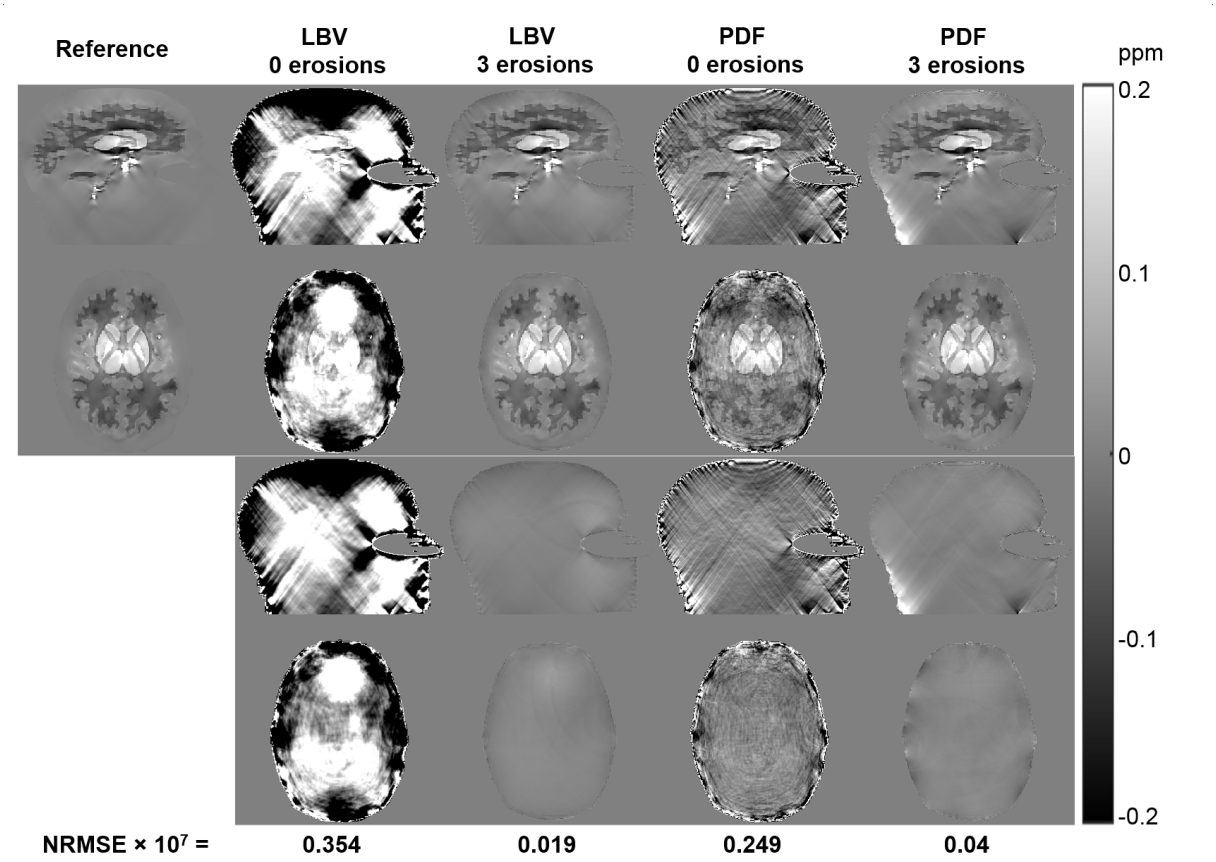

Figure 6.38: Susceptibility maps calculated in the head and neck using non-linear fitting, FSL PRELUDE, LBV or PDF, and TKD (top row). Difference images between the calculated susceptibility maps and the reference susceptibility map are also shown (bottom row) as well as NRMSE in the head and neck.

The results of the comparison of LBV and PDF in the head and neck have shown that LBV is able to remove most of the background fields when the boundaries of the tissue mask are near regions with low susceptibility variations. Such a tissue mask might be difficult to construct in volunteer or patient data where the exact position of the tissue/air interfaces is not known. PDF was also shown to be able to eliminate most of the background fields when used after FSL PRELUDE as the phase unwrapping method. However, it could take 4-5 hours for PRELUDE to unwrap a phase map of the head and neck (chapter 4) whereas LPU only takes a few seconds. It is interesting to note that PDF combined with LPU only failed around the elliptical air space even though the total field map contained larger field variations around the chin (Figure 6.30 b). Possibly, it is the nature of the dipolar fields induced by spherical or elliptical susceptibility sources that is causing this problem. It would be beneficial to compare these two background field removal techniques in volunteer head-and-neck images where such shapes are uncommon (section 6.4).

6.3.4 Conclusions

I compared five popular BFR techniques using a realistic numerical phantom. Results shown in the brain agreed with the conclusions of Schweser et al. [99] even though they studied the methods only up to the BFR stage and without field fitting or phase unwrapping, whereas I compared them in the context of an acquisition and susceptibility mapping pipeline tailored for clinical applications. All methods could eliminate most of the background fields around the deep-brain structures. iLF, SHARP and VSHARP either did not provide local field values at the boundary or these values were inaccurate.

I took the comparison one step further then Schweser et al. by calculating susceptibility maps from all estimated local field maps and the ground truth local field map. Mean susceptibilities in several brain regions were not significantly affected by the background field removal method used.

LBV and PDF provided the most accurate local field and susceptibility maps in the brain. Though the computation times of VSHARP and PDF were longer than those of the other three techniques, all methods could be calculated within one minute.

Since the focus of this thesis is head-and-neck cancer, I investigated the differences between LBV and PDF in the whole head-and-neck phantom as well. LBV combined with LPU was able to remove most of the background fields, but its performance was heavily affected by the number of mask erosions. I hypothesised that this is due to the assumption of LBV being violated when the boundaries of the tissue mask coincide with tissue/air interfaces. PDF was more robust to the number of mask erosions, but it could not remove residual background fields around the elliptical air space when combined with LPU. This could be attributed to the properties of the dipolar fields generated by an elliptical susceptibility source. PDF combined with FSL PRELUDE performed consistently well, but unwrapping a head-and-neck image using PRELUDE could take up to 4-5 hours which is not clinically applicable. Note that though SEGUE (chapter 4) was not used in this comparison, it could be a feasible alternative as I have shown that it provides almost identical unwrapped phase maps to PRELUDE in a much shorter time (section 4.5).

In conclusion, LBV or PDF combined with non-linear fitting and LPU are suitable pipelines for calculating local field maps in the brain. The same two pipelines could be feasible in head-and-neck imaging provided that no elliptical susceptibility sources are present. It would be beneficial to examine whether PDF after LPU can remove residual background fields around the air spaces in acquired, in-vivo images (section 6.4).

6.4 Optimising the QSM pipeline for head-and-neck images

6.4.1 Introduction

As there is no previous literature on the application of susceptibility mapping to head-and-neck images, it was improtant to carefully optimise the entire QSM pipeline for this region. It is very challenging to calculate susceptibility maps in the head and neck due to (section 1.3.3): i) strong background fields induced by the tissue/air interfaces of the oropharyngeal air spaces, ii) signal dropout in bones, iii) chemical shift artifacts originating from fatty tissue, and iv) motion (e.g. due to swallowing). In section 6.1, I compared several different strategies for overcoming (iii). In-phase imaging was found to be the most accurate and robust technique to correct for chemical shift artifacts. Therefore chemical shift artifacts (iii) are removed at the acquisition stage. As I have discussed, some of the other challenges (e.g. motion) can be somewhat mitigated by choosing acquisition parameters (e.g. SENSE acceleration factors and image orientation) (section 6.2). In section 6.3, I evaluated background field removal techniques using ground truth evaluation in a numerical phantom to deal with (i) and found that Projection onto Dipole Fields (PDF, section 2.3.4.1) and the Laplacian Boundary Value method (LBV, section 2.3.3.1) performed well in the head and neck. It is important to test whether these methods are robust in vivo and also to optimise the remaining steps in the QSM pipeline in the head and neck. There are many existing techniques with different core assumptions and properties for field fitting, phase unwrapping, background field removal and susceptibility calculation (chapter 2). Here I assess and compare the state-of-the-art methods in terms of image quality (based on visual assessment and signal-to-noise ratio where applicable, see chapter 3) and computation time using in-vivo head-and-neck images. A summary chart of the optimisation process and the main conclusions can be found in section 6.4.4.

6.4.2 Methods

I acquired images in a healthy volunteer using the optimised parameters and evaluated current field fitting, phase unwrapping, background field removal and susceptibility calculation techniques.

6.4.2.1 Head-and-Neck Data

Multi-echo magnitude and phase images were acquired in the head and neck of a healthy volunteer using the optimal acquisition protocol developed in section 6.2: with FOV = 24×24×22 cm^3 (FH-AP-RL), coronal orientation, a SENSE factor of 2 in the RL direction, 1.25 mm isotropic resolution, $TE_1 = \Delta TE = 4.61$ ms (in-phase timing), 4 echoes, bw = 290 Hz/pixel, TR = 22 ms, flip angle = 12°. Flow compensation on the first echo was also set to "YES". These images were used here to optimise the QSM pipeline.

6.4.2.2 Magnitude and phase noise

In chapter 3, I discussed the evolution of measurement uncertainty along the susceptibility mapping pipeline and concluded that calculating the noise maps for each stage could aid in the selection of the most appropriate methods. Therefore, as a first step, seven regions of interest (ROIs) were manually segmented in the first-echo magnitude image to estimate the initial magnitude noise. Five rectangular, 400-voxel regions were selected within the white matter in a sagittal slice similarly to Figure 3.1. Two additional ROIs (around 300 voxels) were manually drawn around healthy lymph nodes. The uncertainty in each ROI was estimated as the standard deviation of the magnitude. The phase noise was calculated using Equation 3.13.

6.4.2.3 Field fitting and phase unwrapping

Calculating the total field map is the first step in susceptibility mapping (Figure 2.1). It involves the unwrapping and fitting of phase images to estimate a field value at each voxel.

Unwrapping phase images at each echo individually followed by linear fitting to the phase across echoes is a straightforward way of calculating the total field map. This requires a phase unwrapping algorithm that preserves the linearity of the phase across echoes. Unfortunately, one of the fastest and most widely used techniques, Laplacian phase unwrapping (LPU, section 2.2.2.2) does not preserve this linearity as it also tends to remove some of the background fields in a non-linear fashion [98]. FSL PRELUDE (section 2.2.2.1) is considered the ground truth phase unwrapping method [93]. It does not affect the linearity of the phase as it performs the unwrapping by adding integer multiples of 2π to each voxel. However, PRELUDE can take up to a day to unwrap all 4 echoes for head-and-neck phase images (chapter 4). Fortunately, the new, faster phase

unwrapping method, SEGUE (chapter 4), that I have developed can be used here instead to reduce computation times as I have shown that it provides almost identical results to PRELUDE (section 4.5). Another way of estimating the field map is using non-linear fitting (section 2.2.1.3) of the multi-echo complex data over time and then eliminating residual wraps using any spatial phase unwrapping algorithm.

Here I compared total field maps calculated using: linear fitting of the SEGUE unwrapped phase across echoes both with and without magnitude weighting (section 3.3), and non-linear fitting followed by either SEGUE or LPU to eliminate residual wraps. The overall computation times were also measured.

6.4.2.4 Background field removal

In section 6.3, I concluded that non-linear fitting and LPU combined with Laplacian Boundary Value (LBV, section 2.3.3.1) or Projection onto Dipole Fields (PDF, section 2.3.4.1) could be used for calculating the local field map in the head and neck. However, the performance of LBV largely depended on the binary tissue mask (Figure 6.35, left column). Also PDF seemed to be unable to completely remove residual background fields around the elliptical air space of the numerical phantom (Figure 6.35, right column). In this section, I compared these two techniques in a healthy volunteer to assess their performance and robustness in vivo.

Most background field removal techniques rely on a binary tissue mask to separate internal and external susceptibility sources (section 2.3). The edges of the tissue mask determine the boundary conditions for LBV where the internal field variations are assumed to be zero (section 6.3.3.2). The mask also determines the part of the image to be fitted by PDF so it should only contain regions of low noise to avoid overfitting and inaccurate results. For head-and-neck images, the easiest way to create a binary tissue mask is by thresholding one of the magnitude images, for example, as voxels with noisy phase usually appear dark in the magnitude images [84]. However, magnitude images at individual echoes do not necessarily fully characterise the noise in a certain voxel across all the echoes. Fortunately, the non-linear fitting function from the MEDI toolbox [86] also has a noise map output based on Equation 3.21. Thresholding the inverse noise map should provide a better tissue mask for background field removal as it takes into account the noise variation over all echoes. Here I tested masks obtained by thresholding the inverse noise map at 1/3, 1, and 3 times its mean value (Mask 1, Mask 2, and Mask 3 respectively).

6.4.2.5 Susceptibility calculation

I compared five different susceptibility calculation methods by applying them to local field maps calculated by non-linear fitting, LPU and PDF using Mask 2 in the volunteer head-and-neck images. I selected popular, state-of-the-art methods as potential susceptibility calculation techniques: Truncated K-space Division (TKD, section 2.4.1.1), the direct and iterative Tikhonov methods (section 2.4.2.2), Morphology Enabled Dipole Inversion (MEDI, section 2.4.2.3), and iLSQR (section 2.4.2.1).

TKD was used with $\delta = 2/3$ and correction for underestimation using the point spread function (PSF) to minimise streaking artifacts. PSF correction was also implemented for the Tikhonov techniques (section 2.4.2.2). For iterative Tikhonov and MEDI, the inverse noise map was used as the weighting term (normalised by the mean of the inverse noise map so that the optimal regularisation parameters of the direct and iterative Tikhonov methods would be comparable). iLSQR was run with default settings. For all three iterative fitting methods (iterative Tikhonov, MEDI, and iLSQR), Mask 2 from the previous section was used to identify the regions to be fitted as this proved to provide the best local field maps (section 6.4.3.3).

The regularisation parameters of the Tikhonov methods and MEDI were selected using L-curve optimisation (section 2.4.2.4). A range of different α (for the Tikhonov methods) and λ (for MEDI) values were used to calculate the susceptibility map. The residual norm (RN) and the regularisation term (RT) were calculated in each case to give a measure of the quality of the fit and the degree of regularisation respectively and allow an L-curve to be plotted to help select the optimal regularisation parameter.

6.4.3 Results and Discussion

6.4.3.1 Magnitude and phase noise

Figure 6.39 b shows the seven regions of interest: five, rectangular white matter areas (white boxes) and two healthy lymph nodes (red overlay).

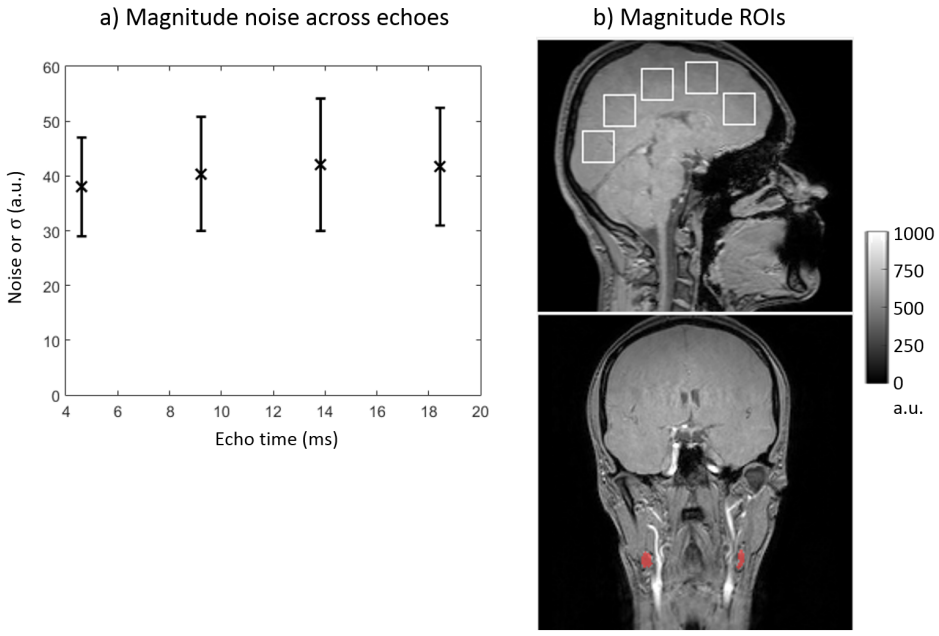

Figure 6.39: Variations in the magnitude noise across echo times (a) and regions of interest in the magnitude image (b). The scatter plot in (a) shows the mean noise across the seven ROIs with error bars equal to their standard deviation.

Figure 6.39 a shows the evolution of the magnitude noise across echoes. Note that the magnitude uncertainty of this data shows even less echo time-dependence than the magnitude uncertainty of the brain images used in chapter 3 (Figure 3.2 a).

Figure 6.40 b shows the profile of the uncertainty in the first-echo phase image along the white line in Figure 6.40 a. This line was selected due to the fact that it goes through both of the manually segmented healthy lymph nodes indicated by the yellow arrows. The phase noise was scaled to ppm using Equation 3.30.

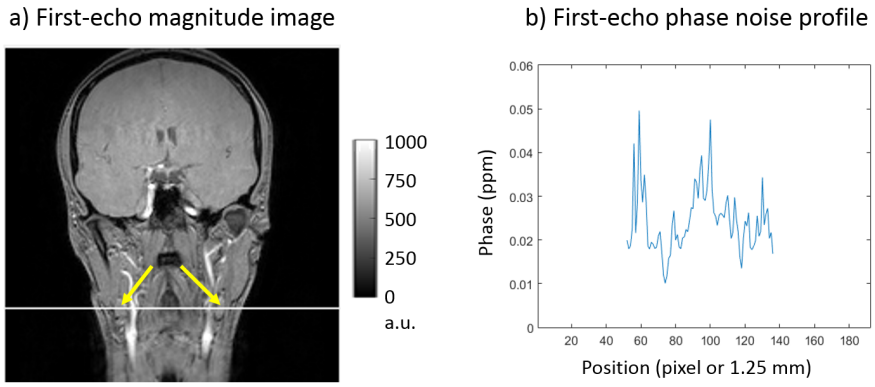

Figure 6.40: The first-echo magnitude image (a) and the phase noise profile (b). The plotted line in (b) shows the variations in phase uncertainty across the neck along the white line in (a). The yellow arrows indicate the healthy lymph nodes that were manually segmented for the estimation of the magnitude noise.

6.4.3.2 Field fitting and phase unwrapping

Figure 6.41 a shows the estimated total field maps as well as their profiles across the neck and the overall computation times. The corresponding noise maps and their profiles are displayed in Figure 6.41 b. These were calculated using Equation 3.20 for the linear fits with and without weighting, while the noise map output of the non-linear fitting function of the MEDI toolbox is displayed in the bottom row.

All three total field maps look very similar and have almost identical profiles. In some instances, the total field values estimated with the simple linear fit (Figure 6.41 a, blue, solid line) tend to be a bit lower than the results of the other two techniques (Figure 6.41 a, arrows). The noise profile of the simple linear fit (Figure 6.41 b, blue, solid line) also tends to be generally higher than that of the other two methods (Figure 6.41 b, arrow). This is another demonstration of the fact that magnitude weighting substantially attenuates the noise in regions with low magnitude SNR, i.e. towards the tissue edges or bony structures (Figure 6.41 b, yellow circles). This result is in accordance with Figure 3.5.

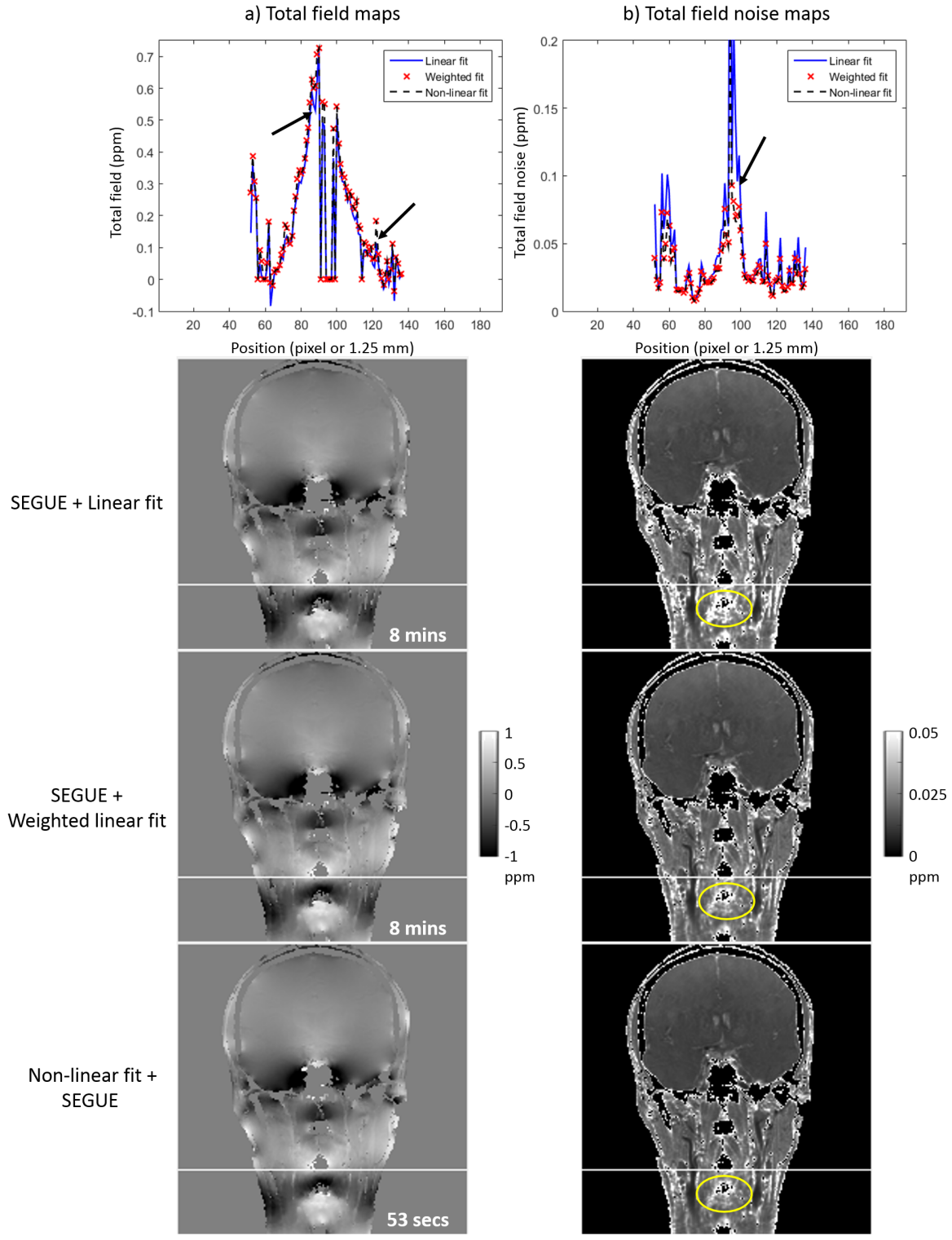

Figure 6.41: Comparison of three different techniques for the estimation of the total field map. The resulting total field maps and their profiles along the white lines is shown in (a). The overall computation times are also displayed in the bottom right corner of each field map. The corresponding noise maps and their profiles along the white lines is shown in (b). The arrows in (a) indicate some voxels where the total field estimated by the linear fit is lower than that calculated by the other two techniques. The arrow and yellow ellipses in (b) indicate regions where the noise of the linear fit total field map was higher than that of the other two techniques.

The magnitude-weighted linear fit and non-linear fitting provided similar maps of the total field and the total field uncertainty. However, using the weighted linear fit requires prior unwrapping of the phase at each echo individually. Since the computation time of SEGUE is longer for later echoes, the overall process takes about 8 minutes. Using SEGUE after non-linear fitting means that spatial unwrapping only has to be performed once. Moreover, residual wraps after non-linear fitting are usually similar to the wraps in the first echo phase image (i.e. there are fewer wraps). Therefore, it only takes about 50 seconds to calculate the total field map using this strategy.

LPU could also be used to remove residual wraps after non-linear fitting as the preservation of phase linearity is not a concern after field fitting has already been performed. Figure 6.42 shows total field maps calculated using non-linear fitting followed by SEGUE (a) or LPU (b). Note that LPU also removed some of the background fields, therefore Figure 6.42 b had lower contrast than Figure 6.42 a. The noise is expected to be similar in the two maps (section 3.4). As a consequence, SNR is obviously lower in the map provided by LPU, but only due to the partial background field removal. Therefore, noise or SNR maps cannot be used in this comparison.

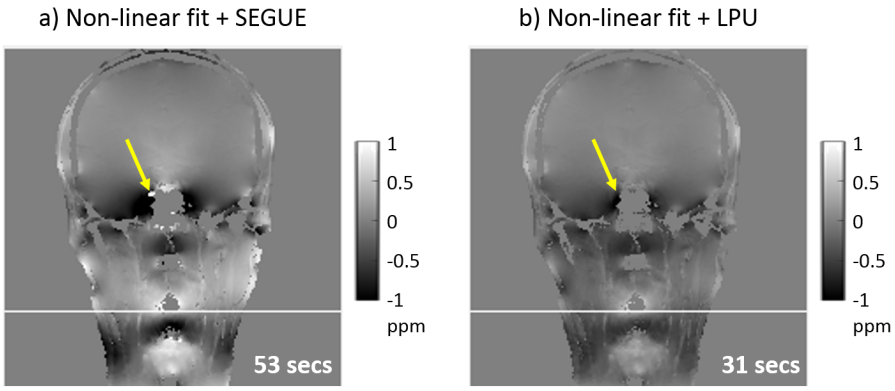

Figure 6.42: Comparison of two different techniques for removing residual phase wraps after non-linear field fitting. The arrows show a residual wrap in the SEGUE unwrapped field map towards the mask edges that is not present in the LPU result.

LPU has several advantages over SEGUE. Even with the accelerated algorithm of SEGUE, LPU is still a lot faster, reducing the overall computation time for estimating the total field map to around 30 seconds. Moreover, it is much more robust against noisy voxels towards the mask edges (Figure 6.42, yellow arrows) and open-ended fringe lines [96]. However, it was shown in section 6.3.3.2, that it cannot be used in conjunction with either PDF or LBV to accurately predict local field variations around ellipsoidal susceptibility sources. Fortunately, in-vivo images are not expected to have such suscep-

tibility sources. Note that since LPU eliminates some of the background fields, it is not suitable for applications requiring an accurate total field map (e.g. distortion correction). Luckily, this is not an issue in QSM as long as the subsequent background field removal method can eliminate all residual background fields.

To summarise, non-linear fitting combined with LPU is a fast and efficient way of estimating the total field map. It remains to be investigated whether residual background fields can be removed from the resulting total field map in vivo.

6.4.3.3 Background field removal

Figure 6.43 shows local field maps in a healthy volunteer estimated by LBV (a) or PDF (b) using the three different masks. All six results were calculated from the total field map obtained using non-linear fitting combined with LPU from the previous section. The first thing to note is that using Mask 3 (bottom row) eliminated most of the voxels around the lymph nodes. This is also reflected in the fact that the corresponding line profiles (black dashed lines in the top row) are mostly zero across the volume for both methods. Secondly, using Mask 1 led to local field maps with large residual background fields (red arrows). Note that the LBV map contained substantially more areas of residual background fields than the PDF map. Moreover, the residual fields in the neck profile in both local field maps using Mask 1 were smaller with PDF compared to LBV (top row, blue solid lines and blue arrows). This further confirms that PDF is more robust to the choice of tissue mask than LBV (section 6.3.3.2).

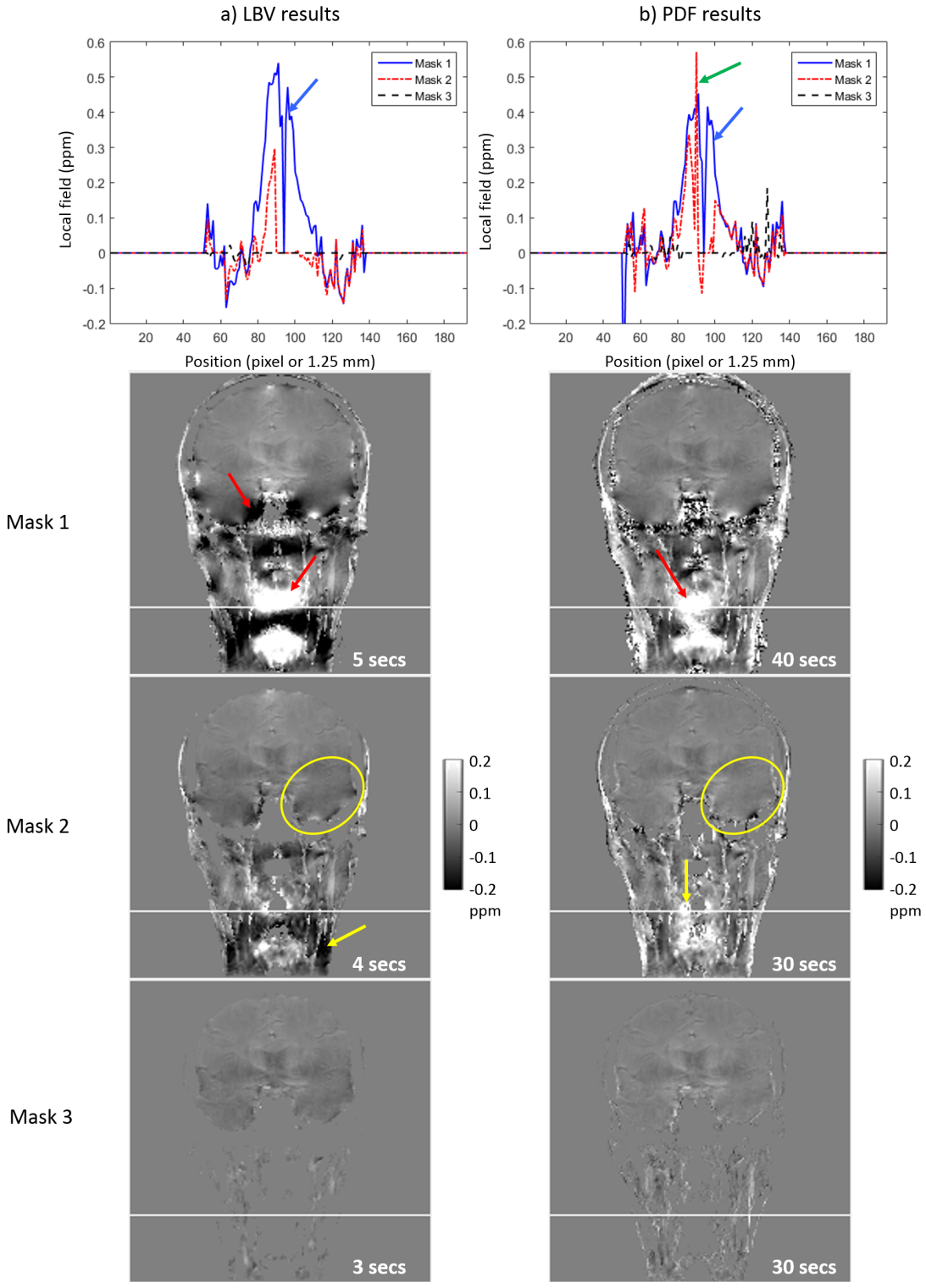

Figure 6.43: Comparison of LBV (a) and PDF (b) for the estimation of the local field map using three different tissue masks. The resulting local field maps and their profiles along the white lines are shown in both columns. Computation times are also displayed in the bottom right corner of each local field map.

Using Mask 2 resulted in acceptable local field maps (by visual assessment). Some residual background fields were present in the PDF map around the spine (Figure 6.43 b, yellow arrow) that led to a sharp spike in the line profile (green arrow). However, the LBV result contained more prominent residual background fields towards the bottom of the neck (Figure 6.43 a, yellow arrow). Furthermore, the PDF results looked smoother in the brain than the LBV results (yellow ellipses). LBV was about ten times faster than PDF, but even PDF's runtime was consistently around half a minute.

Figure 6.44 shows a similar comparison focusing on the previously segmented healthy lymph nodes (slightly hypointense regions indicated by the red arrows). The line profiles in the top row show that both techniques were robust to masking in and around the right node. However, PDF also provided similar field values using Mask 1 and Mask 2 in and around the left node. The contrast of the LBV results in the left node was different for the two tissue masks due to the large residual background fields. The local field maps obtained using Mask 3 had little to no contrast for both techniques (not shown).

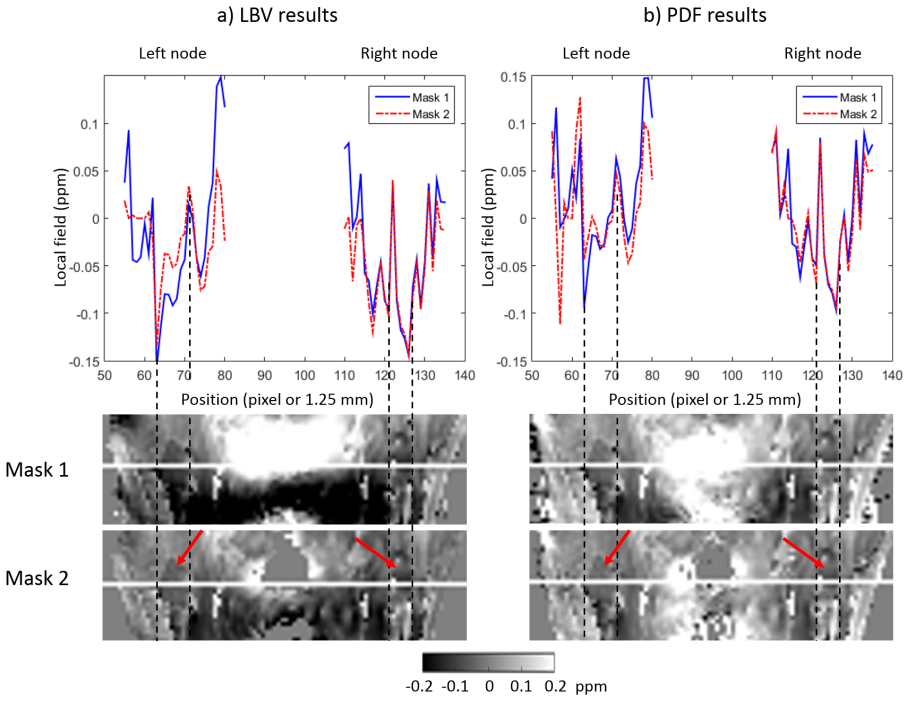

Figure 6.44: Comparison of LBV (a) and PDF (b) for the estimation of the local field map in the segmented lymph nodes. The resulting local field maps and their profiles (in and around the nodes) along the white lines are shown in both columns. The arrows indicate the healthy lymph nodes.

PDF successfully removed the vast majority of the background fields with all three masks. The local field maps did not contain any large residual background fields such as those in Figure 6.35. This supports our hypothesis that the residual fields were caused

by the ellipsoidal air space in the numerical head-and-neck phantom (section 6.3.3.2). Therefore, PDF is a suitable background field removal technique for in-vivo studies.

Areas with large susceptibility gradients need to be avoided when defining a tissue mask for LBV. However, the head-and-neck region contains such areas in abundance, e.g. tissue/air interfaces around the skin, the oropharyngeal airspaces, and the esophagus, and bone/air interfaces around the spine and the skull. Therefore, without carefully designed, individual tissue masks, LBV might not be able to perform adequate background field removal in the head and neck. This lack of robustness means that LBV is not suitable for large-scale clinical studies of the head and neck.

Note that this comparison is mostly qualitative and observational, i.e. the noise maps and SNR maps were not included due to reasons discussed in section 3.4.

In conclusion, though LBV is faster, PDF's greater robustness to the choice of binary tissue mask makes it more suitable for clinical studies. However, it is not yet clear how the mean susceptibility in cancerous lymph nodes is affected by potential residual background fields originating from applying LBV with an imperfect tissue mask. If the final measure is not sensitive to the tissue mask, LBV should be used for background field removal as it is much faster than PDF. Therefore, I decided to use both LBV and PDF in the repeatability study focusing on susceptibility mapping in head-and-neck images (chapter 7). Using Mask 2 (generated by thresholding the inverse noise map at its mean value) seems to provide a good compromise between residual background fields and excluded voxels.

6.4.3.4 Susceptibility calculation

Figure 6.45 shows the log-log plots of the (RN, RT) curves. Note that none of these have the classical L-shape. Regardless of this, $\alpha_{dir} = 0.11$, $\alpha_{iter} = 0.04$, and $\lambda = 160$ were selected as the regularisation parameters corresponding to the point of maximum curvature.

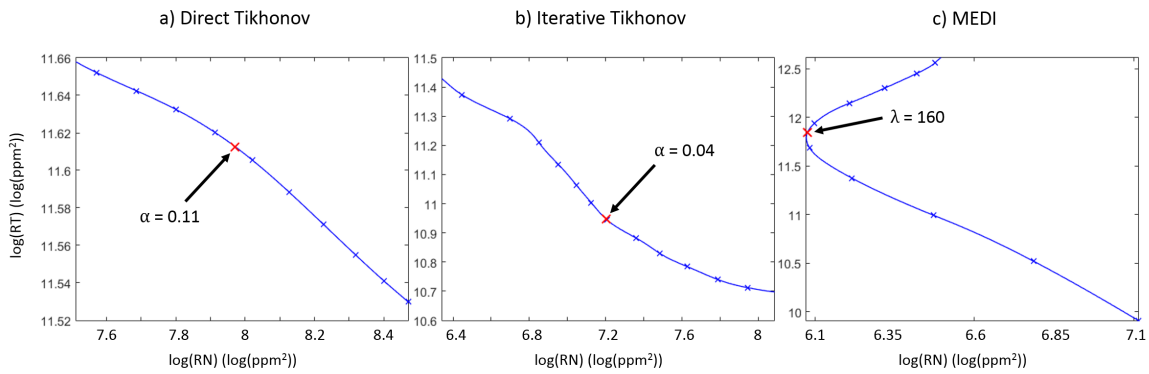

Figure 6.45: L-curve optimisation to select suitable regularisation parameters for the Tikhonov methods and MEDI.

Figure 6.46 shows susceptibility maps calculated using the five candidate methods with optimised parameters. As expected, the direct k-space inversion techniques (b-c) were much faster than the iterative fitting methods (d-f). The TKD result contained characteristic streaks originating from the high absolute susceptibility values near the edges of the tissue mask (a, yellow arrows). These streaks were substantially attenuated by the direct Tikhonov method at no extra computation time cost. There were unrealistically large susceptibility values towards the edges of the tissue mask in the direct Tikhonov result (c, red arrow and ellipse) due to residual background fields in the same regions. These could be improved by the weighting term used in the iterative Tikhonov method (d, red arrow and ellipse). The iterative Tikhonov technique is much slower than the direct k-space inversion methods, but it is still the fastest among the iterative fitting methods and a one minute run time is still feasible for large-scale clinical studies (note that about one minute was needed in total to calculate the local field map). Both MEDI and iLSQR provided susceptibility maps with reduced contrast compared to the other three techniques. This is most apparent in the brain, especially in the globus pallidus (e-f, black arrows). Morever, the line profile of MEDI also shows reduced contrast around one of the segmented healthy lymph nodes (a, green solid line, black arrows). MEDI was also extremely slow compared to all other techniques. The iterative Tikhonov method provided susceptibility maps with visibly less noise than iLSQR (d,f orange circles) as it uses the inverse noise map as a weighting term for the fitting unlike iLSQR.

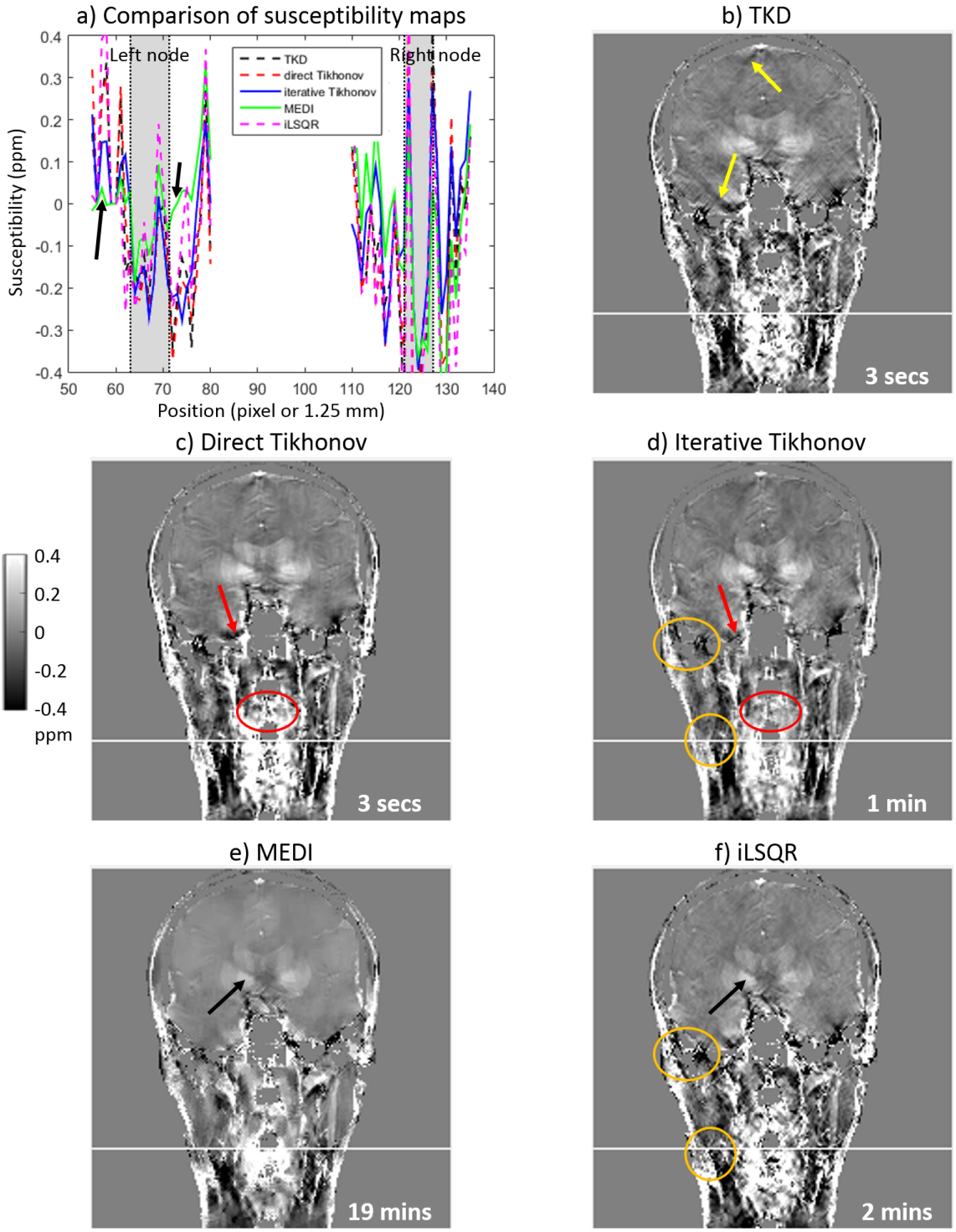

Figure 6.46: Comparison of TKD (b), direct Tikhonov (c), iterative Tikhonov (d), MEDI (e), and iLSQR (f) as susceptibility calculation methods in the head and neck. The resulting susceptibility maps (b-f) and their profiles (in and around the nodes) along the white lines (a) are also shown. The corresponding computation times are displayed in the bottom right corner of each image. The location of the lymph nodes is indicated by the gray background in (a).

Figure 6.47 shows mean susceptibilities calculated in the left and right lymph nodes of susceptibility maps obtained by the five different techniques. There is good agreement between the TKD, direct Tikhonov, and iterative Tikhonov results on both sides. iLSQR and MEDI provided slightly different values than the rest of the methods on the left and right sides respectively.

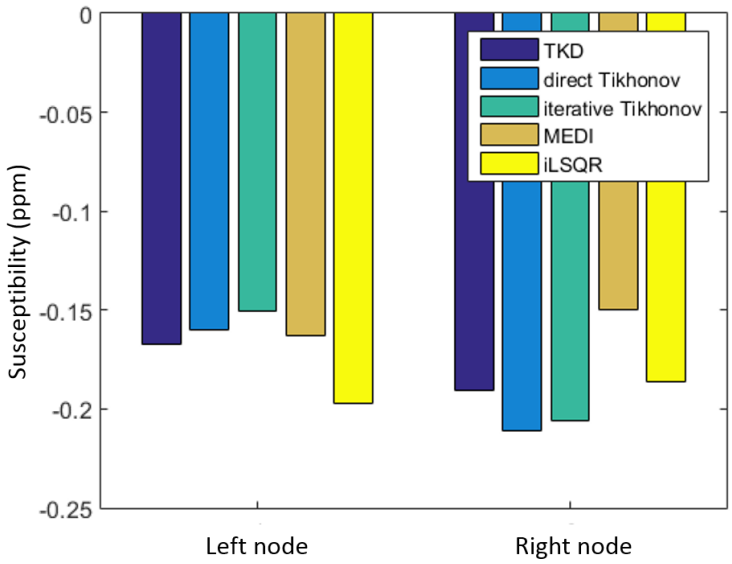

Figure 6.47: Mean susceptibility values measured in the two segmented lymph nodes.

For the k-space inversion methods (TKD and direct Tikhonov), the noise and SNR maps were calculated in the head and neck similarly to section 3.5. The results are shown in Figure 6.48. The direct Tikhonov results contained less noise (a) and had slightly higher SNR (b) than the TKD results across the entire volume including the two lymph nodes.

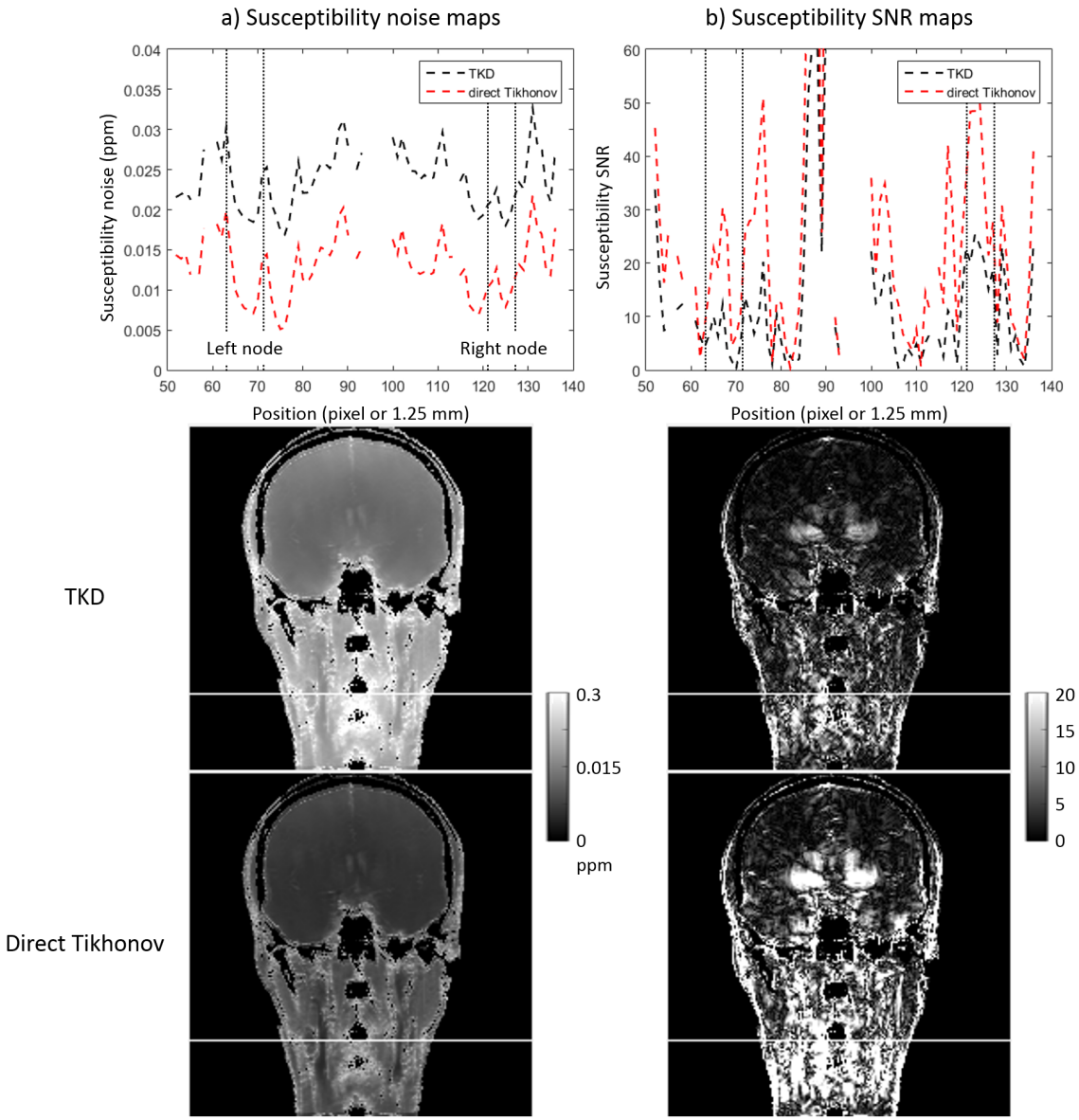

Figure 6.48: Susceptibility noise (a) and SNR (b) maps and profiles (in and around the lymph nodes) for the TKD and direct Tikhonov susceptibility calculation methods. The location of the lymph nodes is indicated by the dotted black lines in the plots in the top row.

Unfortunately, the above estimation of the susceptibility noise and SNR is not straightforward to perform for iterative fitting methods. One might think that using the direct Tikhonov kernel in Equation 3.29 from chapter 3 would give a good approximation for the noise distribution of the iterative Tikhonov technique. However, this approach would not account for the weighting term which is used specifically to reduce artifacts originating from noisy voxels. Therefore such a comparison would not be fair.

Another way of performing a numerical comparison of the methods is to measure SNR in the ROIs initially used for estimating the magnitude noise. The susceptibility is

expected to be fairly homogeneous within the 400-voxels white matter regions. However, there is more heterogeneity onserved in the lymph nodes, therefore these were excluded from the comparison. Susceptibility signal was measured as the mean susceptibility in each region, while the noise was approximated by the standard deviation within each region. Figure 6.49 shows the susceptibility SNR measured in the white matter for all five susceptibility calculation techniques. TKD seems to have slightly lower SNR than the rest, but there does not seem to be a substantial difference between the other four techniques. MEDI has the highest overall SNR because of its regularisation term leading to overly smooth results and very low noise. Therefore, it provides high SNR even with the substantially reduced contrast. However, the same smoothing is likely to attenuate essential features of the susceptibility map [113].

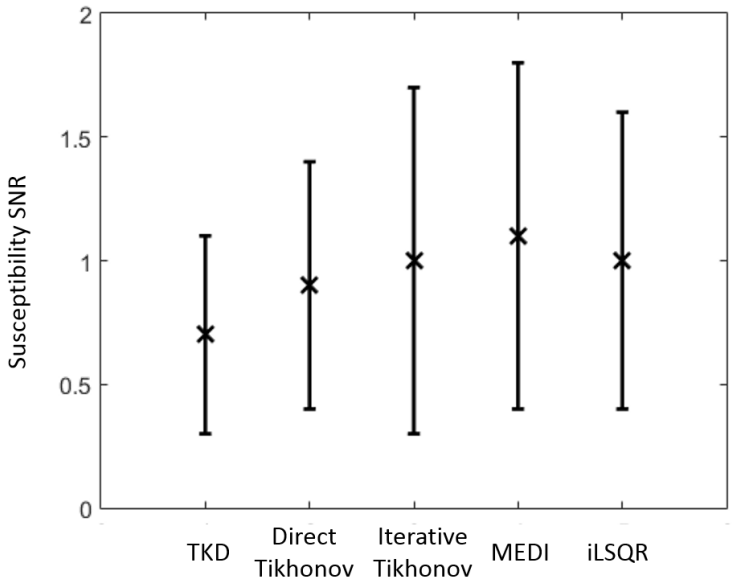

Figure 6.49: Comparison of susceptibility SNR of all five susceptibility calculation methods. The mean of the five SNR values measured in the five 400-voxel white matter regions is shown. The data have error bars equal to the standard deviations of the same five measured SNR values.

In conclusion, none of the techniques provided vastly superior SNR than the rest. Both Tikhonov techniques were able to sufficiently attenuate the streaking present in the TKD susceptibility map in a reasonable runtime. MEDI's computation time is too long for large-scale clinical studies and iLSQR is slower and provides noisier results than the iterative Tikhonov method. Therefore, I propose the direct and iterative Tikhonov techniques as candidate methods for susceptibility calculation in the head and neck.

In general, iterative fitting algorithms are better suited for susceptibility calculation within a mask of such a convoluted shape as these methods do not assume local field maps

outside the tissue mask to be zero but rather unknown. Therefore these methods deal better with edge effects which was demonstrated here. Due to the weighting term, these techniques also tend to perform better noise suppression [188]. Therefore, it is reasonable to use the iterative Tikhonov method instead of its direct version for head-and-neck images. However, it is not obvious if these properties have a substantial effect on the susceptibility measured in cancerous lymph nodes. In our example, mean susceptibilities in the segmented healthy lymph nodes were very similar for the two Tikhonov techniques. If it turns out that the improved susceptibility of the iterative Tikhonov method towards the mask edges does not affect the susceptibility measured in cancerous lymph nodes, direct Tikhonov should be used for susceptibility calculation as it is much faster. Therefore, I decided to include both direct and iterative Tikhonov techniques in the repeatability study focusing on susceptibility mapping in the head and neck (chapter 7).

6.4.4 Conclusions

Here I have optimised the QSM pipeline to produce high-quality susceptibility maps in the head and neck. Figure 6.50 summarises the methods and conclusions of this process. Non-linear fitting and Laplacian phase unwrapping were used to estimate the field map in consideration of their speed and the fact that, combined with LBV or PDF, they could provide accurate local field maps in the head and neck (section 6.3). PDF was found to be a more robust method for eliminating the vast majority of the background fields while LBV was much faster. A binary tissue mask of the head and neck generated by thresholding of the inverse noise map at its mean was used to identify regions with low noise that allowed accurate background field estimation. Iterative Tikhonov regularisation provided the least streaky and noisy susceptibility map with the best contrast out of the three susceptibility calculation techniques based on iterative fitting in the image domain. The susceptibility map obtained using the direct Tikhonov method was very similar to the iterative Tikhonov solution with a few more artifacts towards the mask edges. However, this did not affect mean susceptibilities measured in healthy lymph nodes and the direct approach was much faster.

In summary, the optimal pipeline consists of: 1. Non-linear fitting of the complex signal over echo time, 2. Laplacian phase unwrapping, 3. background field removal using PDF or LBV, 4. susceptibility calculation using iterative or direct Tikhonov. The repeatability study (chapter 7) and initial clinical trials need to establish if the potential residual background fields due to using LBV, or the poorer quality of the susceptibility maps towards the mask edges when using the direct Tikhonov method affect the final

susceptibility measure substantially. In the next chapter, I assess the repeatability of the susceptibility maps using all four potential QSM pipelines in a cohort of healthy volunteers.

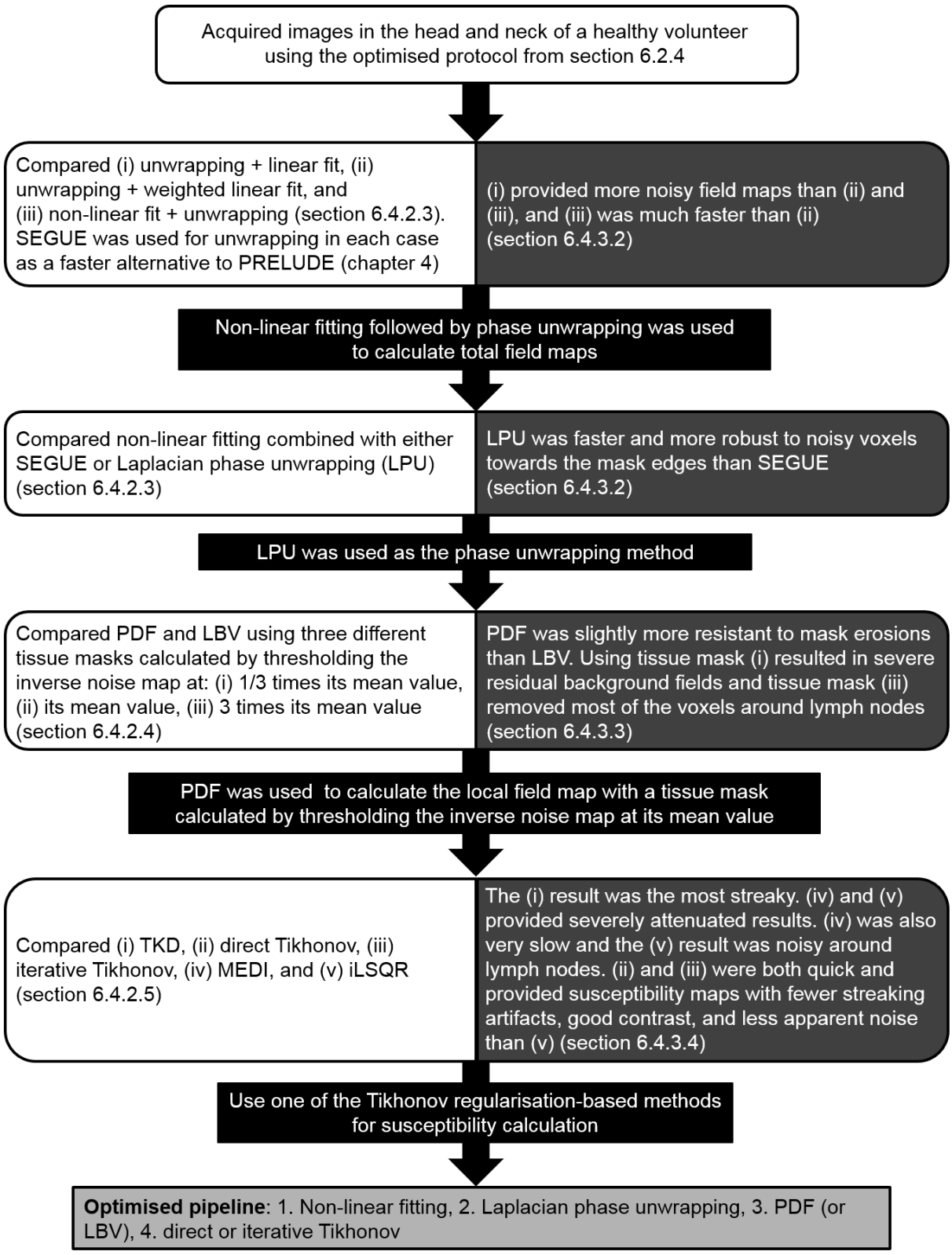

Figure 6.50: Summary chart of the QSM pipeline optimisation.

Chapter 7

QSM Repeatability in the Head and Neck

7.1 Introduction

In this chapter, I investigated the intrasession and intersession repeatability of the optimised acquisition protocol and the candidate susceptibility mapping pipelines from sections 6.2 and 6.4 respectively in healthy volunteers. The main goals of this chapter are to compare all four QSM pipelines from section 6.4 (i.e. non-linear field fitting, Laplacian phase unwrapping followed by either PDF or LBV for background field removal and direct or iterative Tikhonov for susceptibility calculation) in terms of repeatability and to determine if the measured repeatability is sufficiently high to detect hypoxia in head-and-neck cancer (section 1.1).

For the latter, I estimated the expected changes in susceptibility in hypoxic tumours using the back of the envelope calculation from section 1.3.1:

$$\chi_{hypoxic} - \chi_{normoxic} = V \cdot Hct \cdot 3.8 \text{ ppm} \approx \mathbf{0.3 \text{ ppm}} \tag{7.1}$$

where $V = 0.2$ is the vascular density, and $Hct = 0.4$ is the hematocrit level.

Note that previously, Panek et al. [49] have investigated the repeatability of T_2^* measurements in head-and-neck squamous cell carcinoma (HNSCC) and found it to be sufficiently high to detect a 10% change in tissue oxygenation. Since the T_2^* contrast partly originates from microscopic susceptibility variations, this result suggests that QSM should also be repeatable in the head and neck. The advantage of susceptibility over T_2^* mapping is that susceptibility is expected to scale linearly with tissue oxygenation, similarly to how

it has a linear relationship with fat fraction and bone mineral density shown in chapter 8. On the contrary, T_2^* is a complicated function of the oxygen concentration that was modelled to be quadratic in [49].

7.2 Methods

7.2.1 Data acquisition

The local ethics committee approved this study and informed consent was obtained from all participants.

Multi-echo head-and-neck images were acquired in 10 healthy volunteers (age range: 23-30 years, 7 females and 3 males) at 3 T (Achieva, Philips Healthcare, NL) using a 3D gradient-echo pulse sequence previously tailored for structural, head-and-neck QSM (section 6.2): a 16-channel receiver head-and-neck coil, coronal orientation (head-foot = readout direction), field-of-view = 24 cm×24 cm×22 cm, SENSE factor = 2 in the right-left (first phase encoding) direction, 1.25 mm isotropic resolution, 4 echoes, TR = 22 ms, and flip angle = 12°. In-phase echo timing ($TE_1 = \Delta TE = 4.61$ ms) was used to remove the chemical shift-induced phase differences between fatty and water-based tissues (section 6.1). Vendor-supplied first order gradient-moment nulling on the first echo (flow compensation) was turned on which resulted in first order gradient moments at all four echo times being very close to zero (section 6.2.3.3).

All 10 volunteers were scanned using the above sequence at two sessions a week apart, 3 times per session, to investigate both intrasession and intersession repeatability in healthy volunteers.

7.2.2 Susceptibility mapping pipeline

Susceptibility maps were calculated from all complex, multi-echo images using the following susceptibility mapping pipelines previously optimised for head-and-neck images (section 6.4):

1. Non-linear field fitting (section 2.2.1.3)
2. Laplacian phase unwrapping (section 2.2.2.2)

3. Background field removal using Projection onto Dipole Fields (PDF, section 2.3.4.1) or the Laplacian Boundary Value method (LBV, section 2.3.3.1)

4. Susceptibility calculation by solving the inverse problem with Tikhonov regularisation (section 2.4.2.2) either directly in k-space ($\lambda = 0.11$) or iteratively in image space ($\lambda = 0.04$, W = masked inverse noise map) using conjugate gradient minimisation

Zero padding to a matrix size of 256×256×256 was applied before using the direct Tikhonov susceptibility calculation technique in each case to avoid errors introduced by the Fourier and inverse Fourier transform. Head-and-neck tissue masks were generated by thresholding the inverse noise map at the mean of the inverse noise across the image. This simple method provided consistently suitable tissue masks for background field removal (section 6.4.3.3).

7.2.3 Regions of interest (ROIs)

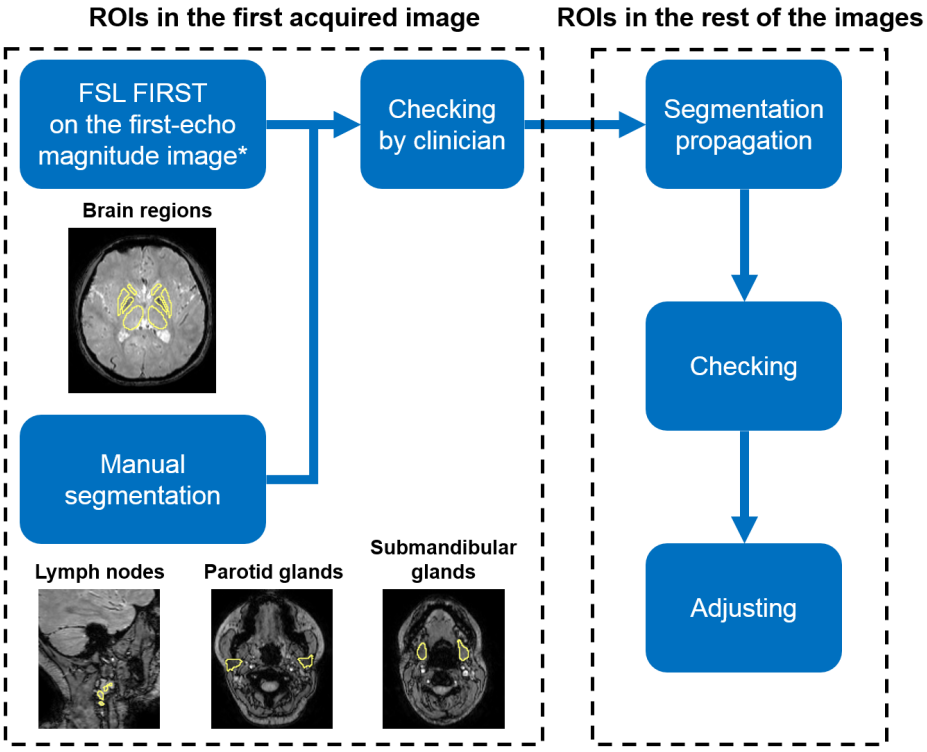

Figure 7.1: Pipeline for segmenting regions of interest in the brain and head and neck. *Delineation of the brain ROIs was done manually for two volunteers where FSL FIRST did not work. Note that the example ROIs are overlaid on last-echo magnitude images for better visibility in each case.

Figure 7.1 shows the pipeline for ROI segmentation. As a first step, ROIs were delineated in the first acquired image (the first image of the first scanning session). Brain regions (thalamus, caudate nucleus, putamen, globus pallidus) were automatically segmented using FSL FIRST [186] on the first-echo magnitude image. This worked reasonably well for most volunteers, but failed in two cases as FSL FIRST was designed to be used on T_1-weighted images, which have more contrast. In these two cases, the aforementioned brain ROIs were manually segmented in single, axial slices on the last-echo magnitude images using ITK-SNAP [184, 185].

Three types of healthy lymph nodes were segmented manually (using ITK-SNAP) on the last-echo magnitude image: small nodes, medium nodes, and the insides of larger nodular structures with a 1-2 voxel margin around them. Two of each of these were identified and delineated per volunteer wherever possible. The parotid and submandibular glands were also manually segmented in single, axial slices. All ROIs delineated in the first acquired images were checked by an experienced radiologist.

ROIs in the remaining five images were segmented by propagating the initial segmentation using a MATLAB-based, b-spline image registration tool [189–191]. The last-echo magnitude image of the first image was non-rigidly registered to the last-echo magnitude images of the rest and the resulting transformations were used to warp the aforementioned segmented ROIs. As a final step, all ROIs were checked visually and manually adjusted in ITK-SNAP if necessary.

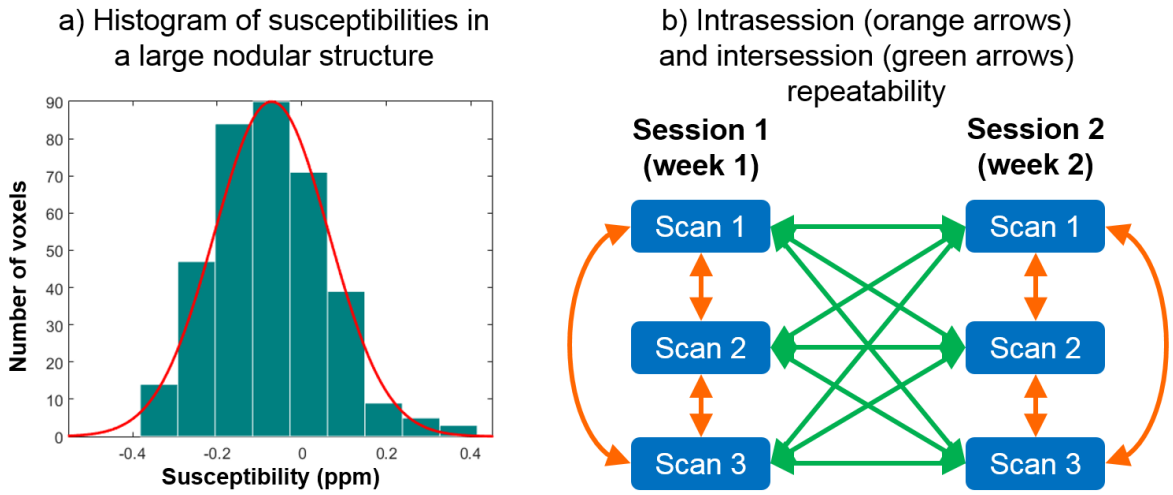

Figure 7.2: Susceptibility histogram in a typical large nodal structure (a) and diagram of the comparisons performed (b) for the intrasession (orange arrows) and intersession (green arrows) repeatability analysis.

Means and medians of susceptibilities were calculated in all regions of interest to compare the repeatability of these different measures in healthy volunteers. To justify the use of mean values, the symmetric histogram of susceptibilities in one of the bigger nodes is displayed in Figure 7.2 a.

7.2.4 Repeatability analysis

Before performing the repeatability analysis, the small and medium nodes were reassigned based on their actual volumes (VOL): small nodes < 300 mm^3; medium nodes > 300 mm^3. This threshold was set based on the distribution of the sizes to make sure that there were a similar number of lymph nodes in both categories. Another reassignment was also performed based on the short axis diameters (SAD) of the nodes: small nodes $<$ 5 mm; medium nodes > 5 mm, as this is the size measure most frequently used in clinical practice.

To evaluate the intrasession repeatability, differences of the measured mean or median susceptibilities were calculated between all pairs of scans acquired in the same session (Figure 7.2 b, orange arrows) and the distributions of these differences were considered for each ROI type. In case of high repeatability, these are expected to be narrow with a mean close to zero. Similarly, to evaluate intersession repeatability, differences of the measured mean and median susceptibilities were computed between all pairs of scans acquired in different sessions (7.2 b, green arrows).

The minimum detectable effect size in a single subject was calculated [192] for the different ROI types in the neck based on the standard deviations of the aforementioned distributions of susceptibility differences, assuming a Gaussian shape, with a type I error rate of $\alpha = 0.05$ and a type II error rate of $\beta = 0.2$.

7.2.5 The effect of fatty fascia on the measured susceptibility of lymph nodes

Many of the healthy lymph nodes were located within the fatty fascia between muscle sheets. However, fat has been repeatedly shown to have a much higher susceptibility than other tissues such as muscle (section 6.1). Therefore, the surrounding fat could confound the susceptibility measurements of lymph nodes e.g. if voxels of the fascia are included in the ROI by mistake, due to partial volume effects, or in case of susceptibility artifacts

originating from the large susceptibility gradient between the lymph node and the fatty fascia. These effects are expected to be more substantial for smaller nodes which have a higher surface-to-volume ratio. To investigate this issue, susceptibility histograms of all voxels in either small nodes, medium nodes, or larger nodular structures (segmented with a margin) were compared.

7.3 Results

7.3.1 Comparison of different QSM processing pipelines

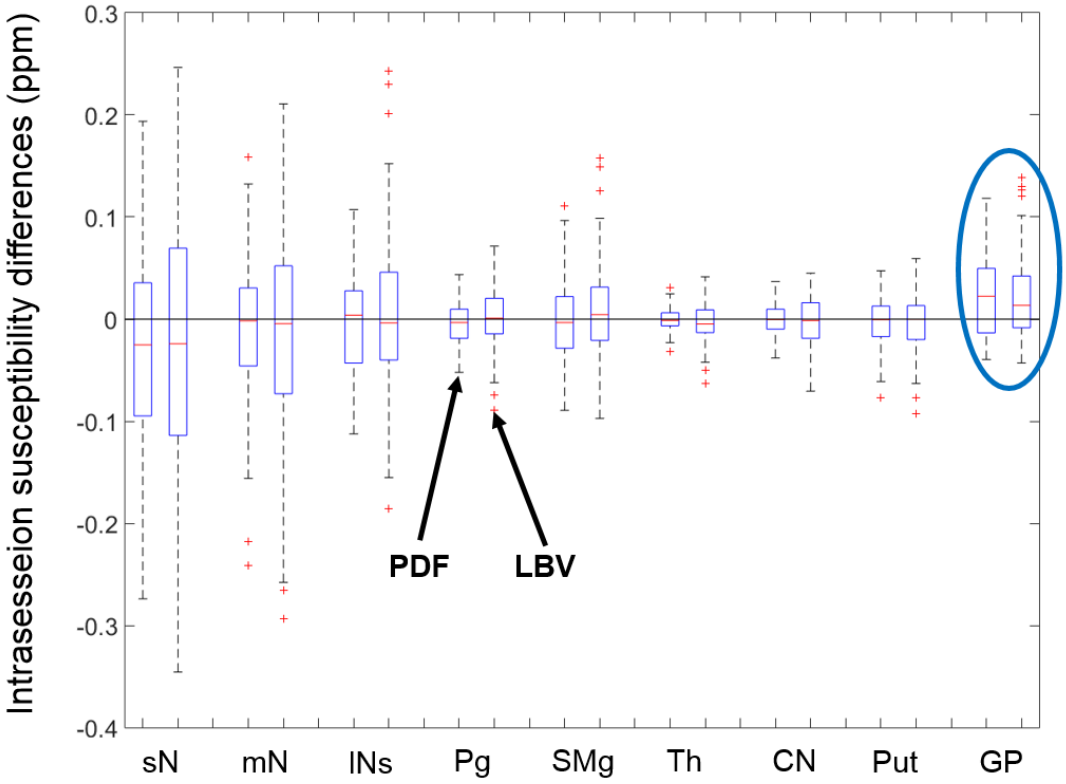

Figure 7.3: Box plots of intrasession mean susceptibility differences in different ROI types: sN —small nodes (VOL < 300 mm^3), mN —medium nodes (VOL > 300 mm^3), lNs —large nodular structures, Pg —parotid glands, SMg —submandibular glands, Th —thalamus, CN —caudate nucleus, Put —putamen, GP —globus pallidus.
For each ROI type, distributions on the left and right sides correspond to susceptibility maps obtained using PDF or LBV respectively (see arrows). All measured susceptibilities were calculated using direct k-space inversion.

Figure 7.3 shows the comparison of the PDF and LBV background field removal methods in terms of intrasession susceptibility repeatability in the head and neck. Here susceptibility maps were calculated using direct k-space inversion. The means of all distributions were very close to zero (within ±0.005 ppm) except for the small nodes and the globus pallidus. Susceptibility repeatability using PDF was higher than with LBV in all ROI types except in the globus pallidus (Figure 7.3, blue circle). We observed similar trends when using iterative fitting to calculate susceptibility maps and for intersession comparisons as well (not shown).

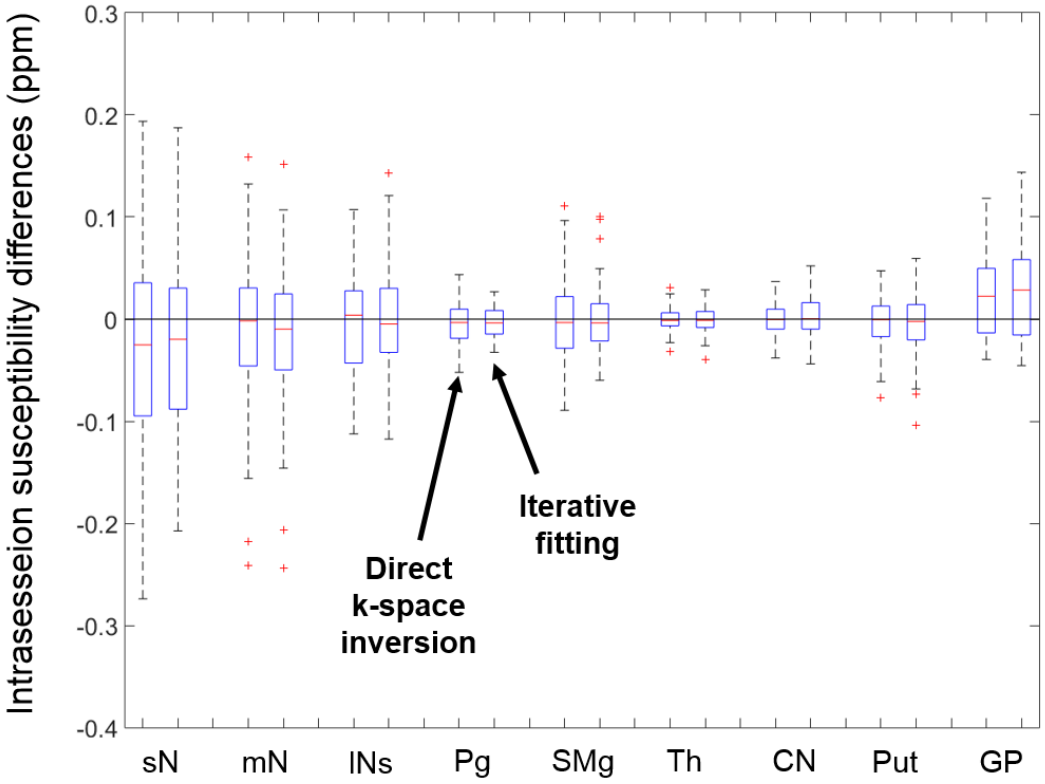

Figure 7.4: Box plots of intrasession mean susceptibility differences in different ROI types: sN —small nodes (VOL < 300 mm^3), mN —medium nodes (VOL > 300 mm^3), lNs —large nodular structures, Pg —parotid glands, SMg —submandibular glands, Th —thalamus, CN —caudate nucleus, Put —putamen, GP —globus pallidus.
For each ROI type, distributions on the left and right sides correspond to susceptibility maps calculated using direct k-space inversion or iterative fitting respectively (see arrows). PDF was used for background field removal in each case.

A similar comparison between direct k-space inversion and iterative fitting is displayed in Figure 7.4. Iterative fitting performed slightly better in terms of repeatability in small and medium nodes, and the parotid and submandibular glands. However, k-space inver-

sion provided marginally improved results in the larger nodular structures and all brain ROIs. Intersession repeatability using these two susceptibility calculation methods was also very similar (not shown).

In all previous comparisons, mean susceptibilities in ROIs was used as the summary measure. Here I compared the repeatabilities of the mean and median of susceptibilities measured in each ROI. Figure 7.5 shows that there was no substantial difference between the two measures in terms of intrasession susceptibility repeatability. I observed similar results for intersession susceptibility repeatability (not shown).

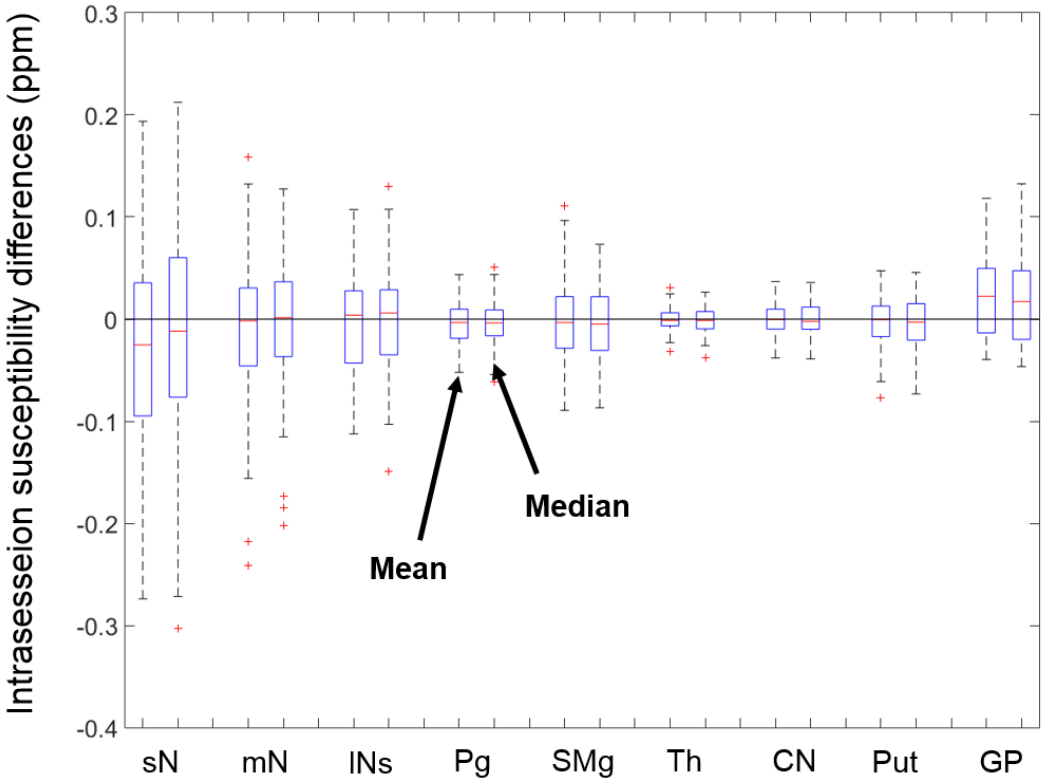

Figure 7.5: Box plots of intrasession mean and median susceptibility differences in different ROI types: sN —small nodes (VOL < 300 mm^3), mN —medium nodes (VOL > 300 mm^3), lNs —large nodular structures, Pg —parotid glands, SMg —submandibular glands, Th —thalamus, CN —caudate nucleus, Put —putamen, GP —globus pallidus.
PDF and direct k-space inversion were used for background field removal and susceptibility calculation respectively in each case.

7.3.2 Histograms of healthy lymph nodes of various sizes

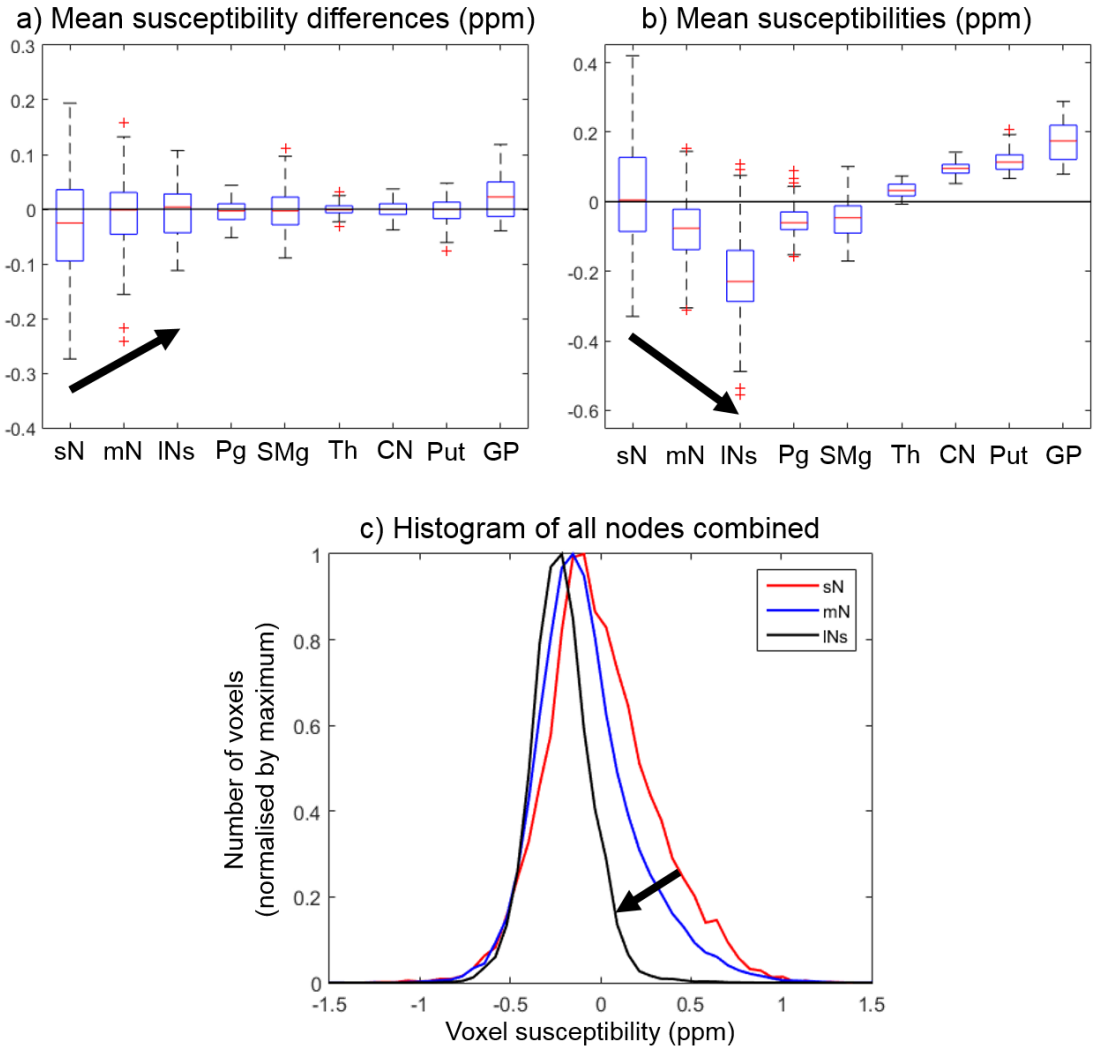

Figure 7.6: Box plots of intrasession mean susceptibility differences (a) and mean susceptibilities (b) in different ROI types: sN —small nodes (VOL < 300 mm^3), mN —medium nodes (VOL > 300 mm^3), lNs —large nodular structures, Pg —parotid glands, SMg —submandibular glands, Th —thalami, CN —caudate nuclei, Put —putamens, GP —globus pallidi.
Normalised susceptibility histograms of all voxels in sN, mN, or lNs are also shown (c). PDF and direct k-space inversion were used for background field removal and susceptibility calculation respectively in each case.

Figure 7.6 a shows the distributions of intrasession mean susceptibility differences calculated using PDF and direct k-space inversion. The arrow indicates that higher repeatability was measured in the medium-sized nodes than in small nodes, and even higher repeatability in large nodular structures. In addition to this, Figure 7.6 b shows that the measured range of mean susceptibilities decreased from small nodes to medium nodes, and again from medium nodes to larger nodular tissue. Moreover, the susceptibility his-

tograms in these three ROI types (Figure 7.6 c) were very similar on the diamagnetic (left) side, but showed different distributions on the paramagnetic (right) side. The histogram of the voxels in larger nodular tissue (Figure 7.6 c, black line) was relatively narrow and symmetric with a mean of around -0.2 ppm. While the susceptibilities corresponding to the maximum number of voxels were close to each other (within 0.1 ppm) for all three ROI types, there were more and more paramagnetic voxels in the medium (Figure 7.6 c, blue line) and small (Figure 7.6 c, red line) nodes as the distributions became more positively skewed.

7.3.3 Detectable effect sizes for different structures

Figure 7.7 shows distributions of both the intrasession (top) and intersession (bottom) mean susceptibility differences calculated using PDF and direct k-space inversion. Standard deviations (SD) are also displayed at the bottom of each plot. Here the small and medium nodes were reassigned based on both volume (VOL) and short-axis diameter (SAD). Repeatability was only marginally higher for the volume-based classification in most cases. The distributions of the intersession differences were generally broader than those of the intrasession differences and their means very slightly further from zero in most cases. Both of these indicate higher intrasession than intersession repeatability in the head and neck.

Small nodes (either VOL < 300 mm^3 or SAD < 5 mm) had the lowest repeatability (both intrasession and intersession) among all tissue types followed by medium-sized nodes. Larger nodular structures (lNs), the submandibular glands (SMg), and the globus pallidus (GP) had similar intrasession SDs (although the distribution of the GP was off-center). The intersession repeatability of both the lNs and the SMg were closer to that of the medium-sized nodes. The GP had similar intrasession and intersession susceptibility difference distributions. The susceptibilities measured in the parotid glands, thalamus, caudate nucleus, and putamen were the most repeatable (both intrasession and intersession) out of all ROI types discussed here.

Minimum detectable effect sizes (MDEs) were calculated for five ROI types (Figure 7.8) based on their intrasession susceptibility difference distributions. Small nodes had the highest detectable effect size (0.27 ppm) followed by medium-sized nodes (0.16 ppm). The effect sizes of the other three ROI types were all around or lower than 0.1 ppm. The minimum detectable effect size was especially low for the parotid glands (0.06 ppm).

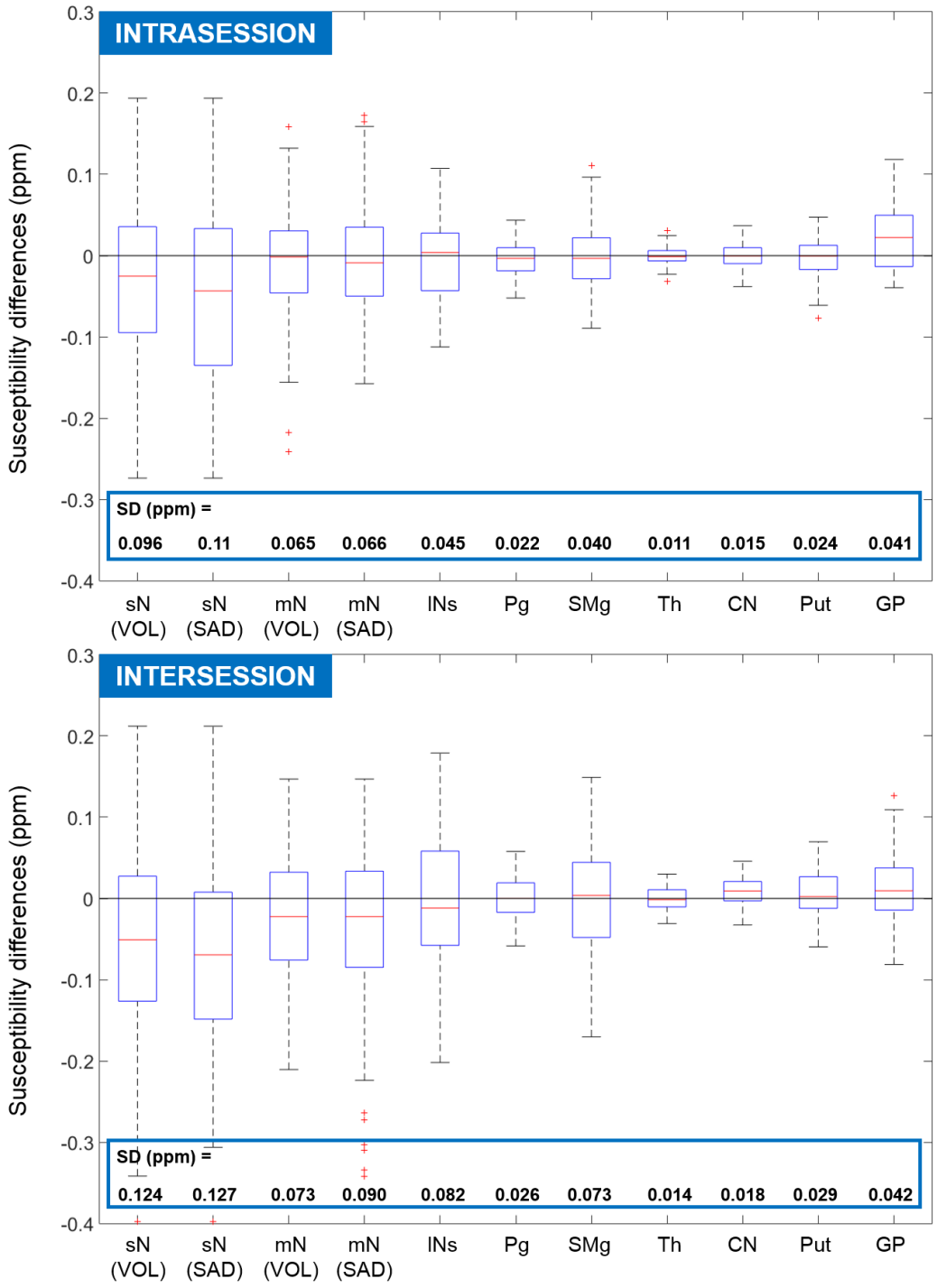

Figure 7.7: Box plots of intrasession (top) and intersession (bottom) mean susceptibility differences in different ROI types: sN —small nodes (both VOL < 300 mm^3 and SAD < 5 mm are shown), mN —medium nodes (both VOL > 300 mm^3 and SAD > 5 mm are shown), lNs —large nodular structures, Pg —parotid glands, SMg —submandibular glands, Th —thalamus, CN —caudate nucleus, Put —putamen, GP —globus pallidus.

PDF and direct k-space inversion were used for background field removal and susceptibility calculation respectively in each case. Standard deviations (SD) of each distribution are displayed at the bottom of both plots.

Region of interest	SD	Detectable effect size
Small node (SAD)	0.110 ppm	0.27 ppm
Medium node (SAD)	0.066 ppm	0.16 ppm
Large nodal structure	0.045 ppm	0.11 ppm
Parotid glands	0.022 ppm	0.06 ppm
Submandibular glands	0.040 ppm	0.10 ppm

Figure 7.8: Minimum detectable effect sizes calculated for five ROI types in the neck based on the intrasession distributions.

7.4 Discussion

Here I investigated the repeatability of the optimised MRI acquisition protocol and QSM pipelines from sections 6.2 and 6.4 respectively. I compared both intrasession and intersession images in 10 healthy volunteers using various brain regions, the parotid and submandibular glands, as well as healthy lymph nodes. I also compared the candidate QSM pipelines from section 6.4 based on the measured repeatabilities, and the mean and median susceptibilities within each region of interest (ROI) as summary metrics. I calculated the minimum detectable effect sizes for ROIs in the neck. I found that PDF provided more repeatable susceptibility maps than LBV, but there was no substantial difference between the two susceptibility calculation methods. In healthy volunteers, the mean and median of susceptibilities within the ROIs seemed equally good metrics.

Susceptibility maps obtained using PDF, as opposed to LBV, as the background field removal (BFR) method had higher intrasession and intersession repeatability combined with either direct or iterative Tikhonov as the susceptibility calculation step. In section 6.3, I have shown and discussed that the result of LBV is sensitive to the exact shape of the tissue mask, because its assumption that the internal field is zero on the mask boundary might be violated. However, my comparison of these two techniques in-vivo in section 6.4 was mostly qualitative, based on visual inspection. Moreover, PDF was shown to have problems removing background fields around ellipsoidal susceptibility sources when combined with Laplacian phase unwrapping in a numerical phantom (section 6.3.3.2), even though the same was not observed in-vivo (section 6.4.3.3). Therefore, I decided not to exclude LBV as a candidate BFR method for our optimised protocol at that stage.

However, this repeatability study unambiguously showed that LBV is less reliable than PDF in large-scale studies. Therefore, I propose PDF as the BFR method of choice for QSM in the head and neck.

Iterative fitting in image space using Tikhonov regularisation (iterative Tikhonov) seemed to provide susceptibility maps of slightly higher repeatability in most ROIs in the neck (most lymph nodes, and the parotid and submandibular glands) compared to using direct k-space inversion (direct Tikhonov). This is expected, as the iterative Tikhonov method accounts for the noise distribution within the tissue as opposed to the direct version. Moreover, the direct Tikhonov method implicitly assumes that the measured field is zero outside of the tissue mask, while the iterative Tikhonov technique does not. This could lead to errors in the measured susceptibility values e.g. if the field perturbations induced by an ROI extend beyond the tissue mask. However, both the repeatability (Figure 7.4) and the measured mean susceptibility values (not shown) were very similar for the two techniques which suggests that either the size or the susceptibility of the aforementioned ROIs is too small for them to induce very large field perturbations. Note that this might not be the case in patients with cancerous lymph nodes which are expected to be larger than healthy nodes [193] and could be strongly paramagnetic due to hypoxia. In brain regions and the large nodular structures, the direct Tikhonov method had slightly better repeatability. Also, this technique is much faster than iterative Tikhonov (section 6.4.3.4). In summary, both susceptibility calculation techniques have similar repeatability in the head and neck of healthy volunteers and both techniques have potential advantages on a theoretical or computational level. I propose both techniques to be tested and compared in head-and-neck images acquired in patients to determine which method is more suitable for a specific application.

Our repeatability analysis does not show any substantial difference between using the mean or the median of susceptibilities within an ROI as a summary metric. This might be because the distribution of susceptibilities in most ROIs is roughly symmetric (e.g. Figure 7.2 a), therefore the mean and median are very similar. This might be the case for healthy lymph nodes, however, distributions are likely to be much more skewed in diseased lymph nodes [194]. Moreover, the median is a more robust metric in general [182]. Therefore, I propose the median to be used in patient studies.

In section 7.3.2, I have shown that the susceptibility distribution of smaller nodes was positively skewed. The histogram of large nodular structures was symmetric, whereas that of the medium nodes and especially the small nodes indicated more and more paramagnetic voxels. This is most likely caused by the inclusion of the surrounding fatty

voxels in these ROIs. In the head and neck, most healthy lymph nodes are located within the fatty fascia between muscle sheets. Fat is known to appear paramagnetic (i.e. bright) in susceptibility maps (section 6.1). If the ROIs are not drawn perfectly, some of these high-susceptibility voxels might be included by accident. Small lymph nodes were affected the most by this as these have relatively large surface areas compared to their volumes. Since only the insides of large nodular structures were segmented with a 1-2 voxel margin around them, there were less fatty voxels accidentally included in these ROIs. Therefore, these structures are expected to have symmetric distributions characteristic of healthy lymph nodes. This explains why large nodular structures have lower mean susceptibilities than medium or small lymph nodes. It also explains why small nodes seem to have poor repeatability as their mean (or median) susceptibility is largely affected by the number of accidentally-included fatty voxels and this can vary from scan to scan. It could be argued that these trends are primarily introduced by the different number of voxels in the three ROI types, i.e. averaging across more voxels gives a more reliable estimate and, therefore, corresponds to higher repeatability. However, the segmented portions of the large nodular structures had similar volumes to the small lymph nodes while the medium-sized nodes were generally much larger. Since the susceptibility measured in large nodular structures was substantially more repeatable than that of the medium nodes, we can assume that the 1-2 voxel margin plays an important role in this result. These observations also provide a guideline for future studies when lymph nodes are to be segmented in the head and neck. To sum up, susceptibility measured in bigger lymph nodes is more reliable in general, but making sure that all surrounding fatty voxels are excluded from the ROI is even more important as these can confound the measured mean or median susceptibilities. Also note that though using the pipeline in Figure 7.1 for segmentation was sufficient to perform this study, a robust, automated segmentation algorithm is needed in the future for multi-centre head-and-neck studies.

Note that the susceptibilities of brain regions in Figure 7.6 b are in accordance with their literature values [22, 111, 119, 178, 179]. Also, all distributions of susceptibility differences were centred around zero apart from those of the small lymph nodes and the globus pallidus. In the previous paragraph, I explained how accidentally including voxels from the surrounding fatty fascia can confound the measurements in small nodes. A similar effect is expected in the globus pallidus as these structures are much more paramagnetic than their surroundings, so imperfect segmentation induces more error. Delineating the small lymph nodes across scans consistently was also challenging, because in some cases it was hard to identify the same small node in different scans. Incorrectly identified nodes might be another factor contributing to the relatively low repeatability of the small nodes.

Nodes reassigned based on their volume (VOL) or short-axis diameter (SAD) had similar repeatabilities, but the latter measure is more widely used in clinical practice.

Intersession repeatability in all ROI types was at least slightly worse than intrasession repeatability. This could be due to real biological changes and/or more errors in the ROI segmentations introduced by the intersession non-rigid image registration than the intrasession registration. The minimum detectable effect size needs to be calculated based on either the intrasession or the intersession standard deviations (SD) with the specific application in mind. For example, if QSM is to be used to identify hypoxic sites in a tumour or assess different oxygen-enhancement techniques [147] in a cancerous lymph node in one session, the intrasession values should be utilised as in Figure 7.8. Note that the calculated effect size of both medium-sized nodes (0.16 ppm) and large nodal structures (0.11 ppm), as well as the parotid (0.06 pm) and submandibular (0.1 ppm) glands seems to be small enough to detect the aforementioned 0.3 ppm difference due to changes in deoxyheamoglobin levels in hypoxic tumours (Equation 7.1). In other words, this level of repeatability is sufficient to detect a 20–50% change in oxygenation. Repeatability of small nodes is not sufficient for identifying hypoxic sites, but note that cancerous lymph nodes tend to be bigger in any case [193]. Panek et al. [49] showed that the repeatability of T_2^* in HNSCC tumours was high enough to detect a 10% change in oxygenation. However, they used a much higher vascular density ($V = 0.85$) in their model. Using the same factor, we should be able to detect a 5–13% change in tissue oxygenation which is similar to their result.

7.5 Conclusions

In this chapter, I have investigated the intrasession and intersession repeatability of the optimised MRI acquisition protocol and susceptibility mapping pipelines from sections 6.2 and 6.4 respectively. I concluded that the measured repeatability in healthy lymph nodes, as well as the parotid and submandibular glands is high enough to detect hypoxia in head-and-neck tumours.

I proposed PDF to be used in head-and-neck QSM as it provided more repeatable results than LBV, but the direct and iterative Tikhonov susceptibility calculation methods should be further compared in patient studies. While there was no substantial difference in using the mean or median within ROIs as a summary metric in this study, the median should be preferred in patient studies as it is more robust in skewed distributions expected in cancerous tissue.

The repeatability of small lymph nodes (either less than 300 mm^3 in volume or 5 mm in short-axis diameter) was not suitable to detect the estimated changes in tissue oxygenation, but cancerous nodes are generally larger than that. I have also demonstrated the importance of accurate ROI segmentation. It is essential to avoid the inclusion of high-susceptibility fatty voxels from the surrounding fascia when delineating lymph nodes.

Chapter 8

Association of Bone Mineral Density and Fat Fraction with Magnetic Susceptibility in Inflamed Trabecular Bone

8.1 Motivation

In collaboration with Dr Timothy J.P. Bray, we have investigated tissue magnetic susceptibility as a surrogate to measure bone mineral density. In a previous study, Bray et al. [71] have shown that R_2^* ($= 1/T_2^*$) could differentiate between normal bone marrow and fat metaplasia (an area with increased fat content) possibly because the difference in magnetic susceptibility resulted in reduced relaxation rates in fat metaplasia. Therefore, QSM could potentially provide a quantitative measure of the diamagnetic bone content. We decided to apply my expertise in susceptibility mapping in challenging anatomical regions to investigate this possibility.

The following chapter has been accepted as a full paper to Magnetic Resonance in Medicine on 20 November 2018. Dr Timothy J.P. Bray has acquired all the data, has drawn regions of interest on the in-vivo images, and drafted the Introduction and Results sections of the paper. I have performed all subsequent processing, delineated regions of interest in the phantoms, prepared all the figures, and drafted the Methods section of the paper. We have contributed equally to the Discussion and Conclusions sections. We have submitted the paper as joint first authors.

8.2 Introduction

The spondyloarthritides are a group of inflammatory diseases involving the spine, lower limb joints, and entheses [66]. New bone formation is a key feature of spondyloarthritis and causes spinal fusion, which contributes to pain, morbidity and disability. Conversely, spondyloarthritis patients may also suffer from bone loss in the form of osteoporosis [65], which contributes to increased fracture risk. Both disease processes cause alterations in bone mineral density (BMD), but this tissue property is difficult to measure using the conventional T_1-weighted and T_2-weighted short tau inversion recovery (STIR) spin echo images which are widely used in clinical practice [67–69]. BMD is routinely measured in the clinic using dual-energy X-ray absorptiometry [195]. However, this method does not provide 3-dimensional spatial information, and cannot account for changes in body and skeletal size leading to errors in the quantification of BMD, e.g. in children. Therefore, there is a clinical need for a quantitative, MRI-based method which can be used to measure the spatial distribution of BMD, and enable the monitoring of new bone formation and bone loss in spondyloarthritis. An MRI-based measure of BMD could also be useful for drug development, as there are a number of emerging therapies designed to inhibit bone formation in spondyloarthritis which currently lack a corresponding biomarker [196].

Previously, Bray et al. have proposed R_2^* as a quantitative biomarker of trabecular BMD as the diamagnetic nature of bony trabeculae is expected to increase the rate of signal decay [71]. They found a positive correlation between BMD and R_2^* in a fat-water-bone phantom (a mixture of peanut oil, agar solution, and granules of bovine bone matrix), and also significantly reduced R_2^* in areas of fat metaplasia (an area with increased bone marrow fat content post inflammation [197]) in patients with spondyloarthritis. However, R_2^* measurements are also influenced by variations in fat content, and the relationship between fat fraction (FF) measurements and R_2^* is complicated. This complexity arises because fat contributes to dephasing both within the voxel, because of the multi-peak fat spectrum [198, 199], and in adjacent voxels, due to field inhomogeneities induced by magnetic susceptibility differences between water-based and relatively more paramagnetic fatty tissue [64,81,141]. Furthermore, R_2^* measurements cannot differentiate between para- and diamagnetic structures [21].

Recently, quantitative susceptibility mapping (QSM) [21,127,129] has been investigated as an alternative method for quantifying BMD, with promising initial results [200, 201]. Dimov et al. showed that susceptibility values were closely correlated with CT measurements of BMD in a porcine hoof, and were able to generate susceptibility maps in which cortical bone was homogenous and diamagnetic, as expected from theory [200]. However,

susceptibility mapping is challenging in the presence of varying fat content, which is a characteristic feature of bone marrow inflammation in spondyloarthritis [71]. Similarly to R_2^* measurements, susceptibility estimates can be confounded by variations in fat content, which contribute to dephasing both within the voxel (due to chemical shift) and in adjacent voxels (due to field inhomogeneities arising from the higher susceptibility of fat relative to water-based tissue [64, 81, 141]).

In this study, we investigated the feasibility of QSM in inflamed bone marrow. The described method was designed to correct for the effect of chemical shift. We also attempted to separate the fat contribution to total susceptibility so that 'fat-corrected' susceptibility measurements could be calculated. We evaluated the relationship between susceptibility, FF, and BMD in dedicated phantoms containing fat, water, and trabecular bone. Furthermore, we evaluated the differences in susceptibility between areas of normal marrow, oedema and fat metaplasia in patients with spondyloarthritis.

8.3 Methods

This study received ethical approval from the Queen Square Research Ethics Committee, London, United Kingdom (Research Ethics Committee reference 15/LO/1475). All patients gave written informed consent prior to study entry.

8.3.1 Fat-Water-Bone Phantom

We investigated the effect of fat fraction (FF) and bone mineral density (BMD) on the calculated susceptibility using a fat-water-bone phantom (Figure 8.1) consisting of varying concentrations of peanut oil, water and decellularized bovine trabecular bone matrix, as previously described [71]. This phantom consists of twenty 5-ml scintillation vials with FF measurements varying by row and BMD measurements varying by column (Figure 8.1 b), with the range of FF and BMD values (0 - 60% and 0 - 150 mg/cm^3 respectively) designed to cover the range of values expected in both normal marrow and disease states [71, 202]. As described previously, FF values in the phantom are calculated by volume and can be regarded as 'reference' FF values rather than true proton density fat fraction (PDFF) measurements, although the two parameters are expected to be very similar [71]. The phantom was immersed in distilled water (without doping) for scanning.

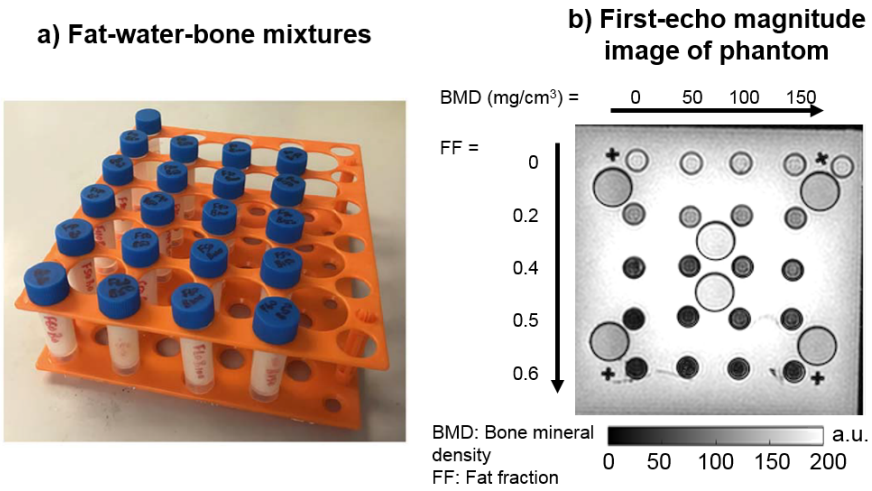

Figure 8.1: Fat-water-bone phantom. Fat fraction (FF) measurements vary by row, whereas bone mineral density (BMD) measurements vary by column. The phantoms were immersed in distilled water for scanning. The larger tubes shown in (b), interspersed between the columns of the phantom, contain fat-water mixtures which were used as a visual check on the quality of fat-water decomposition (i.e. to exclude fat-water swaps) whilst optimising the acquisition.

8.3.2 Fat-Water Phantom

A new fat-water phantom was also created to examine the relationship between susceptibility and fat fraction over the full FF range (0 - 100%). Eleven 50-mL centrifuge tubes were filled with mixtures of water and lard (rather than peanut oil as lard enabled us to create stable, solid phantoms which did not separate at high FF), using sodium dodecyl sulphate (SDS) as a surfactant, with FF values varying from 0% to 100%, in 10% increments. The final SDS concentration in each phantom was 28 mM. Although this phantom allowed us to investigate the susceptibility at higher FF values, the dispersion of lard in water was poorer than that of peanut oil (in the fat-water-bone phantom) leading to visible clumping in the tubes with FF 50 - 80%. Therefore R_2^* values were not measured in this phantom. Again, this phantom was immersed in distilled water for scanning.

8.3.3 Patients and volunteers

This study was performed using data previously acquired by Bray et al. [71] in 18 patients (aged 12 to 30 years) diagnosed with or suspected of having spondyloarthritis. Patients with suspected spondyloarthritis were treated as controls if the subsequent clinical MRI scan and clinical assessment were found to be normal (n = 10).

8.3.4 Data acquisition

MRI magnitude and phase images of the fat-water-bone phantom and the subjects were acquired by Bray et al. [71] at 3T (Ingenia, Philips Healthcare, NL) using a 3D spoiled gradient-echo pulse sequence with monopolar readout gradients, with integrated posterior and anterior surface coils (each with 16 channels). Images of the phantom were acquired coronally, with the following parameters: field of view = 30×30×80 cm^3, resolution = 0.94×0.94×1.5 mm^3, TE_1 = 1.233 ms, ΔTE = 1.951 ms, 6 echoes, TR = 23 ms, flip angle = 3°, bandwidth 1159 Hz/pixel. Images of the patients and volunteers consistent of tilted coronal slices through the sacroiliac joints (parallel to the long axis of the sacrum), field of view = 50×50×80 cm^3, resolution = 1.56×1.56×2 mm^3, TE_1 = 1.17 ms, ΔTE = 1.6 ms, 6 echoes, TR = 25 ms, flip angle = 3°, bandwidth 1894 Hz/pixel. Phantoms and subjects were also imaged using a similar vendor-supplied gradient-echo sequence with bipolar readout gradients (Philips, mDixon Quant, Philips Healthcare, Andover, Massachusetts, USA) [198], which provided proton density fat fraction (PDFF) and R_2^* maps with the same matrix size and field of view as the raw complex data. The mDixon Quant algorithm assumes a 10-peak model of human adipose tissue and a single R_2^* decay term, as previously described [198,199]. Multi-echo images of the new fat-water phantom were acquired with the same sequence used for scanning the fat-water-bone phantom described above.

Subjects also underwent a standard clinical MRI scan on a 1.5T system (Avanto, Siemens, DE) with angled coronal (tilted at the same angle as the gradient-echo images) T_1- and T_2-weighted STIR sequences [203].These images were used only as landmarks for the manual segmentation of normal bone marrow, bone marrow oedema, and fat metaplasia by an experienced radiology registrar (T.J.P.B.). Susceptibility mapping was only applied to the images acquired at 3T.

8.3.5 Susceptibility mapping (QSM) pipeline

Susceptibility maps were obtained from all multi-echo images [204] using the following, optimised QSM pipeline: 1. Three-point Dixon method [76] to estimate a field map without fat-water chemical shift effects, 2. Laplacian phase unwrapping [96] to remove temporal and spatial phase aliasing, 3. Projection onto dipole fields [109] to remove background fields, and 4. direct k-space inversion using Tikhonov regularisation [87,113] to calculate the susceptibility maps.

The three-point Dixon method (step 1) requires only three equally spaced echoes. We used the first, third, and fifth echoes of both the phantom and subject images, as these consistently provided images with the fewest fat-water swapping artifacts by visual inspection. All images were zero-padded to a matrix size of 512×512×128 before steps 2 and 4 to avoid errors introduced by the application of direct and inverse Fourier transforms in these methods. The tilt of the coronal slices was accounted for by defining the dipole kernel to be parallel to the real direction of the main magnetic field in steps 3 and 4. The Tikhonov regularisation parameter was set to $\alpha = 0.05$ in step 4 based on the optimised value in [113].

The background field removal (step 3) requires a binary tissue mask. Initial masks were obtained in each case by thresholding the inverse noise map calculated from the multi-echo magnitude images [86, 87] to exclude high-noise voxels that could introduce streaking into the susceptibility maps. In the phantoms, artifact-inducing structures (i.e. the plastic struts of the vial holders) were manually segmented in the first-echo magnitude images using ITK-SNAP [184,185] and also excluded from the masks. In the patient and volunteer images, bony voxels were often excluded due to their high noise levels. However, this study aimed to calculate susceptibility maps in bone marrow so some of these noisy bony voxels were of interest. We could have adjusted the threshold for the masking step to include these bony areas in the tissue mask but then other noisy, artifact-inducing voxels (e.g. around the tissue/air interfaces in bowel) would be included as well. Therefore, we used the original threshold and added the excluded bone to the tissue mask later. These bony voxels were identified in all subjects using the following scheme: 1. Bones were manually segmented (by A.K.) in the first-echo magnitude image of one of the healthy volunteers (subject 1) in ITK-SNAP [184, 185]. 2. All scanner-provided water images were thresholded so that values in regions with low water signal were set to zero. 3. The thresholded water image of subject 1 was non-rigidly registered to all other thresholded water images using the NiftyReg software [169] with the weight of the bending energy term increased to 0.01 and a final grid size of 7 voxels. 4. Bones were segmented in the rest of the images by applying the resulting transformations to the manually segmented bone region of subject 1. This process provided suitable segmentations in all subjects. We used the thresholded water images here, because the shape and size of subcutaneous fat largely varied across subjects whereas the water images generally looked similar and, therefore, provided more accurate registrations around bony structures. Additionally, the edges of the patient and volunteer tissue masks were eroded by 5 voxels in each slice to further improve the quality of the susceptibility maps.

Since QSM calculates the average susceptibility of the substances (in other words the volume susceptibility [118, 126]) within each voxel, it is expected to have a linear relationship with both fat and bone content (i.e. PDFF and BMD). Therefore, we propose a procedure to estimate BMD-induced susceptibility maps: 1. PDFF and susceptibility maps were measured and calculated. 2. Linear regression was performed between susceptibility and PDFF in voxels without bony trabeculae. 3. The regression parameters and the PDFF map were then used to estimate the contribution of fat to susceptibility in every voxel. 4. The contribution of fat was subtracted from the total susceptibility map resulting in a susceptibility map that is expected to be proportional to BMD assuming that no other para- or diamagnetic components are present. We performed this procedure in all volunteer and patient susceptibility maps. Step 2 was carried out in a rectangular region, including both water-based tissue (gluteal muscle) and subcutaneous fat, manually selected in the middle slice in each subject.

To compare the contributions of BMD to susceptibility and R_2^*, a similar procedure was performed for the scanner-provided R_2^* maps. To model the effects of PDFF on the measured R_2^* [71], we adopted an empirical quadratic fit (instead of the aforementioned linear relationship) in step 2 that provided better fits (e.g. Figure 8.7).

8.3.6 Statistical analysis

For both phantoms, circular regions of interest (ROIs) were manually drawn (by A.K.) on the first-echo magnitude images in eight consecutive slices near the middle of the acquired volumes using ITK-SNAP [184, 185]. Mean susceptibilities and R_2^* values were calculated in all ROIs. 2D linear functions were fitted to the measured susceptibility and R_2^* values as functions of known FF and BMD values in the fat-water-bone phantom. Linear regression was performed between measured susceptibilities and known FF values in the fat-water phantom.

For the patients and healthy controls, areas of normal bone marrow, bone marrow edema, and fat metaplasia were manually segmented on the first-echo magnitude images using landmarks from the T_2-weighted STIR and T_1-weighted images by an experienced radiology resident (T.J.P.B.) as described in [71]. ROIs which were very close to fat-water chemical shift artifacts in the susceptibility maps were excluded from the analysis. This included all ROIs from two subjects (8 ROIs of fat metaplasia and 4 ROIs of normal bone marrow), and two additional ROIs from a third subject (out of 7 ROIs of fat metaplasia). Mean susceptibilities and R_2^* values were calculated in the rest of the segmented ROIs both

before and after removing the contributions of fat as described above (i.e. the same ROIs were used in all four cases). Susceptibility values were referenced to the mean susceptibility within the tissue mask for each subject (this mean susceptibility varied between -0.01 ppm and 0.01 ppm). Multi-level mixed-effects linear regression was used (in MATLAB R2015a) to determine whether there were significant differences in susceptibilities and R_2^* values measured in normal bone marrow, oedema, and fat metaplasia. This test accounts for repeated observations in individual patients.

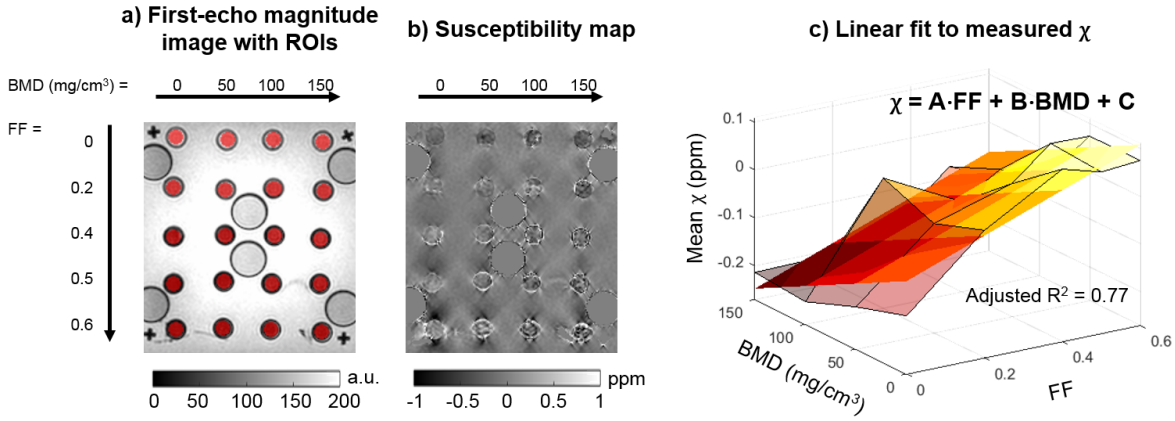

g) Model parameters

	Estimated value	Units	95% conf. int.	p-value
Fat fraction slope (A)	0.31	ppm/100%	(0.20, 0.42)	$2 \cdot 10^{-5}$
Bone mineral density slope (B)	-0.11	ppm/100$\frac{mg}{cm^3}$	(-0.16, -0.07)	$3 \cdot 10^{-5}$
Offset (C)	-0.08	ppm	(-0.13, -0.02)	$9 \cdot 10^{-3}$

Figure 8.2: Results from the fat-water-bone phantom. First-echo magnitude image and susceptibility map are shown in (a) and (b) respectively. The manually drawn circular ROIs are highlighted in red (a). Results of the 2D linear fit between bone mineral density (BMD) and fat fraction (FF) values and susceptibility are shown in (c-g). In (c), the transparent surface corresponds to measured values, while the opaque plane is the fitting 2D linear function.

8.4 Results

8.4.1 Phantoms

Images from the fat-water-bone phantom are shown in Figure 8.2 a, b. Susceptibility measurements were positively related to FF values and negatively related to BMD (Figure 8.2 c, g), with the 2D linear model providing an accurate description of the acquired data (adjusted $R^2 = 0.77$, Figure 8.2 c-g). All coefficients were significant (i.e. $p < 0.01$, Figure 8.2 g). Similarly, in the lard-water phantom covering the full range of FF values (Figure 8.3), there was an approximately linear relationship (adjusted $R^2 = 0.82$) between FF and susceptibility (Figure 8.3 c, d) even towards high FF values. In case of the R_2^* fit, despite the high adjusted R^2 value (0.81), only the BMD slope was significant (not shown).

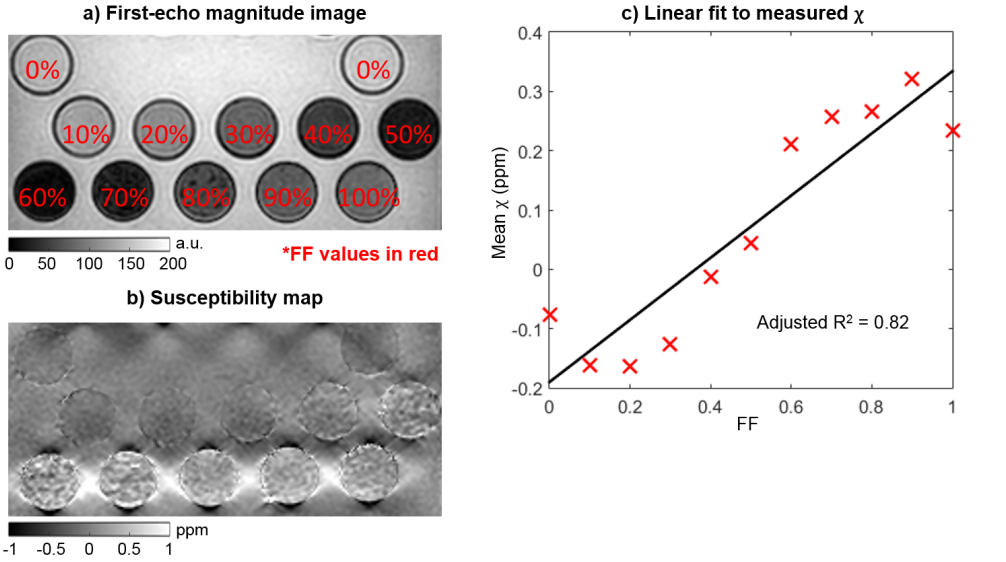

d) Model parameters

	Estimated value	Units	95% conf. int.	p-value
Fat fraction slope	0.52	ppm/100%	(0.35, 0.70)	$2 \cdot 10^{-4}$
Offset	-0.19	ppm	(-0.29, -0.09)	$5 \cdot 10^{-3}$

Figure 8.3: Results from the fat-water phantom. First-echo magnitude image and susceptibility map are shown in (a) and (b) respectively. The linear fit between fat fraction (FF) and susceptibility values is shown in (c-d).

8.4.2 Patients and volunteers

Susceptibility values were significantly increased in areas of fat metaplasia compared to normal marrow (Figure 8.4 a). R_2^* measurements were also significantly reduced in areas of fat metaplasia compared to normal marrow (Figure 8.5 a), in line with previous results [71]. There were no significant differences in susceptibility or R_2^* between normal bone marrow and areas of oedema. However, susceptibility values were significantly lower, and R_2^* values significantly higher in areas of oedema compared to areas of fat metaplasia.

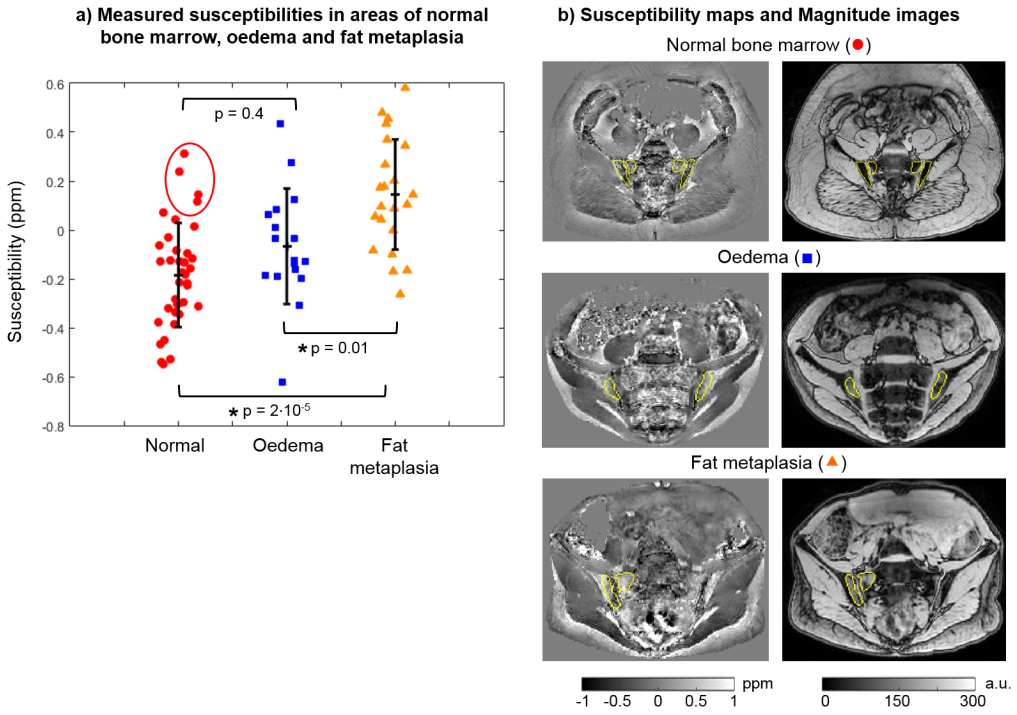

Figure 8.4: Susceptibility maps in patients. Measured mean susceptibilities in areas of normal marrow, oedema, and fat metaplasia are shown in (a). p-values were calculated for each pair and the asterisks indicate statistical significance. The four highest susceptibility values in normal bone marrow (red circle) were measured in the same subject. Susceptibility maps and magnitude images in example subjects are shown in (b).

Proton density fat fraction (PDFF) and susceptibility values within a single, rectangular ROI (overlaid on the susceptibility map) incorporating both muscle and subcutaneous fat, in addition to the results of the linear regression analysis, are shown for a single subject in Figure 8.6. Similarly, Figure 8.7 shows R_2^* and PDFF values within the manually selected ROI (overlaid on the R_2^* map), and the results of the nonlinear regression analysis assuming a quadratic relationship. In both Figure 8.6 and Figure 8.7, the majority of voxels are either almost entirely water based (green arrow and dotted circle) or fat based (blue arrow and dotted circle). Note that the straight line observed at the upper end of the

PDFF range in Figure 8.7 arises due to a lower bound for R_2^* estimates (0.01 ms^{-1}) used by the mDixon Quant algorithm. Model parameters from the linear and quadratic fits between PDFF and susceptibility, and PDFF and R_2^* respectively are shown in Figure 8.8. The coefficients of the quadratic fit (Figure 8.8 b) were highly variable across subjects. While the intercept of the linear fit to susceptibility values also showed large variations across subjects, the susceptibility-PDFF slope was somewhat consistent for regressions with high adjusted R^2 measures (Figure 8.8 a, blue circle).

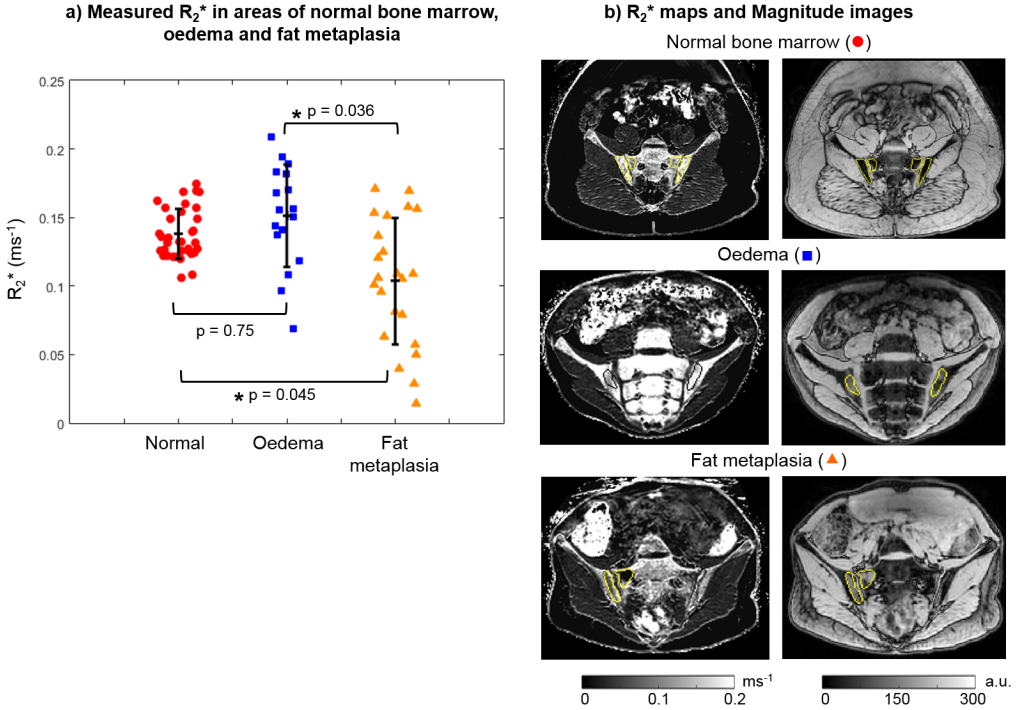

Figure 8.5: R_2^* maps in patients. Mean R_2^* measurements in areas of normal marrow, oedema, and fat metaplasia are shown in (a). p-values were calculated for each pair and the asterisks indicate statistical significance. R_2^* maps and magnitude images in example subjects are shown in (b).

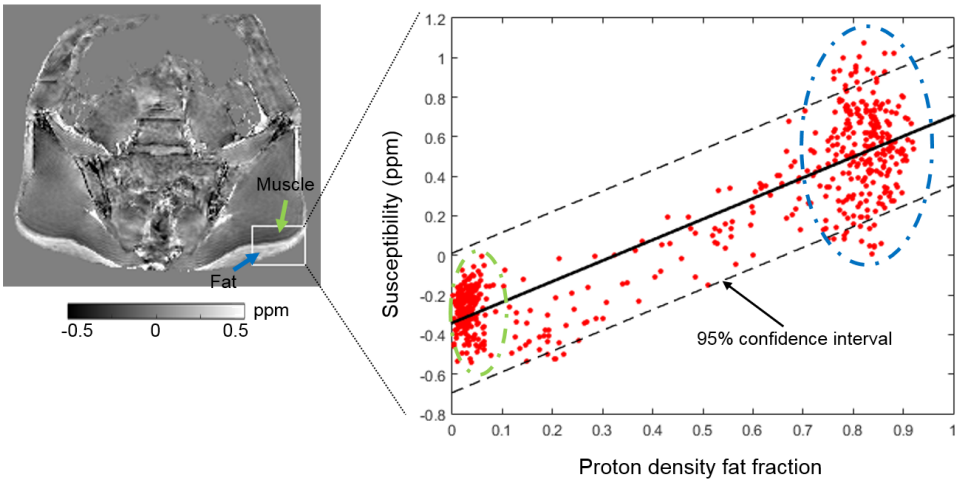

Figure 8.6: Linear regression between PDFF and susceptibility values in a single, representative subject. A rectangular ROI including fat and muscle was manually placed on the middle slice of the susceptibility map. Each point in the scatter plot corresponds to one voxel within this rectangular region (excluding voxels outside the subject). The blue arrow and dotted circle indicate subcutaneous fat and the corresponding points in the scatter plot. The green arrow and dotted circle indicate muscle and the corresponding points in the scatter plot. Results from the regression analysis for each subject are shown in Figure 8.8.

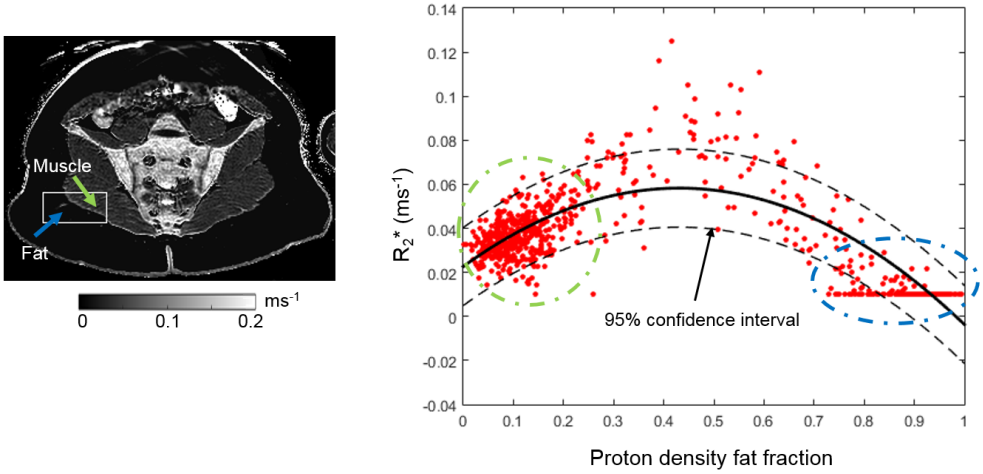

Figure 8.7: Nonlinear regression between PDFF and R_2^* values using a quadratic model. The R_2^* map and the regression of a representative subject are shown. Each point in the scatter plot corresponds to one voxel within this rectangular region (excluding voxels outside the subject). The blue arrow and dotted circle indicate subcutaneous fat and the corresponding points in the scatter plot. The green arrow and dotted circle indicate muscle and the corresponding points in the scatter plot. Results from the regression analysis for each subject are shown in Figure 8.8. Note that the straight line of points at the right lower corner of the plot arises due to the lower bound applied to R_2^* estimates by the mDixon Quant fitting algorithm.

Susceptibility values and R_2^* measurements after removing the fat contribution are shown in Figure 8.9 and Figure 8.10 respectively. There were no significant differences between normal bone marrow and fat metaplasia in either susceptibility or R_2^* maps after performing the adjustment for fat content.

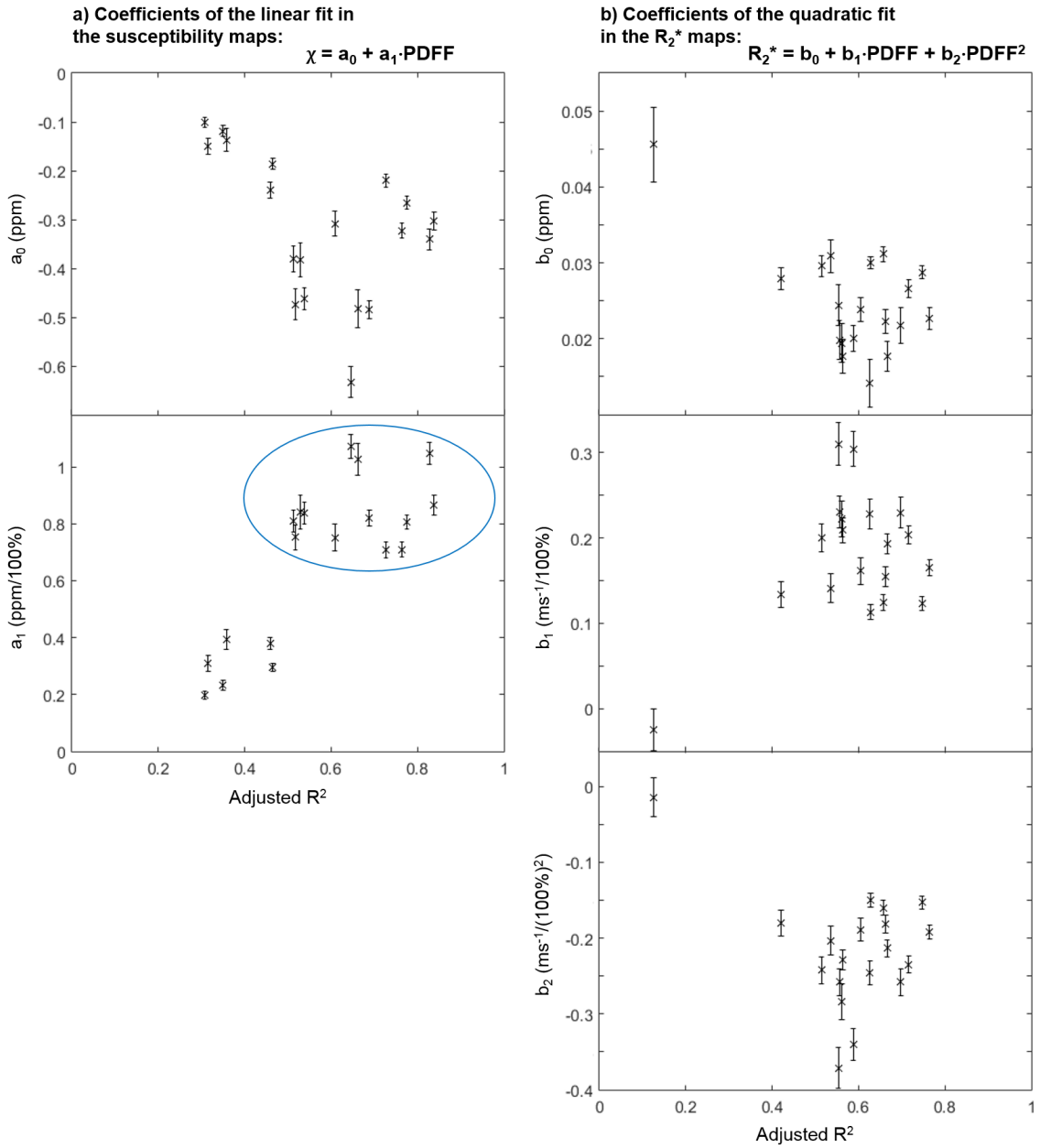

Figure 8.8: Coefficients of the linear and quadratic fits between PDFF and susceptibility (a) or R_2^* (b) respectively. The fitting function is displayed in the top right corner of both subplots. In all five scatter plots, each point corresponds to one subject. Coefficients are shown as a function of the adjusted R^2 of each fit. The error bars indicate the 95% confidence interval of each coefficient. The slope of the linear regression ($\mathbf{a}_1$) seems to be consistent in instances where the adjusted R^2 was high (> 0.5, see blue circle). All other parameters had large variations across subjects.

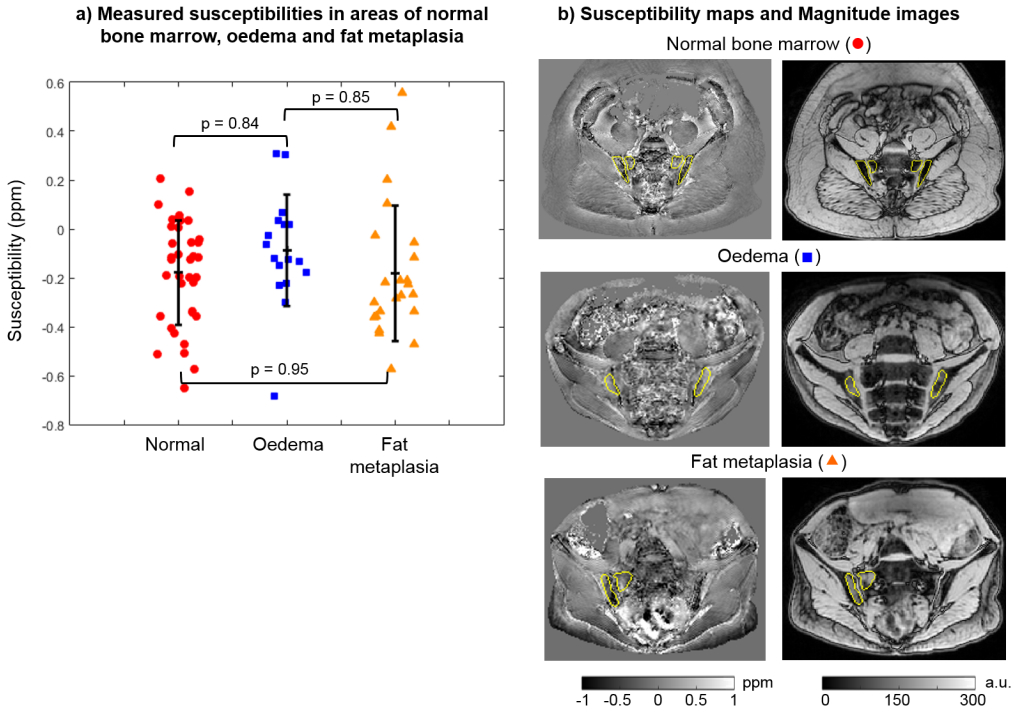

Figure 8.9: Susceptibility maps in patients after removing the fat contribution. Fat-corrected susceptibility measurements in areas of normal marrow, oedema and fat metaplasia are shown in (a). p-values are calculated for each pair. Susceptibility maps and magnitude images in example subjects are shown in (b).

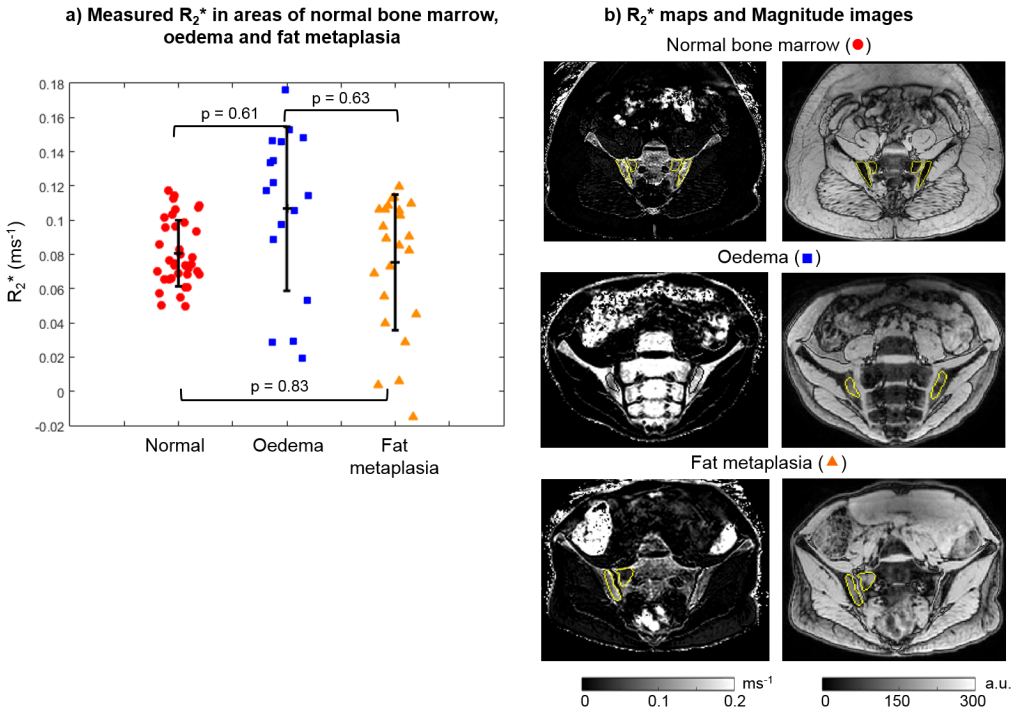

Figure 8.10: R_2^* maps in patients after removing the fat contribution. Fat-corrected R_2^* measurements in areas of normal marrow, oedema, and fat metaplasia are shown in (a). p-values were calculated for each pair. R_2^* maps and magnitude images in example subjects are shown in (b).

8.5 Discussion

In spondyloarthritis, new bone formation and bone destruction contribute to spinal ankylosis and osteoporosis respectively, and are key contributors to morbidity. However, these processes cannot be quantified using conventional spin echo sequences. In this study, we sought to characterize the relationship between bone mineral density (BMD), fat fraction (FF), and susceptibility measurements in inflamed bone marrow, using both phantom and in vivo studies with the aim of investigating susceptibility as a potential biomarker of these processes.

In the fat-water-bone phantom, we observed linear relationships between FF and susceptibility and between BMD and susceptibility. The linear relationship between FF and susceptibility was also observed in a separate, lard-based fat-water phantom covering the full range of FF measurements, although there was a slight non-linear variation which may be related to difficulties in manufacturing a homogeneous lard phantom. In accordance with previous studies [64, 81, 141, 200], our data indicated positive (paramagnetic) susceptibility values for fat, and negative (diamagnetic) susceptibility values for bone. Our results confirm the feasibility of measuring BMD in the bone marrow, and suggest that the contribution of fat to the total susceptibility measurement can be modelled using a simple linear relationship.

Importantly, the results of our phantom study were used to inform the analysis of the in-vivo results, to enable us to estimate the contribution of the fat to the total susceptibility measurement. Using per-patient linear regression analysis in voxels of subcutaneous fat and muscle, we were able to remove the fat contribution to susceptibility measurements in areas of fat metaplasia, oedema and normal marrow, and thereby interrogate the source of susceptibility differences between these regions. Strikingly, we found that susceptibility measurements were significantly increased in areas of fat metaplasia compared to normal marrow, but that this difference was abolished after removal of the fat contribution. This suggests that the contribution of fat content to overall susceptibility is likely to be substantial, and highlights the importance of accounting for the contribution of fat when performing QSM in bone marrow.

Similarly, although there was a significant reduction in R_2^* in areas of fat metaplasia compared to normal marrow, no significant difference was observed in fat-corrected R_2^* measurements. This result implies that the previously-reported reduction in R_2^* [71] in areas of fat metaplasia may actually be a secondary effect of varying fat content: as fat fraction increases from around 50% (normal bone) to about 70 - 90% (fat metaplasia) [71],

the susceptibility distribution inside the voxel becomes more homogenous, and the relaxation rate R_2^* reduces accordingly. This suggestion is in keeping with previous results in muscle, which suggest that R_2^* measurements are highest at intermediate PDFF values, and are at their lowest at the extremes of the PDFF range (i.e. close to 0% and close to 100%) [205]. In contrast, the linear relationship of susceptibility with FF implies that susceptibility measurements are less affected by the microscopic spatial susceptibility distribution, since the susceptibility calculation largely relies on larger-scale phase differences outside the voxel. This is potentially a significant advantage of QSM over R_2^* mapping.

Overall, the results of our study highlight that lipids contribute substantially to both susceptibility and R_2^* estimates in trabecular bone, and can at least partly account for the differences in susceptibility between regions. Accounting for the fat contribution to susceptibility is likely to be essential when imaging trabecular bone in general. If the fat contribution is not separated, changes in susceptibility/R_2^* might be incorrectly attributed to changes in BMD, or other factors.

In this study, we used the individual regression parameters in Figure 8.8 for each subject to remove the contributions of fat from susceptibility and R_2^* maps. For the R_2^* maps, the quadratic model is a heuristic approximation of the observed shape of the PDFF-R_2^* relationship. Therefore, the coefficients vary greatly across subjects (Figure 8.8 b), and the correction is expected to be more accurate if individual fitting parameters are used.

In QSM, the susceptibility of a tissue can only be measured relative to the susceptibility of surrounding tissues, and there is expected to be variation in this susceptibility offset across subjects. This could explain the variability of a_0 in Figure 8.8 a. Though referencing is used to enable comparison of susceptibility across scans, here we used the mean susceptibility within the tissue mask as a reference which might not be ideal. Future studies could explore other potential reference tissues in the pelvic area similarly to what has been done in the brain [177]. This could result in more consistent a_0 values across subjects. The estimated slope (a_1 in Figure 8.8 a) seems to be consistent across subjects for regressions with high adjusted R^2. This is encouraging as the composition of subcutaneous fat and, therefore, the relationship between FF and susceptibility is expected to be similar across subjects. In a few cases (where the adjusted R^2 was lower), the fitted slopes as well as the correlation between susceptibility and FF (not shown) were substantially lower. This might be due to susceptibility errors on the boundary between fat- and water-based tissues introduced by the large susceptibility gradient. Selecting two separate areas (one in subcutaneous fat and one in muscle) could be a way of overcoming this problem in the future, however, here we needed to include the voxels on the boundary (where

FF values are between 0.3 and 0.7) to be able to appreciate the relationships between FF, and susceptibility or R_2^* (Figures 8.6 and 8.7). It could be interesting to explore if a single slope value can be used to robustly remove fat contributions from susceptibility maps. In any case, using individual regression parameters was more appropriate here as the same approach was implemented for the R_2^* maps. Interestingly, the estimated slope values were different in subjects than in the fat-water phantoms (and also varied slightly between the two phantoms), which might be due to differences in susceptibility between different lipids or, in patients, to susceptibility contributions from non-lipid molecules in muscle and/or adipose tissue. Further work is required to investigate this issue.

It is not yet known how bone content or structure changes in areas of oedema and fat metaplasia. In the patients with spondyloarthritis investigated here, the fact that we did not find a significant difference in fat-corrected susceptibility in areas of fat metaplasia argues against a significant change in BMD in these areas. However, it is also possible that we have simply failed to detect this change due to technical limitations arising from the acquisition protocol and/or susceptibility mapping pipeline such as the removal of chemical-shift-induced errors, as discussed in the next paragraph. Also, note that the four highest susceptibility values in normal bone marrow (Figure 8.4 a, red circle) were measured in the same subject, so these unrealistically high values could be due to a processing issue in this subject. We did not find a significant difference in susceptibility between areas of oedema and normal bone marrow. On theoretical grounds we would have expected a reduction in susceptibility (before fat correction) in areas of oedema due to increased water fraction, which would have been expected to disappear after fat correction. However, the changes in fat fraction in areas of oedema are smaller than those observed in fat metaplasia (compared to normal marrow) [71], which may have prevented detection of this effect.

A limitation of this study is that the fat-water decomposition step in the QSM pipeline, aiming to eliminate chemical shift effects, suffered from fat-water swaps in some subjects, which may have contributed to inaccuracies in the calculated susceptibilities. Swaps may be introduced during the region-growing stage of the fat-water decomposition (Dixon) method [75], possibly due to errors or noise in the measured phase data. Empirically, we found that the three-point Dixon method used here was the most robust of the available options in the ISMRM fat-water toolbox [75], although even this did not perform perfectly in all cases. Better results might be achieved by using alternative algorithms for fat-water decomposition. One option is to use manufacturers' own algorithms for fat-water decomposition (and to generate field maps), but this comes at the cost of reduced flexibility and makes it more difficult to translate the approach to other platforms. An-

other possibility is using in-phase echo timing to remove most of the chemical shift phase contributions [142, 206], while also acquiring opposed-phase (or partially opposed-phase) images to calculate PDFF maps.

One of the most crucial features of susceptibility mapping is the generation of the tissue mask. Noisy voxels are prone to introduce far-reaching streaking artifacts and errors into the susceptibility maps. In images of the sacroiliac joint, it is very important to properly exclude areas of bowel as the phase measured in these voxels is often corrupted by motion artifacts and suffers from low signal due to air in the bowel lumen. Therefore, thresholding the inverse noise map seems appropriate here for generating a suitable tissue mask. However, bony voxels are also expected to have low signal. The process described here aiming to keep bony voxels while excluding bowel was simple and provided reasonable tissue masks in most cases, but susceptibility accuracy could potentially be improved using more accurate, automated bone segmentation tools, for example based on multi-atlas information [207].

There is a complex relationship between PDFF and R_2^* measurements, which means that changes in R_2^* in tissue are ambiguous. It might be possible to model this relationship using prior knowledge of fat and water susceptibility and the arrangement of fat and water in the tissue, but this is not trivial and introduces further sources of complexity. Using susceptibility as a marker of BMD has several advantages over R_2^*. Most importantly, the linear relationships observed in the fat-water-bone phantom enable fat-correction to be performed very simply, and the fat-corrected susceptibility measurements to be interpreted unambiguously. Future studies could correlate the measured bone marrow susceptibilities with gold-standard, QCT-based clinical BMD measures [195], however this is subject to ethical constraints relating to the use of ionising radiation, particularly in young patients.

8.6 Conclusions

Quantitative susceptibility measurements are linearly related to both bone mineral density (BMD) and fat fraction (FF), and failure to remove the fat contribution to susceptibility measurements can potentially lead to errors in QSM-based BMD quantification. We propose a method for removing this contribution using a linear fit to susceptibility as a function of FF in a region not containing bone. Comparison of data both with and without this correction suggest that increased fat content is the major contributor to the increase in susceptibility in areas of fat metaplasia relative to normal bone marrow.

Chapter 9

Conclusions and Future Work

In this work, I have optimised MRI data acquisition and the QSM pipeline to produce clinically applicable susceptibility maps of the head and neck. This will facilitate clinical research to assess whether MRI susceptibility values could provide a measure of oxygenation in cancerous lymph nodes and improve prognosis after radiation therapy.

I have shown that low resolution and very low coverage both lead to loss of contrast in susceptibility maps (chapter 5). This can be attributed to the fact that insufficient sampling of the dipolar fields, induced by susceptibility sources within the region of interest, prevents accurate inversion of the field map. Even iterative, fitting methods cannot recover the loss of information induced by low resolution and low coverage (section 5.4.2). At very low coverage, after background field removal, the local field maps also suffer from overattenuation towards the edges of the imaged volume which accounts for about 50% of the overall susceptibility error (section 5.4.3). Two fundamentally different, state-of-the-art background field removal techniques produced similar, attenuated field maps at low resolution and coverage. Therefore, while it is possible that future approaches for QSM could compensate for these susceptibility errors post-acquisition, currently the best way to avoid loss of contrast is to acquire images with sufficient resolution (with a slice thickness of no more than 1.5 mm) and coverage (at least 4-5 times the size of the structure of interest).

Using images acquired in healthy volunteers, I have optimised the MRI acquisition for susceptibility mapping in the head and neck (sections 6.1 and 6.2). I compared several state-of-the-art strategies for overcoming chemical shift-induced errors (section 6.1). The three-point Dixon method (3PD), Simultaneous Phase Unwrapping and Removal of chemical Shift (SPURS), and in-phase imaging provided similar susceptibility maps, but only

in-phase imaging was robust across different subjects and echo times (section 6.1.3.4). I found that a 3D gradient echo sequence with 1.25 mm isotropic resolution (section 6.2.3.2), coronal orientation (head-foot = readout, section 6.2.3.1), four in-phase echoes, full coverage of the head and neck, and a SENSE acceleration factor of 2 in the first phase encoding direction (right-left) provided head-and-neck susceptibility maps with a good balance between signal-to-noise ratio and visible anatomical details in a reasonable scan time (about 6 minutes). Vendor-supplied flow compensation was also used because, although it did not seem to affect the resulting susceptibility maps, it was shown to theoretically improve flow compensation at all four echoes (section 6.2.3.3).

I have also optimised the QSM pipeline for head-and-neck images (sections 6.3 and 6.4). I compared five widely used background field removal techniques in the brain using a realistic numerical phantom (section 6.3). Using ground truth evaluation of the local field and susceptibility maps, I found that these five methods could all eliminate most of the background fields around deep-brain structures, but their performance varied near the brain edges (section 6.3.3.1). My conclusions are in accordance with those of Schweser et al. [99]. I also compared the two most promising background field removal techniques, the Laplacian Boundary Value method (LBV) and Projection onto Dipole Fields (PDF), in a numerical phantom of the head and neck which I developed. I concluded that both methods are applicable in the head and neck provided that no unrealistic, ellipsoidal susceptibility sources are present (section 6.3.3.2). I found non-linear fitting combined with Laplacian phase unwrapping (LPU) to be a quick and robust way of calculating the total field variations (section 6.4.3.2). LBV and PDF were both found to successfully eliminate the residual background fields in vivo (section 6.4.3.3). A simple masking strategy of applying a fixed threshold to the inverse noise map was found to be useful for head-and-neck images. Out of the five susceptibility calculation techniques I compared in this thesis, the direct and iterative Tikhonov methods that I implemented seemed to provide the best balance between streaking artifacts and susceptibility contrast in a reasonable amount of time (section 6.4.3.4). While the direct version is much faster, iterative fitting in image space performed better near the tissue edges as it did not assume field values to be zero outside of the tissue mask.

To quantify the clinical applicability of the optimised MRI acquisition and QSM pipeline, I tested their repeatability using head-and-neck data acquired in 10 healthy volunteers (chapter 7). Each volunteer was scanned three times per session at two sessions a week apart. Regions of interest were delineated in the brain (thalamus, caudate nucleus, putamen, globus pallidus) and the neck (healthy lymph nodes, the parotid and submandibular glands) and the final segmentations were checked by an experienced ra-

diologist. Susceptibility maps calculated using PDF for background field removal were more repeatable than those calculated using LBV (section 7.3.1). Both direct and iterative Tikhonov provided susceptibility maps with equally high repeatability. Though I did not find a substantial difference between using the mean or median susceptibility within regions as a summary metric for healthy volunteers, the median should be used in patient studies as the distribution in diseased tissue is expected to be skewed, for example, by low oxygenation in cancerous lymph nodes. The intersession repeatability was found to be only slightly lower than the intrasession repeatability which shows the stability and robustness of the acquisition and processing techniques I optimised (section 7.3.3). Very small lymph nodes (volume < 300 mm^3 or short-axis diameter < 5 mm) had poor repeatability possibly due to partial volume effects. Minimum detectable effect sizes calculated based on the intrasession results in all other regions indicated that the optimised acquisition and processing pipeline had sufficient repeatability to detect hypoxic sites in head-and-neck cancer.

In collaboration with Dr Timothy J.P. Bray, we investigated QSM as a candidate technique to non-invasively measure bone mineral density in healthy and diseased bone marrow (chapter 8). Using two different phantoms with varying concentrations of fat and bony trabeculae, we showed that susceptibility has a linear relationship with both fat and bone content (section 8.4.1), as opposed to the previously reported non-linear effect these substances have on R_2^* ($= 1/T_2^*$). We measured both R_2^* and susceptibility values in the bone marrow of healthy volunteers (near the sacroiliac joints) and patients with spondyloarthritis (in regions of both oedema and fat metaplasia). Areas of fat metaplasia had significantly increased susceptibilities compared to normal bone marrow in accordance with decreased R_2^* values observed previously by Bray et al. [71] (section 8.4.2). However, fat metaplasia contains both paramagnetic fat and diamagnetic bone. We estimated the contribution of fat to measured susceptibility values for each image using the fat fraction map and a linear fit between fat fraction and susceptibility in a bone-free area (section 8.3.5). Using these updated susceptibility values, there was no significant difference in susceptibility between fat metaplasia and normal bone marrow which indicates that fat is the main source of the susceptibility changes (section 8.4.2). A similar correction applied to the R_2^* maps (approximating the complicated relationship between R_2^* and fat fraction with a quadratic function) also suggested that fat was driving the R_2^* differences in regions of fat metaplasia. In summary, due to the linear relationship between susceptibility and bone content, QSM is a promising technique to non-invasively monitor bone loss and new bone formation in spondyloarthritis provided that the contribution of fat is accounted for.

While optimising the QSM pipeline for head-and-neck images, I was frustrated by the long computation time and occasional failure of the current gold-standard phase unwrapping technique (FSL PRELUDE). To overcome this challenge, I created and developed SEGUE, a phase unwrapping technique based on similar principles to FSL PRELUDE but with much shorter overall computation time (chapter 4). My comparison of the two approaches in the brain, head and neck, and pelvis of a few healthy volunteers, across several echo times, and in numerical phantoms showed that these techniques provided extremely similar unwrapped phase maps. However, SEGUE was 1.5 to 70 times faster than PRELUDE depending on the echo time and anatomical region (section 4.5). I also demonstrated that the chemical-shift-induced residual phase wraps (e.g. in fatty fascia or subcutaneous fat) can be greatly reduced by applying either PRELUDE or SEGUE separately in the fat and water masks. SEGUE will be disseminated through UCL XIP as a collection of MATLAB scripts to help accelerate research on applications of phase imaging (including QSM) in fatty and challenging regions of the body.

Future work will involve histological validation of the optimised head-and-neck QSM technique developed in this thesis as a potential biomarker of hypoxia in head-and-neck cancer. Ten patients with head-and-neck squamous cell carcinoma scheduled for surgical resection of lymph nodes will be recruited. These patients will be scanned with our optimised sequence and receive pimonidazole injection before surgery. Susceptibility values in the resected lymph nodes will be calculated using the optimised QSM pipeline, both with direct and iterative Tikhonov as the susceptibility calculation method, and will be correlated with pimonidazole staining levels (the gold-standard invasive histological method of measuring hypoxia). The direct and iterative Tikhonov techniques will be compared in patients in terms of susceptibility contrast, SNR, and correlation between susceptibility and pimonidazole levels in lymph nodes. It would also be useful to investigate if using only the first three echoes for QSM could provide comparable results to using all four echoes as acquiring only three echoes would further reduce scan time. All patients will be scanned with an additional sequence optimised for measuring fat fraction maps to assess the variability of fat content in cancerous lymph nodes and determine if the contributions of paramagnetic fat to the total susceptibility need to be removed, similarly to what we have done in the bone marrow, for a more accurate measure of tissue oxygenation. My PhD supervisors have been awarded a Cancer Research UK Multidisciplinary Award on the basis of my preliminary work to take this research forward.

The MRI acquisition used to acquire images of the sacroiliac joint in volunteers and patients with spondyloarthritis will be optimised for QSM to potentially increase the sensitivity of this technique to changes in bone content. In-phase imaging will be adopted

to overcome errors introduced by the chemical-shift effect instead of relying on post-acquisition methods that are not robust across subjects. MRI data will be acquired using the optimised protocol in patients and volunteers to investigate the differences in susceptibility between normal bone marrow, oedema, and fat metaplasia using the improved technique.

SEGUE will be tested in a range of clinical and preclinical scenarios to explore the potential applications of this new phase unwrapping method. For example, I will apply it in ex-vivo images of mice without, and at different stages of, prion disease as part of a project to investigate whether QSM reflects histopathological changes.

Finally, the optimised MRI acquisition protocol and QSM pipeline could be tested in thyroid nodules to investigate whether this technique can detect microcalcifications more accurately than other imaging modalities such as ultrasound. In conclusion, this research has provided robust, optimised methods that will be widely applicable to springboard QSM into challenging regions of the human body and beyond.

Bibliography

[1] Donald W McRobbie, Elizabeth A Moore, and Martin J Graves. *MRI from Picture to Proton*. Cambridge University Press, 2017.

[2] International Electrotechnical Commission et al. Medical electrical equipment-part 2-33: Particular requirements for the basic safety and essential performance of magnetic resonance equipment for medical diagnosis. *IEC 60601-2-33 Ed. 3.0*, 2010.

[3] Zhi-Pei Liang and Paul C Lauterbur. *Principles of magnetic resonance imaging: a signal processing perspective*. SPIE Optical Engineering Press, 2000.

[4] Matthew J Cronin, Nian Wang, Kyle S Decker, Hongjiang Wei, Wen-Zhen Zhu, and Chunlei Liu. Exploring the origins of echo-time-dependent quantitative susceptibility mapping (QSM) measurements in healthy tissue and cerebral microbleeds. *NeuroImage*, 149:98–113, 2017.

[5] Surabhi Sood, Javier Urriola, David Reutens, Kieran OBrien, Steffen Bollmann, Markus Barth, and Viktor Vegh. Echo time-dependent quantitative susceptibility mapping contains information on tissue properties. *Magnetic resonance in medicine*, 77(5):1946–1958, 2017.

[6] Samuel Wharton and Richard Bowtell. Fiber orientation-dependent white matter contrast in gradient echo MRI. *Proceedings of the National Academy of Sciences*, page 201211075, 2012.

[7] Jeff H. Duyn, Peter van Gelderen, Tie-Qiang Li, Jacco A. de Zwart, Alan P. Koretsky, and Masaki Fukunaga. High-field MRI of brain cortical substructure based on signal phase. *Proceedings of the National Academy of Sciences*, 104(28):11796–11801, 2007.

[8] Simon Daniel Robinson, Barbara Dymerska, Wolfgang Bogner, Markus Barth, Olgica Zaric, Sigrun Goluch, Günther Grabner, Xeni Deligianni, Oliver Bieri, and Siegfried Trattnig. Combining phase images from array coils using a short echo

time reference scan (COMPOSER). *Magnetic resonance in medicine*, 77(1):318–327, 2017.

[9] Dennis L Parker, Allison Payne, Nick Todd, and J Rock Hadley. Phase reconstruction from multiple coil data using a virtual reference coil. *Magnetic resonance in medicine*, 72(2):563–569, 2014.

[10] Roger C Tam, Andrew Riddehough, and David KB Li. Detection and measurement of coverage loss in interleaved multi-acquisition brain MRIs due to motion-induced inter-slice misalignment. *Medical Image Analysis*, 13(3):381–391, 2009.

[11] Matt A Bernstein, Kevin F King, and Xiaohong Joe Zhou. *Handbook of MRI pulse sequences*. Elsevier, 2004.

[12] DW McRobbie. The absolute signal-to-noise ratio in MRI acceptance testing. *The British Journal of Radiology*, 69(827):1045–1048, 1996.

[13] Richard Lerski, Janet De Wilde, David Boyce, and John Ridgway. *Quality control in magnetic resonance imaging*. Institute of Physics and Engineering in Medicine, 2002.

[14] Klaas P Pruessmann, Markus Weiger, Markus B Scheidegger, Peter Boesiger, et al. SENSE: sensitivity encoding for fast MRI. *Magnetic Resonance in Medicine*, 42(5):952–962, 1999.

[15] Mark A Griswold, Peter M Jakob, Robin M Heidemann, Mathias Nittka, Vladimir Jellus, Jianmin Wang, Berthold Kiefer, and Axel Haase. Generalized autocalibrating partially parallel acquisitions (GRAPPA). *Magnetic Resonance in Medicine*, 47(6):1202–1210, 2002.

[16] John F Schenck. The role of magnetic susceptibility in magnetic resonance imaging: MRI magnetic compatibility of the first and second kinds. *Medical Physics*, 23(6):815–850, 1996.

[17] Varsha Jain, Osheiza Abdulmalik, Kathleen Joy Propert, and Felix W Wehrli. Investigating the magnetic susceptibility properties of fresh human blood for noninvasive oxygen saturation quantification. *Magnetic Resonance in Medicine*, 68(3):863–867, 2012.

[18] Bing Wu, Wei Li, Alexandru Vlad Avram, Sung-Min Gho, and Chunlei Liu. Fast and tissue-optimized mapping of magnetic susceptibility and T2* with multi-echo and multi-shot spirals. *NeuroImage*, 59(1):297–305, 2012.

[19] Ferdinand Schweser, Andreas Deistung, Berengar W Lehr, and Jürgen R Reichenbach. Differentiation between diamagnetic and paramagnetic cerebral lesions based on magnetic susceptibility mapping. *Medical Physics*, 37(10):5165–5178, 2010.

[20] Lin Li and John S. Leigh. Quantifying arbitrary magnetic susceptibility distributions with MR. *Magnetic Resonance in Medicine*, 51(5):1077–1082, 2004.

[21] Karin Shmueli, Jacco A. de Zwart, Peter van Gelderen, Tie-Qiang Li, Stephen J. Dodd, and Jeff H. Duyn. Magnetic susceptibility mapping of brain tissue in vivo using MRI phase data. *Magnetic Resonance in Medicine*, 62(6):1510–1522, 2009.

[22] Christian Langkammer, Ferdinand Schweser, Nikolaus Krebs, Andreas Deistung, Walter Goessler, Eva Scheurer, Karsten Sommer, Gernot Reishofer, Kathrin Yen, Franz Fazekas, et al. Quantitative susceptibility mapping (QSM) as a means to measure brain iron? A post mortem validation study. *NeuroImage*, 62(3):1593–1599, 2012.

[23] Jongho Lee, Karin Shmueli, Masaki Fukunaga, Peter van Gelderen, Hellmut Merkle, Afonso C Silva, and Jeff H Duyn. Sensitivity of MRI resonance frequency to the orientation of brain tissue microstructure. *Proceedings of the National Academy of Sciences*, 107(11):5130–5135, 2010.

[24] Samuel Wharton and Richard Bowtell. Effects of white matter microstructure on phase and susceptibility maps. *Magnetic Resonance in Medicine*, 73(3):1258–1269, 2015.

[25] Macmillan cancer support: `http://www.macmillan.org.uk/information-and-support/head-and-neck-cancers/understanding-cancer/types-head-neck-cancer.html#2936`.

[26] H Mehanna, V Paleri, C M L West, and C Nutting. Head and neck cancer—part 1: Epidemiology, presentation, and prevention. *BMJ*, 341, 2010.

[27] U.S. National Library of Medicine: `https://ghr.nlm.nih.gov/condition/head-and-neck-squamous-cell-carcinoma#statistics`.

[28] H Mehanna, C M L West, C Nutting, and V Paleri. Head and neck cancer—part 2: Treatment and prognostic factors. *BMJ*, 341, 2010.

[29] Paul Roepman, Lodewyk FA Wessels, Nienke Kettelarij, Patrick Kemmeren, Antony J Miles, Philip Lijnzaad, Marcel GJ Tilanus, Ronald Koole, Gert-Jan Hordijk, Peter C van der Vliet, et al. An expression profile for diagnosis of lymph

node metastases from primary head and neck squamous cell carcinomas. *Nature Genetics*, 37(2):182–186, 2005.

[30] MWM Van den Brekel, JA Castelijns, HV Stel, RP Golding, CJL Meyer, and GB Snow. Modern imaging techniques and ultrasound-guided aspiration cytology for the assessment of neck node metastases: a prospective comparative study. *European Archives of Oto-Rhino-Laryngology*, 250(1):11–17, 1993.

[31] Hisham Mehanna, Wai-Lup Wong, Christopher C McConkey, Joy K Rahman, Max Robinson, Andrew GJ Hartley, Christopher Nutting, Ned Powell, Hoda Al-Booz, Martin Robinson, et al. PET-CT surveillance versus neck dissection in advanced head and neck cancer. *New England Journal of Medicine*, 2016.

[32] Alexey Surov, Hans Jonas Meyer, Matthias Gawlitza, Anne-Kathrin Höhn, Andreas Boehm, Thomas Kahn, and Patrick Stumpp. Correlations between DCE MRI and histopathological parameters in head and neck squamous cell carcinoma. *Translational Oncology*, 10(1):17–21, 2017.

[33] Aleksandar F. Dragovic, Jimmy J. Caudell, Sharon A. Spencer, William R. Carroll, Lisle A. Nabell, and James A. Bonner. Locoregional failure and the risk of distant metastasis after modern radiotherapy for head and neck cancer. *Head & Neck*, 35(3):381–387, 2013.

[34] RL Bhalavat, AR Fakih, RC Mistry, and U Mahantshetty. Radical radiation vs surgery plus post-operative radiation in advanced (resectable) supraglottic larynx and pyriform sinus cancers: a prospective randomized study. *European Journal of Surgical Oncology (EJSO)*, 29(9):750–756, 2003.

[35] Gregory T Wolf, Waun Ki Hong, Susan Gross Fisher, Susan Urba, James W Endicott, Lanny Close, Samuel R Fisher, Robert J Toohill, Daniel Karp, Donald M Miller, et al. Induction chemotherapy plus radiation compared with surgery plus radiation in patients with advanced laryngeal cancer. *New England Journal of Medicine*, 324(24):1685–1690, 1991.

[36] Peter Vaupel and Arnulf Mayer. Hypoxia in cancer: significance and impact on clinical outcome. *Cancer and Metastasis Reviews*, 26(2):225–239, 2007.

[37] Marianne Nordsmark, Sren M. Bentzen, Volker Rudat, David Brizel, Eric Lartigau, Peter Stadler, Axel Becker, Markus Adam, Michael Molls, Juergen Dunst, David J. Terris, and Jens Overgaard. Prognostic value of tumor oxygenation in 397 head and neck tumors after primary radiation therapy. An international multi-center study. *Radiotherapy and Oncology*, 77(1):18 – 24, 2005.

[38] James L Tatum. Hypoxia: importance in tumor biology, noninvasive measurement by imaging, and value of its measurement in the management of cancer therapy. *International Journal of Radiation Biology*, 82(10):699–757, 2006.

[39] Audrey P Fan, Karleyton C Evans, Jeffrey N Stout, Bruce R Rosen, and Elfar Adalsteinsson. Regional quantification of cerebral venous oxygenation from MRI susceptibility during hypercapnia. *NeuroImage*, 104:146–155, 2015.

[40] Robert M Weisskoff and Suzanne Kiihne. MRI susceptometry: Image-based measurement of absolute susceptibility of MR contrast agents and human blood. *Magnetic Resonance in Medicine*, 24(2):375–383, 1992.

[41] Douglas A Fein, W Robert Lee, Alexandra L Hanlon, John A Ridge, Corey J Langer, Walter J Curran Jr, and Lawrence R Coia. Pretreatment hemoglobin level influences local control and survival of T1-T2 squamous cell carcinomas of the glottic larynx. *Journal of Clinical Oncology*, 13(8):2077–2083, 1995.

[42] CJ Seda, AS Salas, Cristina García Sánchez, JM Blasco, IO García, JM Sánchez, CB Ruíz, SM Navarro, and RA López. Thrombocytosis and hematocrit as prognostic factors in renal carcinoma. *Arch Esp Urol*, 64(9):883–890, 2011.

[43] Mark W Dewhirst, CY Tso, Regina Oliver, Cindy S Gustafson, Timothy W Secomb, and Joseph F Gross. Morphologic and hemodynamic comparison of tumor and healing normal tissue microvasculature. *International Journal of Radiation Oncology* Biology* Physics*, 17(1):91–99, 1989.

[44] Takuya Hinoda, Yasutaka Fushimi, Tomohisa Okada, Koji Fujimoto, Chunlei Liu, Akira Yamamoto, Tsutomu Okada, Aki Kido, and Kaori Togashi. Quantitative susceptibility mapping at 3 T and 1.5 T: Evaluation of consistency and reproducibility. *Investigative radiology*, 50(8):522–530, 2015.

[45] Atsushi Ogasawara, Shingo Kakeda, Keita Watanabe, Satoru Ide, Issei Ueda, Yu Murakami, Junji Moriya, Koichiro Futatsuya, Toru Sato, Shingo Nakayamada, et al. Quantitative susceptibility mapping in patients with systemic lupus erythematosus: detection of abnormalities in normal-appearing basal ganglia. *European Radiology*, 26(4):1056–1063, 2016.

[46] Kofi Deh, Thanh D Nguyen, Sarah Eskreis-Winkler, Martin R Prince, Pascal Spincemaille, Susan Gauthier, Ilhami Kovanlikaya, Yan Zhang, and Yi Wang. Reproducibility of quantitative susceptibility mapping in the brain at two field strengths from two vendors. *Journal of Magnetic Resonance Imaging*, 42(6):1592–1600, 2015.

[47] P-Y Lin, T-C Chao, and M-L Wu. Quantitative susceptibility mapping of human brain at 3T: a multisite reproducibility study. *American Journal of Neuroradiology*, 36(3):467–474, 2015.

[48] Xiang Feng, Andreas Deistung, and Jürgen R Reichenbach. Quantitative susceptibility mapping (QSM) and R2* in the human brain at 3 T: Evaluation of intra-scanner repeatability. *Zeitschrift für Medizinische Physik*, 28(1):36–48, 2018.

[49] Rafal Panek, Liam Welsh, Alex Dunlop, Kee H Wong, Angela M Riddell, Dow-Mu Koh, Maria A Schmidt, Simon Doran, Dualta Mcquaid, Georgina Hopkinson, et al. Repeatability and sensitivity of measurements in patients with head and neck squamous cell carcinoma at 3T. *Journal of Magnetic Resonance Imaging*, 44(1):72–80, 2016.

[50] Mahesh A Varia, Dennise P Calkins-Adams, Lillian H Rinker, Andrew S Kennedy, Debra B Novotny, Wesley C Fowler, and James A Raleigh. Pimonidazole: a novel hypoxia marker for complementary study of tumor hypoxia and cell proliferation in cervical carcinoma. *Gynecologic Oncology*, 71(2):270–277, 1998.

[51] Hilde LK Janssen, Karin MG Haustermans, Debbie Sprong, Gerard Blommestijn, Ingrid Hofland, Frank J Hoebers, Elke Blijweert, James A Raleigh, Gregg L Semenza, Mahesh A Varia, et al. Hif-1α, pimonidazole, and iododeoxyuridine to estimate hypoxia and perfusion in human head-and-neck tumors. *International Journal of Radiation Oncology* Biology* Physics*, 54(5):1537–1549, 2002.

[52] Mary C Frates, Carol B Benson, J William Charboneau, Edmund S Cibas, Orlo H Clark, Beverly G Coleman, John J Cronan, Peter M Doubilet, Douglas B Evans, John R Goellner, et al. Management of thyroid nodules detected at US: Society of Radiologists in Ultrasound consensus conference statement. *Radiology*, 237(3):794–800, 2005.

[53] Enrico Papini, Rinaldo Guglielmi, Antonio Bianchini, Anna Crescenzi, Silvia Taccogna, Francesco Nardi, Claudio Panunzi, Roberta Rinaldi, Vincenzo Toscano, and Claudio M Pacella. Risk of malignancy in nonpalpable thyroid nodules: predictive value of ultrasound and color-Doppler features. *The Journal of Clinical Endocrinology & Metabolism*, 87(5):1941–1946, 2002.

[54] Jason D Iannuccilli, John J Cronan, and Jack M Monchik. Risk for malignancy of thyroid nodules as assessed by sonographic criteria. *Journal of Ultrasound in Medicine*, 23(11):1455–1464, 2004.

[55] Stavros K Kakkos, Chrisoula D Scopa, Apostolos K Chalmoukis, Dionissios A Karachalios, John D Spiliotis, John G Harkoftakis, Dionissios D Karavias, John A Androulakis, and Apostolos G Vagenakis. Relative risk of cancer in sonographically detected thyroid nodules with calcifications. *Journal of Clinical Ultrasound*, 28(7):347–352, 2000.

[56] Kristin A Seiberling, Jose C Dutra, Tom Grant, and Sanija Bajramovic. Role of intrathyroidal calcifications detected on ultrasound as a marker of malignancy. *The Laryngoscope*, 114(10):1753–1757, 2004.

[57] Zhaohui Lu, Yiming Mu, Haiqing Zhu, Yukun Luo, Qinglong Kong, Jingtao Dou, and Juming Lu. Clinical value of using ultrasound to assess calcification patterns in thyroid nodules. *World Journal of Surgery*, 35(1):122–127, 2011.

[58] Osamu Fukuoka, Iwao Sugitani, Aya Ebina, Kazuhisa Toda, Kazuyoshi Kawabata, and Keiko Yamada. Natural history of asymptomatic papillary thyroid microcarcinoma: time-dependent changes in calcification and vascularity during active surveillance. *World Journal of Surgery*, 40(3):529–537, 2016.

[59] Iwao Sugitani, Kazuhisa Toda, Keiko Yamada, Noriko Yamamoto, Motoko Ikenaga, and Yoshihide Fujimoto. Three distinctly different kinds of papillary thyroid microcarcinoma should be recognized: our treatment strategies and outcomes. *World Journal of Surgery*, 34(6):1222–1231, 2010.

[60] Bu Kyung Kim, Young Sik Choi, Hye Jung Kwon, Jun Seop Lee, Jae Joon Heo, You Jin Han, Yo-Han Park, and Jeong Hoon Kim. Relationship between patterns of calcification in thyroid nodules and histopathologic findings. *Endocrine Journal*, 60(2):155–160, 2013.

[61] Ferdinand Schweser, KH Herrmann, A Deistung, M Atterbury, PA Baltzer, HP Burmeister, WA Kaiser, and Jürgen Rainer Reichenbach. Quantitative magnetic susceptibility mapping (QSM) in breast disease reveals additional information for MR-based characterization of carcinoma and calcification. In *Proceedings of the International Society for Magnetic Resonance in Medicine*, 2011.

[62] Andreas Deistung, Ferdinand Schweser, Benedikt Wiestler, Mario Abello, Matthias Roethke, Felix Sahm, Wolfgang Wick, Armin Michael Nagel, Sabine Heiland, Heinz-Peter Schlemmer, et al. Quantitative susceptibility mapping differentiates between blood depositions and calcifications in patients with glioblastoma. *PLOS ONE*, 8(3):e57924, 2013.

[63] Weiwei Chen, Wenzhen Zhu, IIhami Kovanlikaya, Arzu Kovanlikaya, Tian Liu, Shuai Wang, Carlo Salustri, and Yi Wang. Intracranial calcifications and hemorrhages: characterization with quantitative susceptibility mapping. *Radiology*, 270(2):496–505, 2014.

[64] Alexey V Dimov, Tian Liu, Pascal Spincemaille, Jacob S Ecanow, Huan Tan, Robert R Edelman, and Yi Wang. Joint estimation of chemical shift and quantitative susceptibility mapping (chemical QSM). *Magnetic Resonance in Medicine*, 73(6):2100–2110, 2015.

[65] Michel Neidhart, Xenofon Baraliakos, Christian Seemayer, Caren Zelder, Renate E Gay, Beat A Michel, Heinrich Boehm, Steffen Gay, and Jürgen Braun. Expression of cathepsin K and matrix metalloproteinase 1 indicate persistent osteodestructive activity in long-standing ankylosing spondylitis. *Annals of the rheumatic diseases*, 68(8):1334–1339, 2009.

[66] Jürgen Braun and Joachim Sieper. Ankylosing spondylitis. *The Lancet*, 369(9570):1379–1390, 2007.

[67] Corinne Fisher, Yiannis Ioannou, Margaret Hall-Craggs, and Debajit Sen. Enthesitis related arthritis; a new era of understanding. *Ann Paediatr Rheum*, 1(1):8–16, 2012.

[68] Walter P Maksymowych, Robert D Inman, David Salonen, Suhkvinder S Dhillon, Martin Williams, Millicent Stone, Barbara Conner-spady, Janice Palsat, and Robert GW Lambert. Spondyloarthritis research Consortium of Canada magnetic resonance imaging index for assessment of sacroiliac joint inflammation in ankylosing spondylitis. *Arthritis Care & Research*, 53(5):703–709, 2005.

[69] Walter P Maksymowych, Stephanie Wichuk, Praveena Chiowchanwisawakit, Robert G Lambert, and Susanne J Pedersen. Development and preliminary validation of the spondyloarthritis research consortium of Canada magnetic resonance imaging sacroiliac joint structural score. *The Journal of rheumatology*, 42(1):79–86, 2015.

[70] M Rudwaleit, S Schwarzlose, ES Hilgert, J Listing, J Braun, and J Sieper. MRI in predicting a major clinical response to anti-tumour necrosis factor treatment in ankylosing spondylitis. *Annals of the rheumatic diseases*, 67(9):1276–1281, 2008.

[71] Timothy JP Bray, Alan Bainbridge, Shonit Punwani, Yiannis Ioannou, and Margaret A Hall-Craggs. Simultaneous quantification of bone edema/adiposity and structure in inflamed bone using chemical shift-encoded MRI in spondyloarthritis. *Magnetic resonance in medicine*, 79(2):1031–1042, 2018.

[72] Huanzhou Yu, Ann Shimakawa, Charles A McKenzie, Ethan Brodsky, Jean H Brittain, and Scott B Reeder. Multiecho water-fat separation and simultaneous R2* estimation with multifrequency fat spectrum modeling. *Magnetic Resonance in Medicine*, 60(5):1122–1134, 2008.

[73] Filippo Del Grande, Francesco Santini, Daniel A Herzka, Michael R Aro, Cooper W Dean, Garry E Gold, and John A Carrino. Fat-suppression techniques for 3-T MR imaging of the musculoskeletal system. *Radiographics*, 34(1):217–233, 2014.

[74] ISMRM Fat-Water Separation Workshop: `http://www.ismrm.org/workshops/FatWater12/`.

[75] Houchun Harry Hu, Peter Börnert, Diego Hernando, Peter Kellman, Jingfei Ma, Scott Reeder, and Claude Sirlin. ISMRM workshop on fat–water separation: insights, applications and progress in MRI. *Magnetic Resonance in Medicine*, 68(2):378–388, 2012.

[76] Johan Berglund, Lars Johansson, Håkan Ahlström, and Joel Kullberg. Three-point dixon method enables whole-body water and fat imaging of obese subjects. *Magnetic Resonance in Medicine*, 63(6):1659–1668, 2010.

[77] Jingfei Ma. Dixon techniques for water and fat imaging. *Journal of Magnetic Resonance Imaging*, 28(3):543–558, 2008.

[78] Diego Hernando, P Kellman, JP Haldar, and Z-P Liang. Robust water/fat separation in the presence of large field inhomogeneities using a graph cut algorithm. *Magnetic Resonance in Medicine*, 63(1):79–90, 2010.

[79] Chen Cui, Xiaodong Wu, John D Newell, and Mathews Jacob. Fat water decomposition using globally optimal surface estimation (GOOSE) algorithm. *Magnetic Resonance in Medicine*, 73(3):1289–1299, 2015.

[80] Junmin Liu and Maria Drangova. Method for B0 off-resonance mapping by non-iterative correction of phase-errors (B0-NICE). *Magnetic Resonance in Medicine*, 74(4):1177–1188, 2015.

[81] Jianwu Dong, Tian Liu, Feng Chen, Dong Zhou, Alexey Dimov, Ashish Raj, Qiang Cheng, Pascal Spincemaille, and Yi Wang. Simultaneous phase unwrapping and removal of chemical shift (SPURS) using graph cuts: application in quantitative susceptibility mapping. *IEEE Transactions on Medical Imaging*, 34(2):531–540, 2015.

[82] Huanzhou Yu, Charles A McKenzie, Ann Shimakawa, Anthony T Vu, Anja Brau, Philip J Beatty, Angel R Pineda, Jean H Brittain, and Scott B Reeder. Multi-echo reconstruction for simultaneous water-fat decomposition and T2* estimation. *Journal of Magnetic Resonance Imaging*, 26(4):1153–1161, 2007.

[83] Simon Robinson, Horst Schödl, and Siegfried Trattnig. A method for unwrapping highly wrapped multi-echo phase images at very high field: UMPIRE. *Magnetic Resonance in Medicine*, 72(1):80–92, 2014.

[84] H. Gudbjartsson and S. Patz. The Rician distribution of noisy MRI data. *Magnetic Resonance in Medicine*, 34(6):910–914, 1995. cited By 0.

[85] Tian Liu, Cynthia Wisnieff, Min Lou, Weiwei Chen, Pascal Spincemaille, and Yi Wang. Nonlinear formulation of the magnetic field to source relationship for robust quantitative susceptibility mapping. *Magnetic Resonance in Medicine*, 69(2):467–476, 2013.

[86] MRI Research Lab Cornell. MEDI toolbox: `http://weill.cornell.edu/mri/pages/qsm.html`.

[87] Bryan Kressler, Ludovic de Rochefort, Tian Liu, Pascal Spincemaille, Quan Jiang, and Yi Wang. Nonlinear regularization for per voxel estimation of magnetic susceptibility distributions from MRI field maps. *IEEE Transactions on Medical Imaging*, 29(2):273, 2010.

[88] Stephan Witoszynskyj, Alexander Rauscher, Jürgen R Reichenbach, and Markus Barth. Phase unwrapping of MR images using Phi UN-a fast and robust region growing algorithm. *Medical Image Analysis*, 13(2):257–268, 2009.

[89] Wei Xu and Ian Cumming. A region-growing algorithm for InSAR phase unwrapping. *IEEE T. Geoscience and Remote Sensing*, 37(1):124–134, 1999.

[90] Hussein S. Abdul-Rahman, Munther A. Gdeisat, David R. Burton, Michael J. Lalor, Francis Lilley, and Christopher J. Moore. Fast and robust three-dimensional best path phase unwrapping algorithm. *Appl. Opt.*, 46(26):6623–6635, 2007.

[91] R. Cusack and N. Papadakis. New robust 3-D phase unwrapping algorithms: Application to magnetic field mapping and undistorting echoplanar images. *NeuroImage*, 16(3, Part A):754 – 764, 2002.

[92] Mark Jenkinson. Fast, automated, N-dimensional phase-unwrapping algorithm. *Magnetic Resonance in Medicine*, 49(1):193–197, 2003.

[93] Simon Daniel Robinson, Kristian Bredies, Diana Khabipova, Barbara Dymerska, José P Marques, and Ferdinand Schweser. An illustrated comparison of processing methods for MR phase imaging and QSM: combining array coil signals and phase unwrapping. *NMR in Biomedicine*, 2016.

[94] FSL PRELUDE: `http://fsl.fmrib.ox.ac.uk/fsl/fslwiki/FUGUE/Guide`.

[95] Marvin A. Schofield and Yimei Zhu. Fast phase unwrapping algorithm for interferometric applications. *Opt. Lett.*, 28(14):1194–1196, 2003.

[96] Ferdinand Schweser, Andreas Deistung, Karsten Sommer, and Jürgen Rainer Reichenbach. Toward online reconstruction of quantitative susceptibility maps: Superfast dipole inversion. *Magnetic Resonance in Medicine*, 69(6):1581–1593, 2013.

[97] Emma Biondetti. Optimising MRI susceptibility mapping to image brain arteriovenous malformations. Upgrade thesis, University College London, UK, 2016.

[98] Emma Biondetti, David L Thomas, and Karin Shmueli. Application of Laplacian-based methods to multi-echo phase data for accurate susceptibility mapping. In *Proceedings of ISMRM 24th Annual Meeting, Singapore*, page 1547, 2016.

[99] Ferdinand Schweser, Simon Daniel Robinson, Ludovic de Rochefort, Wei Li, and Kristian Bredies. An illustrated comparison of processing methods for phase MRI and QSM: removal of background field contributions from sources outside the region of interest. *NMR in Biomedicine*, 30(4):e3604, 2017.

[100] Douglas C Noll, Dwight G Nishimura, and Albert Macovski. Homodyne detection in magnetic resonance imaging. *IEEE Transactions on Medical Imaging*, 10(2):154–163, 1991.

[101] Y. Wang, Y. Yu, D. Li, K.T. Bae, J.J. Brown, W. Lin, and E.M. Haacke. Artery and vein separation using susceptibility-dependent phase in contrast-enhanced MRA. *Journal of Magnetic Resonance Imaging*, 12(5):661–670, 2000.

[102] E. Mark Haacke, Yingbiao Xu, Yu-Chung N. Cheng, and Jürgen R. Reichenbach. Susceptibility weighted imaging (SWI). *Magnetic Resonance in Medicine*, 52(3):612–618, 2004.

[103] Ferdinand Schweser, Andreas Deistung, Berengar Wendel Lehr, and Jürgen R. Reichenbach. Quantitative imaging of intrinsic magnetic tissue properties using MRI signal phase: An approach to in vivo brain iron metabolism? *NeuroImage*, pages 2789–2807, 2011.

[104] Bing Wu, Wei Li, Arnaud Guidon, and Chunlei Liu. Whole brain susceptibility mapping using compressed sensing. *Magnetic Resonance in Medicine*, 67(1):137–147, 2012.

[105] STI Suite software package: `http://people.duke.edu/~cl160/`.

[106] Hongjiang Wei, Yuyao Zhang, Eric Gibbs, Nan-Kuei Chen, Nian Wang, and Chunlei Liu. Joint 2D and 3D phase processing for quantitative susceptibility mapping: application to 2D echo-planar imaging. *NMR in Biomedicine*, 2016.

[107] Dong Zhou, Tian Liu, Pascal Spincemaille, and Yi Wang. Background field removal by solving the Laplacian boundary value problem. *NMR in Biomedicine*, 27(3):312–319, 2014.

[108] Yan Wen, Dong Zhou, Tian Liu, Pascal Spincemaille, and Yi Wang. An iterative spherical mean value method for background field removal in MRI. *Magnetic Resonance in Medicine*, 72(4):1065–1071, 2014.

[109] Tian Liu, Ildar Khalidov, Ludovic de Rochefort, Pascal Spincemaille, Jing Liu, A John Tsiouris, and Yi Wang. A novel background field removal method for MRI using projection onto dipole fields (PDF). *NMR in Biomedicine*, 24(9):1129–1136, 2011.

[110] Sam Wharton, Andreas Schäfer, and Richard Bowtell. Susceptibility mapping in the human brain using threshold-based k-space division. *Magnetic Resonance in Medicine*, 63(5):1292–1304, 2010.

[111] Hongfu Sun and Alan H. Wilman. Background field removal using spherical mean value filtering and Tikhonov regularization. *Magnetic Resonance in Medicine*, 71(3):1151–1157, 2014.

[112] Tian Liu, Pascal Spincemaille, Ludovic de Rochefort, Bryan Kressler, and Yi Wang. Calculation of susceptibility through multiple orientation sampling (COSMOS): A method for conditioning the inverse problem from measured magnetic field map to susceptibility source image in MRI. *Magnetic Resonance in Medicine*, 61(1):196–204, 2009.

[113] Christian Langkammer, Ferdinand Schweser, Karin Shmueli, Christian Kames, Xu Li, Li Guo, Carlos Milovic, Jinsuh Kim, Hongjiang Wei, Kristian Bredies, et al. Quantitative susceptibility mapping: report from the 2016 reconstruction challenge. *Magnetic Resonance in Medicine*, 79(3):1661–1673, 2018.

[114] Ludovic de Rochefort, Tian Liu, Bryan Kressler, Jing Liu, Pascal Spincemaille, Vincent Lebon, Jianlin Wu, and Yi Wang. Quantitative susceptibility map reconstruction from MR phase data using bayesian regularization: Validation and application to brain imaging. *Magnetic Resonance in Medicine*, 63(1):194–206, 2010.

[115] Wei Li, Bing Wu, and Chunlei Liu. Quantitative susceptibility mapping of human brain reflects spatial variation in tissue composition. *NeuroImage*, pages 1645–1656, 2011.

[116] Christopher C Paige and Michael A Saunders. LSQR: An algorithm for sparse linear equations and sparse least squares. *ACM Transactions on Mathematical Software*, 8(1):43–71, 1982.

[117] Wei Li, Nian Wang, Fang Yu, Hui Han, Wei Cao, Rebecca Romero, Bundhit Tantiwongkosi, Timothy Q Duong, and Chunlei Liu. A method for estimating and removing streaking artifacts in quantitative susceptibility mapping. *Neuroimage*, 108:111–122, 2015.

[118] Chunlei Liu, Wei Li, Karen A Tong, Kristen W Yeom, and Samuel Kuzminski. Susceptibility-weighted imaging and quantitative susceptibility mapping in the brain. *Journal of magnetic resonance imaging*, 42(1):23–41, 2015.

[119] Berkin Bilgic, Adolf Pfefferbaum, Torsten Rohlfing, Edith V Sullivan, and Elfar Adalsteinsson. MRI estimates of brain iron concentration in normal aging using quantitative susceptibility mapping. *NeuroImage*, 59(3):2625–2635, 2012.

[120] Jing Liu, Tian Liu, Ludovic de Rochefort, James Ledoux, Ildar Khalidov, Weiwei Chen, A. John Tsiouris, Cynthia Wisnieff, Pascal Spincemaille, Martin R. Prince, and Yi Wang. Morphology enabled dipole inversion for quantitative susceptibility mapping using structural consistency between the magnitude image and the susceptibility map. *NeuroImage*, 59(3):2560 – 2568, 2012.

[121] Per Christian Hansen and Dianne Prost O'Leary. The use of the L-curve in the regularization of discrete ill-posed problems. *SIAM Journal on Scientific Computing*, 14(6):1487–1503, 1993.

[122] WA Edelstein, GH Glover, CJ Hardy, and RW Redington. The intrinsic signal-to-noise ratio in NMR imaging. *Magnetic Resonance in Medicine*, 3(4):604–618, 1986.

[123] Harry H Ku. Notes on the use of propagation of error formulas. *Journal of Research of the National Bureau of Standards*, 70(4), 1966.

[124] Olaf Dietrich, José G Raya, Scott B Reeder, Maximilian F Reiser, and Stefan O Schoenberg. Measurement of signal-to-noise ratios in MR images: influence of multichannel coils, parallel imaging, and reconstruction filters. *Journal of Magnetic Resonance Imaging: An Official Journal of the International Society for Magnetic Resonance in Medicine*, 26(2):375–385, 2007.

[125] Emma Biondetti, Anita Karsa, David L Thomas, and Karin Shmueli. Evaluating the precision of multi-echo combination methods for susceptibility mapping by analysing the propagation of single-echo phase noise into multi-echo field and susceptibility maps. In *Proceedings of ISMRM 26th Annual Meeting, Paris*, page 2191, 2018.

[126] Yi Wang and Tian Liu. Quantitative susceptibility mapping (QSM): decoding MRI data for a tissue magnetic biomarker. *Magnetic Resonance in Medicine*, 73(1):82–101, 2015.

[127] JR Reichenbach, F Schweser, B Serres, and A Deistung. Quantitative susceptibility mapping: concepts and applications. *Clinical Neuroradiology*, 25(2):225–230, 2015.

[128] E Mark Haacke, Saifeng Liu, Sagar Buch, Weili Zheng, Dongmei Wu, and Yongquan Ye. Quantitative susceptibility mapping: current status and future directions. *Magnetic Resonance Imaging*, 33(1):1–25, 2015.

[129] Sarah Eskreis-Winkler, Yan Zhang, Jingwei Zhang, Zhe Liu, Alexey Dimov, Ajay Gupta, and Yi Wang. The clinical utility of qsm: disease diagnosis, medical management, and surgical planning. *NMR in Biomedicine*, 30(4):e3668, 2017.

[130] Jyrki Ahveninen, Wei-Tang Chang, Samantha Huang, Boris Keil, Norbert Kopco, Stephanie Rossi, Giorgio Bonmassar, Thomas Witzel, and Jonathan R Polimeni. Intracortical depth analyses of frequency-sensitive regions of human auditory cortex using 7T fMRI. *NeuroImage*, 143:116–127, 2016.

[131] John Ashburner. Preparing fMRI data for statistical analysis. *fMRI Techniques and Protocols*, pages 155–181, 2016.

[132] Paulo Branco, Daniela Seixas, and São Luís Castro. Temporal reliability of ultra-high field resting-state MRI for single-subject sensorimotor and language mapping. *NeuroImage*, 2016.

[133] Pedro Lima Cardoso, Barbara Dymerska, Beáta Bachratá, Florian Ph S Fischmeister, Nina Mahr, Eva Matt, Siegfried Trattnig, Roland Beisteiner, and Simon Daniel Robinson. The clinical relevance of distortion correction in presurgical fMRI at 7T. *NeuroImage*, 2016.

[134] Jonathan CW Brooks, Wendy-Elizabeth Davies, and Anthony E Pickering. Resolving the brainstem contributions to attentional analgesia. *Journal of Neuroscience*, 37(9):2279–2291, 2017.

[135] Mark S Graham, Ivana Drobnjak, Mark Jenkinson, and Hui Zhang. Quantitative assessment of the susceptibility artefact and its interaction with motion in diffusion MRI. *PLOS ONE*, 12(10):e0185647, 2017.

[136] Kaikai Shen, Jurgen Fripp, Kerstin Pannek, Joanne George, Paul Colditz, Roslyn Boyd, and Stephen Rose. A spatio-temporal atlas of neonatal diffusion MRI based on kernel ridge regression. In *Biomedical Imaging (ISBI 2017), 2017 IEEE 14th International Symposium on*, pages 126–129. IEEE, 2017.

[137] Megan M Herting, Robert Kim, Kristina A Uban, Eric Kan, Andrea Binley, and Elizabeth R Sowell. Longitudinal changes in pubertal maturation and white matter microstructure. *Psychoneuroendocrinology*, 81:70–79, 2017.

[138] Venkateswaran Rajagopalan and Erik P Pioro. Differential involvement of corticospinal tract (CST) fibers in UMN-predominant ALS patients with or without cst hyperintensity: A diffusion tensor tractography study. *NeuroImage: Clinical*, 14:574–579, 2017.

[139] Reko Kemppainen, Sami Suilamo, Terhi Tuokkola, Paula Lindholm, Martin H Deppe, and Jani Keyriläinen. Magnetic resonance-only simulation and dose calculation in external beam radiation therapy: a feasibility study for pelvic cancers. *Acta Oncologica*, 56(6):792–798, 2017.

[140] Mark Jenkinson, Christian F. Beckmann, Timothy E.J. Behrens, Mark W. Woolrich, and Stephen M. Smith. FSL. *NeuroImage*, 62(2):782 – 790, 2012.

[141] Samir D Sharma, Roland Fischer, Bjoern P Schoennagel, Peter Nielsen, Hendrik Kooijman, Jin Yamamura, Gerhard Adam, Peter Bannas, Diego Hernando, and Scott B Reeder. MRI-based quantitative susceptibility mapping (QSM) and R2* mapping of liver iron overload: Comparison with SQUID-based biomagnetic liver susceptometry. *Magnetic resonance in medicine*, 78(1):264–270, 2017.

[142] Anita Karsa, Shonit Punwani, and Karin Shmueli. Fat correction of MRI phase images for accurate susceptibility mapping in the head-and-neck. In *Proceedings of ISMRM 26th Annual Meeting, Paris*, page 4988, 2018.

[143] Anita Karsa and Karin Shmueli. SEGUE: a Speedy rEgion-Growing algorithm for Unwrapping Estimated phase. In *Proceedings of ISMRM 26th Annual Meeting, Paris*, page 666, 2018.

[144] Stephen M. Smith. Fast robust automated brain extraction. *Human Brain Mapping*, 17(3):143–155, 2002.

[145] Sofia Chavez, Qing-San Xiang, and Li An. Understanding phase maps in MRI: a new cutline phase unwrapping method. *IEEE Transactions on Medical Imaging*, 21(8):966–977, 2002.

[146] C Tudisca, D Price, M Forster, H Fitzke, and S Punwani. Exploration of change of T2* of metastatic and normal cervical lymph nodes caused by 100% oxygen breathing. In *Proceedings of the 22nd Annual Meeting of the ISMRM, Milan*, page 0555, 2014.

[147] Jens Overgaard. Hypoxic modification of radiotherapy in squamous cell carcinoma of the head and neck–a systematic review and meta-analysis. *Radiotherapy and Oncology*, 100(1):22–32, 2011.

[148] Christian Langkammer, Tian Liu, Michael Khalil, Christian Enzinger, Margit Jehna, Siegrid Fuchs, Franz Fazekas, Yi Wang, and Stefan Ropele. Quantitative susceptibility mapping in multiple sclerosis. *Radiology*, 267(2):551–559, 2013.

[149] Xiaojun Guan, Min Xuan, Quanquan Gu, Peiyu Huang, Chunlei Liu, Nian Wang, Xiaojun Xu, Wei Luo, and Minming Zhang. Regionally progressive accumulation of iron in Parkinson's disease as measured by quantitative susceptibility mapping. *NMR in Biomedicine*, 30(4):e3489, 2017.

[150] Manju Liu, Saifeng Liu, Kiarash Ghassaban, Weili Zheng, Dane Dicicco, Yanwei Miao, Charbel Habib, Tarek Jazmati, and E Mark Haacke. Assessing global and regional iron content in deep gray matter as a function of age using susceptibility mapping. *Journal of Magnetic Resonance Imaging*, 44(1):59–71, 2016.

[151] Yeonsil Moon, Seol-Heui Han, and Won-Jin Moon. Patterns of brain iron accumulation in vascular dementia and Alzheimers dementia using quantitative susceptibility mapping imaging. *Journal of Alzheimer's Disease*, 51(3):737–745, 2016.

[152] Sarah Eskreis-Winkler, Kofi Deh, Ajay Gupta, Tian Liu, Cynthia Wisnieff, Moonsoo Jin, Susan A Gauthier, Yi Wang, and Pascal Spincemaille. Multiple sclerosis lesion geometry in quantitative susceptibility mapping (QSM) and phase imaging. *Journal of Magnetic Resonance Imaging*, 42(1):224–229, 2015.

[153] Jingwei Zhang, Tian Liu, Ajay Gupta, Pascal Spincemaille, Thanh D Nguyen, and Yi Wang. Quantitative mapping of cerebral metabolic rate of oxygen (CMRO2) using quantitative susceptibility mapping (QSM). *Magnetic Resonance in Medicine*, 74(4):945–952, 2015.

[154] Jeam Haroldo Oliveira Barbosa, Antonio Carlos Santos, Vitor Tumas, Manju Liu, Weili Zheng, E Mark Haacke, and Carlos Ernesto Garrido Salmon. Quantifying brain iron deposition in patients with Parkinson's disease using quantitative susceptibility mapping, R2 and R2*. *Magnetic Resonance Imaging*, 33(5):559–565, 2015.

[155] Sina Straub, Frederik B Laun, Julian Emmerich, Björn Jobke, Henrik Hauswald, Sonja Katayama, Klaus Herfarth, Heinz-Peter Schlemmer, Mark E Ladd, Christian H Ziener, et al. Potential of quantitative susceptibility mapping for detection of prostatic calcifications. *Journal of Magnetic Resonance Imaging*, 45(3):889–898, 2017.

[156] Andreas Schäfer, Birte U Forstmann, Jane Neumann, Sam Wharton, Alexander Mietke, Richard Bowtell, and Robert Turner. Direct visualization of the subthalamic nucleus and its iron distribution using high-resolution susceptibility mapping. *Human Brain Mapping*, 33(12):2831–2842, 2012.

[157] Gilles Hollander, Max C Keuken, Pierre-Louis Bazin, Marcel Weiss, Jane Neumann, Katja Reimann, Miriam Wähnert, Robert Turner, Birte U Forstmann, and Andreas Schäfer. A gradual increase of iron toward the medial-inferior tip of the subthalamic nucleus. *Human Brain Mapping*, 35(9):4440–4449, 2014.

[158] Wei Li, Chunlei Liu, and Bing Wu. Quantitative susceptibility mapping: Pulse sequence considerations. In *Proceedings of Workshop on MRI Phase Contrast and QSM, Cornell University, Ithaca New York*, page 19, 2013.

[159] Dong Zhou, Junghun Cho, Jingwei Zhang, Pascal Spincemaille, and Yi Wang. Susceptibility underestimation in a high-susceptibility phantom: Dependence on imaging resolution, magnitude contrast, and other parameters. *Magnetic Resonance in Medicine*, 78(3):1080–1086, 2017.

[160] H Sun, P Seres, and AH Wilman. Structural and functional quantitative susceptibility mapping from standard fMRI studies. *NMR in Biomedicine*, 30(4):e3619, 2017.

[161] Ahmed M Elkady, Hongfu Sun, and Alan H Wilman. Importance of extended spatial coverage for quantitative susceptibility mapping of iron-rich deep gray matter. *Magnetic Resonance Imaging*, 34(4):574–578, 2016.

[162] Anita Karsa, Emma Biondetti, Shonit Punwani, and Karin Shmueli. The effect of large slice thickness and spacing and low coverage on the accuracy of susceptibility mapping. In *Proceedings of the 24th Annual Meeting of the ISMRM, Singapore*, page 1555, 2016.

[163] Anita Karsa, Shonit Punwani, and Karin Shmueli. Resolution and coverage for accurate susceptibility maps: Comparing brain images with simulations. In *Proceedings of ISMRM 25th Annual Meeting of the ISMRM, Honolulu*, page 3677, 2017.

[164] Emma Biondetti, Anita Karsa, David L Thomas, and Karin Shmueli. Evaluating the accuracy of susceptibility maps calculated from single-echo versus multi-echo gradient-echo acquisitions. In *Proceedings of ISMRM 25th Annual Meeting of the ISMRM, Honolulu*, page 1955, 2017.

[165] I George Zubal, Charles R Harrell, Eileen O Smith, Amy L Smith, and P Krischlunas. Two dedicated software, voxel-based, anthropomorphic (torso and head) phantoms. In *Proceedings of the International Workshop, National Radiological Protection Board, Chilton, UK*, pages 6–7, 1995.

[166] Ninon Burgos, M Jorge Cardoso, Kris Thielemans, Marc Modat, Stefano Pedemonte, John Dickson, Anna Barnes, Rebekah Ahmed, Colin J Mahoney, Jonathan M Schott, et al. Attenuation correction synthesis for hybrid PET-MR scanners: application to brain studies. *IEEE Transactions on Medical Imaging*, 33(12):2332–2341, 2014.

[167] University College London Centre for Medical Image Computing. Niftyweb: `http://niftyweb.cs.ucl.ac.uk/`.

[168] F Prados Carrasco, Manuel Jorge Cardoso, Ninon Burgos, CAM Wheeler-Kingshott, and Sebastien Ourselin. Niftyweb: web based platform for image processing on the cloud. page 2201. International Society for Magnetic Resonance in Medicine (ISMRM), 2016.

[169] Marc Modat, Gerard R Ridgway, Zeike A Taylor, Manja Lehmann, Josephine Barnes, David J Hawkes, Nick C Fox, and Sébastien Ourselin. Fast free-form deformation using graphics processing units. *Computer Methods and Programs in Biomedicine*, 98(3):278–284, 2010.

[170] C Granziera, A Daducci, A Donati, G Bonnier, D Romascano, A Roche, M Bach Cuadra, D Schmitter, S Klöppel, R Meuli, et al. A multi-contrast MRI study of microstructural brain damage in patients with mild cognitive impairment. *NeuroImage: Clinical*, 8:631–639, 2015.

[171] Bing Yao, Tie-Qiang Li, Peter van Gelderen, Karin Shmueli, Jacco A de Zwart, and Jeff H Duyn. Susceptibility contrast in high field MRI of human brain as a function of tissue iron content. *NeuroImage*, 44(4):1259–1266, 2009.

[172] Jason M Zhao, Chekesha S Clingman, M Johanna Närväinen, Risto A Kauppinen, and Peter van Zijl. Oxygenation and hematocrit dependence of transverse relaxation rates of blood at 3T. *Magnetic Resonance in Medicine*, 58(3):592–597, 2007.

[173] AM Peters, MJ Brookes, FG Hoogenraad, PA Gowland, ST Francis, PG Morris, and RW Bowtell. Comparison of T2* measurements in human brain at 1.5, 3 and 7 T. *Magnetic Resonance Imaging*, 25(6):748–753, 2007.

[174] J.P. Marques and R. Bowtell. Application of a Fourier-based method for rapid calculation of field inhomogeneity due to spatial variation of magnetic susceptibility. *Concepts in Magnetic Resonance Part B: Magnetic Resonance Engineering*, 25B(1):65–78, 2005.

[175] Issel Anne L Lim, Andreia V Faria, Xu Li, Johnny TC Hsu, Raag D Airan, Susumu Mori, and Peter CM van Zijl. Human brain atlas for automated region of interest selection in quantitative susceptibility mapping: application to determine iron content in deep gray matter structures. *NeuroImage*, 82:449–469, 2013.

[176] Emma Dixon, David Thomas, Anna Barnes, and Karin Shmueli. Variation of regions of interest (ROIs) using different tools for automatic ROI generation: The impact on reported magnetic susceptibility values in QSM. In *Proceedings of ISMRM 25th Annual Meeting in Honolulu*, page 3658, 2017.

[177] Sina Straub, Till M Schneider, Julian Emmerich, Martin T Freitag, Christian H Ziener, Heinz-Peter Schlemmer, Mark E Ladd, and Frederik B Laun. Suitable reference tissues for quantitative susceptibility mapping of the brain. *Magnetic Resonance in Medicine*, 78(1):204–214, 2017.

[178] Zhe Liu, Youngwook Kee, Dong Zhou, Yi Wang, and Pascal Spincemaille. Preconditioned total field inversion (TFI) method for quantitative susceptibility mapping. *Magnetic Resonance in Medicine*, 78(1):303–315, 2017.

[179] Andreas Deistung, Andreas Schäfer, Ferdinand Schweser, Uta Biedermann, Robert Turner, and Jürgen R Reichenbach. Toward in vivo histology: A comparison of quantitative susceptibility mapping (QSM) with magnitude-, phase-, and R2*-imaging at ultra-high magnetic field strength. *NeuroImage*, 65:299–314, 2013.

[180] Hongjiang Wei, Russell Dibb, Kyle Decker, Nian Wang, Yuyao Zhang, Xiaopeng Zong, Weili Lin, Daniel B Nissman, and Chunlei Liu. Investigating magnetic susceptibility of human knee joint at 7 Tesla. *Magnetic resonance in medicine*, 78(5):1933–1943, 2017.

[181] Philips Achieva 3T: `http://www.philips.co.uk/healthcare/product/HC889204/diamond-select-achieva-30t-tx-refurbished-mr-scanner`.

[182] Emma Dixon. Applications of MRI magnetic susceptibility mapping in PET-MRI brain studies. PhD thesis, University College London, UK, 2018.

[183] Christopher A Lane, Thomas D Parker, Dave M Cash, Kirsty Macpherson, Elizabeth Donnachie, Heidi Murray-Smith, Anna Barnes, Suzie Barker, Daniel G Beasley, Jose Bras, et al. Study protocol: Insight 46–a neuroscience sub-study of the MRC national survey of health and development. *BMC neurology*, 17(1):75, 2017.

[184] Paul A Yushkevich, Joseph Piven, Heather Cody Hazlett, Rachel Gimpel Smith, Sean Ho, James C Gee, and Guido Gerig. User-guided 3D active contour segmentation of anatomical structures: significantly improved efficiency and reliability. *NeuroImage*, 31(3):1116–1128, 2006.

[185] ITK-SNAP software package: `www.itksnap.org`.

[186] Brian Patenaude, Stephen M Smith, David N Kennedy, and Mark Jenkinson. A Bayesian model of shape and appearance for subcortical brain segmentation. *Neuroimage*, 56(3):907–922, 2011.

[187] Ludovic de Rochefort, Ryan Brown, Martin R Prince, and YI Wang. Quantitative MR susceptibility mapping using piece-wise constant regularized inversion of the magnetic field. *Magnetic Resonance in Medicine*, 60(4):1003–1009, 2008.

[188] Shuai Wang, Tian Liu, Weiwei Chen, Pascal Spincemaille, Cynthia Wisnieff, A John Tsiouris, Wenzhen Zhu, Chu Pan, Lingyun Zhao, and Yi Wang. Noise effects in various quantitative susceptibility mapping methods. *IEEE Transactions on Biomedical Engineering*, 60(12):3441–3448, 2013.

[189] Daniel Rueckert, Luke I Sonoda, Carmel Hayes, Derek LG Hill, Martin O Leach, and David J Hawkes. Nonrigid registration using free-form deformations: application to breast MR images. *IEEE Transactions on Medical Imaging*, 18(8):712–721, 1999.

[190] Seungyong Lee, George Wolberg, and Sung Yong Shin. Scattered data interpolation with multilevel b-splines. *IEEE Transactions on Visualization and Computer Graphics*, 3(3):228–244, 1997.

[191] MATLAB b-spline: `https://uk.mathworks.com/matlabcentral/fileexchange/20057-b-spline-grid-image-and-point-based-registration`.

[192] Howard S Bloom. Minimum detectable effects: A simple way to report the statistical power of experimental designs. *Evaluation review*, 19(5):547–556, 1995.

[193] MWM Van den Brekel, HV Stel, JA Castelijns, JJ Nauta, I Van der Waal, J Valk, CJ Meyer, and GB Snow. Cervical lymph node metastasis: assessment of radiologic criteria. *Radiology*, 177(2):379–384, 1990.

[194] Lesley D McPhail and Simon P Robinson. Intrinsic susceptibility MR imaging of chemically induced rat mammary tumors: relationship to histologic assessment of hypoxia and fibrosis. *Radiology*, 254(1):110–118, 2009.

[195] Vicente Gilsanz. Bone density in children: a review of the available techniques and indications. *European journal of radiology*, 26(2):177–182, 1998.

[196] Judith Rademacher and Denis Poddubnyy. Emerging drugs for the treatment of axial spondyloarthritis. *Expert opinion on emerging drugs*, 23(1):83–96, 2018.

[197] Walter P Maksymowych, Stephanie Wichuk, Praveena Chiowchanwisawakit, Robert G Lambert, and Susanne J Pedersen. Fat metaplasia and backfill are key intermediaries in the development of sacroiliac joint ankylosis in patients with ankylosing spondylitis. *Arthritis & rheumatology*, 66(11):2958–2967, 2014.

[198] Guido M Kukuk, Kanishka Hittatiya, Alois M Sprinkart, Holger Eggers, Jürgen Gieseke, Wolfgang Block, Philipp Moeller, Winfried A Willinek, Ulrich Spengler, Jonel Trebicka, et al. Comparison between modified Dixon MRI techniques, MR spectroscopic relaxometry, and different histologic quantification methods in the assessment of hepatic steatosis. *European Radiology*, 25(10):2869–2879, 2015.

[199] Jimin Ren, Ivan Dimitrov, A Dean Sherry, and Craig R Malloy. Composition of adipose tissue and marrow fat in humans by 1H NMR at 7 Tesla. *Journal of lipid research*, 49(9):2055–2062, 2008.

[200] Alexey V Dimov, Zhe Liu, Pascal Spincemaille, Martin R Prince, Jiang Du, and Yi Wang. Bone quantitative susceptibility mapping using a chemical species–specific signal model with ultrashort and conventional echo data. *Magnetic resonance in medicine*, 79(1):121–128, 2018.

[201] Jianqi Li, Huimin Lin, Tian Liu, Zhuwei Zhang, Martin R Prince, Kelly Gillen, Xu Yan, Qi Song, Ting Hua, Xiance Zhao, et al. Quantitative susceptibility mapping (QSM) minimizes interference from cellular pathology in R2* estimation of liver iron concentration. *Journal of Magnetic Resonance Imaging*, 2018.

[202] S Majumdar, HK Genant, S Grampp, DC Newitt, V-H Truong, JC Lin, and A Mathur. Correlation of trabecular bone structure with age, bone mineral density, and osteoporotic status: in vivo studies in the distal radius using high resolution magnetic resonance imaging. *Journal of Bone and Mineral Research*, 12(1):111–118, 1997.

[203] J Sieper, M Rudwaleit, X Baraliakos, J Brandt, J Braun, R Burgos-Vargas, M Dougados, KG Hermann, R Landewe, W Maksymowych, et al. The Assessment of SpondyloArthritis international Society (ASAS) handbook: a guide to assess spondyloarthritis. *Annals of the rheumatic diseases*, 68(Suppl 2):ii1–ii44, 2009.

[204] Anita Karsa, Timothy J P Bray, Alan Bainbridge, Shonit Punwani, Margaret A Hall-Craggs, and Karin Shmueli. Bone marrow susceptibility as a marker of bone mineral density in spondyloarthritis. In *Proceedings of ISMRM 26th Annual Meeting, Paris*, page 4989, 2018.

[205] Thomas Loughran, David M Higgins, Michelle McCallum, Anna Coombs, Volker Straub, and Kieren G Hollingsworth. Improving highly accelerated fat fraction measurements for clinical trials in muscular dystrophy: origin and quantitative effect of R2* changes. *Radiology*, 275(2):570–578, 2015.

[206] DG Disler, TR McCauley, LM Ratner, CD Kesack, and JA Cooper. In-phase and out-of-phase MR imaging of bone marrow: prediction of neoplasia based on the detection of coexistent fat and water. *AJR. American journal of roentgenology*, 169(5):1439–1447, 1997.

[207] Ninon Burgos, Filipa Guerreiro, Jamie McClelland, Benoît Presles, Marc Modat, Simeon Nill, David Dearnaley, Uwe Oelfke, Antje-Christin Knopf, Sébastien Ourselin, et al. Iterative framework for the joint segmentation and CT synthesis of MR images: application to MRI-only radiotherapy treatment planning. *Physics in Medicine & Biology*, 62(11):4237, 2017.